Diffusion tensor imaging of the brain : towards quantitative clinical tools

Vikash Gupta

UNIVERSITÉ DE NICE - SOPHIA ANTIPOLIS

ÉCOLE DOCTORALE STIC
SCIENCES ET TECHNOLOGIES DE L'INFORMATION ET DE LA COMMUNICATION

T H È S E

pour obtenir le titre de

Docteur en Sciences

de l'Université Nice - Sophia Antipolis
Mention : Traitement Numérique du Signal

Préesentée et soutenue par

Vikash Gupta

Imagerie du tenseur de diffusion du cerveau: vers des outils cliniques quantitatifs.

Thèse dirigée par Xavier Pennec

préparée à l'INRIA Sophia Antipolis, Projet Asclepios

soutenue le 25 March 2015

Jury :

Rapporteurs :	Christian Barillot	-	CNRS, INRIA-Rennes
	Christophe Destrieux	-	UFR de Médecine, Université Tours
Directeur :	Xavier Pennec	-	INRIA-Sophia Antipolis
Co-Directeur :	Nicholas Ayache	-	INRIA-Sophia Antipolis
Président :	Jean-François Mangin	-	CEA, UNATI, NeuroSpin
Invité:	Matteo Vassallo	-	Centre Hospitalier de Cannes

UNIVERSITY OF NICE - SOPHIA ANTIPOLIS

DOCTORAL SCHOOL STIC

SCIENCES ET TECHNOLOGIES DE L'INFORMATION ET DE LA COMMUNICATION

P H D T H E S I S

to obtain the title of

PhD of Science

of the University of Nice - Sophia Antipolis

Specialty : Traitement Numérique du Signal

Defended by

Vikash Gupta

Diffusion tensor imaging of the brain: towards quantitative clinical tools.

Thesis Advisor: Xavier Pennec

prepared at INRIA Sophia Antipolis, Asclepios Team

defended on March 25, 2015

Jury :

Reviewers :	Christian Barillot	-	CNRS, INRIA-Rennes
	Christophe Destrieux	-	UFR de Médecine, Université Tours
Advisor :	Xavier Pennec	-	INRIA-Sophia Antipolis
Co-Advisor :	Nicholas Ayache	-	INRIA-Sophia Antipolis
President :	Jean-François Mangin	-	CEA, UNATI, NeuroSpin
Invited :	Matteo Vassallo	-	Centre Hospitalier de Cannes

Acknowledgements

I would like to express by sincere gratitude and thanks to my thesis advisor Xavier Pennec. It was because of his guidance, patience and motivation that I was able to complete my dissertation. His knowledge and enthusiasm in research has always been a source of great admiration and motivation for me and kept me pushing during these last three and a half years. I will like to thank him for answering my endless questions and taking time whenever I needed. It is a great honor and privilege to work with Xavier. Someone who is not less than a role model, a source of constant inspiration and for whom I have great personal regard and respect.

I would also like to thank my thesis reviewers Christophe Desteriux and Christian Barillot for their comments and suggestions that has gone under improving the content of the thesis. The precise and detailed comments of Prof. Desteriux on the chapters concerning neuroanatomy and MR physics were very insightful and helped me to better understand the subject. It is a great pleasure to have Jean-François Mangin on the jury of the thesis.

I would like to thank my co-supervisor Nicholas Ayache, for supporting my thesis and creating a very conducive and friendly environment in the lab for research. His involvement in the team to encourage interaction among the team members and clinicians outside the team were very useful for the progress of the thesis. I would also like to thank Isabelle Strobant for organizing the paper work for all the years and being supportive and accommodating at Asclepios.

It is impossible to complete a PhD thesis without the support of a lot of friends. I would like to express my sincere thanks to all the lab members with whom I worked and were always there to extend help and support in the time of need. I would like to thank Ezequiel Germia, Adityo Prakosa, Benoit Bleuze and Vincent Garcia for introducing me to the lab tools and answering many questions. I would also like to thank Marco Lorenzi, Christof Seiler and Herve Lombaert for sharing interesting thoughts and ideas and keeping the spirits up. I would also like to thanks Nicolas Cordier and Hakim Fadil for sharing lots of coffee, video games and game time with me. I would like to thank Bishesh Khanal for being an amazing office mate and participating in discussions and Stephanié, Liliane, Marine, Kristine, Federico Spadoni, Matthieu, Jan Margeta, Loic Le Folgoc, Rocio and Sophie. I would also like to thank Chloé Audigier for being a very good friend throughout these years. Japan was a very good trip because of Chloé and Ozan Oktay and I will always treasure the memories.

I have made some very good friends outside lab who were very supportive during all this time. I would like to thank Paula Craciun for all the nice walks, movie nights, dinners and long conversations. Knowing her is a privilege. I would like

to thank Ratnesh Kumar for all the support and discussions during his time here and the lunch escapes. I would like to thank Clara Schneberger for being awesome all this time and making me laugh when I was sad and keeping me fed and alive during the long periods of thesis writing.

I would like to thank Deepesh Agarwal who has been a part of my life and activities during last three years in France as a room mate and friend. It was a great joy to share a common space, ideas, thoughts and have multiple heated debates about life and everything around it. It was a pleasure to meet my fellow masters students Alejandro Mottini, Mauricio Jost and Rodrigo Cofre Torres who made my time in Nice fun. I would like to thank Nino Dzotsenidze and Julia Koehler, the two very important persons in my life, who have always believed in me and pushed and motivated me. Knowing them is a privilege. Sayantan Chaterjee, Karthik Anantharaman, Raktim Mitra, Mukul Singhee, Indrani Biswas, Pooja Varshneya, Satabdi Basu, Tracie Prater have been awesome and very supportive friends over all these years. I would like to thank Milind Shastri for an unbelievable support, valuable suggestions and discussions. Last but not the least I will like to thank Florence Navarro for being utterly supportive and understanding through out this last year. I treasure all these friendships.

Nothing will be possible without the support of my parents and my sister. They have supported every single decision I have made. Even though some of them were very difficult decisions, they supported my education and everything else. So, I thank them sincerely and I will always be indebted for them.
Thank you everyone!!

Abstract

The thesis explores three major methodological questions in clinical brain DTI, in the context of a clinical study on HIV. The first question is how to improve the DTI resolution. The second problem addressed in the thesis is how to create a multimodal population specific atlas. The third question is on the computation of statistics to compare white matter (WM) regions among controls and HIV patients.

Clinical DTIs have low spatial resolution and signal-to-noise ratio making it difficult to compute meaningful statistics. We propose a super-resolution (SRR) algorithm for improving DTI resolution. The SRR is achieved using anisotropic regularization prior. This method demonstrates improved fractional anisotropy and tractography.

In order to spatially normalize all images in a consistent coordinate system, we create a multimodal population specific brain atlas using the T1 and DTI images from a HIV dataset. We also transfer WM labels from an existing white matter parcellation map to create probabilistic WM atlas. This atlas can be used for region of interest based statistics and refining manual segmentation.

On the statistical analysis side, we improve the existing tract based spatial statistics (TBSS) by using DTI based registration for spatial normalization. Contrary to traditional TBSS routines, we use multivariate statistics for detecting changes in WM tracts. With the improved method it is possible to detect differences in WM regions and correlate it with the neuropschylogical test scores of the subjects.

Keywords: Clinical DTI, Super-resolution, Multimodal brain atlas, Population based statistical analysis, HIV.

Résumé

La thèse explore trois questions méthodologiques en imagerie de diffusion (DTI) clinique du cerveau, dans le contexte d'une étude sur le VIH. La première question est comment améliorer la résolution du DTI. Le deuxième problème est comment créer un atlas multimodal spécifique à la population. La troisième question porte sur le calcul des statistiques pour comparer les zones de matière blanche entre les contrôles et patients.

Les DTI cliniques ont une résolution spatiale et un rapport signal sur bruit faibles, ce qui rend difficile le calcul de statistiques significatives. Nous proposons un algorithme de super-résolution pour améliorer la résolution qui utilise un a priori spatial anisotrope. Cette méthode démontre une amélioration de l'anisotropie fractionnelle et de la tractographie.

Pour normaliser spatialement les images du cerveau dans un systéme de coordonnées commun, nous proposons ensuite de construire un atlas multimodal spécifique á la population. Ceci permet de créer un atlas probabiliste de la matière blanche qui est consistant avec l'atlas anatomique. Cet atlas peut être utilisé pour des statistiques basées sur des régions d'intérêt ou pour le raffinement d'une segmentation.

Enfin, nous améliorons les résultats de la méthode TBSS (Tract-Based Spatial Statistics) en utilisant le recalage des images DTI. Contrairement á la méthode TBSS traditionnelle, nous utilisons ici des statistiques multivariées. Nous montrons que ceci permet de détecter des différences dans les régions de matière blanche qui étaient non significatives auparavant, et de les corréler avec les scores des tests neuro-psychologiques.

Contents

List of Figures

Chapter 1

Introduction

Contents

The human body is considered to be the penultimate result of evolution. It is one of the most complex life forms nature has ever conceived. The brain is at the center stage of all activities of mankind. It is the center for all our thoughts, executive and sensory functions, voluntary and involuntary actions, control and planning. The structure and function of brain is still a less understood. It is amazing, how can we predict the motion of stars and galaxies thousands of light-years away, yet we do not completely understand the mechanisms of brain which exists inside our body. It is estimated that human brain is composed of 100 billion neurons, which make around 100 trillion synaptic connections in the brain [Zimmer 2010]. So, it is necessary that we make efforts in order to understand the brain.

A deeper understanding of brain has direct implications on the society and its future. We have come a long way in computing. The computations which used to take hours to complete can now be completed in a matter of minutes. The systems around us are becoming more and more intelligent with every passing decade. But, the complexities, intelligence and efficiency of the systems created by us does not even come close to the sophisticated design of our own brain. Why it is that we cannot create a system which is as smart as our own brain? With the advent of faster computing mechanisms it is now possible to study the brain in detail. There are several projects like the BigBrain Project, Human Connectome Project and Human Brain Project which are solely dedicated for understanding different aspects of structural and functional properties of brain.

The brain is composed of cerebrum, cerebellum and the brain stem. These three structures include both gray and white matter. It is protected inside the skull which is composed of 24 different bones. In popular images of brain we see lot of gyrations on the surface of cerebral cortex. It is believed that the cerebral cortex plays an important role in thought, attention, perpetual awareness and consciousness. Typically it is 2 to 4 millimeters in thickness. One of the main

reasons that the humans are considered "intelligent" species is because of the thickness of cerebral cortex. For lower animals (like rat) the surface of cortex is smooth and do not present as many gyrations. It is believed that as humans evolved it grew in order to accomodate more information for their day-to-day activities. Because there was no more volumetric space in skull, it started to fold and form complex gyrations on the surface. Figure 1.1 shows a comparison of brain shapes and sizes across different species.

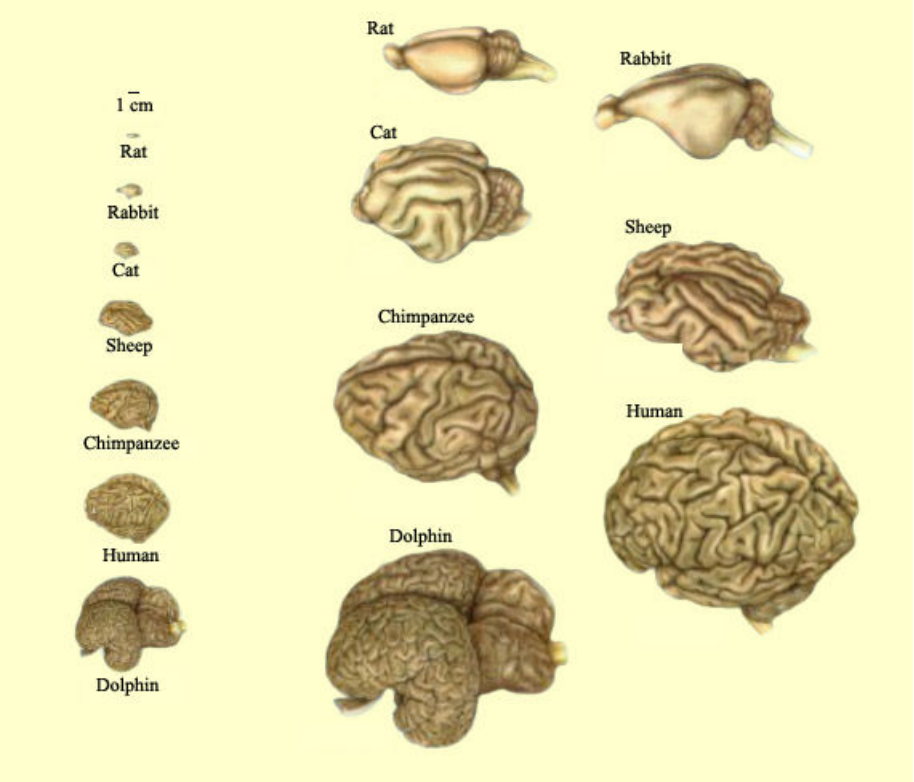

Figure 1.1: A comparison of the shape and sizes of brain across different species. The cortical gyrations increases in complexity as we move from rats, rabbits to higher and more complex species like chimpanzee, humans and dolphins. Adapted from www.thebrain.mcgill.ca

At a tissue level the brain is composed of white and grey matter. Before the development of neuroimaging techniques, dissection was the only way to study the structure of brain and its tissues. However, now it is possible to study the brain in-vivo. There are many different imaging techniques in place which are useful for studying the brain. For example, computed tomography (CT) is used to quickly view brain injuries, magnetic resonance imaging (MRI) is used for creating high resolution 3D image of the brain, functional magnetic resonance imaging (fMRI) is used to map activation in different parts of brain, positron emission tomography (PET) and single-photon emission computed tomography

(SPECT) are used for measuring blood flow and glucose metabolism in the brain tissues, perfusion imaging is used for imaging the blood flow, diffusion magnetic resonance imaging (dMRI) is used for study the white matter structures and their connections. For a complete understanding of the functions of brain these different imaging modalities should be fused in one single consistent coordinate system.

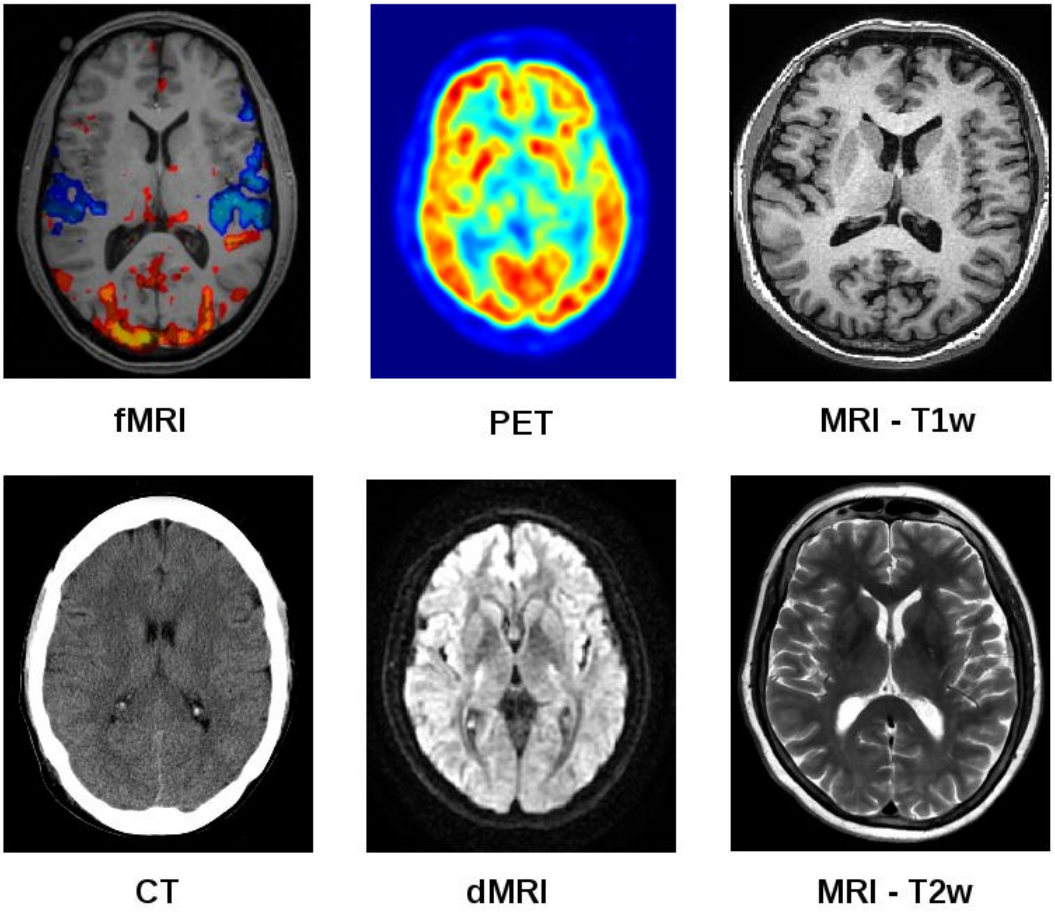

Figure 1.2: Different imaging modalities used for brain imaging. fMRI shows regions of brain activity due to visual stimulus. PET shows regional glucose use. MRI-T1w is an anatomical image of the brain. CT is used for detecting brain lesions. dMRI shows an undiffused B0 image. MRI-T2w is used for detecting white matter lesions.

The thesis will focus on diffusion tensor imaging (DTI) of the brain in a clinical setting. The diffusion tensors are second order symmetric positive definite matrices and are used to model local water diffusion in brain tissues. Water molecules diffuse preferentially along the axon of a nerve cell. DTI uses this local water diffusion to construct an image of white matter tracts using tractography algorithms. They reveal in great detail the connections between different regions of brain.

Furthermore, diffusion tensor imaging and fiber tractography allows us to compute statistical analysis on the tract geometry and diffusion properties along the tracts and across population. This kind of statistical studies are important in order to understand brain diseases associated with white matter fibers. For clinical usage, different scalar metrics like fractional anisotropy (FA), mean diffusivity (MD) and apparent diffusion coefficient (ADC) have been derived.

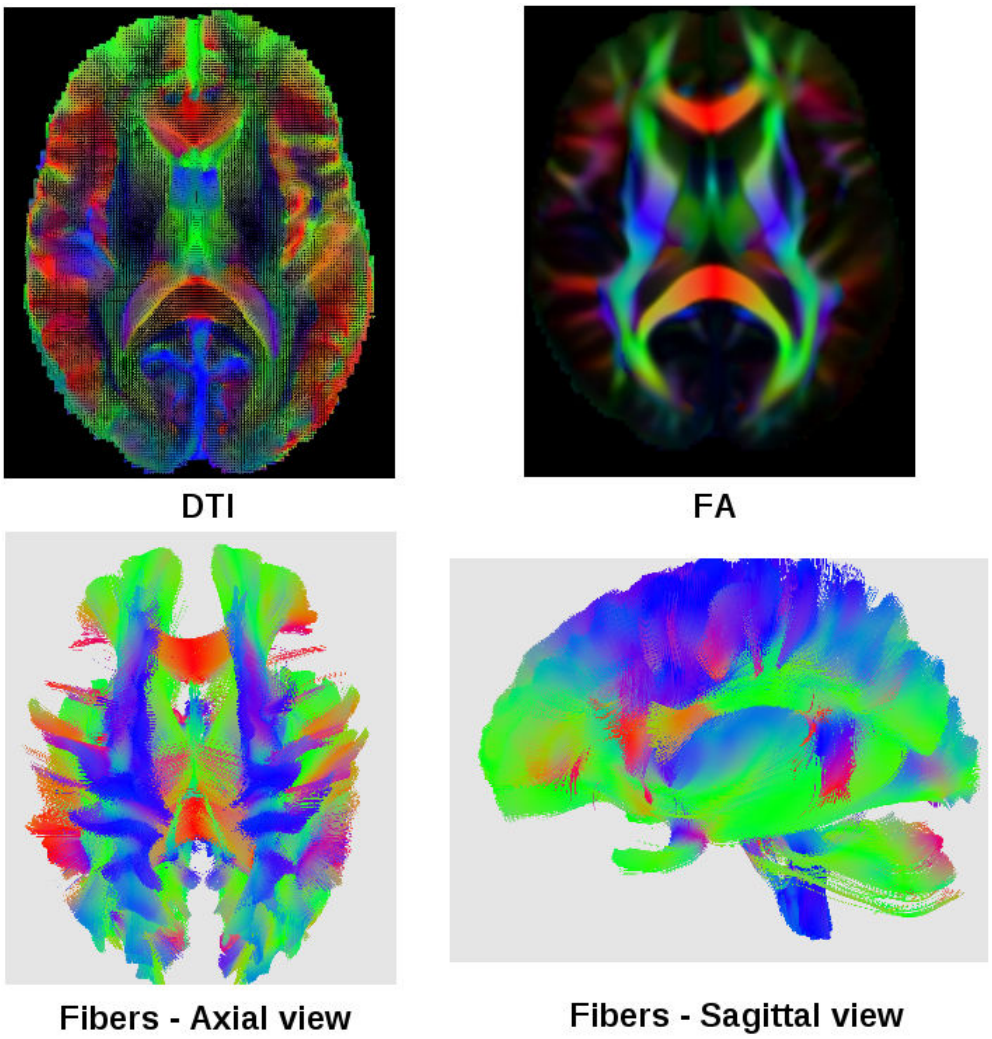

Figure 1.3: Diffusion tensor image (DTI) of the brain (top left). An associated fractional anisotropy (FA) directional map (top right). The lower row shows the axial and sagittal view of fiber tractography on DTI.

With these imaging techniques in place, it is possible to track the changes in brain over long periods of time and over a large population. Neurodegeneration is a process of progressive loss in brain tissue leading to loss in structure and function. Some examples of neurodegenerative diseases are Alzheimer's diseases,

Huntington's disease, Parkinson's disease, amyotrophic lateral sclerosis (ALS), HIV related dementia. There are many reasons for progressive neurodegeneration including normal aging, genetic mutations, proteing misfolding, accumulation of intracellular toxic proteins and disease related infections like in HIV. It is important to understand the disease progression and regions of the brain affected by them for better therapy planning and identifying the subjects in the early stages of the disease.

The thesis aims at understanding the changes in white matter regions of the brain caused by HIV/AIDS using multivariate statistical analysis on diffusion tensor images (DTIs). DTI is an imaging modality predominantly used for in-vivo imaging of white matter tracts. The clinical DTI acquisitions are often noisy and have low spatial resolution and signal-to-noise ratio. They also suffer from artifacts due to magnetic field inhomogeneity and magnetic susceptibility susceptibility. The imaging artifacts often hamper the statistical analysis negatively. An example of the low resolution scans acquired during a routine clinical acquisition is shown in figure 1.4. The image has a resolution of $0.9375 \times 0.9375 \times 5.5$ mm^3. Because of the low resolution in the Z direction, we see that it is difficult to recognize brain structures in the coronal and sagittal view.

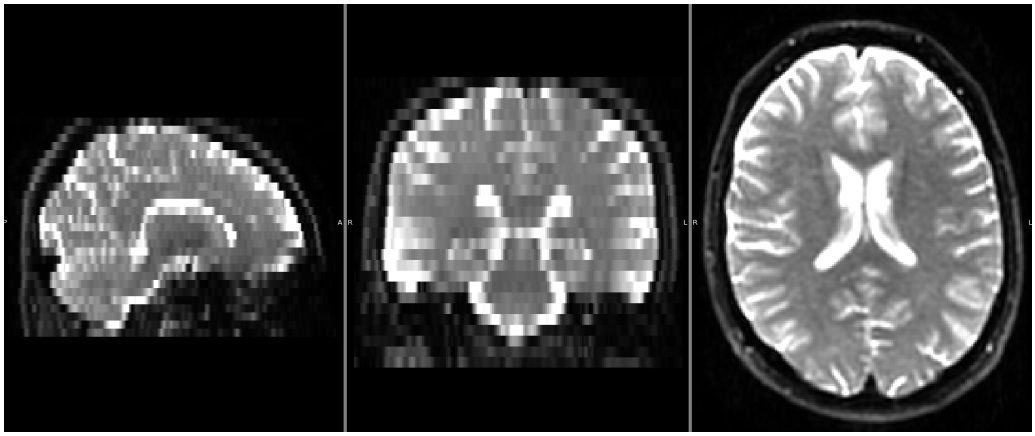

Figure 1.4: An example of B0 (undiffused) image acquired during a routine clinical DTI acquisition. We will study these clinical images in this thesis. Left: Sagittal view, Middle: Coronal view, Right: Axial view. The low resolution of the image is visible in the coronal and sagittal views. Courtesy: NEURADAPT study

Brain imaging in itself has two different aspects. On one hand, we have imaging done in research environment where there is lot of time to acquire the data multiple times with very well equipped MR scanners (typical magnetic field strength 7.0 T to 11.0 T). On the other hand, we have clinical brain images where the scans should be performed quickly in order to minimize the discomfort of the patients. For the same reasons, multiple scans are often not an option in the clinics. Also

the clinical scanners are not well equipped in terms of magnetic field strength (typically 1.5 T to 3.0 T) and scanning protocol capabilities. Thus, the challenges encountered in a clinical environment are different to that in the in these two different scenarios are totally different.

In this thesis, we will focus on clinical DTIs. The thesis presents a super-resolution method for increasing the spatial resolution of DTI. The method is suitable for clinical setting as it requires a single DTI acquisition. Further, we present a method for computing a probabilistic population specific multimodal brain atlas using the T1 and DTI images. The DTI template is used for carrying out tract based spatial statistics (TBSS) for identifying regions of differences in white matter among HIV/AIDS patients. Contrary to the traditional routines, the proposed is improved with DTI based spatial normalization and multivariate statistical tools.

1.1 HIV and the Brain

Human immunodeficiency virus (HIV) causes acquired immunodeficiency syndrome (AIDS). AIDS leads to progressive decline in the immune system leading to life-threatening infections. In the absence of treatment the life-expectancy is estimated to be around ten years depending on the HIV subtype. According to a July-2014 survey conducted by UNAIDS[1], more than 35 million people are living with HIV/AIDS. In 2013, 1.5 million people died and 240,000 people were newly infected from AIDS. Nearly every hour 240 people contract to this disease. Since its beginnings around 78 million people have contracted to HIV and around half of them have died. According to World Health Organization (WHO), the usage of combination antiretroviral therapy (cART) the disease progression can be reduced leading to huge reductions in death and suffering if the appropriate cART is administered in the early stages of the disease.

CD4 cells are a type of white blood cell which fights infection. HIV can affect the CD4 cells by binding to their surface or entering the cells and multiplying as the cells multiply. The decrease in the CD4 cell counts weakens the immune system of the body leading to eventual death. The CD4 cell count in blood and viral load is used as biomarkers to assess the level of disease progression.

HIV can cross the hematoencephalic barrier (blood-brain barrier) leading to HIV associated neurocognitive disorders (HAND). HAND causes compromised attention, long and episodic memory loss, language disorders and visual agnosia. The figure 1.5 shows regions of tissue losses in cerebral cortex of the brain. Most of the tissue losses are associated with regions controlling movement, memory and planning. Along with the cerebral cortex, HIV is believed to cause detrimental changes in white matter tracts affecting brain connectivity and cognitive loss.

[1] Joint United Nations Programme on HIV/AIDS

HIV also affects cerebral blood flow [Ances 2009], metabolism and diffusion in the central nervous system.

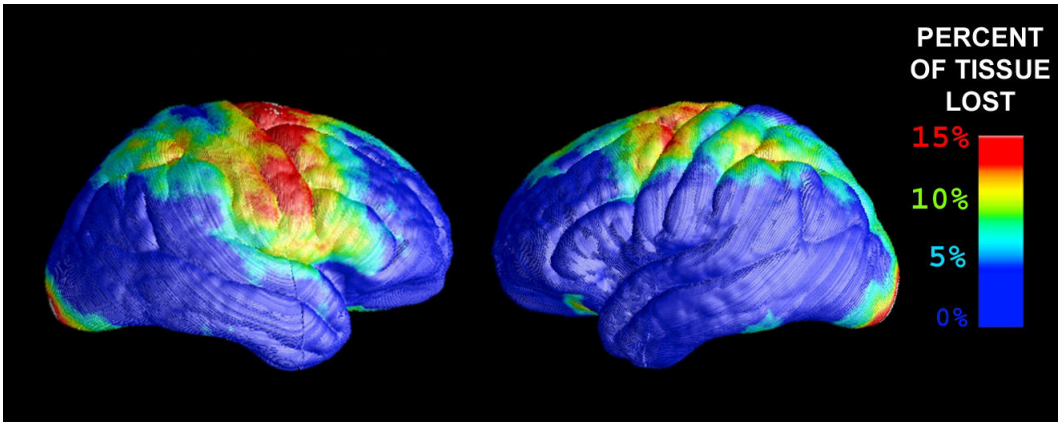

Figure 1.5: Brain tissue loss due to HIV/AIDS. Most damages are observed in regions controlling movement, memory and planning. [Thompson 2005]

HIV associated biomarkers (CD4 cells count and viral load) are not strongly correlated with the neurologic impairment and new neuroimaging biomarkers are needed to detect and follow the progression of HIV associated neurocognitive disorders [Clifford 2013]. In [Tucker 2004], the authors present a review of different neuroimaging techniques like single-photon emission computed tomography (SPECT), positron emission tomography (PET), magnetic resonance imaging (MRI), functional magnetic resonance imaging (fMRI), diffusion tensor imaging (DTI) and perfusion imaging to elucidate changes in the brain caused by HIV/AIDS. The different imaging modalities capture different aspects of changes associated with the central nervous system.

In this thesis, we assess differences in the white matter integrity between controls and HIV patients. The neurological disorders caused by HIV/AIDS are clinically assessed using neuropsychological (NP) tests. Despite the usage of cART, white matter abnormalities have been reported specifically in frontal white matter and corpus callosum [Schouten 2011]. There is a need for understanding and correlating the white matter changes in the brain with the NP test scores. Only with a clear understanding of the brain regions targeted by the HIV the search for a suitable neuroimaging biomarker can begin. Thus, an extensive statistical analysis on brain images of HIV patients is quintessential.

1.2 Clinical Context

The human brain is composed of white and gray matter. The white matter connects different regions of the brain and acts as signal highways for nerve impulses. With the advent of diffusion weighted magnetic resonance imaging (DW-MRI or dMRI), it is possible to image the white matter *in-vivo*. It is now possible to reconstruct the white matter tracts and study the connections they make among different regions of the brain. The tractography data makes it possible to study the neural architecture and navigate through the intricate brain pathways. The local diffusion of water molecules can be modeled as a second-order symmetric positive definite tensor also called the diffusion tensor. Due to the advancement in scanning technology and introduction of stronger magnets, more sophisticated techniques have also emerged such as diffusion spectral imaging (DSI), q-ball imaging and high angular resolution diffusion imaging (HARDI). The latter techniques produce high resolution diffusion images and high quality tractography data.

The advanced imaging techniques are suited in research scenarios and are not used in routine clinical setup for two primary reasons. The first reason is the longer acquisition time required by these imaging protocols, which is not feasible in a clinical setting. The second reason is that the clinical scanners are not well equipped for using the advance imaging protocols and upgrading the scanners in hospital is a very expensive undertaking. Majority of the scanners used in France has a magnetic field strength of 1.5 Tesla and relatively few have a strength of 3.0 Tesla. 3.0 Tesla scanners are now widely accepted as a clinical standard. However, we are still obtaining a lot of imaging data from 1.5 Tesla scanners. Hence, it only makes sense to continue developing tools for the retrospective studies rather than discarding the data.

Diffusion tensor imaging is the current clinical norm and looks promising for near future. The very next question one can ask is how to make population based studies on these clinical data. Furthermore, how to design an "optimal" workflow for statistical analysis on these datasets? The clinical DTIs are often plagued with a low spatial resolution, low signal-to-noise ratio (SNR), motion artifacts and geometric distortions related to magnetic susceptibility and magnetic field inhomogenity. Among the array of limitations presented by the clinical datasets, the readily available clinical data gives an opportunity to understand the disease. There is a need for developing sophisticated statistical tools that can help us understand the data and draw inferences on disease progression, changes in the white matter structure integrity due to disease and how the changes are reflected in the day-to-day functioning of an individual.

The diffusion tensors and the DTI metrics (FA, MD and ADC) are incorrectly estimated because of the partial volume effects in the low resolution clinical DTI. In order to overcome the underestimation of tensors few super-resolution

algorithms have been suggested. However, they require multiple acquisitions of the same subject. Multiple acquisitions of the same patient is not suitable in routine clinical environment because of the increased cost and discomfort to a patient. Therefore, we propose a super-resolution algorithm which uses a single clinical acquisition to improve the DTI resolution using anisotropic regularization prior.

The thesis presents an exploratory statistical analysis of DTI of HIV/AIDS subjects. The statistical analysis is done in the context of NEURADAPT study, an initiative by the Nice University Hospital. The goal of this study is to detect statistically significant differences between a cohort of HIV/AIDS patients and controls. For conducting such population based studies, we need a brain template for normalizing the data. The brain template should also be a statistical representation of the dataset. A method for building a probabilistic multimodal population specific brain template using the anatomical T1-weighted image and the diffusion tensor image has been proposed. We successfully transferred white matter labels from the ICBM white matter parcellation map on this template making room for ROI based statistics on the population. The brain template is also used for normalizing the DTI data to a common space for conducting tract based spatial statistics.

In the clinical scenario, the diffusion tensor is often reduced to scalar metrics like fractional anisotropy (FA), mean diffusivity (MD) and apparent diffusion coefficient (ADC). By doing so, we loose lot of directional information. The thesis extends the univariate statistical analysis to a multivariate full tensor based statistical analysis. We conclude that with the multivariate statistics it is possible to detect regions of white matter which were not detectable with the univariate FA based statistics. We develop robust methods to extract clinically relevant information from low quality clinical diffusion tensor images. With the proposed multivariate statistical analysis the changes observed in the white matter tracts can be correlated with the changes observed in clinical neuropsychological test scores.

1.3 Organization and contribution of the thesis

Chapter 2 presents an anatomical description of brain with a focus on white matter tracts and their functions. The chapter outlines some of the pathologies associated with specific tracts. Furthermore, it also presents a brief description about nerve cells and their structures. An understanding of different anatomical regions of brain is quintessential in understanding and localizing the changes in white matter structures caused due to HIV/AIDS.

Chapter 3 outlines the physics associated with magnetic resonance imaging and the common imaging protocols used in clinical settings. We discuss the nuclear magnetic resonance, signal localization in the brain, k-space and different k-space

filling techniques used in practice. The chapter also presents a qualitative discussion on different pulse sequences used in routine clinical practice. Furthermore, it outlines the advantages and drawbacks of each of the imaging techniques and how they can be combined as per the need of the situation.

Chapter 4 discusses a super-resolution algorithm for estimating diffusion tensors using a single low-resolution clinical quality dMRI acquisition. Since the clinical diffusion images are low in spatial resolution and suffer from partial volume effects, the diffusion tensors are underestimated. Recently few tools have emerged in the medical imaging community, which tackle the super-resolution problem using multiple image acquisition. It is often not possible to multiple acquisition of the same subject in a clinical scenario as it is both expensive and uncomfortable for a patient to go through scanner multiple times. The algorithm presented in this chapter uses single image acquisition to produce the high resolution tensor images. We show the effectiveness of the tool with improved fractional anisotropy maps and fiber tractography.

Chapter 5 discusses the construction of a population specific multimodal atlas. In this chapter, we first discuss a brief history of brain atlases in chronological order. The discussion is followed by a workflow designed to build the multimodal atlas. Such multimodal atlases can be used for finding voxel wise correspondences across different modalities. Traditionally the statistical analysis is carried out either on the anatomical T1-weighted image or on the diffusion tensor images. However, it feels intuitive that a joint study may give a higher statistical power to the analysis. For region of interest (ROI) based statistical studies, it is necessary that the regions are clearly delineated on the template. A trusted approach for defining ROIs is manual delineation by experts. However, quite often these methods are time consuming and error prone. The chapter also discusses a method to define probabilistic white matter regions. We believe that such probabilistic ROI definition could be used for ROI based statistics and serve as a guiding tool for experts during manual segmentation.

Chapter 6 presents an exploratory statistical analysis of white matter tracts to detect statistically significant differences between controls and HIV/AIDS patients. We discuss some of the statistical tools like voxel based morphometry (VBM), tensor based morphometry (TBM) and tract based spatial statistics (TBSS). The traditional TBSS methods makes voxel wise comparison of fractional anisotropy values in the white matter tract skeleton. We suggest methods to improve TBSS using DTI based normalization and multivariate analysis for comparing the controls and HIV patients. We found that using the multivariate statistical tests are more sensitive to differences between the two groups of population. The changes are correlated with the neuropsychological (NP) test scores observed in patients.

Chapter 7 presents a discussion on various insights in the context of clinical brain diffusion tensor imaging. We discuss some of the initiatives taken for

longitudinal DTI analysis on the Alzheimer's disease patients. Our initiatives failed to reach any conclusive results The reasons for non-conclusive results are discussed in this chapter. A discussion on the quality of clinical data and suggestions for future population based studies is presented. We discuss some of the prospective future work in the light of present findings incorporated in the thesis. We discuss the future of population based studies and what can be done more to have a better understanding of progressive neurodegenerative diseases.

1.4 Publications from the thesis

Conference articles

1. Vikash Gupta, Nicholas Ayache, and Xavier Pennec. Improving DTI Resolution from a Single Clinical Acquisition: A Statistical Approach using Spatial Prior. In Kensaku Mori, Ichiro Sakuma, Yoshinobu Sato, Christian Barillot, and Nassir Navab, editors, Proceedings of Medical Image Computing and Computer Assisted Intervention 2013 (MICCAI), volume 8151, Nagoya, Japan, pages 477-484, September 2013. Springer.

Invited Talks

1. Vikash Gupta, Xavier Pennec, Nicholas Ayache. Towards Higher Resolution Analysis of Clinical Brain Diffusion Images, 1st International Symposium on Deep Brain Connectomics, Clermont-Ferrand, France. 2012

Submitted

1. Vikash Gupta, Gregoire Malandain, Nicholas Ayache, and Xavier Pennec. A framework for creating population specific multimodal brain atlas using clinical T1 and diffusion tensor images, in Medical Image Computing and Computer Assisted Intervention, (MICCAI) 2015

In preparation

1. Vikash Gupta, Nicholas Ayache, and Xavier Pennec. A multivariate statistical analysis using full DTI information to detect changes in white matter among HIV/AIDS patients.

Chapter 2

Brain Anatomy: White matter tracts

Contents

2.1 Neuroanatomy

The human brain is undoubtedly one of the most complex parts of the human body. It is responsible for almost all of the voluntary actions in the human body. The brain can be broadly classified into the gray matter (GM) and white matter (WM). The gray matter consists of the neuronal cell bodies, glial cells, mylinated and unmylinated axons and blood carrying capillaries. On the contrary, the white matter is composed of long mylinated axons and are mostly responsible for connecting different regions of brain and facilitating the flow of brain signals among the different parts. The CSF is a bodily fluid, that is present in the brain and spine. The brain is literally floating in the CSF, which is also responsible for its basic mechanical and immunological protection. Even after almost 100 years of dedicated research, the functional aspects of the brain is less understood. However, the good news is that we know quite a lot today about the anatomy of the brain and its organization.

2.1.1 Lobes of the brain

The human brain is divided into left and right hemispheres by the longitudinal fissure. Each of these hemispheres are further classified into six major lobes. These

lobes refer to the different sections of the cerebrum. Before we delve into classification of white matter tracts in detail, it is important to study the different lobes of the brain because white matter fibers are responsible for connecting these different lobes. The different lobes are shown in the figure 2.1. The six lobes are frontal lobe, parietal lobe, occipital lobe, temporal lobe, limbic lobe and insular cortex. The frontal lobe is associated with motor functions, planning, reasoning, judgement, memory and impulse control. It is located in the anterior part of brain. The parietal lobe is responsible for integrating sensory information, spatial sensing and navigation. The paretial lobe is separated from the frontal, occipital and the temporal lobes by the central sulcus, parieto-occipital sulcus and the lateral sulcus respectively. The occipital lobe, is located in the rearmost part of the brain and is associated with visual processing. The last of all, i.e., temporal lobe is associated with visual memories, processing sensory input, language comprehension and storing new memories and emotions. The temporal lobes are located ventral to the lateral fissure which clearly limits them from the frontal and anterior part of the parietal lobe. Posteriorly, the temporal lobe is continued with the parietal and occipital lobes without any distinctly defined limit. The limbic lobe is a part of cerebral cortex on the medial surface of each cerebral hemisphere and is associated with emotional evaluation of several emotions like fear, anxiety and panic.

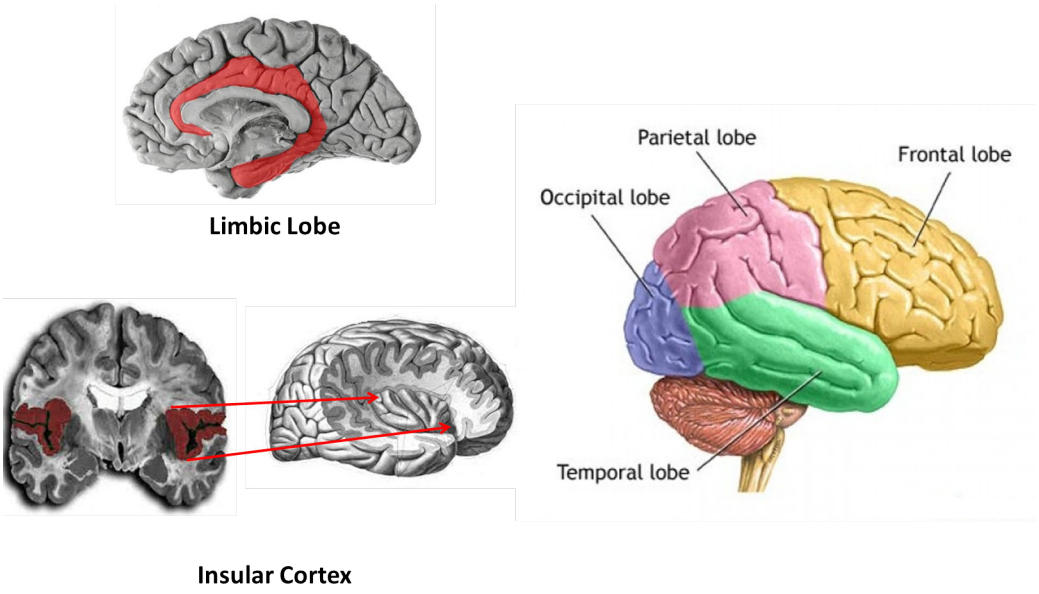

Figure 2.1: Different lobes of the brain.

2.1.2 The cells in the central nervous system

The white matter fibers connect the different regions of the brain. They are the signal carrying highways for the central nervous system (CNS). The building blocks of white matter tracts are neurons or nerve cells. It is estimated that on an

average the human brain has a hundred billion neurons and each of them has 7000 synaptic connections to the other neurons. The other type of cells in the central nervous system are called glial cells.

Glial cells are non-neuronal cells that act as a support mechanism for neurons. They supply nutrients and oxygen required for the neurons. In addition, they also provide mechanical support and destroy the pathogens and remove the dead neurons.

Neurons are the central actors in the CNS. They specialize in receiving and sending electrical signals required for normal functioning of human body. A neuron consists of three major parts: dendrites, the cell body or soma and axons. The figure 2.2 depicts different parts of a typical neuronal cell. The length of the axon of a typical neuron could be as long as few micrometers to that of two meters. The dendrites of a neuron acts as signal receivers from the axon terminal of another neurons. The axon carries the signal forward to its terminal where it is transmitted to the connecting neurons. A neuron can have multiple dendrites but it always has one single axon. The myelin sheath forms an electrical insulation around the axon and is typically composed of the glial cells. The name myelin sheath derives from the myelin, an electrically insulating material.

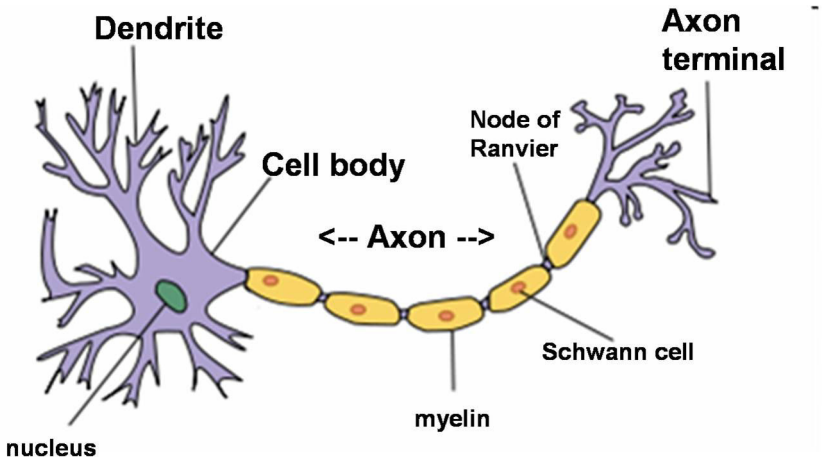

Figure 2.2: Structure of a typical neuron. The different parts of neuron: dendrite, cell body and axon. Adapted from Wikipedia

Based on the structure and polarity of nerve cells, they can be characterized into *unipolar, bipolar, multipolar* and *pyramidal* cells. The unipolar cells have a single extension form the cell body. This extension serves both as an axon and dendrite. The bipolar neuron as the name suggests has one axon and one dendrite emerging from the soma at opposite ends. The multipolar neuron are the most common types of nerve cells. The nerve cells have multiple dendrons and one single axon emerging out of soma. The figure 2.2 is a schematic representation of a multipolar

neuron. Depending on axonal length, the multipolar nerve cells are called either *type I* (cells with long projecting axon,e.g., Purkinje cells and pyramidal cells) or *type II* cells (the ones with very short axons). The pyramidal cells are characterized by a triangular shaped soma, an axon and multiple basal dendrites.

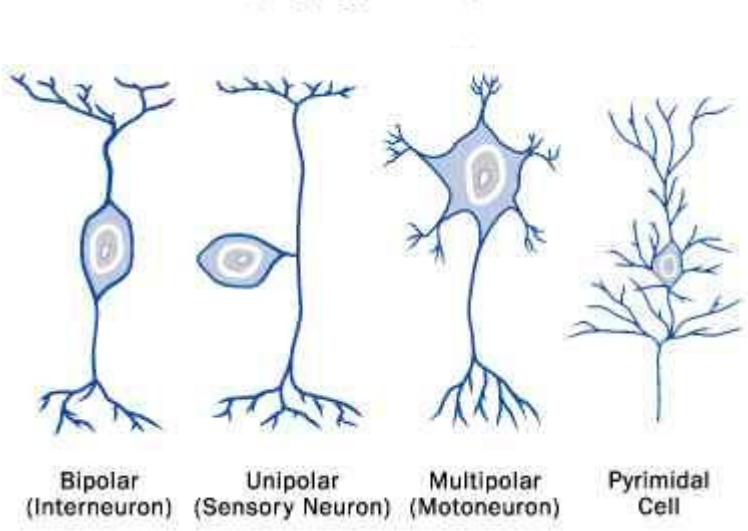

Figure 2.3: Different types of Neurons

2.2 White matter fascicles

The nerve axons form bundles and are organized as suited by the needs. Based on their functions and areas of connectivity, they are divided into three broad categories as follows,

1. Association fibers
2. Projection fibers
3. Commisural fibers

2.2.1 Association fibers

The association fibers consists of white matter tract bundles that connect different regions of cortex within the same hemisphere. The short association fibers (SAF) connect different gyri within the same lobe, whereas the long association fibers (LAF) connect the different lobes of brain. The SAF are mostly located in the peripheral white matter, whereas the LAF are situated in the deep brain. The common long association fibers are uncinate fascicles, cingulum, occipitofrontal fascicles, fornix, arcuate fascicles, and inferior longitudinal fascicles.

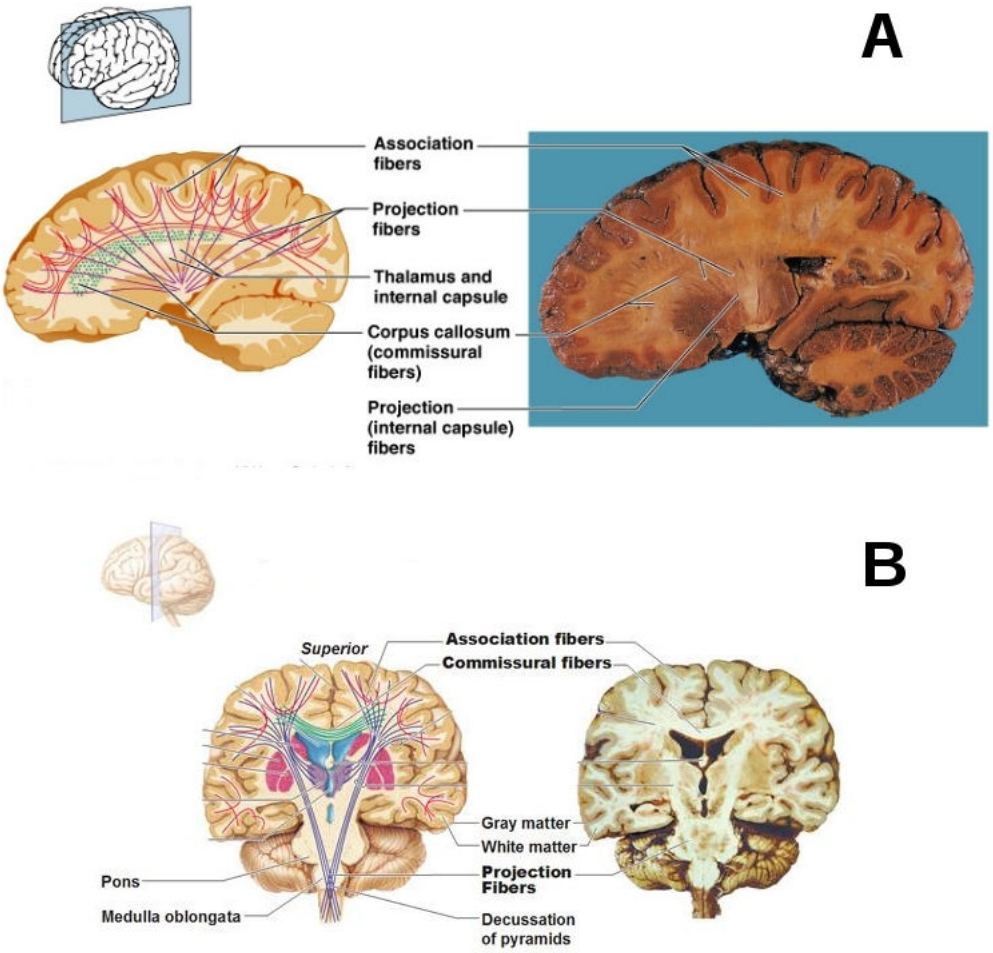

Figure 2.4: Different white matter fascicles. The schematic on the left shows association fibers (both short and long) in red, the projection fibers in purple gyrating out of the lower part of brain. The commisural fibers are shown in green penetrating into the plane of paper connecting the two cerebral hemispheres. A: sagittal view. B: coronal view

Uncinate Fascicles

The uncinate fascicles are the fibers connecting frontal and temporal lobes. The other two being cingulate and the superior longitudinal fascicles. It is interesting to note that an asymmetry exists between the left and the right uncinate fascicles. This asymmetry is attributed to specialized brain functions which are lateralized such as, language. It was found that there is a loss of asymmetry between among schizophrenia patients [Kubicki 2002]. The exact function of uncinate fascicles is

still a matter of debate. However, it is believed that they play an important role in memory and emotion [Hasan 2009].

Cingulum

The cingulum is a C-shaped white matter fiber bundle connection frontal and the temporal lobes. It is located just above corpus callosum and beneath cingulate gyrus. The cingulate gyrus is located on the medial surface of brain and is divided into anterior and posterior cingulate. Changes in anterior section is related to depression and apathy, whereas changes in posterior section is related to more cognitive functions (like attention, visual-spatial skills and memory). A damage to cingulum is often related to traumatic brain injuries (TBI) [Tanner 2010]. In a recent study, damage to cingulum was associated with mild cognitive impairment [Metzler-Baddeley 2012]. It is a part of Papez circuit identified by James Papez in 1937. The circuit is involved in memory and emotions. So, any damage to cingulum is often associated with compromised cognitive and emotional abilities.

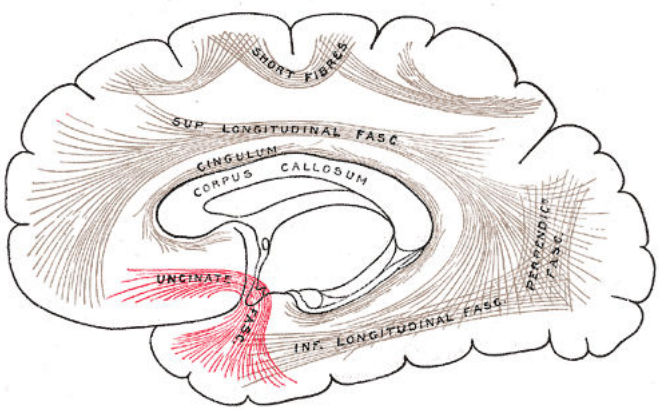

Figure 2.5: Schematic showing unicinate fasiculus (in red), inferior longitudinal fasiculus and cingulum. Adapted from wikipedia.

Arcuate Fascicles

The arcuate fascicles also known as superior longitudinal fascicle is an association fiber connecting lateral temporal and parietal with the ipsilateral frontal cortex. There is still debate about the exact regions of connections in these three lobes. However, it is believed that the temporal projection of the arcuate fasicles connects to the Wernicke's area [1] and the frontal projection connects to the Broca's area[2]. This particular tract is largely associated with the language comprehension and

[1] named after a German neurologist Carl Wernicke in 1874. It refers to a section in brain responsible for written and verbal language comprehension.

[2] named after a French neurologist Pierre Paul Broca in 1861. It is associated with complex syntax comprehension in language, language production, action recognition and speech associated gestures.

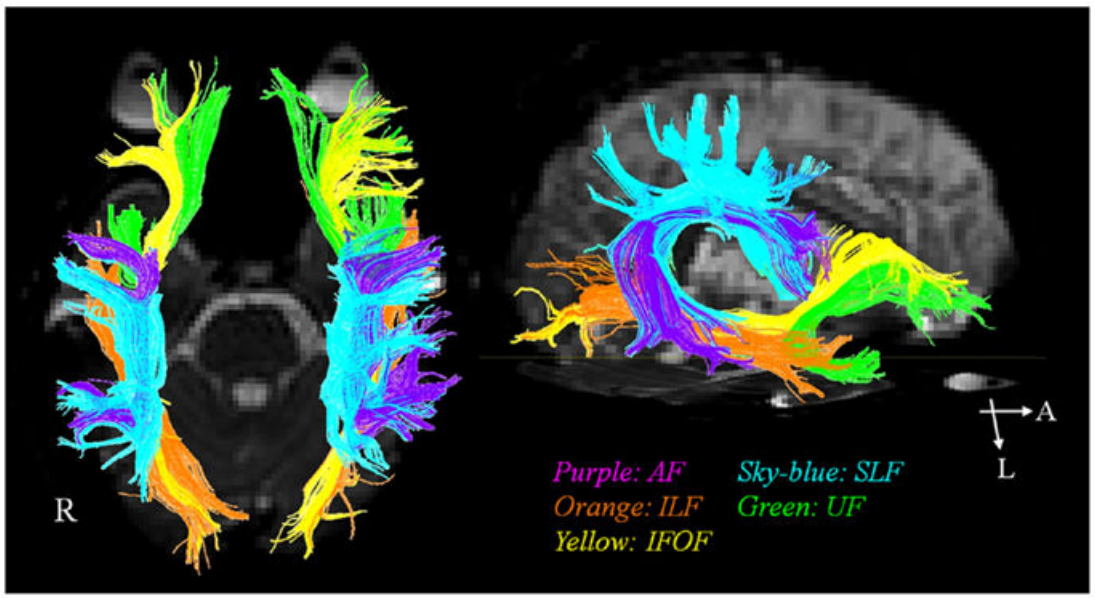

Figure 2.6: Tractography showing Arcuate fascicles(AF), inferior longitudinal fascicles (ILF), inferior occipitofrontal fascicles(IFOF), superior longitudinal fascicles (SLF), uncinate fascicles(UF). Adapted from [Jang 2013]

speech production. The posterior segment (temporo-parietal) of arcuate fascicles is symmetrical, the long segment (temporo-frontal) is lateralized to the left and the anterior segment (fronto-parietal) is lateralized to the right [Catani 2007]. This is consistent with the fact that the left hemisphere is associated with language processing in most of right handed subjects. Conduction aphasia is highly associated with the damage of this particular fiber tract. [Bernal 2009]

Inferior longitudinal fascicles

Classically inferior longitudinal fascicles (ILF) are referred to the white matter tracts connecting the ipsilateral occipital and temporal lobes. However, existence and delineation of these tracts are often challenged against another tract connecting the above mentioned lobes,i.e., inferior fronto-occipital fascicles (IFOF) [Ashtari 2012]. One of the reasons for such a disagreement is the spatial and functional overlap between the ILF and IFOF. Damage in ILF is associate with thought disorders, visual amnesia, visual hypo-emotionality and hallucinations [Shinoura 2007, Ashtari 2012]

Occipitofrontal Fascicles

The occipitofrontal fascicle is a set of association fibers connecting the ipsilateral frontal and occipital lobes. The white matter bundle is subdivided into inferior and

superior segments. However some authors claim the existence of superior occipitofrontal fascicles (SOF) [Türe 1997]. The SOF is claimed to connect the frontal to the ipsilateral parietal lobe and is associated with spatial awareness and symmetrical processing. It is often linked with late life depressions. The inferior occipitofrontal fascicles (IFOF) connects the ipsilateral frontal and posterior parietal and temporal lobes. It is known to intermingle with uncinate fascicles. It is associated with the integration of auditory and visual cortical areas with prefrontal cortex. Any damage can also cause visual hallucinations [Kier 2004].

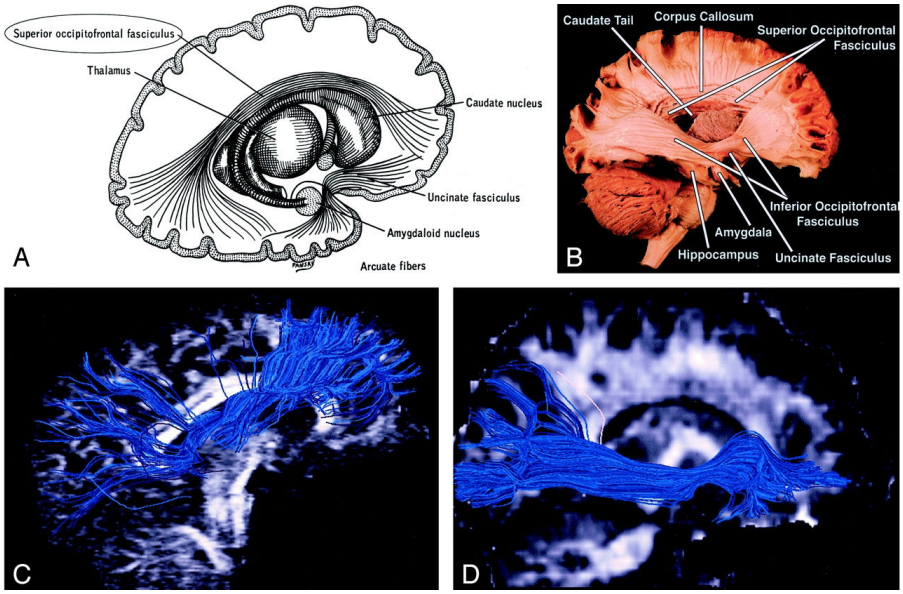

Figure 2.7: Superior and inferior Occipitofrontal fasciculus. A. Superior occipitofrontal fascicles arching over the caudate nucleus and connecting the frontal and occipital lobes. B. A dissection showing the location of the superior and inferior occipitofrontal fascicles along with other white matter tracts. C and D. Tractography showing the superior and inferior occipitofrontal fasciculus. Adapted from [Jellison 2004]

Middle longitudinal fascicles

Middle longitudinal fascicles (Mdlf) is a long association fiber bundle medial to the arcuate fascicles and extend to the superior temporal gyrus. This fiber bundle runs superficially over the inferior occipitofrontal fascicles. The existence of the fiber bundle was debated because of the presence of adjacent arcuate fascicles and inferior occipitofrontal fascicles until recently. Their existence was reported by [Makris 2009] using DTI studies. However, DTI is susceptible to low spatial resolution and noise making it difficult to confirm their existence until recently. A fiber dissection study [Maldonado 2013] confirmed the existence of Mdlf. Similar to their existence, the function of Mdlf is not clearly understood. [Makris 2009] suggested

that Mdlf are associated with attention-processing and conduction of linguistic information in the dominant hemisphere. However, another study using intraoperative subcortical electrostimulation shows no interference in picture naming and post operative permanent language deficits after Mdlf resection [De Witt Hamer 2011].

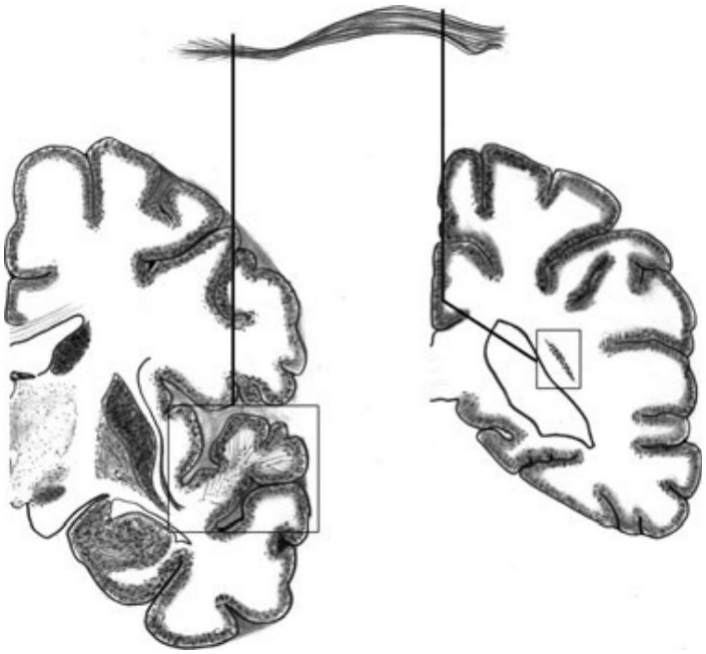

Figure 2.8: Middle longitudinal fascicles. Fiber bundle running medial to arcuate fascicles and penetrate superior temporal gyrus. Adapted from [Maldonado 2013]

2.2.2 Projection fibers

The projection fibers are fibers joining the cortex to the subcortical and spinal areas. The main projection fibers are fornix, thalamic radiations and long corticofugal fibers. In regards to the projection fibers, it is important to understand the difference between the *efferent* and *afferent* neurons. The efferent neurons are also known as the motor neurons. They carry the responses from the brain to the muscles. On the contrary, the afferent neurons are also known as sensory neurons. They bring the stimuli from the sensory organs (e.g., skin, tongue etc.) to the central nervous system.

Fornix

The fornix is a C-shaped fiber bundle connecting hippocampus to the hypothalamus. Unlike other association fibers, the structure of fornix is more complicated. A schematic diagram of fornix is shown in figure 2.9. The fornix is located on the

medial region of cerebral hemisphere. As seen in figure 2.9, different parts of fornix lie on either side of the mid sagittal plane. It arcs around the thalamus and connects medial temporal lobes to the hypothalamus. The fornix begins at the fimbria which lies at the superomedial aspect of the hippocampus. The fimbria is continued by the *crus of the fornix* which turns around the posterior aspect of the thalamus toward the midline. Both the crus then join to form the *body of the fornix*, which anteriorly splits again into two columns ending on the mammillary body. The fornix plays an important role in formation and consolidation of declarative memories and is an important component of the Papez circuit (or the limbic system) [Thomas 2011]. A damage to the fornical tracts may result in anterograde amnesia [Gaffan 1991].

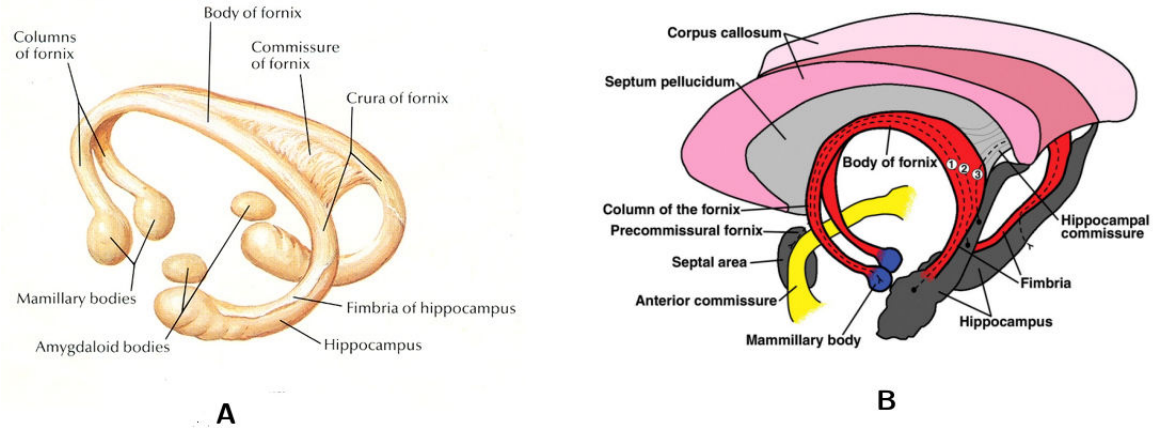

Figure 2.9: Schematic representation of the fornix showing its different parts. A. 3D representation of the fornix showing the different sections, adapted from http://www.medecine.unige.ch. B. A schematic representation of fornix (in red) showing its location with respect to the neighboring structures, adapted from [Thomas 2011]

Thalamic radiations

The thalamic radiations connects the thalamus and the cerebral cortex. The fibers run obliquely through the internal capsule towards the cerebral cortex. The thalamic radiations are divided into anterior (to the frontal lobe), superior (to the parietal lobe), posterior (to the occipital lobe) and inferior (to the temporal lobe) thalamic radiations. The posterior thalamic radiations are also known as optic radiations or Gratiolet radiation. In [Peltier 2006], the authors present a detailed anatomical study of the optic radiations. As the name suggests, they are responsible for carrying visual information to the visual cortex.

Figure 2.10: White matter fibers emanating out of the thalamus towards the cerebral cortex. Adapted from [Gluhbegovic 1980]

Corticofugal fibers

The corticofugal fibers connect the motor cortex and the cerebral peduncle through the internal capsule. These WM tracts are descending motor fibers originating from the primary motor cortex, supplementary motor area, ventral, dorsal premotor area and from the retrocentral area. A damage to the corticofugal fibers decreased motor function in post-infarct patients.

2.2.3 Commisural fibers

The commisural fibers are the white matter tracts that connect the left and right hemispheres of the brain. Corpus callosum comprise the largest network of brain fibers connecting the two cerebral hemispheres. The fornix discussed above can also be considered to form a part of the commisural fibers for its unique geometry. Both the crus of the fornix are connected by forniceal commissure. The other major fiber bundles are anterior and posterior commisure. They are the tracts responsible for communication between the two cerebral hemispheres.

2.2.3.1 Corpus callosum

Corpus callosum is the largest and most easily recognizable fiber bundle in the brain. It starts from cortical areas of one hemisphere and terminate into the corresponding areas of other hemisphere. Though, there is debate about the fact that corpus callosum fibers only connect the exactly corresponding regions of the two hemispheres. A rough estimate suggest that there are around 200 million axonal projections involved in the corpus callosum. It has four anatomical subdivisions:

genu, rostrum, body and *splenium*. The genu is the anterior end of the corpus callosum which is bent downward and backward. It connects the medial and the lateral surfaces of the frontal lobes. The anterior most part of corpus callosum is the genu which projects inferiorly and posteriorly and is tapered to form the rostrum. It is continuous with the genu above and the lamina terminalis below. The mid section of the corpus callosum is called the body or the trunk. The region is composed of comparatively thicker axons as compared to the ones in genu or the splenium. The axons in the trunk of the corpus callosum are directed toward the cerebral cortex to form corona radiata, which include fibers of cortico-spinal tract and thalamic radiations. The splenium is the posterior most part of the corpus callosum. The body of corpus callosum tapers down as we move in the posterior direction before it enlarges to form splenium. It connects the occipital lobes forming the forceps occipitalis or forceps major. Agenesis of corpus callosum is a rare congenital disorder marked by partial or total absence of corpus callosum. Some of the common symptoms include vision impairment, poor motor coordination, low perceptions of pain and swallowing difficulties. Deterioration in the the white matter integrity in corpus callosum is also noticed in other brain related diseases like HIV/AIDS, Alzhiemers among many others.

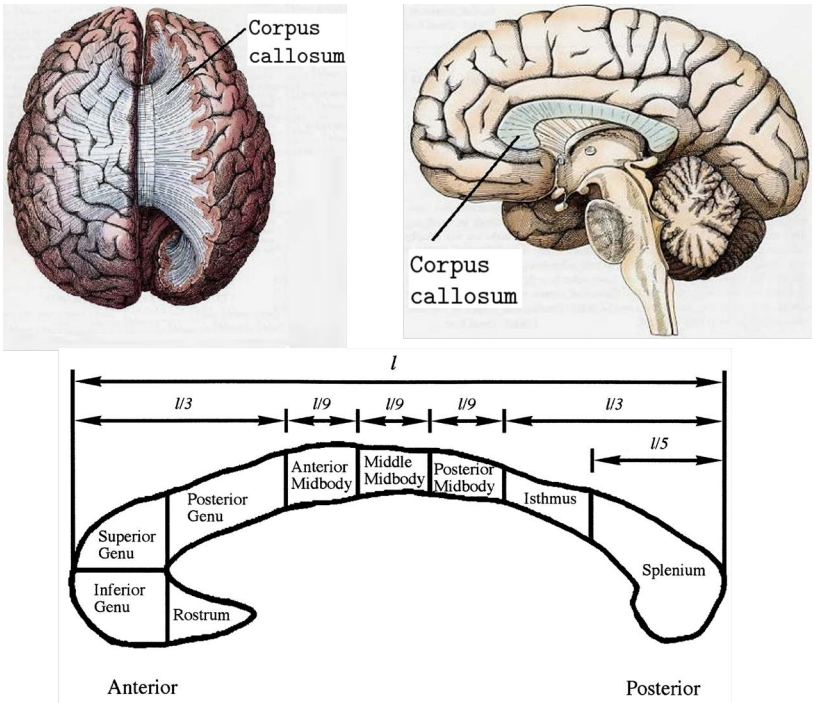

Figure 2.11: Different sections of the corpus callosum. Adapted from [Highley 1999]

Anterior commisure

The anterior commisure is a bundle of white matter fibers consisting of two to three million mylineated axons. It connects the left and right temporal cortices. It also contains crossing fibers from the olfactory tracts

Posterior commisure

The posterior commisure are a bundle of nerve fibers that crosses the mid-sagittal plane immediately above the cerebral aqueduct at the junction of third ventricle.

The line joining the anterior and posterior commisure also known as the AC-PC line is used as a reference for brain atlases, particularly the Talairach atlas. The anterior and posterior commisures are shown in the figure 2.12.

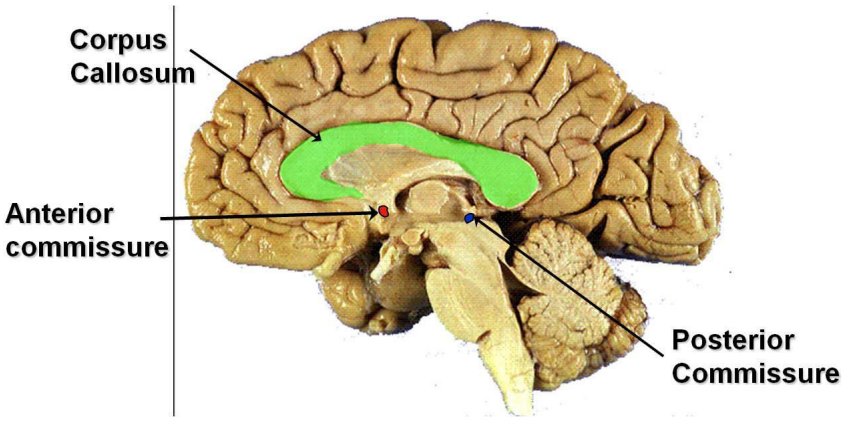

Figure 2.12: Anterior and posterior commisure and the corpus callosum(in green)

2.2.4 Cerebellum

The cerebellum (also known as little brain) is located at the posterior end of the brain just below the occipital and temporal lobes and posterior to the brain stem. It is composed of white matter tracts along with a densely folded gray matter (called the cerebellar cortex). The cerebellum, even with its small volume (10% of the total brain) is known to contain around 50% of the total nerve fibers. Two major fissures divide the cerebellum into 3 parts. The primary fissure separates the cerebellum into anterior and posterior lobe. The posterolateral fissure separates the posterior lobe from the flocculonodular lobe. In the left-right direction the cerebellum is divided into two hemispheres by a mid-section called the vermis. These different section are shown in the figure 2.13. The cerebellum is attributed to normal movement and motor control. A cerebellar dysfunction is linked with ipsilateral movement disorder.

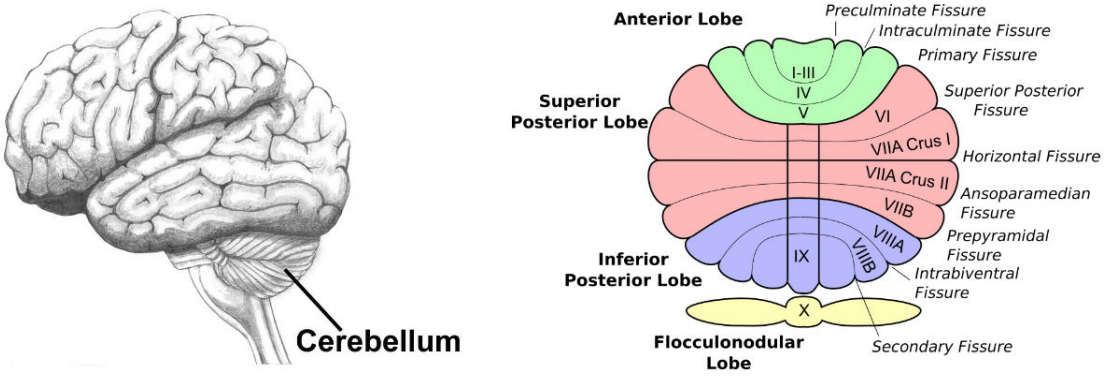

Figure 2.13: Location of cerebellum (left). Flattened cerebellum showing different sections and subdivisions (right)

2.3 Conclusions

This chapter presents an overview of the general anatomy of the brain with special emphasis on white matter tracts. The list of major white matter tracts presented in this chapter is not exhaustive by any means. The anatomy and connections of the short association fibers connecting adjacent gyri of the cerebral cortex is less understood as compared to the long prominent white matter tracts discussed in this chapter. Majority of the DTI studies also do not discuss the structure of the SAF, which leaves an area for further exploration. However, the idea was to give a general overview of the shape, location and primary function of the major white matte tracts. The chapter also gives some information about the different cell types composing the brain and the structure of neuron. An overview of these white matter tracts is essential to understand the correlation between the clinical neuropsychological testing and the statistical analysis conducted on diffusion tensor images.

Chapter 3

Neuroimaging: From Diffusion to Diffusion Tensor Imaging

Contents

3.1 Introduction

As discussed in the previous chapter, the anatomy of the human brain is one of the most complex among the different parts of the body. This complexity exist at both micro-scopic and macroscopic levels. The intricate white matter fiber structures, the convoluted cortical surface and the foldings of the brain hold between them deep secrets which are unfolding slowly with the scientific progress in the field of neuroimaging.

Before the advent of modern non-invasive medical imaging techniques, the study was limited to post-mortem studies. In fact, the curiosity of humans regarding brain anatomy could be dated to as far back as ancient Egypt in 1700 B.C. to the Edwin Smith Papyrus [Breasted 2006]. However, here we are talking about noninvasive neuroimaging. In this chapter I will discuss some of the tools that were developed in the field and a little background about different techniques that exist today. Later, we will focus specifically on magnetic resonance imaging (MRI), in particular diffusion weighted imaging, the physics behind it and the associated protocols.

3.1.1 History

Almost all the sources point to the Italian neuroscientist Angelo Mosso, who conducted the first ever "human circulation balance" for measuring the redistribution of blood (1882) in the brain during emotional and intellectual activity. This is regarded as the forerunner of modern functional magnetic resonance imaging (fMRI) and positron emission tomography (PET) scans. He investigated several critical variable which are relevant even today in the days of computational neuroimaging, such as signal-to-noise ratio (SNR), the appropriate choice of the experimental paradigm and the need for simultaneous recording of different physiological parameters. The details of the experiments were published recently in [Sandrone 2014].

Another technique worth mentioning is *pneumoencephalography* which was introduced in 1918 by an American neurologist named Walter Dandy. The process involved injection of filtered air into one or both the lateral ventricles of the brain via small trephine holes[1]. The injected air displaces the CSF providing better contrast for X-ray imaging. The drained CSF was slowly replaced by natural production. This process was not good at resolving the soft tissue like brain and was also accompanied with greater risk for patients.

Around 9 years later, a Portuguese neurologist named Egas Moniz introduced cerebral angiography. In this process a contrast agent is injected through a catheter inserted in a large artery (like femoral artery). As the contrast agent spreads through the brain arteries, a series of X-ray images were taken followed by another series of images as it spreads through the venous system. This kind of imaging is still used to detect brain aneurysms[2] and blood vessel lesions.

It was not until 1970s that computed tomography or computed axial tomography (CT or CAT scans respectively) became the forerunner of truly non-invasive medical imaging by the efforts of William H. Olendrof, Godfrey Newbold Hounsfield and Allan McLeod Cormack. For their effors Cormack and Hounsfield were

[1] a burr hole made in the skull using an instrument known as trephine.
[2] a localized bulge in the wall of a blood vessel.

awarded Nobel prize in 1979. Olendrof not getting the Nobel is still a matter of controversy. Earlier scanners used to build two dimensional images. However, 3D image reconstruction is possible with the modern CT scanners. It build an image based on the principal of differential absorption of X-rays by different tissue types. The hard tissues like bone absorb X-rays much better than air and water. The X-ray absorption by the soft-tissue lies somewhere in between. The CT scanning technique makes use of this differential absorption rate between tissues to produce the CT image. The effective radiation dose from CT ranges from 2 to 10 mSv, which is about the same as the average person receives from background radiation in 3 to 5 years. A CT scan is best suited for viewing bone injuries, lung and chest injuries and detecting cancers. On the other hand, MRI is used for soft tissue evaluation. A typical CAT scan may take upto five minutes. However, the actual scan time is less than 30 seconds. CT scans are widely used in emergency rooms.

The concept of positron emmision tomography (PET) scan was suggested in late 1950s by David E. Kuhl, Luke Chapman and Roy Edwards. It used trace amounts of short-lived radioactive material to map functional brain processes. During a radioactive decay, a positron[3] is emitted which immediately meets an electron. The both anihilate and emit two gamma photons running in opposite direction. The emitted photons are detected by a gamma camera which permits image reconstruction. Areas of high brain activity are also associated with high radioactivity. The radioactive materials commonly used are short-lived isotopes of carbon (C-11), nitrogen (N-13), oxygen (O-15), fluorine (F-18) or rubidium (Ru-82). These radio tracers are used because they combine with glucose, water or ammonia used by the body. PET scanning is more closer to functional imaging of the brain. A closely related scanning technique is single-photon emission computed tomography or SPECT. This technique uses gamma-ray emitting radio isotope and a gamma-ray camera to reconstruct the image.

However, truly noninvasive neuroimaging became popular with the introduction of magnetic resonance imaging (MRI) by Herman Carr in 1952. MRI had its humble beginnings when Herman Carr produced a one-dimensional MR image in his thesis. But, it was not until 1970s that MRI reached its full potential. The first cross-sectional magnetic resonance image of a living mouse was produced in 1973 by Paul Lauterbur. The techniques were further improved by Peter Mansfield which reduced the scan timing from hours to a matter of few minutes. Both, Paul Lauterbur and Sir Peter Mansfield were awarded the Nobel Prize in Physiology in 2003 for their contributions in MR imaging techniques. In the subsequent sections, the physics behind MRI will be explained leading to diffusion tensor imaging.

The physics of MRI could get very complicated and convoluted as we progress into the finer details of MR acquisition. In the following sections, I will cover the basics

[3] an anti-particle to electron with a positive charge and same mass as an electron

of MR imaging, the quantum physics aspect of it followed by the popular acquisition protocols.

3.2 Physics of Magnetic Resonance Imaging

For understanding the physics involved in magnetic resonance imaging, it is important to understand some basic quantum mechanics and the physics behind nuclear magnetic resonance (NMR).

Nuclear spin

The human body composed mostly of water and fat. Water has a large number of hydrogen atoms, which are used for MR imaging. There is another reason for using the hydrogen atoms for imaging, but it will be discussed later as we progress. These hydrogen atoms are aligned randomly in our bodies in absence of any external magnetic field. Each of these hydrogen atoms (and all the other atoms in general) are spinning about their axis producing a small magnetic field[4]. These tiny atoms act as small magnets with their polarity defined by the direction of spin (clockwise or anticlockwise). When an external magnetic field is applied, these tiny magnets align themselves either along the direction of the applied magnetic field or in a direction against it. This is shown in figure 3.1. Because of the spinning nature of the atoms (nuclei), they have a spin angular momentum which make them precess (wobble). The frequency of precession is linearly related to the strength of the magnetic field and is called Larmor frequency. Thus, if B_0 is the strength of the applied magnetic field, γ be the gyro magnetic ratio, then the Larmor frequency, ω is given by the following linear relation,

$$\omega = \gamma B_0. \tag{3.1}$$

One of the other reasons for using hydrogen atoms in the MR imaging other than its abundance is that the gyromagnetic ratio for hydrogen is the highest (42.6 MHz/T) when compared to the other elements found in the human body. What it implies is that for a given magnetic field strength, the precession frequency is highest for hydrogen atoms. So, imaging can be performed with lower magnetic field strength. This idea will become more clearer as we progress in the chapter. The atoms aligned in parallel to the applied magnetic field are in low energy state compared to the ones aligned in the antiparallel direction. The natural tendency of the particles is to remain in a low energy state. Consequently, there are more protons in the low energy state (aligned parallel to the magnetic field) compared to that in the high energy state (aligned anti-parallel to the magnetic field). The difference in the parallel and anti-parallel protons increases with the increase in the strength of the magnetic field. For a clinical MR scanner (typically of strength 1.5 T) there are only nine protons per million which are in excess. On a first thought this does not

[4] refer Maxwell's equations

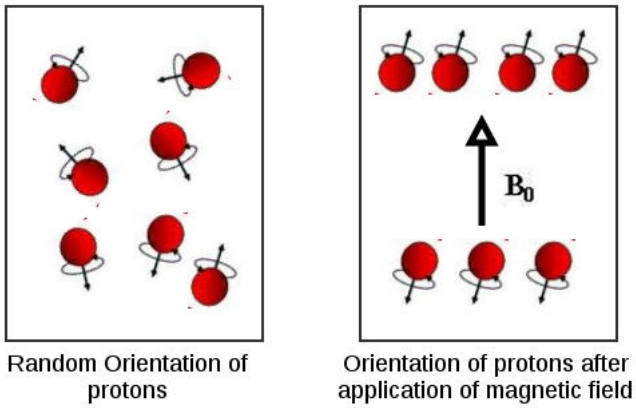

Figure 3.1: The atoms are randomly oriented in the absence of any magnetic field (left). On application of a magnetic field (B_0), the protons get aligned in directions parallel or anti-parallel to the applied magnetic field.

sound like a big number. But calculations show that in total for every single voxel of water with size $2{\times}2{\times}5\,mm^3$ there are around 6 million billion protons in excess. The total sum of the magnetic field of each single proton gives the *net magnetization* of the system's magnetic field.

3.2.1 Excitation pulse

Traditionally the applied magnetic field, $\mathbf{B_0}$ is considered to be directed along the z-axis in a Cartesian system. The net magnetization, $\mathbf{M}$ is precessing around the z-axis at the Larmor frequency ω. One should understand, that even though the individual protons are precessing around the z-axis, the net magnetization vector $\mathbf{M}$ does not precess because all the protons are precessing out of phase, $\mathbf{M}$ will have a large component along the z-axis but no components along the xy-plane. Only the z components of all the protons add up to give the net magnetization vector and the other components cancel out because of the random phase distribution.
If a radio frequency (RF) pulse is applied along the x axis, the net magnetization vector $\mathbf{M}$ flips and starts precessing about the magnetic field axis. The angle of flip depends on the strength and duration of RF pulse. In most of the pulse sequences the angle of flip is 90° making the magnetization vector flip on the xy plane. The RF-pulse is an electro-magnetic wave which has a weak magnetic field component $\mathbf{B_1}$. The protons initially aligned to the z-axis will now also start precessing along the x-axis at the Larmor frequency corresponding to $\mathbf{B_1}$,i.e., $\omega_1 = \gamma\mathbf{B_1}$. After the RF excitation, we have two different magnetic field in the system, one is the applied strong magnetic field $\mathbf{B_0}$ ($\approx$1.5 T) and the weak magnetic field due to the RF-excitation $\mathbf{B_1}$ ($\approx$50 mT).

As the protons are precessing along two axes (z and x), the net result is a spiral

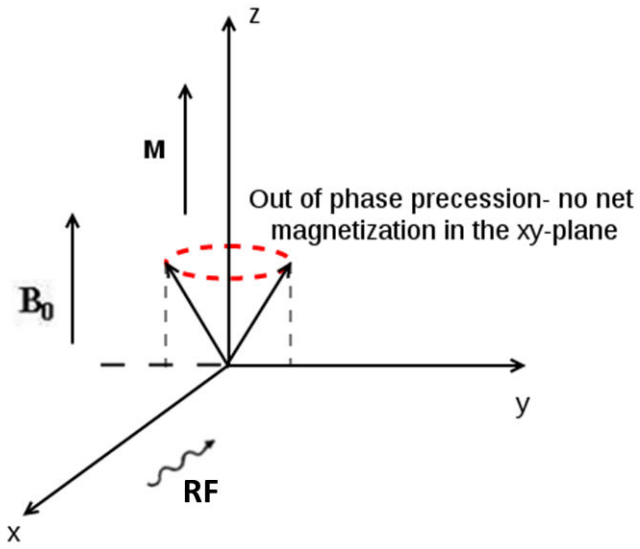

Figure 3.2: Schematic coordinate system showing the direction of magnetic field $\mathbf{B_0}$, the net magnetization vector $\mathbf{M}$ and the direction of the applied radio-frequency pulse.

motion into the $x-y$ plane. This spiral motion is called *nutation*. The RF-pulse has a sinusoidal waveform, mathematically it is represented as $\cos(\omega t)$, where ω is the frequency of the waveform. In order to achieve *resonance*, the waveform frequency ω should be equal to the Larmor frequency as per the external magnetic field $\mathbf{B_0}$. During resonance, the RF pulse adds extra energy to the protons. If the RF pulse is sent at a frequency other than the Larmor frequency, there will be no resonance and the energies of the protons will not be added and the magnetization vector will not flip into the xy-plane. This is also known as *transverse* magnetization.

The flip angle of the magnetization vector depends on the duration for which the RF pulse is applied. In the figure 3.3, a flip-angle θ, on the application of a RF-pulse (frequency ω_1 and magnetic componentB_1) for a period of time τ is given by,

$$\theta = \omega_1 \tau. \tag{3.2}$$

Now, since the frequency ω_1 is related to the magnetic field strength and gyromagnetic of the proton γ by the relation in equation 3.1, we have

$$\theta = \gamma \, \mathrm{B}_1 \, \tau \tag{3.3}$$

That is

$$\tau = \frac{\theta}{\mathrm{B}_1 \, \gamma} \tag{3.4}$$

Another interesting phenomena that happens due to the application of RF-pulse excitation is the **phase coherence**. Before the RF pulse excitation, all the protons

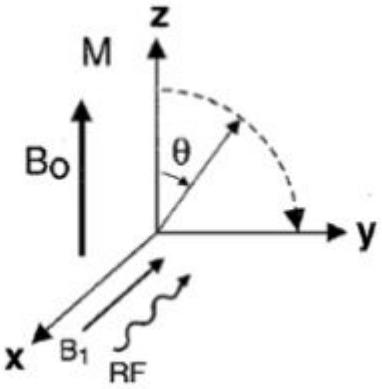

Figure 3.3: Flip angle calculation. The magnetization vector **M** and the applied magnetic field $\mathbf{B_0}$ are directed along the z axis. The RF pulse is applied along the x axis which has a magnetic component B_1. θ denotes the flip-angle. Adapted from [Hashemi 2012]

were precessing but not in phase. The transverse magnetization is only possible if all the tiny magnets, i.e., the protons precess in phase. These two phenomena of transverse magnetization and phase coherence are interlinked.

3.2.2 Bloch Equation

The macroscopic behaviour of magnetization vector as a result of magnetic interactions can be described with Bloch equations. The Bloch equation named after the Nobel laureate Felix Bloch[5] states

$$\frac{d\mathbf{M}}{dt} = \mathbf{M} \times \gamma\mathbf{B}, \tag{3.5}$$

where the symbols have the usual meanings. The equation 3.5 states that the vector describing the rate of change of **M** is perpendicular to both **B** and **M**. When the RF-excitation is applied, the total effective magnetic field is given by,

$$\mathbf{B_{eff}} = \mathbf{B_0} + \mathbf{B_1}, \tag{3.6}$$

where $\mathbf{B_1}$ is the oscillating magnetic field due to the RF pulse. Due to the application of the RF pulse a transverse magnetization is induced in the system. After the RF pulse is stopped, the magnetization vector relaxes through two different process called T1 and T2 relaxation. These relaxation process will be discussed in the following sections. When these two relaxation processes are taken into account, the Bloch equations are modified as,

$$\frac{d\mathbf{M}}{dt} = \mathbf{M} \times \gamma\mathbf{B_{eff}} - \frac{M_x\vec{i} + M_y\vec{j}}{T_2} - \frac{(M_z - M_0)\vec{k}}{T_1}, \tag{3.7}$$

[5] awarded Noble Prize in physics in 1952

where $\mathbf{M} = [M_x, M_y M_z]$ and M_0 is the steady state nuclear magnetization . T_1 and T_2 are the relaxation time periods. Further simplification of the equation and a closed form solution for the rate of change of $\mathbf{M}$ can be obtained. However, the derivations are not important to understand the excitation and relaxation process.

3.2.3 Relaxation

As mentioned in the previous section, the phase coherence and transverse magnetization are interlinked and that the protons start dephasing and loosing the transverse magnetization as soon as the RF excitation pulse is turned off. One point to remember here is that though the excitation process is interlinked, the relaxation process for both the mechanisms are independent of each other. The reversal of the magnetization vector, $\mathbf{M}$ from the xy-plane to the z-axis is called T1 relaxation (also called *longitudinal* or *spin-lattice relaxation*) and the process of dephasing is called T2 relaxation (also called *transverse* or *spin-spin relaxation*). The T1 and T2 relaxations are independent of each other, because the T1 relaxation occurs on the z-axis while the latter occurs on the xy-plane.

T1-relaxation

The rate of recovery of the magnetization vector $\mathbf{M_z}$ to the z-axis has a time constant denoted by $1/T1$. Hence the name T1 relaxation. The T1 relaxation times differ for different tissue types, ranging from 300 ms in fat to several seconds in the CSF. This difference in the relaxation times is used to generate the contrast between different tissue types. Not all the protons are bound to the molecules in the same manner, the protons in the fat tissue are tightly bound compared to that in water. The tightly bound protons will release their energy to the surrounding protons much quickly than the ones which are contained in looser bonds such as water. This explains the shorter recovery time for the fat tissue. The pulse sequences used for generating a T1 contrast image is called the T1-weighted sequences. The equation for the recovery of the magnetization vector $\mathbf{M_z}$ is given by

$$\mathbf{M_z}(t) = \mathbf{M_0}(1 - e^{-t/T1}), \tag{3.8}$$

where $\mathbf{M_0}$ is magnetization vector due to the external magnetic field. The figure below shows a typical T1 relaxation curve
At this point, we introduce two more terminologies, TR and TE. TR or the repetition time is the time between two RF excitation pulses, whereas, TE or the echo time is the time between 90-degree RF pulse and MR signal sampling time, which corresponds to the maximum echo. These terms will be explained in more detail in the later sections along with pulse sequences. The T1 sequences generate good contrast between the gray and the white matter tissue and is subsequently used for anatomical brain images.

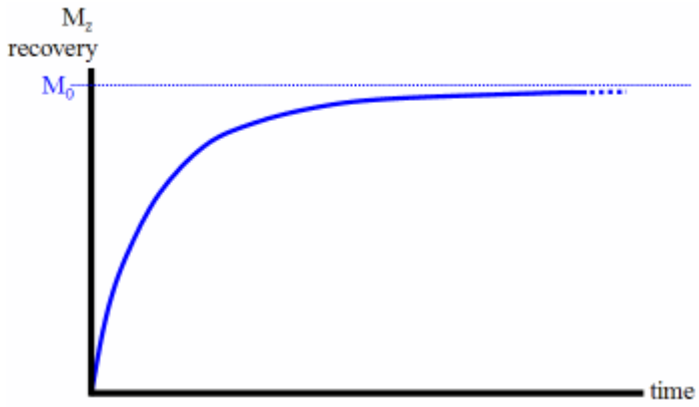

Figure 3.4: T1 relaxation curve.

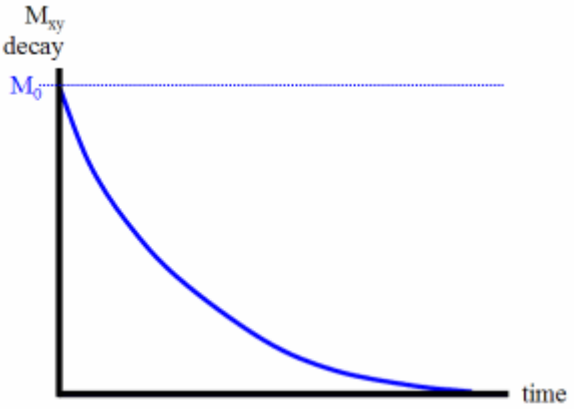

Figure 3.5: T2 relaxation curve

T2-relaxation

The T2 relaxation or *spin-spin relaxation* is used for describing the decay of the transverse magnetization vector ($\mathbf{M_{xy}}$) after the removal of RF excitation pulse. The time constant for the decay of this signal is generally denoted as T2, hence the name T2 relaxation. Similar to the recovery equation for T1 relaxation, the signal in this case also decays exponentially following the equation,

$$\mathbf{M_{xy}}(t) = \mathbf{M_{xy}}(0)\ e^{-t/T2} \tag{3.9}$$

The figure 3.5 shows the T2 relaxation curve. The T2 relaxation time is shorter than that of the T1 relaxation. The decay in the transverse magnetization vector is caused by the local magnetic field inhomogenity, which is caused by the variations in the local magnetic susceptibility. Because of the differences in the magnetic susceptibility, there are variations in the Larmor frequency which leads to subsequent decoherence in the magnetization vectors. The spins will also dephase if there are inhomogenities in the applied magnetic field, which is unavoidable due to limitations on magnet construction. These two factors contribute in the rapid decay of the

transverse magnetization compared to the recovery time needed for magnetization vector $\mathbf{M_z}$. The actual decay rate (T2*) when the magnetic field inhomogeneties are taken into account is given by,

$$\frac{1}{T2^*} = \frac{1}{T2} + \gamma\, \Delta B_0, \tag{3.10}$$

where ΔB_0 is the magnetic inhomogenity within a single voxel. T2-weighted images are often used for detecting tissue pathologies, because changes in the water content is often associated with changes in the tissue composition.

During the relaxation process, the protons release the extra energy, which they acquired due to RF-excitation. This energy is also released in the form of radio frequency waves which are then picked up by a receiver coil to produce an image. The receiver coil is placed at right angles to the main magnetic field. As mentioned before, the RF has both electrical and magnetic components. Our aim here is to pick up the magnetic field in the released RF wave. This magnetic field in turn generates a current in the receiver coil, which is the acquired signal and is translated into an image.

3.2.4 Signal Localization

In the previous sections, we have discussed the physics behind RF excitation and relaxation. However, it is important to know where the signal is localized in the body. In most of the imaging techniques, the entire body (in this particular case head) is not subjected to the RF excitation pulse at once, but a single slice in any direction is selected and only the protons contained in that slice are excited by the RF pulse. This is achieved using a gradient magnetic field. The gradient field is expressed as a function of position as,

$$\mathbf{B}(t) = \mathbf{B_0} + \mathbf{G}(t)\mathbf{r}, \tag{3.11}$$

where $\mathbf{G}(t)$ is the gradient applied and $\mathbf{r}$ is the position vector. The gradient magnetic field is achieved using gradient coils.
The figure 3.6 shows the construction of the gradient coils. Essentially in the most simplest form, they are loops of wire carrying current. We know from Biot-Savart Law that a current carrying loop produces magnetic field. This magnetic field is superimposed on the existing $\mathbf{B_0}$ and produces a gradient magnetic field in each of the three directions which is important to localize the signal to a single voxel. The encoding gradients required for a localization in 3D are

1. slice-select gradient
2. phase-encoding gradient
3. frequency-encoding gradient

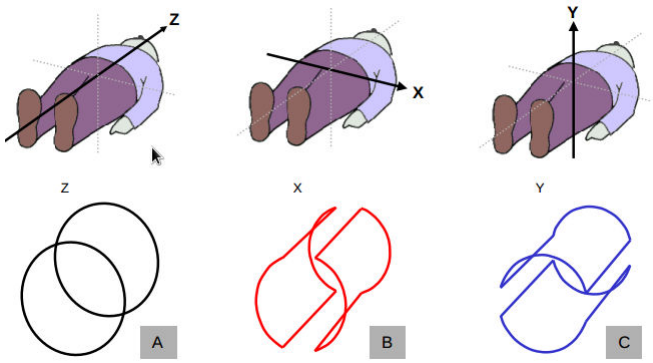

Figure 3.6: A schematic construction of gradient coils along the three axes in a scanner. The figures A, B and C represent the construction for the gradient coils in the x, y and z axes respectively. Adapted from www.mri-physics.net

Slice-select gradient

The slice-select direction can be directed along one of the axes depending on the slice-direction desired. For sake of demonstration, here the slice-select direction is oriented along the body (that is along the direction of $\mathbf{B_0}$ or z-axis). The gradient along this direction G_z varies in a linear fashion creating a nonuniform magnetic field along this direction. The linearly varying gradient magnetic field is shown in

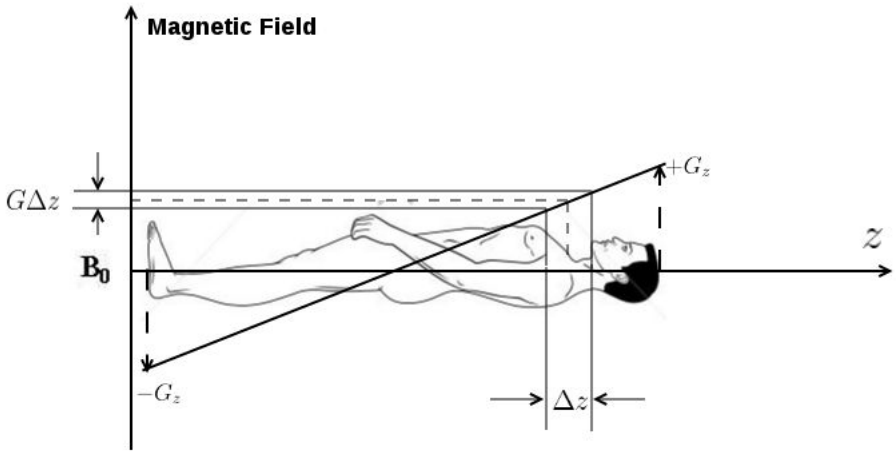

Figure 3.7: Slice-select direction and linearly varying magnetic field (G_z)

figure 3.7. The external magnetic field is $\mathbf{B_0}$ and so the total magnetic field at a distance z is $\mathbf{B_0} + z\ G_z$. With the linearly varying magnetic field, each section (slice) of the body will have its own resonating frequency. Depending on the slice being activated, the Larmor frequency is calculated using equation 3.1 and a RF-pulse of the same frequency is transmitted. However, from a practical point of view, in order to activate a slice of thickness Δz, a RF-pulse of a range of frequencies is sent.

The range of frequencies can be calculated based on equation 3.1 and the figure 3.7,

$$\Delta\omega = \gamma G_z \, \Delta z \tag{3.12}$$

The slices can be made thicker or thinner by decreasing or increasing the gradient. At this point of time, we have information regarding the position of the slice in the body but we have no information about the exact location of the signal within the slice or the plane of acquisition.

Phase-encoding gradient

The second encoding is the phase-encoding gradient which is applied in the anterior-posterior direction (along the y-axis). It induces a similar magnetic field gradient in this direction. When the magnetic gradient G_y is applied along this axis, it throws the protons out of phase. After the phase encoding gradient stops, they are still spinning at the same frequency but remain out of phase. This process is called phase-encoding. The protons in the same row perpendicular to the gradient direction will have be in phase as shown in figure 3.8.

Frequency-encoding gradient

After the phase-encoding gradient is applied, another magnetic gradient called the frequency-encoding gradient, G_x is switched on in the left-right direction (x-axis). The protons on the right will acquire a higher frequency than the ones on the left of the slice due to the higher magnetic field, thus creating a frequency difference. Since the frequency turns back to ω_0 at the end of the G_x gradient, the signal has to be recorded during the application of G_x.

With all the three gradient directions combined, it is now possible to determine precisely the location of the signal in a Cartesian frame. The whole process of creating phase differential in each voxel is shown in figure 3.8.
The figure 3.9 shows the time sequence in which the RF pulse excitation are applied. The typical pulse sequences commonly will be discussed in the chapter later.

3.3 $k-$space

$k-$space is the raw data or signal that is acquired from the MR scanner. It is the space in which the MRI data is acquired. The MR image we see is the Fourier transform of the $k-$space. In this section, we will discuss qualitatively about $k-$space briefly.

As discussed in the previous section, there are three different and independently controlled magnetic gradient field in the scanner, $\mathbf{G} = [G_x \; G_y \; G_z]$,

$$\mathbf{G} = \nabla \mathbf{B_z},$$

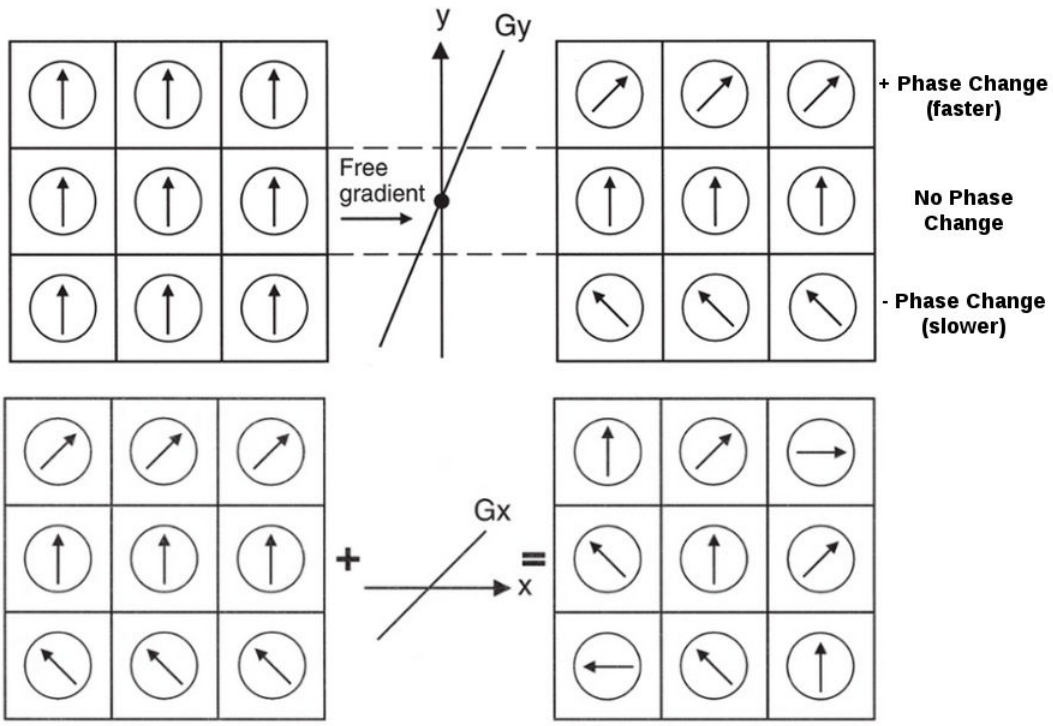

Figure 3.8: A schematic showing the effects of the gradient directions G_y and G_x on the selected slice. The nine voxels represent the different voxels in the same slice. When the G_y gradient is applied, the different rows of the slice dephase spin with different frequencies and become dephased. After G_y stops, they remain dephased although precessing again with the same frequency. The magnetization vector G_x creates additional phase difference across the row. Adapted from [Hashemi 2012]

.

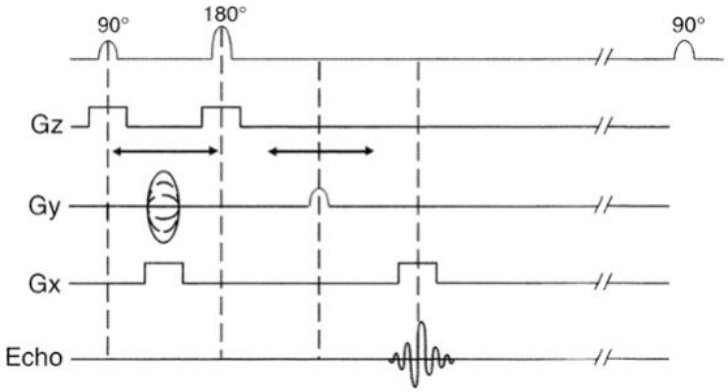

Figure 3.9: An example of pulse sequences.

where $\mathbf{B_z}$ is the total magnetic field along the z-axis and ∇ represents the gradient operator. For a linear gradient as discussed in the chapter,

$$\mathbf{B_z}(\mathbf{r}) = \mathbf{G} \cdot \mathbf{r}$$

We know from equation 3.1, that for a given magnetic field it is possible to compute precessional frequency $\omega = \gamma \mathbf{B_z}$. In a rotating frame of reference **add the section before**, we have

$$\omega = \gamma \mathbf{G} \cdot \mathbf{r} \tag{3.13}$$

The phase is the time-integral of the precessional frequency w and is given by,

$$\Phi(\mathbf{r}, t) = \int_0^t \omega(\mathbf{r}, \mathrm{d}\tau)\ \mathrm{d}\tau \quad = \int_0^t \gamma \mathbf{G}(\tau) \cdot \mathbf{r}\ \mathrm{d}\tau \tag{3.14}$$

So, for any particular position $\mathbf{r}$, we can write

$$\Phi(\mathbf{r}, t) = \gamma \left(\int_0^t \mathbf{G}(\tau)\ \mathrm{d}\tau \right) \cdot \mathbf{r} \tag{3.15}$$

If we define $k(t)$ as,

$$k(t) = \gamma \left(\int_0^t \mathbf{G}(\tau)\ \mathrm{d}\tau \right) \tag{3.16}$$

Then equation 3.15 can be simply written as

$$\Phi(\mathbf{r}, t) = k(t) \cdot \mathbf{r} \tag{3.17}$$

Now, we know that the signal acquired in MRI, $S(t)$ is a vector sum of all the transverse magnetization pulse. Thus,

$$S(t) \propto \int \mathbf{M_{xy}}(\mathbf{r}, t) \mathrm{d}\mathbf{r} \tag{3.18}$$

Substituting from equation 3.9

$$\mathbf{M_{xy}}(\mathbf{r}, t) = \mathbf{M_{xy}}(\mathbf{r}, \mathbf{0}) e^{-ik(t).\mathbf{r}} \tag{3.19}$$

The image is the transverse magnetization at the time, $t = 0$. We call the image $\mathrm{Im}(\mathbf{r})$. Thus,

$$S(t) \propto \int \mathrm{Im}(\mathbf{r}) e^{-ik(t).\mathbf{r}} \mathrm{d}\mathbf{r} \tag{3.20}$$

If $S(t)$ is expressed as a function of k instead of time, t we can write,

$$S(k) = \int \mathrm{Im}(\mathbf{r}) e^{-ik.\mathbf{r}} \mathrm{d}\mathbf{r} \tag{3.21}$$

The above expression is the definition for Fourier transform of the image and thus is the k-space. An inverse Fourier transform will result in the MR image.

$k-$ space representation and MR image

The acquired data in $k-$space can be schematically represented by the box shown in figure 3.10. The signals with low frequency are around the center, whereas the signals in high frequencies are spaced on the periphery of the image. The low frequency signals contain information about the signal-to-noise ratio (SNR) and contrast of the image. The high frequencies contain information about the spatial resolution. The $k-$space is symmetrical about the origin in both x and y axes.

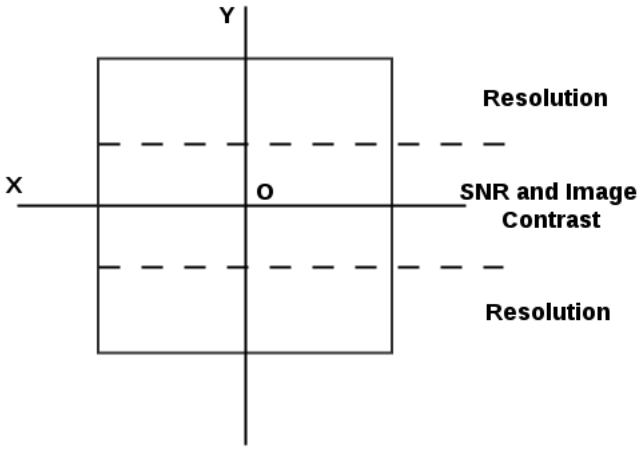

Figure 3.10: The middle section of the $k-$space corresponds to the signal-to-noise ratio and the contrast of the image. The peripheral regions correspond to the image resolution information.

The above discussion becomes more clear with few examples. In figure 3.11, the MR image and the corresponding $k-$space is shown. It can be seen in the figure, that if the MR image is constructed only from the signal in the center of the $k-$space it has good contrast but very low resolution. In the bottom row, the MR image is constructed only from the signals on the periphery of the $k-$ space. As one can see, the image has sharp contours but almost no contrast information.

3.4 Pulse sequences

A pulse sequence is a sequence of events induced in the system for a MR image acquisition. The events are the RF excitation pulse, RF echo and gradient switches. The pulse sequences are generally shown on a pulse diagram, which consist of horizontal lines with the events marked at appropriate time points. An example is shown in figure 3.9. Over the years, a number of variations of pulse sequences were suggested in order to increase the acquisition speed, image contrast and SNR. It is up to the user to determine the sequence parameters (TR, TE, field of view and flip angle) for imaging and to find the right balance between speed of acquisition,

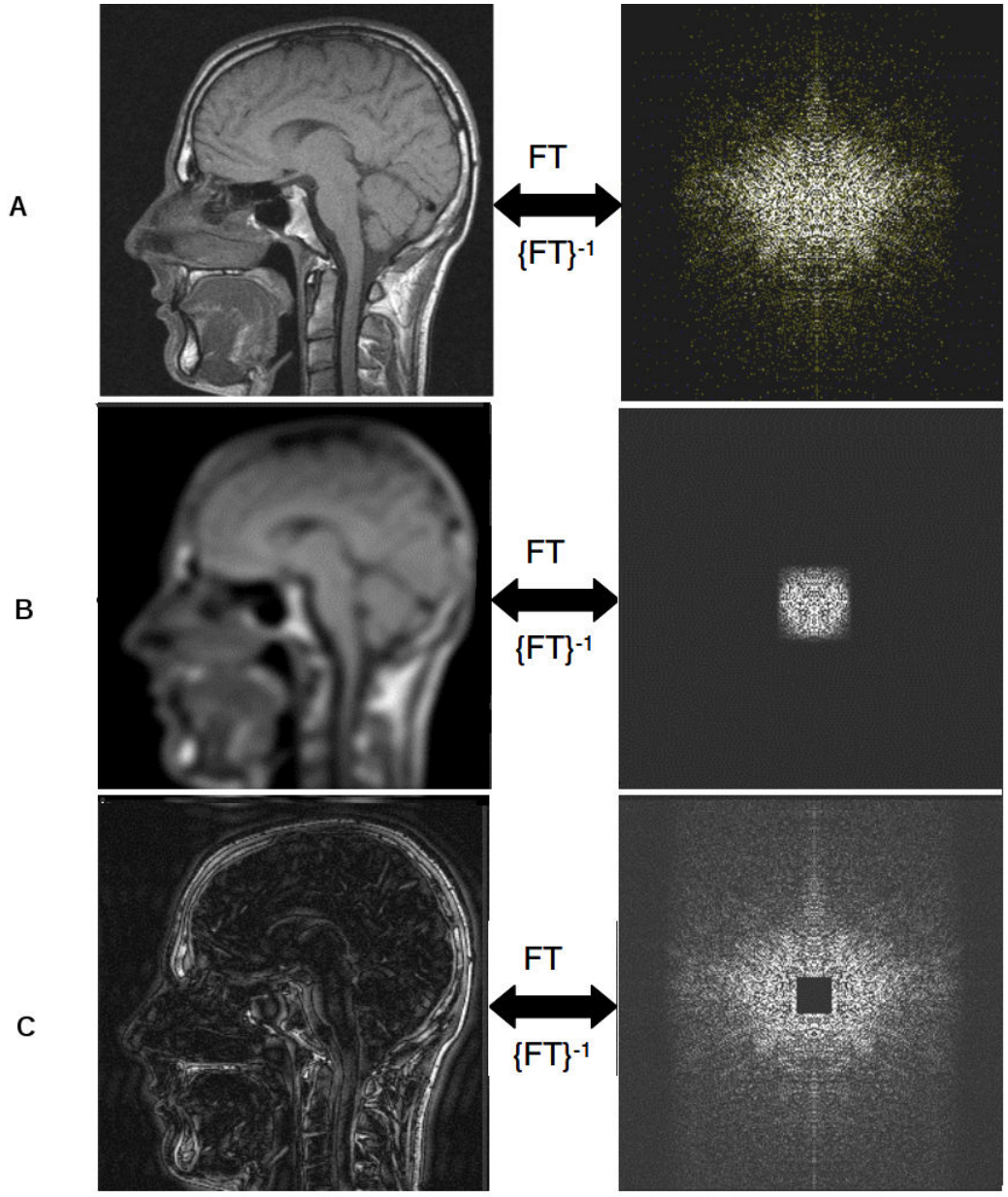

Figure 3.11: The left column shows the magnetic resonance image and the right column shows the corresponding k-space. The top row (A) shows the full $k-$space and the corresponding MR image. The middle row (B) shows the image constructed from only the central section of the $k-$space which contains the image contrast information but the image is blurry as it does not contain any information about the image resolution. The bottom row (C) shows image constructed from only the information in periphery of $k-$ space. The image has no contrast information.

image contrast and resolution. The pulse sequences can be broadly categorized into two families,

1. Spin-echo sequences
2. Gradient-echo sequences

The spin-echo sequences are characterized by the presence of 180° rephasing pulses. On the contrary, the gradient echo sequences are characterized by the absence of any such rephasing pulse, but a gradient reversal pulse. A number of different variations of these two pulse sequences exist in the literature and we will discuss few of them in the following sections.

3.4.1 Spin Echo (SE) sequence

The spin-echo sequence was one of the first sequence to be used in MRI acquisitions. The SE sequence is composed of a 90 degree RF pulse, a 180 degree pulse and a signal echo. As soon as the 90-degree excitation pulse is applied, the transverse magnetization starts to dephase due to T2 relaxation. A 180-degree pulse is applied, which causes the dephasing magnetization to rephase. The echo produced is received by a RF coil. The SE sequence produces strong signal, however it requires longer acquisition time because of the rephasing step. The figure 3.12 describes the whole process of signal activation.

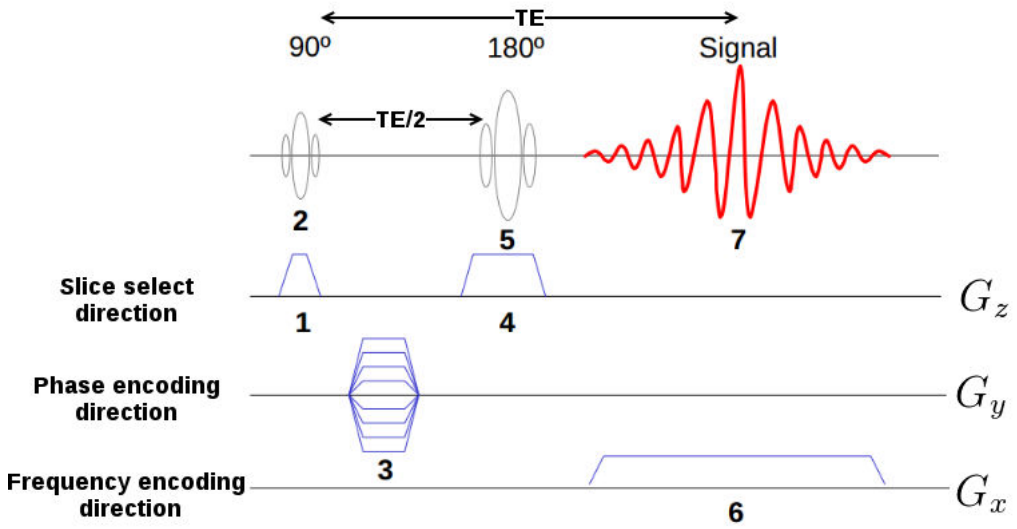

Figure 3.12: Events involved in spin-echo sequence. 1. Switching on the slice-select gradient. 2. A 90-degree RF pulse for transverse magnetization. 3. Phase-encoding gradient is switched on. 4. The slice-select gradient is switched on again. 5. A rephasing 180-degree RF pulse is sent. 6. Frequency-encoding gradient is switched on. 7. Signal echo is received by the receiver coil.

A spin-echo sequence has three important parameters, TR, TE and number of repetitions of RF excitation. TR is the time between two 90-degree excitation pulses. It is important that we allow long enough TR in order to have full recovery of the transverse magnetization before applying the next RF pulse. Failing to do so will lead to loss of signal in the following iterations of the sequence pulses. The TE is the time interval between the 90-degree RF excitation signal and the echo. In T1 and T2 weighted images, the TR and TE parameters are optimized for their respective relaxation periods. Using a spin-echo sequence, a T1, T2 and proton density images can be produced. Typical values of TR and TE are shown in the table 3.1.

	TR (ms)	**TE** (ms)
T1 weighted	600	10
T2 weighted	3000	100
Proton density	3000	19

Table 3.1: Approximate values of TR and TE for T1-weighted, T2-weighted and proton density images.

For the sake of demonstration, lets consider a brain scan, containing 25 slices in the superior-inferior direction (along $z-$axis). From the table 3.1, we see that for a T1-weighted acquisition the TR and TE values are 600 and 10 millisecond respectively. If each slice has a resolution of 256x256 voxels, time required to scan the whole brain will be,

$$\begin{aligned}\text{Total time} &= \text{TR} \times \text{number of lines to be scanned} \times \text{number of slices} \\ &= (600 \times 256 \times 25)/60000 \ \text{ minute} \\ &= 64 \ \text{ minute.}\end{aligned}$$

64 minute is a long time to scan a brain in a clinical setting. Also, if a subject is kept under scanner for such a long period of time, the scan is bound to have artifacts due to head motion inside the scanner. In the following section, we will discuss more practical variants of the spin-echo sequence.

3.4.2 Fast spin-echo sequence

As mentioned in the previous section, the SE sequence takes a very long time to be of any practical use. Again looking at the same example of a T1-weighted acquisition (refer to table 3.1), the signal is acquired only during TE, that is 10 millisecond. This implies that a large amount of time (590 millisecond) during which the T1-relaxation is taking place is not used at all. This is called *dead period*. The idea behind the present method is to utilize this dead period.

Multi-slice SE sequence

As soon as the first line in a particular slice is scanned, the slice-select gradient is moved to the adjacent slice and the process continues until the first line of every single slice is scanned. The same process is followed with the second line until the whole brain is scanned. This process reduces the dead period considerably resulting a total scan time of 2-3 minutes. The pulse diagram for this pulse sequence is shown in figure 3.13.

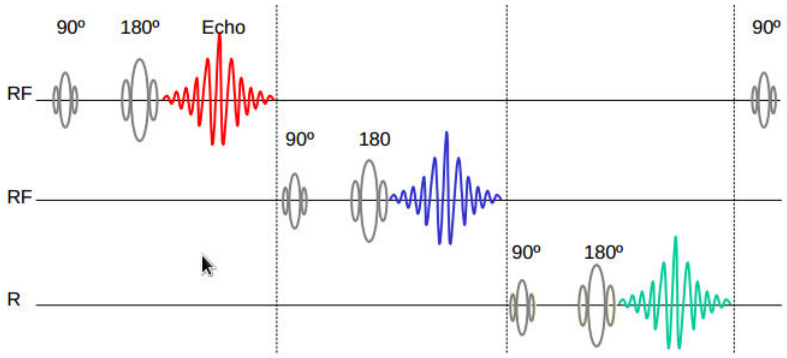

Figure 3.13: Pulse diagram for multi-slice spin-echo sequence. The three lines represent the same row of voxels in 3 different slices.

Multi-echo SE sequence

The multi-echo SE sequence goes with many names such as: turbo spin echo (TSE) and rapid acquisition and refocussing echoes (RARE). The sequence was first introduced by [Hennig 1986]. Contrary to the conventional spin-echo sequence where only a single refocusing 180 degree RF pulse is applied, in RARE a series of refocusing pulses are applied in same TR. Because of the multiple RF excitation pulses there will be multiple echoes which can be used to fill multiple lines in the $k-$space.

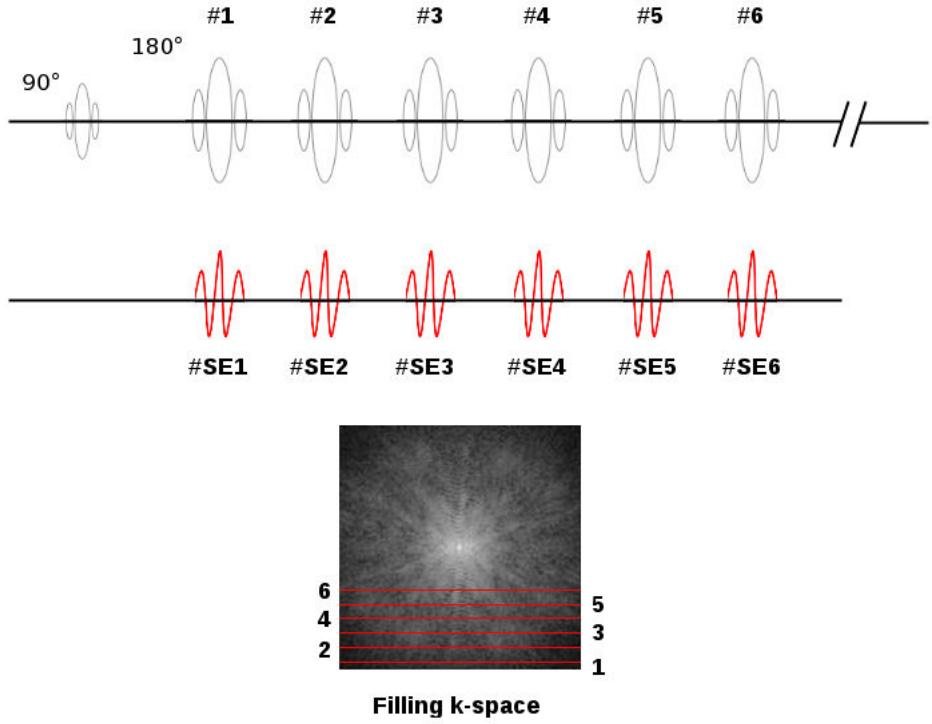

Figure 3.14: A train of refocusing 180° RF pulses follow after the initial 90° during the same TR. Each of the refocusing pulsed produce a spin echo (represented as SE), which is used to fill the $k-$space.

The *echo train length* (ETL) is the number of 180° RF pulses used in the sequence. The number typically ranges from 3 to 32. The time difference between the successive RF pulses is called the *echo spacing* (ESP). The echo corresponding to the central section of the $k-$space is called the *effective echo time*. Since different sections of the $k-$space are filled with different spin-echos, each section will have a different T2 weighting. So, the question that arises is what are the factors that define the image contrast? In figure 3.11 we have discussed that the central section of the $k-$space is the one that define the image contrast. So, the echo corresponding to the central section also determines the contrast for the image. In figure 3.13 it is shown that the $k-$ space is being filled serially. The bottom row is filled with the first echo, the following row from the bottom is filled with the second echo and so on. However, it is possible to assign any of the echos to the central section of the $k-$space, thus changing the effective echo time and the image contrast. Sequences with high ETL have poorer contrast and spatial resolution compared to the ones with low ETL. It is obvious that the echo train length is also the factor determining the increase in the acquisition speed compared to the conventional spin echo sequence.

The major advantage of using a multi-echo spin sequences lies in its faster acquisition schemes as compared to the conventional spin-echo scheme. It is possible to acquire high resolution images, while maintaining a good SNR. Because of the faster acquisition there are less artifacts due to head motion. However, the multi-echo spin sequence does not come without its own drawbacks. A high ETL corresponds to closely spaced 180° RF pulses which does not give enough time to the protons to dephase and loose the magnetization to the surrounding tissue. Thus, the T2 weighted image acquired using the sequence is less sensitive to the magnetic susceptibility effects. This might not sound like a bad thing, but a reduced susceptibility also means that it is difficult to detect tissue changes due to brain hemorrhage like deoxyhemoglobin and hemosiderin compared to the conventional spin-echo sequence. [Hashemi 2012]. There is natural limitation on the number of slices that can be acquired using this scheme. The number of slices depend on the ETL. If the ETL is 16, we can only acquire 16 slices, thus enforcing an upper bound on the resolution. As discussed above, the effect of echo train length is demonstrated in figure 3.15.

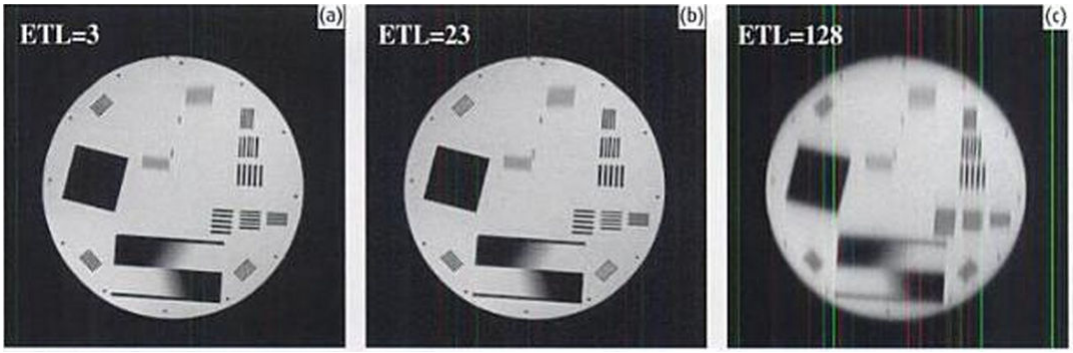

Figure 3.15: Effect of echo train length (ETL) on the image resolution. **a**. ETL =3, TR = 600 ms, TE=12 ms, scan time=52 sec. **b**. ETL=23, TR=600 ms, TE=128 ms, scan time=6 sec. **c**. ETL=128, TR=∞ (single shot), TE=87 ms, scan time=1 sec. Vertical phase encoding direction. Loss in spatial resolution increases with increase in ETL. There is significant loss in resolution in the figure c and subtle resolution loss in figure b. Adapted from [Hashemi 2012]

Ultrafast spin echo

The ultrafast spin echo sequence is similar to the multi-echo SE sequence, but faster as the name suggests. The sequence exploits the symmetrical nature of the $k-$space. It only records the early echos in the system to fill just a little more than half the $k-$space and the missing sections are filled using its symmetry properties. Since the sequence aims to fill the whole $k-$space with a single 90° RF pulse, the TR is very long. For the same reason, it is also called *single shot* sequence The long echo

trains leads to decrease in the strength of late echo signals and thus a decrease in the SNR. These sequences are often used for T2-weighted imaging. The acquisition time is reduced to half, but there is also a loss in the SNR of the image and spatial resolution in the phase encoding direction. The effect can be seen in figure 3.15 c. With this method it is possible to scan the whole brain under 30 seconds.

3.4.3 Gradient recalled echo (GRE)

The gradient recalled echo (GRE) is characterized by a flip angle lower than 90 degree and an absence of 180 degree rephasing RF pulse. Because of the lower flip-angle, the magnetization component in the $xy-$plane is reduced by a factor of sine of the flip angle. A lower flip-angle also allows a quick recovery of the the longitudinal magnetization vector, which means a shorter TR and TE compared to the spin-echo sequences. The shorter TR and TE allows a quick scan time. As mentioned before in section 3.2.3 the decay in transverse magnetization occurs because of spin-spin tissue specific relaxation and the inhomogeneities in the magnetic field and magnetic susceptibility. The signal obtained using the GRE sequence is T2* weighted, because in GRE there is no refocussing 180° pulse.

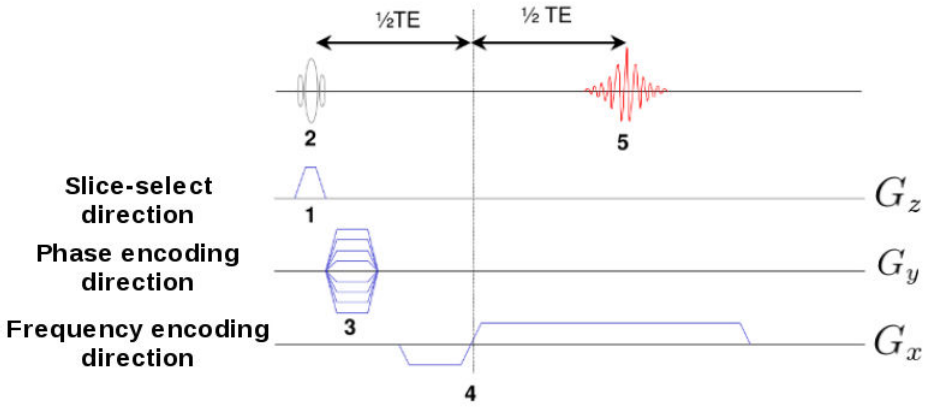

Figure 3.16: Events involved in gradient recalled echo (GRE) pulse sequence. 1. Slice select gradient is switched on. 2. RF excitation pulse is sent. 3. Phase encoding gradient is switched on. 4. Negative frequency gradient is switched on and then polarity is changed to positive. 4. Echo at TE.

Instead of the 180° RF pulse, a dephasing and rephasing gradient is applied as shown in figure 3.17. The dephasing gradient is applied such that all the magnetization vectors go out of phase and then they rephase again with the rephasing gradient. The rephasing magnetization vectors add up in phase at TE and thus produce an echo. A frequency or read-out gradient is applied at this time for the signal acquisition.

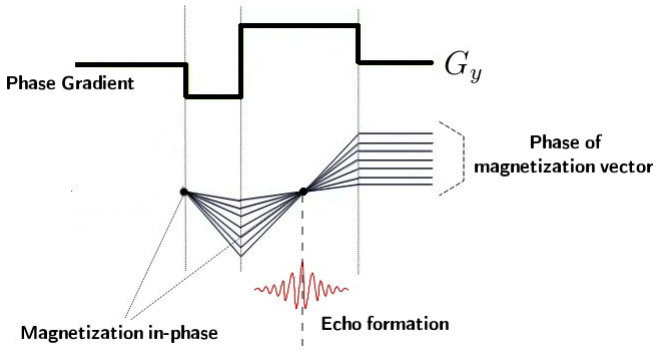

Figure 3.17: Echo formation in GRE. The magnetization vectors are out of phase for the first half of the pulse gradient

It may so happen that the magnetization vector reaches a steady state, that is, it never fully recovers after repeated RF excitation pulses. This happens because the recovery in each TR matches exactly the effect of excitation pulse. Depending on how the residual transverse magnetization is accounted for in image acquisition, there are two different types of GRE; spoiled gradient recalled echo and steady state gradient recalled echo.

Spoiling transverse magnetization

The term "spoiling" refers to the the destruction of the residual (steady state) transverse magnetization before the next RF excitation pulse. There are three methods for spoiling the gradient, which are

1. using a longer TR, that is, TR >> T2/T2* relaxation times.
2. applying a spoiling gradient.
3. changing the RF excitation pulse also called RF spoiling.

The spoiling method is used for faster acquisition techniques in conjunction with spin-echo and multispin echo sequences or gradient echo sequences described above. The first method for spoiling is very simple. It just asks for a longer TR. A longer TR ($>$ 200 ms) is good enough for a complete dephasing of the transverse magnetization as TR >> T2. The method is simple but it unnecessarily increases the acquisition time because one has to wait for the complete relaxation period. The spoiling gradient scheme involves applying additional variable gradients at the end of each RF cycle. The strength of the spoiling gradient can be varied linearly or semi-randomly over the whole acquisition period. The gradients are spatially varying and so the spoiling is not spatially uniform. The best spoiling method is RF spoiling. This method involves applying a phase offset to each successive RF pulse, which causes a phase shift in the successive steady state transverse magnetization vectors.

One can think of it as applying the same flip angle but in a different direction, preventing the steady state build up. This method is better than the previous two because it does not generate any eddy currents and is spatially invariant. The spoiling techniques are in common use and are included in most of the scanners from GE, Siemens and Phillips, though with different names. This method has its advantages in terms of speed of acquisition but the images produced have a low SNR because of the short TR and increase in chemical shift artifacts have also been reported [Hashemi 2012].

3.5 Echo planar imaging

Echo planar imaging is the fastest MRI acquisition protocols available compared to all others discussed above. EPI sequences need a hardware modification and is provided with all the major scanner companies. Due to the fast acquisition routines, it has found its applications in many fields like diffusion weighted imaging (DWI), perfusion imaging and functional magnetic resonance imaging (fMRI). The basic principle of EPIs is to fill the $k-$space using a series of gradient echos as discussed in the case of GRE. The switching of the dephasing and rephasing gradients is done very fast and can be done in a sinusoidal fashion. The two variants of EPI are single shot EPI and multiple shot EPI.

Single shot EPI

In single shot EPI, the reversing gradients are applied after a single RF-pulse (shot) is applied. Usually 128 reversing gradients are applied during a single $T2^*$ decay and each reversing gradient is used to fill one line in the $k-$space. The single shot EPI acquisitions are very demanding in terms of the scanner hardware because of the fast switching gradients. Depending on whether the phase encoding gradient is kept on continuously during the whole readout time period or is switched on and off between the readout gradient, the single shot EPI is called either **non-blipped** or **blipped** acquisition. The non-blipped and blipped pulse sequences are shown in figure 3.18. The manner in which the corresponding $k-$spaces are filled is also shown in the figure. The zigzag filling as in the case of non-blipped EPI presents artifacts during Fourier transform. The blipped EPI was suggested in order to overcome these artifacts. Figure 3.19 shows a typical pulse sequnce schematic for blipped single shot EPI acquisition.

Multishot EPI

The multishot EPI is similar to the single shot EPI, except the fact that instead of having the readout in a single RF pulse, the readout is divided into multiple RF pulses or shots. The multishot EPI takes longer than the single shot EPI, thus increasing the chances of motion artifacts.

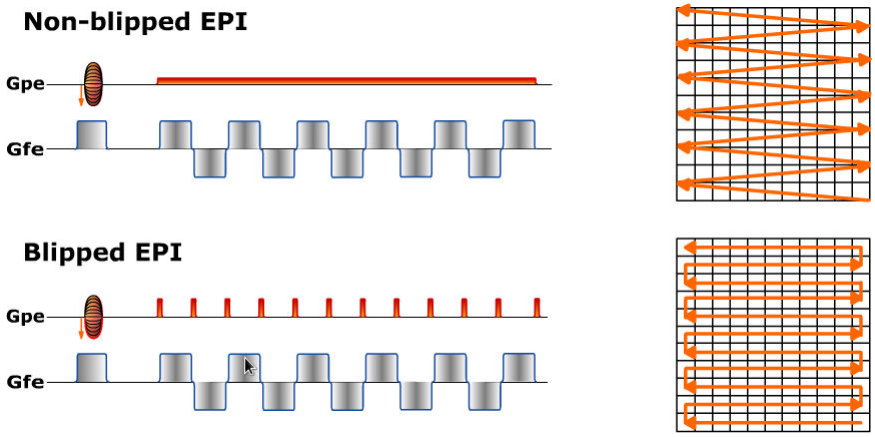

Figure 3.18: Schematic showing the non-blipped and the blipped single shot EPI pulse sequences. G_{pe} and G_{fe} are the phase encoding and the frequency encoding (readout) gradient respectively. On the right the figure shows the corresponding $k-$space filling. For the non-blipped EPI the $k-$ space is filled in a zig-zag fashion and the blipped case it is filled in a serial odd-even (left to right and right to left) manner. Adapted from courses on www.imaios.com/

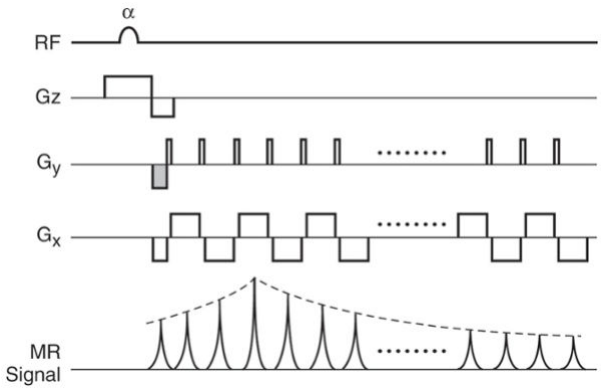

Figure 3.19: A schematic of pulse sequences for single shot blipped EPI sequence. The MR signal peaks due to the initial phase offset in the phase encoding gradient direction G_y. Adapted from [Hashemi 2012]

.

EPI related artifacts

One of the major problems of single shot EPI is that any error in phase propagates through the whole $k-$space. This error is not present in the other spin-echo sequences because after every dephasing-rephasing cycle a new RF pulse is applied. The single shot EPI method produces significant magnetic susceptibility artifacts near the sinus and air-tissue interfaces. The susceptibility artifacts are reduced in multishot echo sequences and shortening the TE. Apart from the susceptibility

artifacts, ghosting of the image can also happen not due to the motion of the subject but due to eddy currents induced in the system by the rapidly switching gradients. For example, in case of EPI sequences, after filling the $k-$space (in odd-even fashion), the $k-$space lines obtained with the negative lobe of the phase gradient has to be reversed. During this reversal process, there might be a phase mismatch due to system inaccuracies and time delays. This artifact is also called **Nyquist** or **N/2 ghosting**. An example of Nyquist ghosting is shown in figure 3.20.

Figure 3.20: Nyquist ghosting in MR imaging using EPI pulse sequences.

These artifacts are common in the diffusion magnetic resonance imaging (dMRI). In the next sections, we will discuss the principles behind diffusion imaging, the pulse sequences used in dMRI and the related artifacts.

3.6 Principle of Diffusion: Einstein's equation

Molecules in a fluid are in constant random motion due to the thermal agitation. This random motion is called Brownian motion [Brown 1828]. In an isotropic media (such as water), the rate of diffusion is same in all directions and can be completely described using the scalar self-diffusion coefficient D. In 1855, Adolf Fick postulated that the particle flux is directed from areas of high concentration to that of low concentration and is proportional to the local concentration of the particles [Fick 1855]. Thus, giving the first Fick's law,

$$\mathbf{J} = -D\nabla n(\mathbf{r}, t), \tag{3.22}$$

where the $\mathbf{J}$ is the diffusion flux, $n(\mathbf{r}, t)$ is the number (concentration) of particles at position $\mathbf{r}$ at time t. Again, according to the law of conservation of mass the rate

of change of $n(\mathbf{r}, t)$ is related to the local diffusion flux divergence as,

$$-\nabla.\mathbf{J} = \frac{\partial n}{\partial t}. \tag{3.23}$$

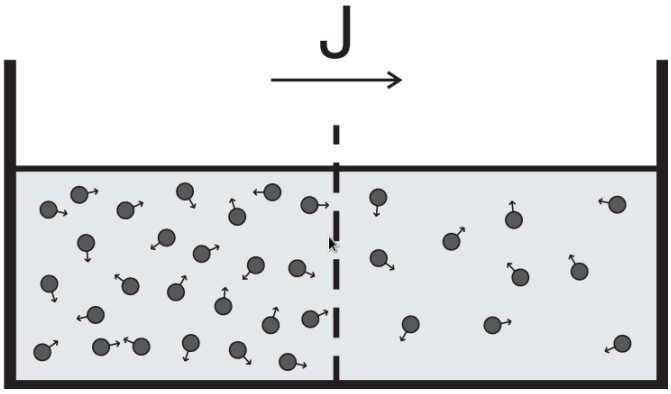

Figure 3.21: Fick's first law. The net flux **J** is directed from regions of high concentration on the left to the regions of low concentration on the right. Adapted from [Baseer 2009]

Substituting in equation 3.22, we have the second Fick's law

$$\frac{\partial n}{\partial t} = D\nabla^2 n \tag{3.24}$$

In 1905, Einstein rewrote the Fick's law as a stochastic process [Einstein 1905]. With a conditional probability $P(\mathbf{r}|\mathbf{r}', t)$ that a particle at $\mathbf{r}$ will move to a position $\mathbf{r}'$ in time t, the number of particles at position $\mathbf{r}'$ at time t is given by,

$$n(\mathbf{r}', t) = \int n(\mathbf{r}, 0)P(\mathbf{r}|\mathbf{r}', t)\, dr\mathbf{r}, \tag{3.25}$$

The conditional probability also obeys the Fick's law of diffusion. From the second Fick's law, we have

$$\frac{\partial P(\mathbf{r}|\mathbf{r}', t)}{\partial t} = D\nabla^2 P(\mathbf{r}|\mathbf{r}', t) \tag{3.26}$$

Considering the conditional probability at $t = 0$, as a Dirac delta function, that is, $P(\mathbf{r}|\mathbf{r}', 0) = \delta(\mathbf{r}' - \mathbf{r})$, the solution for the above equation is a Gaussian distribution [Jones 2010],

$$P(\mathbf{r}|\mathbf{r}', t) = (4\pi Dt)^{-3/2}\exp\left(-\frac{\mathbf{r}' - \mathbf{r}}{4Dt}\right) \tag{3.27}$$

On computing the *ensemble average*[6] of the above distribution, we have

$$< (\mathbf{r}' - \mathbf{r})^2 >= 6Dt. \tag{3.28}$$

The above equation is the famous Einstein's equation for diffusion. From a statistical perspective, the diffusion is reflected as the mean square distance traversed by the molecules in a given period of time.

[6] an average of all the possible microstate of the system

Effect of diffusion on MR signal: A qualitative explanation

So far we have seen that in typical pulse sequences, the tissue is excited with a RF pulse and the transverse magnetization is refocused either with a 180° pulse (spin-echo) or a gradient reversal pulse (GRE). In these two sequences, the refocusing pulse leads to the cancellation of the phase due to magnetic field inhomogenities and produce an echo at TE. In the absence of any diffusion, the magnetic spins dephase and rephase after the application of the 180° (or the gradient reversal pulse) because there is no difference in the magnetic field throughout the system. On the other hand, if there is a drift in the protons due to diffusion, there will be a difference in the magnetic field across the system. This difference will lead to a difference in dephasing and rephasing of the proton spins. There is a partial rephasing of the spins leading to a incoherent phase distribution. This phenomena leads to a signal attenuation at TE. The attenuation of the signal depends on the micro-structural integrity of the tissue sample (as the diffusion is also dependent on the tissue properties) and the pulse sequence used.

3.6.1 The Diffusion Tensor

If we conduct a thought experiment, which involved tracking a water molecule through an isotropic medium, the rate of diffusion will be same in all directions and thus the probability of finding the particle will be also isotropic. For a given time t, the translational displacement of the particle around the initial starting point will be a sphere. This is exactly the phenomena explained by the Einstein's diffusion equations described above. Taking our thought experiment a step further, if we consider tracking the water molecules in anisotropic media, we will find that the rate of diffusion is no longer isotropic. The diffusion is more directed along the anisotropy of the medium than across it. The phenomena can be visualized in the figure 3.22. Following from the equation 3.27, the voxel averaged displacement distribution is given by,

$$P(\mathbf{R}, t|0) = \frac{1}{\sqrt{|\mathbf{D}|(4\pi t)^3}} \exp(-\frac{\mathbf{R^T D^{-1} R}}{4t}), \tag{3.29}$$

where $\mathbf{R}$ is the distance traversed by the water molecule, $|\mathbf{D}|$ is the determinant of the diffusion coefficient $\mathbf{D}$. The diffusion coefficient is a second order positive definite tensor. The above equation describes a three dimensional ellipsoid in the displacement space. The diagonal elements of the diffusion ellipsoid is proportional to the second moment of diffusion along the three orthogonal coordinate axes and the off-diagonal terms yield the correlation between the displacements along the orthogonal axes. The diffusion coefficient in an anisotropic media is a generalized representation of the diffusion in isotropic media. When all the eigen values of $\mathbf{D}$ are equal, the rate of diffusion is isotropic, whereas when the eigen values are different the rate of diffusion is higher along the direction of higher eigen value. Traditionally, the three eigen values are represented as $[\lambda_1, \lambda_2, \lambda_3]$.

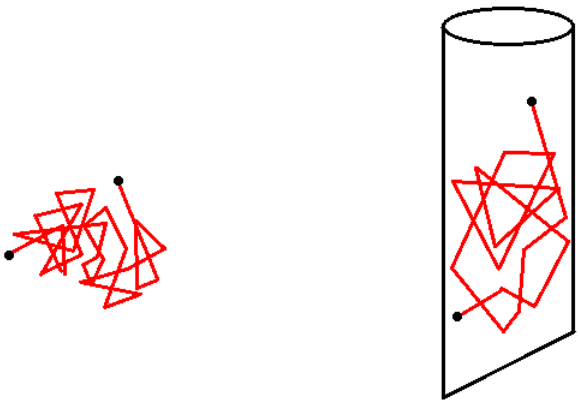

Figure 3.22: Isotropic diffusion (left) showing equal probabilities in all directions and anisotropic diffusion (right) highly probably to diffuse along the anisotropy of the media.

Scalar metrics: Shape and size of diffusion tensor

For the purpose of analysis and also visualization, various scalar metrics are derived from the diffusion tensor. One of the most important criteria for the scalar metrices is that they should be rotationally invariant. One of the first rotationally invariant parameters are the eigenvalues of the diffusion tensor. In this section, we will look at some of the commonly used scalar values derived from the diffusion tensor and their physical meaning.

Trace

The trace of a diffusion tensor is the sum of eigen values of the diffusion tensor, that is

$$\text{Trace}(D) = \lambda_1 + \lambda_2 + \lambda_3. \tag{3.30}$$

The trace gives an estimate of the size of the diffusion tensor. The trace values are often used in monitoring stroke.

Mean Diffusivity (MD)

The mean diffusivity is the average of the eigen values of the diffusion tensor and is given by,

$$\text{MD} = \frac{\lambda_1 + \lambda_2 + \lambda_3}{3} \tag{3.31}$$

Fractional Anisotropy (FA)

Fractional anisotropy is one of the most common scalar measures in use. It gives a measure of how elongated or round the diffusion tensor is. The value of FA ranges

between 0 and 1. The lower FA values (close to 0) correspond to the cerebrospinal fluid, whereas the regions with higher FA values (close to 1) correspond to that of white matter tracts. The FA can be computed as,

$$\mathrm{FA} = \sqrt{\frac{(\lambda_1 - \lambda_2)^2 + (\lambda_2 - \lambda_3)^2 + (\lambda_3 - \lambda_1)^2}{2(\lambda_1^2 + \lambda_2^2 + \lambda_3^2)}}. \tag{3.32}$$

3.6.2 Bloch-Torrey Equation

The Bloch equation (equation 3.7) gives the rate of change of magnetization vector in presence of a magnetic field. However, it does not take into account the diffusion phenomena. These equations were modified later by H.C. Torrey in 1956 to incorporate the diffusion phenomena [Torrey 1956]. For the time evolution of the transverse magnetic field (M_{xy}), the Bloch-Torrey equations can be written as,

$$\frac{d\mathbf{M}}{dt} = \mathbf{M} \times \gamma\mathbf{B_{eff}} - \frac{M_x\vec{i} + M_y\vec{j}}{T_2} - \frac{(M_z - M_0)\vec{k}}{T1} + \nabla\cdot(\mathbf{D}\nabla\mathbf{M}), \tag{3.33}$$

where symbols have their usual meanings. The evolution of the transverse magnetization component M_{xy} is presented in [Johansen-Berg 2009]. The equation is,

$$\frac{\partial M_{xy}}{\partial t} = -i\omega_0 M_{xy} - \frac{M_{xy}}{T_2} - i\gamma(\mathbf{G}\cdot\mathbf{r})M_{xy} + D\nabla^2 M_{xy}, \tag{3.34}$$

where $i = \sqrt{-1}$, ω_0 is the Larmor frequency, γ is the gyro-magnetic ratio, $\mathbf{G}$ is the magnetic gradient and $\mathbf{r}$ is the voxel location where the RF pulse is induced.

3.6.3 Stejskal-Tanner equations

In the year 1965, Stejskal and Tanner proposed a pulse gradient spin echo sequence (PGSE) for measuring the diffusion coefficient $\mathbf{D}$ [Stejskal 1965]. Unlike the previous pulse sequences discussed before, in PGSE there was a distinction between the pulse duration δ and the time difference between the two pulses Δ. The total phase change induced by the first gradient will be,

$$\phi_1 = -\gamma(\delta G)x_1, \tag{3.35}$$

where x_1 is the position of the particle on the application of the first gradient pulse G. The differential magnetic field is the product of the gradient and the duration δ for which it is applied. The magnetization due to the static magnetic field B_0 is ignored as that will be the same for all the protons. Similarly for the particle at position x_2, the phase change will be,

$$\phi_2 = -\gamma(\delta G)x_2. \tag{3.36}$$

The net phase change is the difference $\phi_1 - \phi_2 = -\gamma G\delta(x_1 - x_2)$. In the original paper [Stejskal 1965], the authors showed that the attenuated transverse magnetization $M_{xy}(\mathbf{r})$, hereon referred to as $S(\mathbf{r})$ can be written as

$$S(\mathbf{r}) = S_0(\mathbf{r})\exp\left[-\gamma^2||\mathbf{G}||^2\delta^2\left(\Delta - \frac{\delta}{3}\right)\mathrm{D}\right], \tag{3.37}$$

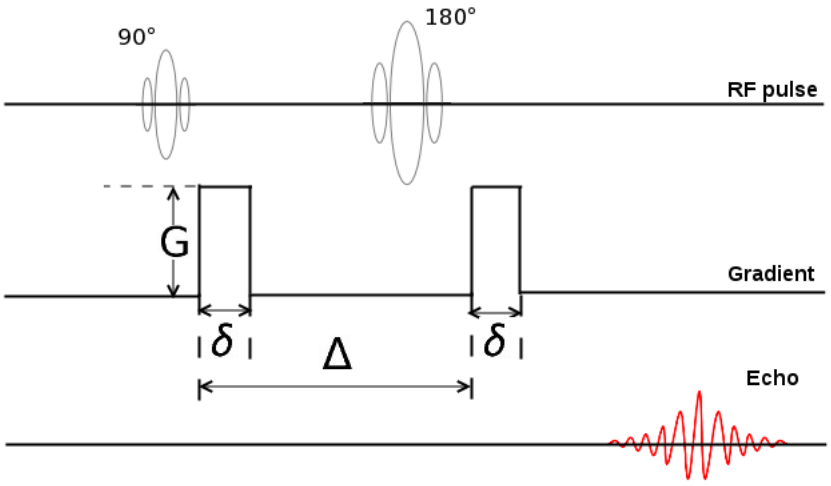

Figure 3.23: Schematic showing the pulse gradient spin echo scheme introduced by [Stejskal 1965]. The duration of the pulse is denoted by δ and the time difference between the gradient pulse is Δ.

where $S_0(\mathbf{r})$ is the initial transverse magnetization. The term b-factor also known as the diffusion weighting factor introduced by [Le Bihan 1986] is defined as

$$\mathrm{b} = \gamma^2 ||\mathbf{G}||^2 \delta^2 \left(\Delta - \frac{\delta}{3}\right), \tag{3.38}$$

reducing the equation 3.37 to

$$S(\mathbf{r}) = S_0(\mathbf{r}) \exp(-b\mathrm{D}) \tag{3.39}$$

The term b-factor only depends on the acquisition parameters and refers to the measurement sensitive to diffusion. A b-value of zero will lead to a T2 weighted EPI image. In clinical settings typically a b-value of 1000 is used. A higher b-value will increase the contrast in pathogenic regions at the cost of low SNR. The dependence of b-value on the image is shown in figure 3.24. High b-value diffusion weighted imaging is an active area of research and lot of work has been done in this regard [Meyer 2000, Ichikawa 2006, Kim 2010].

For anisotropic diffusion the equation 3.39 needs to be written in a more general form as suggested by [Westin 2002] as

$$S(\mathbf{r}) = S_0(\mathbf{r}) e^{-\mathrm{bG^T DG}}. \tag{3.40}$$

The diffusion matrix D being a 3×3 symmetric matrix, we need at least six measurements along six non-collinear gradient directions and an unattenuated image S_0 to estimate the six parameters of the diffusion tensor. The equation 3.40 is linear in the log domain, thus,

$$\ln(S(\mathbf{r})) = \ln(S_0(\mathbf{r})) - \mathrm{bG^T DG}. \tag{3.41}$$

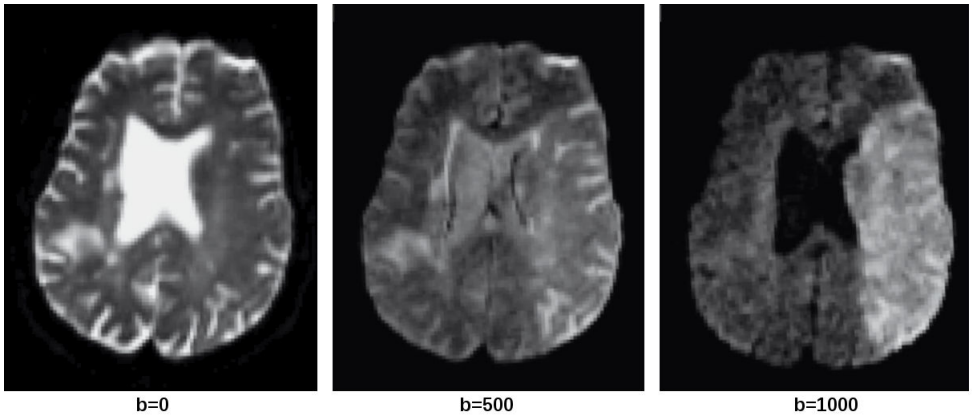

Figure 3.24: Effect of b-values on diffusion weighted imaging. The image on the left is undiffused image (b = 0), while the one on the extreme right is strongly diffused with a b-value equal to 1000. The middle image shows intermediate diffusion between the two. Adapted from [Graessner 2011]

There will be linear system of six such equations which should be solved for the six terms in the diffusion tensor D. In practice, more than six diffusion images are acquired to solve the system of equations. Over the years, various sophisticated tools are designed for the estimation of diffusion tensors which will be discussed in chapter 4.

3.6.4 Pulse sequence for DWI acquisition

The two major concerns regarding the diffusion weighted imaging are the bulk head motion of the subject and the eddy current distortions induced in the image due to fast switching gradients. Various pulse sequences were designed in the past for diffusion weighted imaging, while taking into account these two problems. In this section, we are going to discuss the single shot EPI and multi-shot EPI sequences for diffusion imaging. The EPI technique could be used for diffusion imaging by combining it with a diffusion weighted preparatory pulse followed by a single shot EPI sequence as shown in the figure 3.25.

EPI based methods for diffusion weighted imaging

We discussed a single shot EPI sequence and its pros and cons in the previous section. The single shot EPI sequence is faster than traditional SE and GRE sequences and thus is more suited for diffusion imaging. However, the images produced with this sequence has ghosting and susceptibility related artifacts. In addition the diffusion weighted images (DWIs) are typically low in spatial resolution as the resolution is limited by the $T2^*$ relaxation periods. The single shot diffusion weighted imaging can be combined with parallel imaging protocols like SENSitivity Encoding (SENSE) [Bammer 2001]. With the EPI-SENSE protocol, the susceptibility and

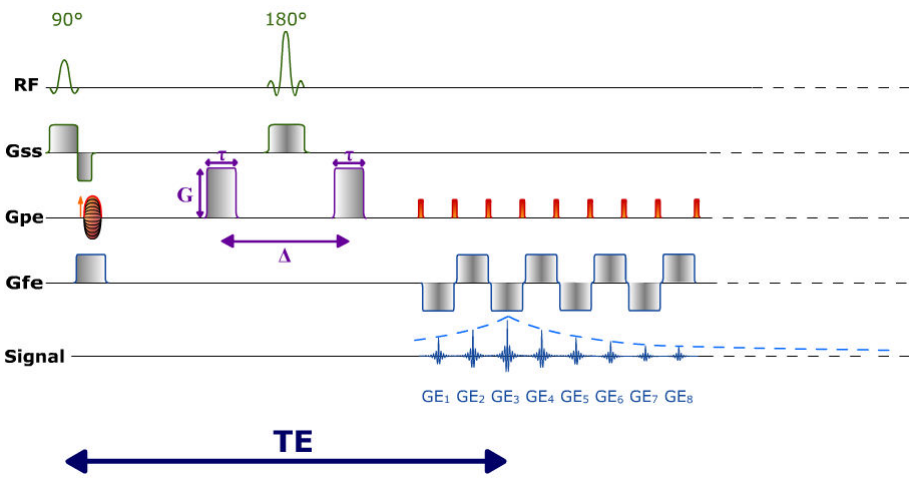

Figure 3.25: A typical diffusion weighted EPI pulse protocol. The diffusion gradient preparatory pulse (shown in purple) is followed by a single shot EPI sequence. However the EPI sequence could be multishot too. G_{ss}, G_{pe} and G_{fe} are the slice select, phase encoding and frequency encoding directions respectively. Adapted from courses on www.imaios.com

blurring artifacts are diminished. The parallel imaging leads to a decrease in the signal readout time leading to improvement in spatial resolution of the DWI because the EPI readout time is decreased. The figure 3.26 shows a comparison of the images acquired using the conventional single shot EPI sequence and EPI-SENSE protocol.

Non-EPI based methods for diffusion weighted imaging

Single Shot methods

The single shot methods are very popular in the case of diffusion weighted imaging. The DWI are highly susceptible to any kind of head motion (e.g. bulk head motion due to turning the head and pressure pulsations from the heart) because the phase introduced due to head motion is much larger than the phase used to encode the spatial location in the brain. However, if the imaging is completed with a single shot, the phase change due to head motion is constant through out the image and so it does not produce any motion related artifacts.

Line scanning method (LDSI): The line scan methods can be viewed as 1D MRI. In a conventional MR imaging setup, the images are acquired on a single 2D plane (slice) using the RF excitation and refocusing pulses. The two pulses are applied in a tilted fashion as shown in the figure 3.27. The method was first introduced by [Chenevert 1991] and further developed for practical imaging by [Gudbjartsson 1996] The pulses are shown in red and yellow and the scanned column is shown in white. The image is reconstructed by arranging all the columns

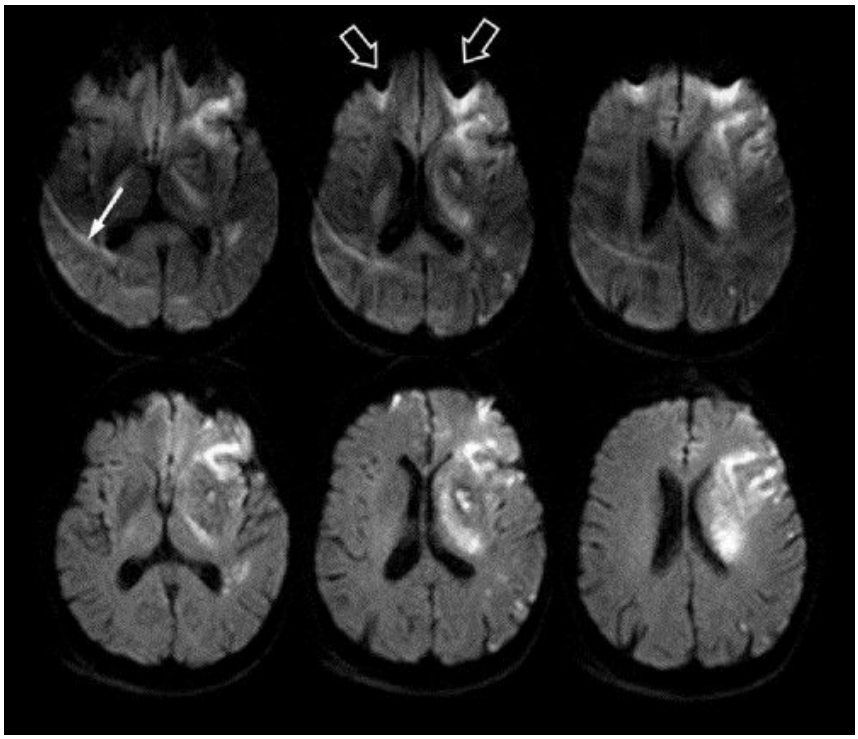

Figure 3.26: Comparison of magnetic susceptibility artifacts between single shot EPI (top) and EPI-SENSE (bottom). With the SENSE-EPI protocol there is a significant reduction in the susceptibility artifacts in the frontal lobe (open arrows). There is a significant reduction in the artifacts due to chemical shift (arrow). Adapted from [Bammer 2003]

next to each other as shown in figure 3.27 d. Because of such unique encoding planes, the method is robust towards susceptibility artifacts and eddy current distortions present is conventional single shot EPI methods. [Jones 2010]. The

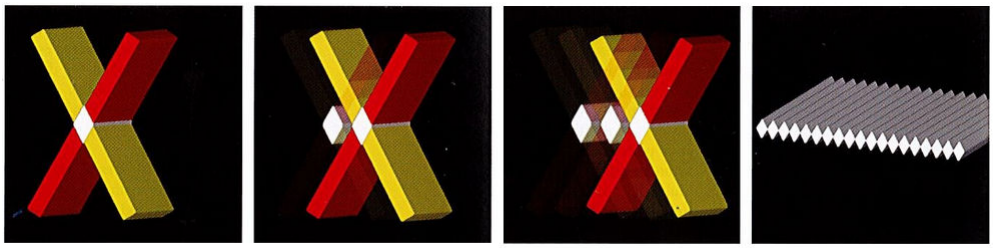

Figure 3.27: Line scanning method for diffusion imaging. The red and yellow planes show the planes for RF excitation and the refocusing pulses. (A). The diamond shape region at the intersection of the pulses is encoded with the frequency encoding along its length. (B,C) A series of such rods are encoded and (D) arranged to form a 2D plane. Adapted from [Jones 2010].

other single shot methods worth mentioning are SS-FSE (single shot fast spin-echo) or HASTE (half-Fourier acquisition single shot turbo spin-echo). Similar to single shot methods, multshot spin echo methods can also be employed for diffusion imaging.

Radial and Spiral $k-$space filling techniques: So far in this chapter we have only discussed pulse sequences that fill the $k-$space in a linear fashion according to the Cartesian coordinate system. However, there are techniques which employ other methods of filling up the $k-$space. The radial $k-$space sampling produced very high oversampling (in the Nyquist sense) of the central $k-$space as can be seen in the figure 3.28. Thus, the radial acquisition methods are inherently inefficient. However, this oversampling can be taken care of by deliberately undersampling the data during the image reconstruction process. What it means is that the image can be reconstructed using a subset of the projections in the center of the $k-$space [Jiang 2005, Sarlls 2005]. Because of the oversampled central $k-$space region, the images produced have higher spatial resolution compared to linear sampling (see figure 3.10). The images are also isotropic in-plane and are less sensitive to motion artifacts. Each radial line in the $k-$space when transformed individually into image space is a projection of 2D image on a 1D line. For this reason, the method is sometimes called *projection reconstruction.*

PROPELLER: Periodically rotated overlapping parallel lines with enhanced reconstruction or PROPELLER is another radial imaging technique where the $k-$space is filled using radial strips instead of radial lines [Pipe 2002]. The strips are distributed over a circle, where the width of the strip is same as the diameter of the circle. The data in each blade is acquired within a TR time-period. This

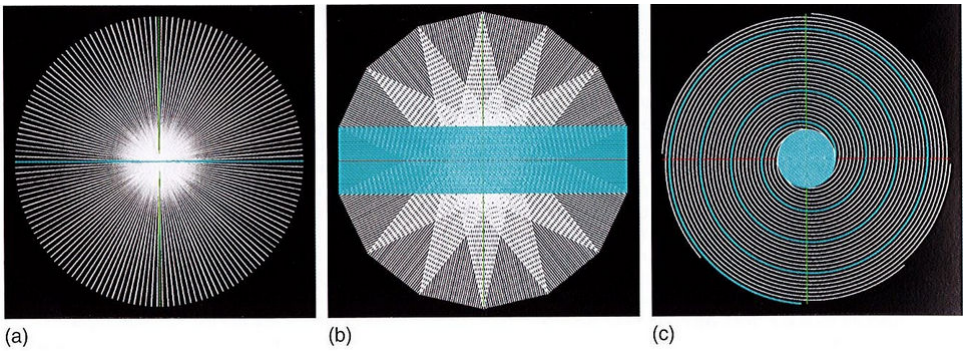

Figure 3.28: Non-Cartesian $k-$space filling trajectories: (a) radial (b) PROPELLER (c) spiral trajectories. The blue section shows the $k-$space filled in a single TR. The complete $k-$space is filled with multiple TRs. Adapted from [Jones 2010]

method is robust to motion related artifacts. As each strip can be used to produce an image, there is an inherent redundancy in the $k-$space. The redundancy exists in the circle common to all the strips in the center of $k-$space and can be used to estimate subject motion (both bulk head motion and subtle head motions related to breathing and pulsations). The PROPELLER method is quite robust to the geometric warping seen commonly in the diffusion images when compared to the SS-EPI methods (figure 3.29). In the figure 3.29, pronounced artifacts can be seen in the infarcted[7] regions. The patient (a,b) has infracts in the temporal lobe, while the other has infracts in the pons. The acquisition is based on the fast spin echo sequences and arbitrarily high resolution images are possible with FSE based PROPELLER. However, the method has low SNR properties. Also, the T2 relaxation times may lead to narrow stripes. The narrow stripes lead to poor phase estimation and thus greater phase inconsistencies between the stripes. The k-space trajectory for this method is shown in figure 3.28 b.

Another variant of PROPELLER is Turboprop suggested by the same authors [Pipe 2006]. Compared to PROPELLER which uses single RF refocusing pule to fill each strip, Turboprop uses single RF pulse to fill multiple stripes in the k-space. So, the method is faster than PROPELLER. There can be loss in signal in the later stripes due to absence of refocusing pulses.

Spiral k-space filling: Another non-Cartesian k-space filling method is spiral filling. The method can be useful for diffusion imaging, for example SNAILS (self navigated interleaved spirals) introduced by [Liu 2004]. For spiral imaging the readout gradients varies continuously (switching between positive and negative) as compared to fast switching gradients. Thus, the method puts less stress on the gradient switching system of the scanner. In the figure 3.28 c, one can see that similar to the other two radial methods, the center of the k-space is oversampled,

[7] an area in the tissue that undergoes necrosis due to obstructed blood supply.

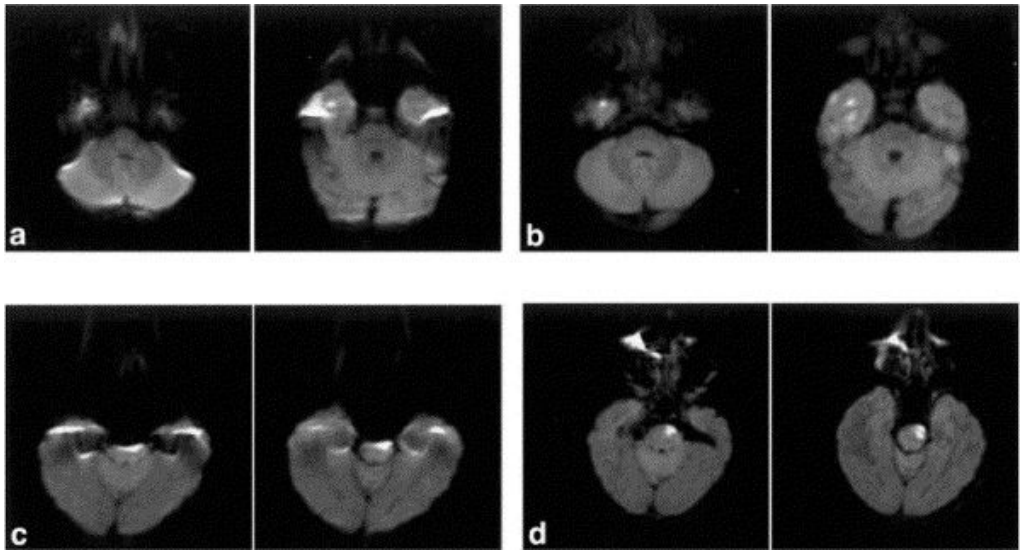

Figure 3.29: Comparison of artifacts between SS-EPI (a,c) and PROPELLER (b,d) for two patients, one with temporal lobe infracts (a,b) and other with infracts in the pons (c,d). Adapted from [Bammer 2003]

.

which makes the method robust to motion artifacts. The edges of the k-space is sparsely sampled as is quite evident from the figure 3.28 c. The data is acquired with a single RF pulse.

The navigation echo is a method for motion compensation during MRI and is used both in PROPELLER and SNAILS. The method involves selecting a line from the center of the k-space in a periodical manner. Then the similarity is computed between each navigator and the data based on the maximum similarity is chosen. Since, in both spiral and radial scanning techniques, the center of the k-space is oversampled, it provides enough navigator echos for good motion correction. In the SNAILS method, the periodicity of the scan is inherent in the system and so the term self-navigating.

3.7 Conclusions

In this chapter, we discussed a brief history of noninvasive neuroimaging techniques in particular the magnetic resonance imaging. The physics behind nuclear magnetic resonance was discussed followed by the common terminologies involved in the process like excitation pulses, transverse magnetization and relaxation times. A qualitative description of signal localization in MR imaging process was discussed. We also discussed relationship between k-space and MR image and the different k-space filling techniques. A qualitative review of different pulse sequences commonly used for MR image acquisition was presented along with the pros and cons of each

method. The idea was to present the building blocks of the acquisition techniques and show how some of them can be combined to achieve more sophisticated pulse sequences. Designing an appropriate pulse sequence for a given imaging requirement is a complicated task. Keeping that in mind, we discussed few of the commonly used echo planar imaging techniques. We also discussed the principle behind diffusion weighted imaging and diffusion tensors, the physics of diffusion and the pulse sequences designed for diffusion weighted imaging.

Chapter 4

Super-resolution of clinical diffusion tensor images

Contents

4.1 Low Spatial Resolution in clinical DTI

Using diffusion weighted imaging (DWI), we can peer into deep white matter (WM) fibers, their structures and the associated pathologies. DTI is currently playing an important role in the study of diseases related to white matter, ranging from white matter dementia to assisting neurosurgeons for better surgical planning. Generally, clinical DTI acquisitions has low spatial resolution (typical acquisitions are 2 - 5.5

mm in each direction). However, it is often desirable to visualize high resolution (HR) images. HR diffusion weighted images requires either prolonged acquisition time or using scanners with stronger magnetic fields (7 T and 11 T), compared to the ones used on regular basis (1.5 T and 3.0 T). Both of these options are not suitable for clinical scenarios. So, resampling the low resolution DTI to a high resolution space is currently the only option available to clinicians. Furthermore, in the realm of population based statistical studies, even if the HR image acquisitions are performed, it is required that the DTI is resampled to a common image template. One solution is to employ algorithmic improvements to the present tensor estimation methods while taking into account the model degradation due to the partial volume (PV) effects. A recent algorithm performs super-resolution on DWI using multiple anisotropic orthogonal acquisitions [Scherrer 2012]. Unlike the method presented in [Scherrer 2012], we suggest a tensor estimation algorithm which requires a single DWI acquisition, thus making it even more suited to the clinical environment.

4.1.1 Partial Volume Effects

Quite an impressive amount of work pertaining to various tensor estimation methods has been done in the past. But unfortunately few of them take into account the effects of partial volume. These tensor estimation methods typically favor fitting a single tensor model [Fillard 2007] to the the acquired data. But in the voxels with PVE, a single tensor model will not be sufficient to describe the true diffusion chatacteristics. In [Alexander 2001], the authors showed that a single diffusion tensor model maybe misleading if two or more tissue compartments are present within the voxel. In fact using a single tensor model in such voxels leads to underestimation of tensors. The fractional anisotropy (FA) maps computed from such underestimated tensors misrepresent the white matter integrity in the brain and also compromise tractography related studies.

Partial volume effect (PVEs) is observed when two or more different tissue types co-exist in the same voxel. The presence of PVE in the diffusion weighted images leads to underestimation of the tensors and also affect the subsequent tractography [Vos 2011]. Everyone agrees on the adverse affects of partial volume on fiber tractography, segmentation and disease specific statistical studies [Kubicki 2007, Pfefferbaum 2003, Hwang 2007].

Some authors have suggested multi-compartment tensor models, which overcome the limitations posed due to single diffusion tensor model and partial volume effects. One such model was proposed by [Behrens 2003]. The authors propose a partial volume model of local diffusion using a ball-and-stick model. The model assumes that diffusion within the axons is unidirectional and along the axon, whereas the diffusion outside the axons is isotropic in nature. The isotropic diffusion is modeled using a ball. Another two-compartment model was suggested by [Alexander 2008]. Unlike, the ball and stick model, the cylinder used to represent the axon has a

non-zero diameter. The extra-axonal component is represented as a cylindrically symmetric tensor. The major eigenvector is directed along the direction of fiber orientation. The diffusivities of the intra and extra axonal space are assumed to be same. The CHARMED method [Assaf 2005] assumes the total signal decay in case of diffusion imaging has two contributors: one is the Gaussian (hindered) and another is the non-Gaussian (restricted) effects. The Gaussian contribution is due to the extra-axonal compartment and the non-Gaussian contribution is due to the intra-axonal compartment of the voxel.

In the spirit of multi-compartment models DTI models with three or more compartments were also explored. For example, in AxCaliber proposed by [Barazany 2009] the authors use a three compartment model. The authors use the two compartment model presented in CHARMED and add another free diffusing component with fixed diffusion coefficient for modeling the diffusion due to CSF contamination. Another multi-compartment model which accounts for multiple fiber orientation is called diffusion directions imaging (DDI) [Stamm 2011, Stamm 2012a, Stamm 2012b]. DDI is essentially a new parametric model of the diffusion probability density function (pdf) and can be acquired under time limits comparable to that of clinical DTIs.

For most of the multi-compartment models one needs to know the volume fraction of contribution within the voxels. For techniques like CHARMED and AxCaliber, the diffusion signal has to be measured at multiple b or q values which is expensive in terms of scanning time. The multiple compartment models can be used for a more accurate description of the white matter structure, if the number of compartments are known in advance. The different models do not agree on the same description of the white matter tracts because of the presence of non-collinear white matter bundles in the same voxel. In [Stamm 2014b, Stamm 2014a], the authors propose to determine the optimal white matter fascicle configuration as a *model selection problem* in-order to avoid the problem of over-fitting.

Contrary to the existing multi-compartment models, our method aims to increase the DTI resolution with a single tensor model. We believe that in the higher resolution a single voxel would contain a single tissue type and a single tensor model is sufficient to explain the signal attenuation in such cases. This super-resolution algorithm is motivated by clinical applications, where single tensor models and the associated DTI metrics like FA, MD and ADC are used more often compared to the multi-tensor models.

4.1.2 Super-resolution reconstruction

One of the first super-resolution algorithms proposed by Peled et al. uses a combination of spatially shifted single shot DWIs to create HR images [Peled 2001]. This method uses eight repeated low resolution scans with a shifted field of view

and different b-values each time. In another study, inter slice reconstruction [Greenspan 2002] using super-resolution was suggested in which each volume acquisition is spatially shifted in the slice-select direction and super-resolution is achieved using the Irani-Peleg's [Irani 1993] back-projection method. But this method was not extended for DTI studies. Super-resolution on diffusion weighted images using multiple anisotropic orthogonal DWI scan has been reported recently [Scherrer 2012]. All these methods of super-resolution require multiple acquisitions of the same subject. Though this might be an acceptable practice in a research environment, but it will be difficult and even undesirable in a clinical setting. Contrary to previous methods, we propose a HR tensor reconstruction algorithm which does not require multiple acquisitions. It also accounts for the PV in the low resolution DWIs, producing DTI at higher resolutions.

4.2 Statistical Tensor Reconstruction with spatial prior at any resolution

The diffusion tensor D is related to each DWI S_i corresponding to the encoding gradient g_i and the image with null gradient S_0 using the Stejskal-Tanner equation [Stejskal 1965], $S_i = S_0 e^{-b{g_i}^T D g_i}$. The diffusion tensor D is a second order symmetric positive definite matrix. In this work, we base our tensor estimation model on variational methods for joint estimation and smoothing of DTI [Fillard 2007] in the Log-Euclidean framework.

4.2.1 A discrete signal degradation model: From high resolution to low resolution images

The observed signal in a voxel in the low resolution (LR) image, can be modeled as the weighted sum of intensities of the voxels in the high resolution (HR) image composing the one in the LR image.

$$S^{LR}(x_k) = \sum_j \alpha_{kj} S^{HR}(y_j), \tag{4.1}$$

where $S^{LR}(x_k)$ is the signal intensity in the voxel x_k of the low resolution image and y_j is a voxel in the high resolution image which composes the voxel x_k and α_{kj} is the corresponding spatial weight of y_j in x_k. This tensor estimation problem is inherently ill-posed, as an infinite number of combinations of high resolution tensors will satisfy the equation 4.1. The proposed algorithm favors the solution which promotes more structures in the white matter regions. A pictorial representation of the image degradation model is shown in figure 4.1. The figure on the left is a low resolution diffusion image, whereas on the right represents two possible high-resolution tensor configuration for the same low resolution diffusion image. The red and the black voxel on the left show identical diffusion tensor, even though the underlying micro-structure in the voxels is different. This loss of

information is due to the spatial averaging of the signals as modeled in equation 4.1. The two images on the right (in figure 4.1) shows two of the infinitely many possible configurations. Of the two, the bottom right image shows a configuration which could detect more structures (shown in green) and thus will be favored by the proposed super-resolution algorithm.

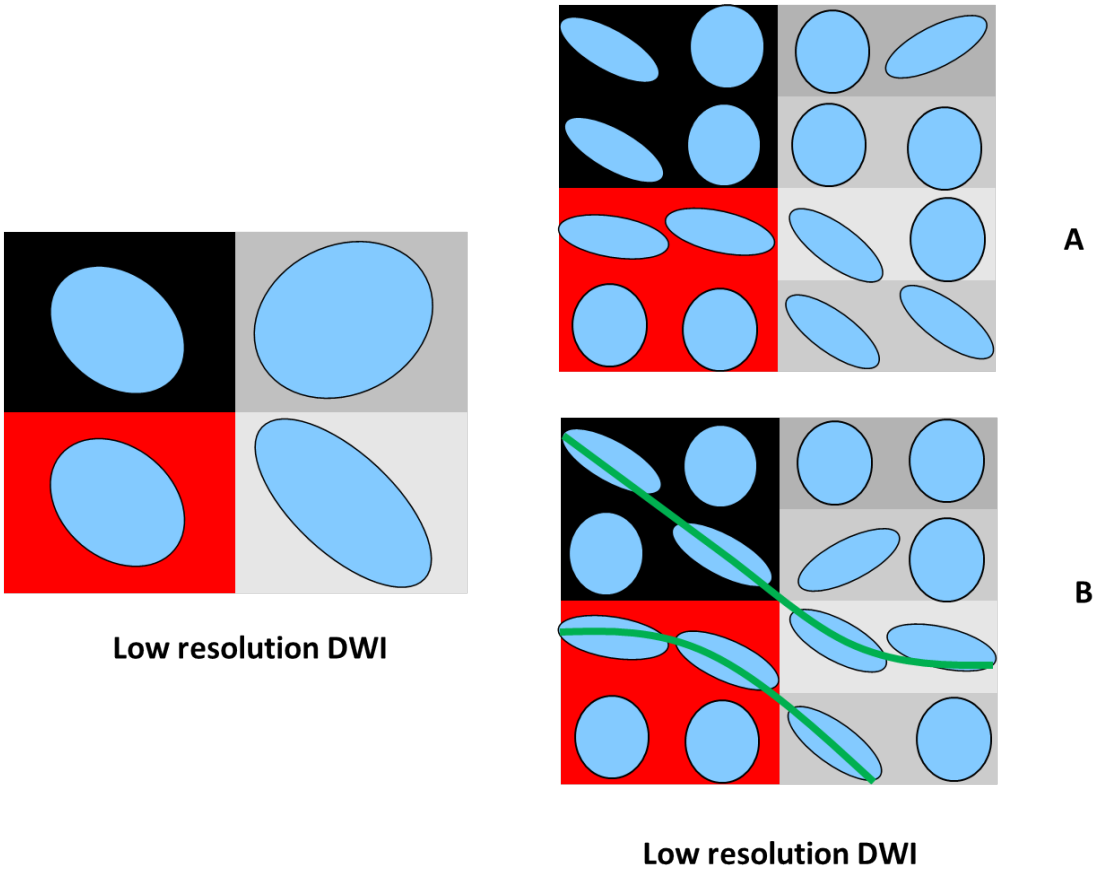

Figure 4.1: Image degradation model. The red and black voxels in the low resolution diffusion weighted image (DWI) show identical diffusion tensors, whereas the underlying micro-structure in both the voxels are different. Spatial averaging leads to loss of information which is modeled in equation 4.1. The images on the right show two of the infinitely many possible solutions for resolving the low resolution DWI on the left. The solution in figure **B** will be favored against the solution in figure **A** because it tries to favor more structures.

Based on the above model, each LR gradient image, S_i^{LR} can be written in terms of the underlying HR tensors (D^{HR}) and the S_0^{HR} (image with null gradient in high

resolution).

$$S_i^{LR}(x_k) = \sum_j \alpha_{kj} {S_0}^{HR}(y_j) e^{-b{g_i}^T D^{HR}(y_j) g_i}, \tag{4.2}$$

where g_i is the pulse gradient. For the sake of convenience, we will write S_i^{LR} as S_i and expand the term using equation 4.2, when necessary. x_k and y_j will always correspond to the LR and HR image indices respectively. In effect, the goal is to predict the underlying higher resolution tensor image from low resolution diffusion weighted images.

4.2.2 Tensor Estimation

The signal attenuation in diffusion weighted imaging is characterized by the Stejskal-Tanner equation:

$$S_i = S_0 e^{-b{g_i}^T D g_i}, \tag{4.3}$$

where D is the diffusion tensor, b is the sensitivity factor and g_i is the pulse gradient. Over the years, a number of tensor estimation schemes have been suggested. Some of them are available as software packages and are used extensively in the medical imaging community. Some of the software packages available for tensor estimation are Slicer, MedInria, camino, FSL.

In this section, we will broadly discuss some of the tensor estimation algorithm families. The first of them is the direct tensor estimation method followed by the least square formulation for tensor estimation. In the least square formulation, different constraints for positive definiteness of the tensors are discussed followed by some approaches for joint tensor estimation and regularization.

A direct tensor estimation method was suggested by [Westin 2002]. The method requires one baseline image (S_0) and six diffusion weighted images ($S_i, i = 1, ..., 6$). The Stejskal-Tanner equations are linear in the log domain. It relies on the decomposition of the diffusion tensor D in an orthonormal tensor basis ${g_i g_i}^T$. The tensor can be solved by solving the linear sum:

$$\mathrm{D} = \sum_{i=1}^{6} \log_e \frac{S_0}{S_i} {g_i g_i}^T. \tag{4.4}$$

The method produces a very noisy tensor field because only seven diffusion images ($S_0, ..., S_6$) are used. This particular tensor estimation method is not robust to noise.

Tensor estimation using least squares are used more often than the direct estimation methods because these methods use information from all the diffusion images and so the tensor estimation is robust with respect to noise (for example [Basser 1994, Poupon 1999]). The least squares tensor estimation is summarized using the following equation:

$$\min_{\mathrm{D}} \sum_{i=1}^{n} \left[\frac{1}{b} \ln \frac{S_0}{S_i} - {g_i}^T \mathrm{D} g_i \right]^2. \tag{4.5}$$

The methods mentioned above does not take into account the positive definite constraint on the diffusion tensor matrix. Several methods have been suggested in order to account for the positivity constraint on the diffusion tensor [Tschumperlé 2003, Wang 2004]. The authors in [Tschumperlé 2003] suggest a positive constrained minimization of the least-square criterion coupled with an anisotropic regularization term. The tensor estimation is posed as a variational formulation problem:

$$\min_{\mathrm{D}\in P(3)} \int_{\Omega} \sum_{i=1}^{n} \left[\frac{1}{b} \ln \frac{S_0}{S_i} - {g_i}^T \mathrm{D} g_i \right]^2 + \alpha\, \phi(||D||)\, d\Omega, \tag{4.6}$$

where $P(3)$ is the space of second order symmetric positive definite tensors, α is the weighting factor for the regularization term and $\phi(.)$ is a regularizing ϕ-functional. The positive-definite constrain used in the tensor estimation is discussed in [Chefd'hotel 2002]

The noise in the diffusion tensor images are known to be Rician-distributed [Gudbjartsson 1995]. An appropriate denoising scheme is needed for estimating the true signal from the DTI data. A non-local means (NLM) filter was proposed for denoising the diffusion tensor images [Wiest-Daesslé 2007, Wiest-Daesslé 2008]. The authors presented a modified NLM adopted for denoising Rician-corrupted DTI data with high b-values (3000 s/mm^2). The biases due to noise are more pronounced in the routine clinical DTIs as the images have to be acquired rapidly, often at the expense of image quality. The clinical DTIs are usually acquired at a comparatively lower b-value (700-1000 s/mm^2). Another method was proposed by [Fillard 2007] on joint estimation and denoising of clinical diffusion tensor images. The method uses a variational approach for diffusion tensor estimation. The authors propose a maximum likelihood strategy to exploit the assumption of Rician-distributed noise. The method presented in the chapter is based on this maximum likelihood strategy and variational approach.

The Log-Euclidean metric was described in [Arsigny 2006a]. The method exploits the bijective relationship that exists between the symmetric positive definite matrix and its logarithm. The method boils down to taking the matrix logarithm of the diffusion tensors, running all the computations and then transforming the logarithm of the tensors through an exponential map. The method applies a natural constraint on the positive definiteness of the diffusion tensors as the logarithm of a negative entity is not defined.

Maximum-likelihood estimation versus Least-squares estimation

Most of the early tensor estimation methods discussed above use a least-square approach for tensor estimation. The method presented in this chapter builds on the maximum-likelihood estimation (MLE) based tensor estimation algorithm

presented in [Fillard 2007]. The least-squares estimation (LSE) has no or minimal assumptions on the distribution of the data. MLE has many optimal properties, such as, sufficiency (complete information about the parameter of interest), consistency (estimation measures true underlying value with increasing number of observations), efficiency (lowest possible variance of parameter estimates) and parameterization invariance (estimate is independent of the choice of parameterization used) [Myung 2003]. On the contrary, no such property can be attributed to the LSE approach. The LSE is a mostly used for linear regression and probably a not an adequate method for parameter estimation. It is because of such nice properties, MLE is an attractive approach for tensor estimation.

We would like to estimate the higher resolution tensors $\mathrm{D}(\mathrm{y_j})$ from the observed signals $S_i^{LR}(x_k)$. As can be seen in equation 4.2, any infinite number of combinations of diffusion tensors will result in the same observed signal. Thus, the tensor estimation problem is *ill-posed*. In such a scenario, it is desirable to restrict the solution space to the most meaningful ones by adding a priori information about the system. For the tensor estimation problem we have used a non-stationary spatial prior to restrict our solution space.

With the above image degradation model, we solve the inverse problem of estimating tensors in the HR space. This is an inverse problem because in equation 4.2, for a given signal $S_i(x_k)$ infinitely many combinations of $D(y_j)$ is possible. In the Log-Euclidean framework, the diffusion tensor D is parameterized using $\mathrm{D} = \exp(\mathrm{L})$. Following [Fillard 2007], the tensor estimation can be looked as a variational formulation, i.e., one should minimize the following energy functional,

$$\mathrm{E}(\mathrm{S_0}, \mathrm{L}) = \frac{1}{2}\mathrm{Sim}(\mathrm{S_0}, \mathrm{L}) + \frac{\lambda_\mathrm{s}}{2}\mathrm{Reg}(\mathrm{S_0}) + \frac{\lambda_\mathrm{L}}{2}\mathrm{Reg}(\mathrm{L}), \tag{4.7}$$

where Sim(.) is the data fidelity term and $\mathrm{Reg}(\mathrm{S_0})$, Reg(L) are the regularization priors on the image with λ_s and λ_L as their respective weights. In [Fillard 2007], the tensor estimation is done in the same resolution as that of acquisition. However, in this paper, we aim to estimate tensors at a resolution higher than the acquisition resolution. The LR acquired signal and the HR estimated tensors are linked through the degradation model described in equation 4.2. Thus, this is also a problem of finding the most optimally distributed tensor field, which is anatomically coherent and also accounts for the observed signal.

4.2.3 Likelihood Criteria for Tensor Estimation

The observed signal in the DWI can be modeled as $\tilde{S}_i = S_i + \eta$, where $\tilde{S}_i$ is the observed DWI, S_i is the true image (as in eq. 4.2) and η is the associated noise model. As described in [Fillard 2007], the data attachment term E(.) corresponds to a maximum likelihood estimator (MLE) adapted to the noise model. The MLE

for the probability density function of a given noise model is

$$\mathrm{Sim}_{ML}(.) = -\sum_{i=0}^{N}\sum_{x_k}\log\Big[p(\tilde{S}_i(x_k)|S_i(x_k))\Big], \tag{4.8}$$

where $S_i(x_k)$ is same as in equation 4.2 and $p(.)$ is the probability density function of the the noise model. Unlike [Fillard 2007], here $E(.)$ is a function of two variables; the HR image with null gradient, $S_0(y_j)$ and the HR tensor field, $L(y_j)$. Both are related to the Sim_{ML} through equation 4.2. The maximization is achieved using the steepest descent algorithm. The gradient of $\mathrm{Sim}_{ML}(S_0(y_j), L(y_j))$ is obtained by differentiating equation 4.8:

$$\nabla\mathrm{Sim}_{ML} = \Big[\frac{\partial\mathrm{Sim}_{ML}}{\partial S_0(y_j)} \qquad \frac{\partial\mathrm{Sim}_{ML}}{\partial L(y_j)}\Big]^T. \tag{4.9}$$

Taking partial derivatives of equation 4.8 with respect to $S_0(y_j)$ and $L(y_j)$, we obtain:

$$\frac{\partial\mathrm{Sim}_{ML}}{\partial S_0(y_j)} = -\sum_{i=0}^{N}\sum_{x_k}\Big[\frac{p'(\tilde{S}_i(x_k)|S_i(x_k))}{p(\tilde{S}_i(x_k)|S_i(x_k))}\Big]\frac{\partial\tilde{S}_i(x_k)}{\partial S_0(y_j)}, \tag{4.10}$$

$$\frac{\partial\mathrm{Sim}_{ML}}{\partial L(y_j)} = -\sum_{i=0}^{N}\sum_{x_k}\Big[\frac{p'(\tilde{S}_i(x_k)|S_i(x_k))}{p(\tilde{S}_i(x_k)|S_i(x_k))}\Big]\frac{\partial\tilde{S}_i(x_k)}{\partial L(y_j)}, \tag{4.11}$$

where $p'(.)$ is the derivative of $p(.)$ with respect to $\tilde{S}_i(x_k)$. From here on, we will denote $r(.) = p'(.)/p(.)$ for the ease of computation. Differentiating equation 4.2, we get

$$\frac{\partial\tilde{S}_i(x_k)}{\partial S_0(y_j)} = \quad \alpha_{kj}\exp[-bg_i^T\exp(L(y_j))g_i], \tag{4.12}$$

$$\frac{\partial\tilde{S}_i(x_k)}{\partial L(y_j)} = -b\,\alpha_{kj}\,S_0(y_j)\exp[-bg_i^T\exp(L(y_j))g_i]\;\partial_{G_i}\exp(L(y_j)), \tag{4.13}$$

where $\partial_{G_i}\exp(L(y_j)) = \partial[g_i^T\exp(L(y_j))g_i]/\partial L(y_j)$ is the directional derivative of the matrix exponential and $G_i = g_ig_i^T$. A detailed implementation for computing $\partial_{G_i}\exp(L(y_j))$ is available in [Fillard 2007]. In the following sections, we will discuss the MLE on the Gaussian noise model followed by brief implementation details.

4.2.3.1 MLE on the Gaussian Noise

The likelihood on the Gaussian noise with zero mean and variance σ^2 on the LR image $p(\tilde{S}_i|S_i)$ is given by,

$$p(\tilde{S}_i|S_i) = \frac{1}{\sigma\sqrt{2\pi}}\exp\Big(-\frac{(\tilde{S}_i - S_i)^2}{2\sigma^2}\Big). \tag{4.14}$$

Differentiating equation 4.14 with respect to S_i, we have

$$p'(\tilde{S}_i|S_i) = \frac{1}{\sigma\sqrt{2\pi}}\exp\Big(-\frac{(\tilde{S}_i - S_i)^2}{2\sigma^2}\Big)\Big[\frac{\tilde{S}_i - S_i}{\sigma^2}\Big]. \tag{4.15}$$

Thus, we have

$$r(\tilde{S}_i|S_i) = \frac{\tilde{S}_i - S_i}{\sigma^2}. \tag{4.16}$$

4.2.3.2 MLE on the Rician Noise

In the clinical environment, typically the images have a low SNR and the real nature of noise is Rician [Wang 2004], which is equivalent to adding Gaussian noise in the k-space. The likelihood in case of Rician noise $p(\tilde{S}_i|S_i)$ described in [Sijbers 1998] is given by

$$p(\tilde{S}_i|S_i) = \frac{\tilde{S}_i}{\sigma^2}\exp\Big(-\frac{\tilde{S}_i{}^2 + S_i^2}{2\sigma^2}\Big)I_0\Big(\frac{S_i\tilde{S}_i}{\sigma^2}\Big), \tag{4.17}$$

where I_0 is the modified zero-th order Bessel function of the first kind. Differentiating equation 4.17 with respect to S_i, we get

$$p'(\tilde{S}_i|S_i) = \frac{\tilde{S}_i}{\sigma^2}\exp\Big(-\frac{\tilde{S}_i{}^2 + S_i^2}{2\sigma^2}\Big)I_0\Big(\frac{S_i\tilde{S}_i}{\sigma^2}\Big)\Big[\beta\frac{\tilde{S}_i}{\sigma^2} - \frac{S_i}{\sigma^2}\Big], \tag{4.18}$$

where $\beta = I_0'/I_0$. Implementation details for β can be found in [Fillard 2007]. Similarly, we have

$$r(\tilde{S}_i|S_i) = \frac{\beta\tilde{S}_i - S_i}{\sigma^2}. \tag{4.19}$$

4.2.4 Non-Stationary Spatial Prior

Anisotropic regularization promotes smooth images in homogeneous areas while respecting the edges. In this paper, the anisotropic behavior is achieved using a ϕ-functional, i.e., $\mathrm{Reg}(s) = \int_\Omega \phi(||\nabla s||)$, where s is the intensity (scalar or tensor) of the voxel of image Ω. In our implementation, we use $\phi(s) = 2(1 + s^2/\kappa^2) - 2$, with κ as the image normalization factor [Fillard 2007]. The gradient of $\mathrm{Reg}(s)$ is

$$\nabla\mathrm{Reg}(s) = -2\psi(||\nabla s||)\triangle s - 2\nabla^T(\psi(||\nabla s||))\nabla s, \tag{4.20}$$

where $\psi(s) = \phi'(s)/s$. The anisotropic regularization is a spatial Markov random field (MRF), when ∇s is discritized for instance using finite difference. The anisotropic smoothening of posterior probabilities is equivalent to the Maximum A Posteriori (MAP) solution of a discrete MRF, making the full criterion in equation 4.7 a MAP estimator.

Overall, the proposed HR tensor estimation method is similar to the one proposed in [Fillard 2007], in terms of the variational formulation. However, the total energy E(.) is constrained through the signal degradation model in equation 4.2. The novelty of the method lies with the fact that it estimates the tensors in HR while taking into account the unavoidable partial volume effects during acquisition, to produce an anatomically coherent tensor field.

4.3 Maximum Likelihood Estimation (MLE)

In this chapter, the tensor estimation problem is presented as a variational formulation. The optimal tensors are obtained by minimizing the variational energy, $\mathrm{E}(\mathrm{S}_0, \mathrm{L})$ in equation 4.7. The equation consists of three terms: the data-fidelity term, the regularization term on the undiffused B_0 image and the regularization term on the matrix logarithm of diffusion tensors. Each of the terms are weighted by their respective weights and the weights represent our trust in the observed data versus the amount of regularization we want to put into our estimation. We already discussed the maximum likelihood estimator on the Gaussian and Rician noise models as well as the regularization terms in the previous sections. In this section, we are going to discuss the maximum likelihood estimator, the optimization method and the numerical issues therein.

The principle of maximum likelihood estimation states that the desired probability distribution is the one that makes the observed data "most likely". This means that one must find the values of the parameters (diffusion tensor) that maximizes the likelihood of the probability function. The resulting parameter values are the MLE estimate. In our problem, depending on the choice of noise model (Gaussian or Rician), we will have different MLE estimates. However, one must understand that the MLE estimates need not exist or unique. For computational reasons, the the MLE estimate is obtained by maximizing the log-likelihood of the function which is equivalent to minimizing the negative of the log-likelihood of the function. The data-fidelity term (Sim_{ML}) in equation 4.8 is also defined as negative of the log-likelihood of the probability function. In case of highly non-linear problem as that of tensor estimation, it is not always possible to have an analytic solution to the minimization problem. Thus, we resort to iterative non-linear optimization schemes for finding the optimal parameters that maximizes the log-likelihood of the probability distribution.

4.3.1 Steepest descent

The total energy $\mathrm{E}(\mathrm{S}_0, \mathrm{L})$ is minimized using the steepest descent algorithm with line search.

$$S_0{}^{t+1} = S_0{}^{t} - \frac{dt_s}{2}\Big[\frac{\partial \mathrm{Sim}}{\partial S_0} + \lambda_s \nabla \mathrm{Reg}(\mathrm{S}_0)\Big] \tag{4.21}$$

$$L^{t+1} = L^{t} - \frac{dt_L}{2}\Big[\frac{\partial \mathrm{Sim}}{\partial L} + \lambda_L \nabla \mathrm{Reg}(\mathrm{L})\Big], \tag{4.22}$$

where dt_s and dt_L are the step sizes for steepest descent. The two images S_0 and L are optimized alternately, until convergence. The step-sizes are reduced by half if the the total variational energy is not decreased, until the step-size are too small ($dt_s > 1e{-}6,\ dt_L > 1e{-}10$), that is the total energy E cannot be minimized any further. It is important to note that the optimization function does not necessarily guarantee unique global maxima. The estimation is also dependent on the choice of initial

parameters for the iterative optimization scheme to follow. Depending on the choice of initial tensor estimate, the steepest-descent algorithm could either prematurely stop and return a sub-optimal set of tensors. We found that a linearly resampled tensor field with log-Euclidean interpolation is a reasonable initial estimate for the optimization scheme.

4.3.2 Numerical Issues

The steepest descent algorithm mentioned above has two drawbacks. The first problem is the huge disparity in scales between the gradient of the similarity criteria ($\frac{\partial Sim}{\partial L}$) and the gradient of the regularization term ($\nabla Reg(L)$) which makes it difficult to choose the weighting factor (λ_L) for regularization.

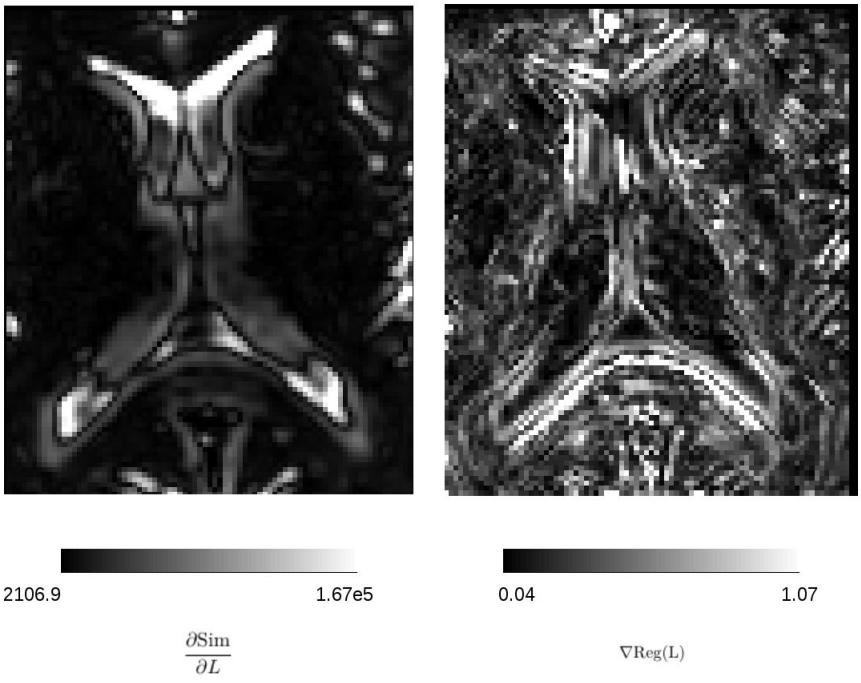

Figure 4.2: Extracted section of the brain near the ventricles. The image on the left shows the gradient of the similarity criteria and the one on the right shows the gradient of the regularization term. The disparity in scales of the two terms is highlighted using the color bar.

The figure 4.2 shows the scaling issue between the two terms under consideration. From the gray scale bar one can easily deduce that the term on the left is higher by a factor of 100000. It should also be observed that the values are particularly higher in the cerebro-spinal fluid (CSF) regions.

The other problem is that the gradient of the similarity criteria is scaled with respect

to the B0 image. Using the equations 4.13 and 4.11, the differential of the similarity criteria can be written as,

$$\frac{\partial Sim(.)}{\partial L(y_j)} = -\sum_{i=0}^{N}\sum_{x_k} r(.)\, b\, \alpha_{kj}\, \boldsymbol{S_0(y_j)} exp[-b g_i^T exp(L(y_j)) g_i] \partial_{G_i}[exp(L(y_j))] \tag{4.23}$$

The above term is scaled with respect to the undiffused B0 image (S_0). In a B0 image, the intensity of the CSF is much higher compared to the surrounding tissue which accordingly scales the derivative and creates artifacts in the tensor estimation. In the figure 4.3 the artifacts created during the tensor estimation in the CSF regions are shown.

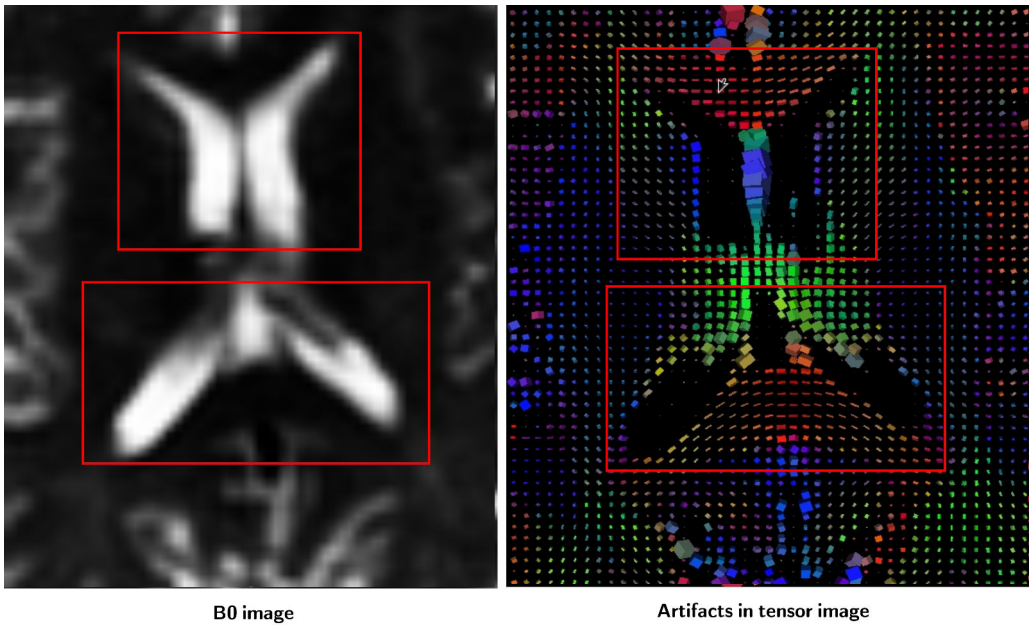

Figure 4.3: The scaling in the derivative term due to the B0 image creates artifacts in the tensor estimation. The artifacts are the voids in the CSF region in the tensor field shown in the image on the right. The voids actually contains tensors which are really small compared to the ones in the surrounding tissue and thus appear as empty spaces. The intensity in the CSF regions in the B0 image is much higher compared to the surrounding tissue which scales the differential of the data-fidelity term causing the artifact. The red boxes enclose the ventricles where the artifacts are most pronounced.

4.3.3 Preconditioning with an approximate Hessian

The scaling issues discussed in the previous section can be solved using a preconditioner. The derivative of the similarity criteria needs to be preconditioned for an accelerated convergence. However it is better if the preconditioning term has a

mathematical significance in the equation. Taking inspiration from the Newton's method in optimization, the inverse of the approximate Hessian matrix is chosen as a preconditioning term. The derivation for the approximate Hessian matrix and related explanations are available in appendix A. The Hessian term is

$$H(y(j)) \approx b^2 S_0(y(j))^2 \sum_{x_k} \alpha_{kj}^2 \tag{4.24}$$

Using the Hessian matrix, the modified differential of the similarity criteria becomes,

$$\frac{\partial Sim_{ML}}{\partial L} = -\left(\frac{1}{b\, S_0(y_j) \sum\limits_k \alpha_{kj}^2}\right) \sum_k \alpha_{kj}\, r(.) \exp[-b g_i^T \exp(L(y_j)) g_i]\, \partial_{G_i} \exp(L(y_j)) \tag{4.25}$$

With the addition of the term, the scaling issue is resolved and the convergence is quicker.

4.4 Comparison between Tensor Resampling and HR Tensor Reconstruction

4.4.1 Simulated LR acquisition

Data were acquired using a GE 1.5T scanner, with 24 encoding gradient directions (with a b-value of 700 s/mm^2). The image has $256 \times 256 \times 26$ voxels of size $0.9375 \times 0.9375 \times 5.5$ mm^3. The images are downsampled by a factor of 2 in the axial plane and the tensor field is estimated. This LR tensor field is then resampled to the original image size using Log-Euclidean interpolation [Arsigny 2006a]. The HR tensor estimation is also used to estimate tensors at the original resolution from the downsampled images. In figure 4.4, the fractional anisotropy maps from both tensor resampling and HR estimation methods are shown. The FA map computed from the HR tensor estimation, is better contrasted and less blurry when compared with the one computed from resampling the LR tensor image to the original resolution.

4.4.2 Increase in FA on real data

In this section, we use a real dataset from Siemens 1.5T scanner, with 21 encoding gradient directions and a b-value of 1000 s/mm^2. The image has $80 \times 80 \times 40$ voxels of size $3 \times 3 \times 3.3$ mm^3. Several WM tracts, which were not visible before can now easily be seen in the FA map, when it is computed with HR tensor estimation method.

In figure 4.5, the FA maps are overlaid on the corresponding B0 image for better anatomical reference. In both the axial and coronal views, the external capsule and the corpus callosum can be clearly demarcated with the HR tensor estimation method. We observed an increase in FA values by 42.73% in the WM regions (circled regions in figure 4.5) with the proposed method.

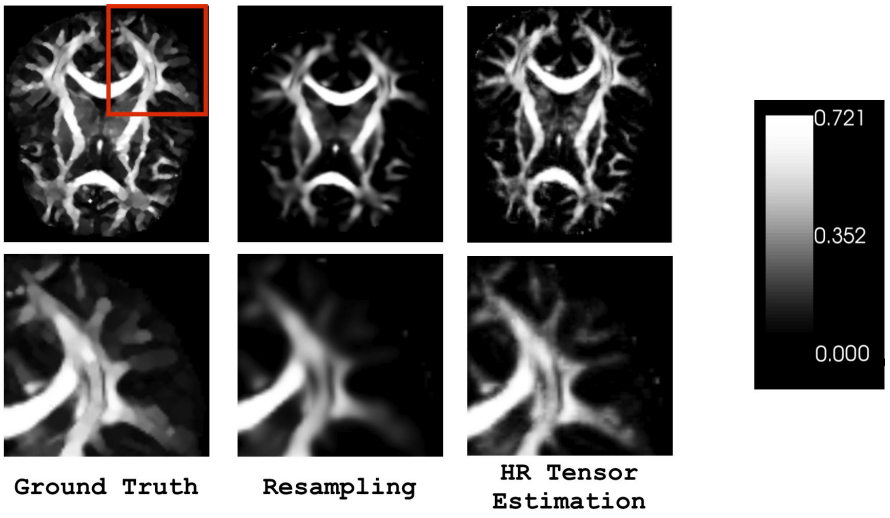

Figure 4.4: Simulated LR acquisition: Top row shows axial views of the ground truth, FA computed from resampled tensor field and HR tensor estimation. The FA map computed from HR tensor estimation method is better contrasted than the one computed from resampled tensor field. The bottom row shows the zoomed region (red square).

4.4.3 Error map for the simulated images

With the proposed high resolution tensor estimation method, the error on the FA images is lower than the FA images computed after tensor resampling. The figure 4.6 shows axial view of the squared error between the FA maps computed from tensor resampling and the proposed method. The graph shows the variation of the squared error along a horizontal row of voxels for a quantitative assessment.

4.4.4 Influence on Tractography: Quantitative Evaluation

The same data set as in section 4.4.1 is used for fiber tracking experiment. However, in this case the HR tensor estimation is done at 1 mm isotropic resolution and the tensor field is resampled to the same resolution. The proposed method shows statistically significant increase in the fiber lengths, when compared with tensor resampling. A one tailed t-test on fiber lengths gives a p-value less than $2e-16$. The fiber-tracking is done using MedINRIA 1.90 DTI-Track tool. All the voxels with FA > 0.25, are considered as seed voxels for fiber tracking. The increase in FA values in WM regions (section 4.4.2), leads to an 82.36% increase in the number of seed voxels for HR tensor estimation and thus denser fibers. The fornix of the brain is tracked and the results are compared in figure 4.7 for tensor resampling (top-left) and HR tensor estimation (top-right). There is a 25% increase in the mean length of fibers with proposed tensor estimation method compared to tensor resampling. The bottom row in figure 4.7 shows the histogram for fiber length distribution for

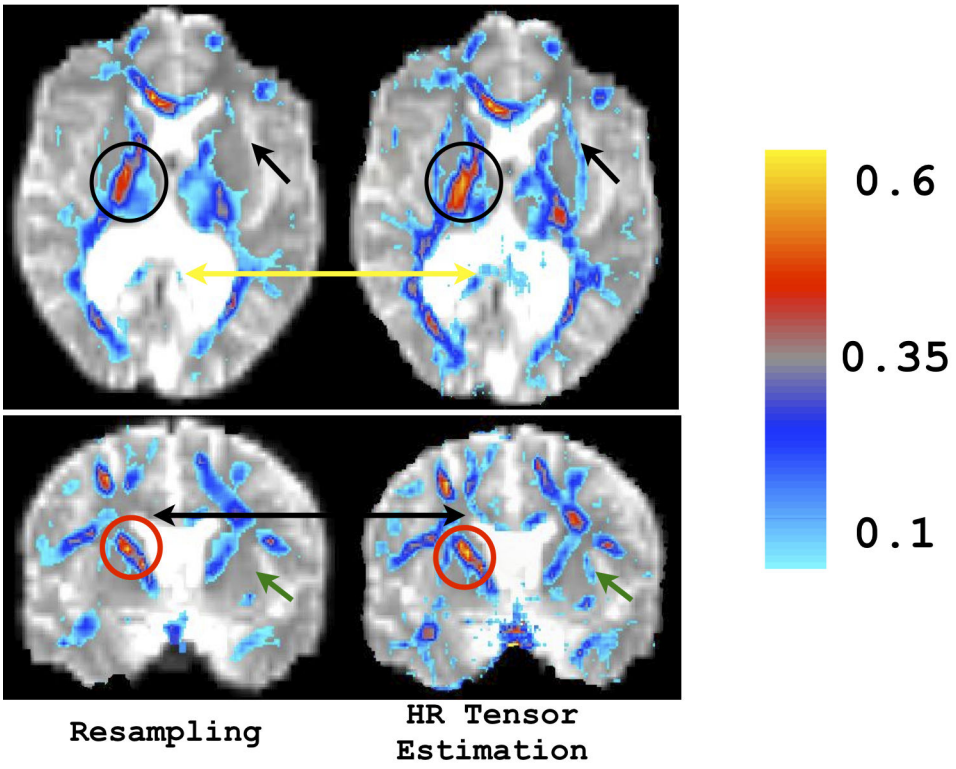

Figure 4.5: Influence on FA in real clinical data: The axial and coronal views show that the external capsule and part of corpus callosum can be demarcated using the HR tensor estimation. The corresponding circles show regions with considerable increase in FA.

the respective methods.

4.5 Conclusions

In this chapter, we tackled the problem of resampling low resolution DTI data on higher resolution for tractography or statistical analysis purposes at the population level. We propose to replace the resampling step by a DTI reconstruction at the high resolution using a MAP estimator including a spatial prior. The method is compared with tensor resampling method on simulated low resolution data as well as real clinical data. Results showed better contrasted and less blurry FA maps on the simulated data. It was also shown that the error in the FA computed using the proposed method is less than the one computed using tensor resampling. On the real data, considerable increase in FA is registered, making certain WM tracts like parts of corpus callosum and external capsule recognizable. These white matter regions were not visible in the FA maps computed using tensor resampling. Fiber tracking with the HR tensor estimation shows statistically significant increase in the

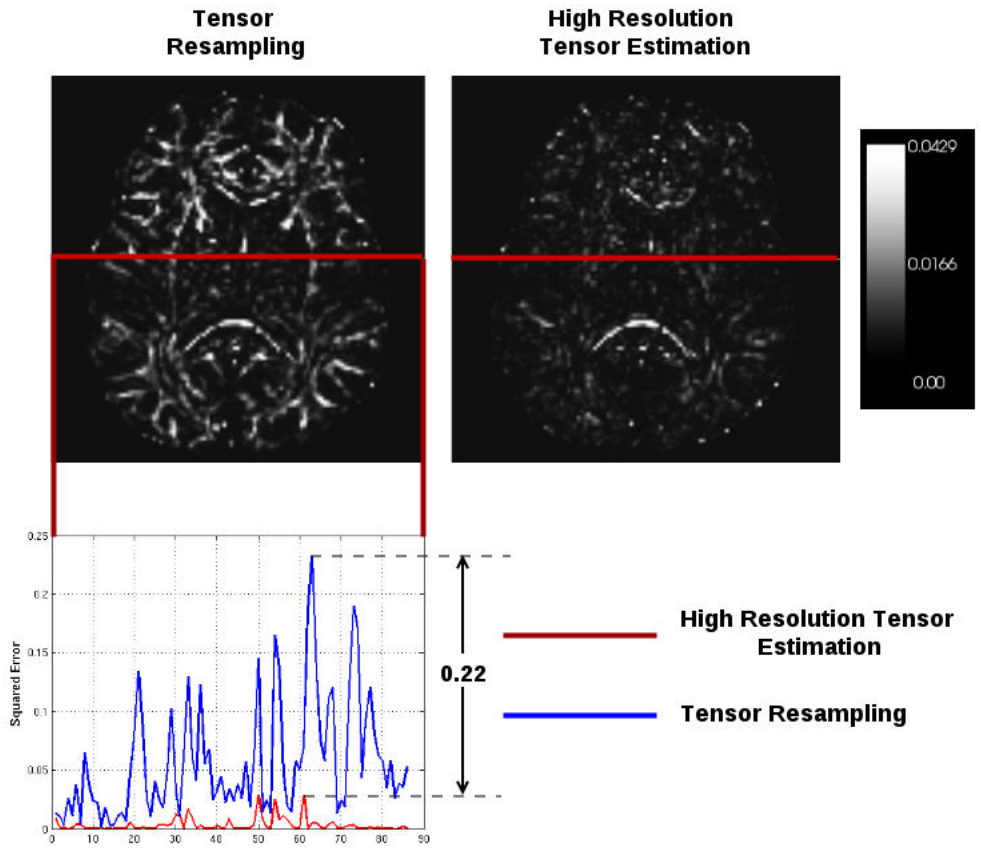

Figure 4.6: **Top Left:** Squared error between the FA maps computed from tensor resampling and the ground truth. **Top right:** Squared error between the FA maps computed from the proposed method and the ground truth. The graph in the bottom row shows the variation of the squared error along the voxels on the red line.

length and number of fibers. Tractography results were shown for the fornix region of the brain. The partial volume effect is very pronounced in this region of the brain and so the increase in the number of tracts through the fornix is a promising result that the proposed method works well in the presence of partial volume effects.

In terms of future work, there is still room for substantial improvements and testing in the tensor estimation algorithm. One of the ideas is to incorporate the anatomical information from the T1-weighted image and possibly the white and gray matter segmentation maps for estimation. The T1-weighted image has a higher spatial resolution than that of the diffusion images. With a little generality, it is possible to estimate tensors in any geometrical space we want, e.g., the subject T1 space or any template space. For example, the B0 and T1 images for the same subject is

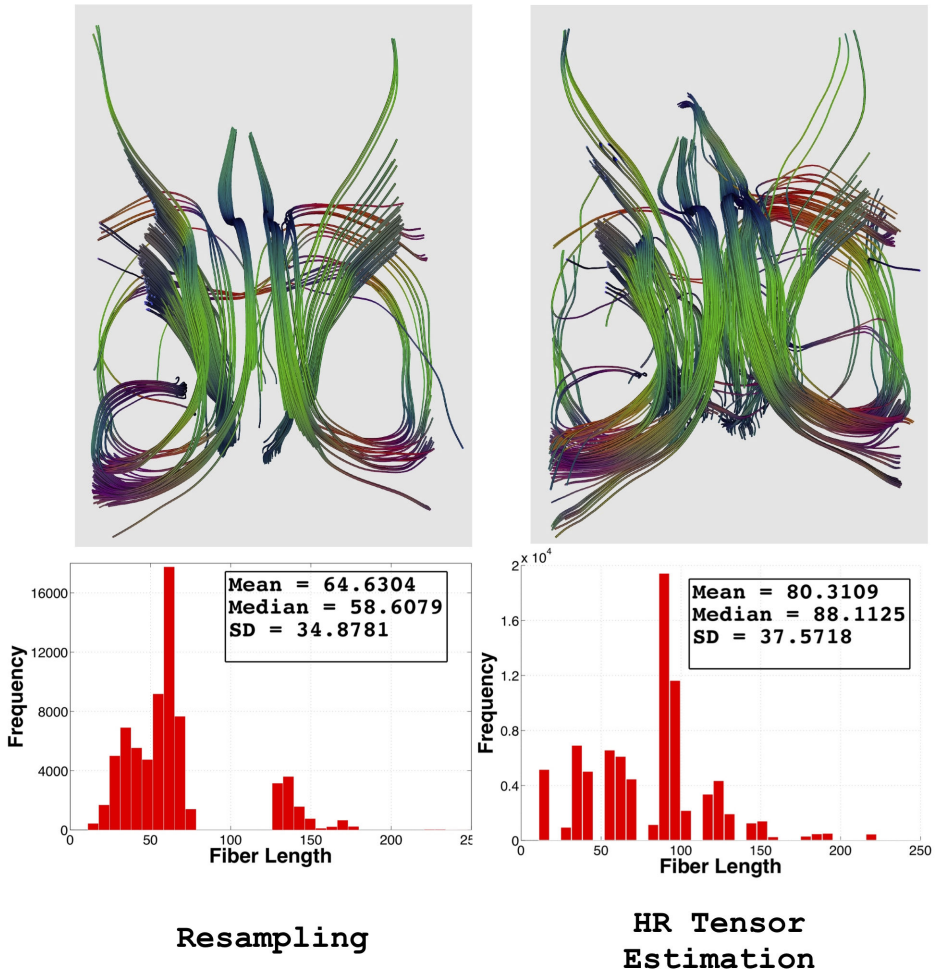

Figure 4.7: The top row shows comparatively denser fiber bundle in fornix of the brain for HR tensor estimation method (superior-inferior view) and a quantitative comparison of fiber lengths is shown in bottom row.

separated by a rigid transform. Using this transform and the geometry of the space, it is possible to generate a correspondence map of the two images and compute the spatial weights of the high resolution voxels that constitute the low resolution voxel. The present state of algorithm uses anisotropic regularization as a spatial prior in the variational formulation. The formulation uses a $\phi-$ functional which promotes smooth images in the homogeneous areas, while respecting the edges (section 4.2.4). However, such a formulation does not make any use of the T1 weighted images. The $\phi-$ functional could be modified in order to make use of the high resolution anisotropic information in the T1-weighted images as,

$$Reg(\nabla L + \gamma \nabla I_{T1}) = \int_{\Omega} \phi(||\nabla L + \gamma \nabla I_{T1}||) \tag{4.26}$$

where γ is the weighting factor for the anatomical T1 image, L is the matrix

logarithm of the tensor image and I_{T1} is the T1 image. The gradient of the modified regularization can be computed similarly as in section 4.2.4.

A comparison between the proposed approach and multi-compartment model in terms of fiber tractography needs to be investigated. It remains to be investigated if multi-compartment models can be used for super-resolution algorithms like the one mentioned in this chapter. A formal validation of the proposed model using multi-resolution data needs to be done.

We were not able to use the algorithm for statistical studies presented in the following chapters because the DTI data in the NEURADAPT study has a spatial resolution of $0.9375 \times 0.9375 \times 5.5$ mm^3. The voxels were too big in the z-direction and there is not enough information to increase the resolution in a meaningful manner. It will be interesting to see how multi-compartment models combine with super-resolution will affect the statistical results in the future.

Chapter 5

A multimodal atlas for statistical study on clinical brain images

Contents

5.1 Introduction

The human brain is one of the most complex organs in the body. To add to the complexity, the diversity of the brain in terms of shape, size and structural organization is uncanny. In order to understand and quantify the differences in the the brain across a population as well as to differentiate the changes between healthy and diseased population, the need of a brain atlas is inevitable. With more and more medical image data being available, it is logical for statisticians and neuroimaging experts to design a framework for comparing structural and functional changes across a population, for voxel based analyses of time-dependent changes as in the case of progressive neurodegenerative diseases such as Alzheimer's disease.

In order to detect such changes, spatial normalization is of utmost importance. Spatial normalization is the process of transforming all the images in a given population to a common image space, called the template. In medical image analysis, problems like registration, label propagation, segmentation can be looked as sub problems of the broader subject of spatial normalization. Even for voxel based morphometry, deformation based morphometry, or tract based spatial statistics spatial normalization is an indispensable tool. One of the challenges with different imaging modalities is to design the optimal workflow for spatial normalization.

Spatial normalization requires the user to define a common template space to which all the images will be normalized (registered) using affine or nonlinear registrations or both. Some of the celebrated atlases are the sterotaxic atlas by Talairach [Talairach 1988], the ICBM atlas [Mazziotta 2001], and the MNI152 [Grabner 2006] atlas families.

5.1.1 History of brain atlases

One of the earliest attempt to understand the human brain was by Franz Joseph Gall using a technique called *phrenology* in 1796. Gall believed that the personality traits, mental and intellectual prowess of a human were reflected on the external shape of the skull. He hypothesized that the changes in different areas of the skull, the bumps and differences in geometry are caused by the pressure exerted by the brain underneath. He believed that the brain was divided into twenty-seven different areas. The process involved feeling the brain with hands and often measuring the size of the brain with callipers. These measurements were used to assess the character and personality traits of the subject. Gall conducted his experiments on 120 subjects in his life time. Though not really accepted and often considered controversial during his time, the method laid the ground work for future brain studies. The idea of phrenology influenced the subsequent work done by the French anatomist Pierre Paul Broca who is well known today for *Broca's area*.

Following Gall's work, the German anatomist Korbinian Broadmann introduced Broadmann areas [Brodmann 1909] which are defined based on maps of cortical areas of humans and other primates. Almost 100 years later, Broadmann areas still remain the primary reference for the cytoarchitectural organization of the human cortex. He used cell staining to identify the organization of the human cortex. According to Broadmann, the brain is divided into 52 areas. In 1908, with the efforts of Victor Horsley and Robert H. Clarke, the Horsley-Clarke apparatus was designed for stereotactic neurosurgery. This invention was one of the most important steps towards the construction of brain atlases in the sense that it formally defined a stereotactic frame. The stereotactic frame uses Cartesian coordinate system to locate the different brain structures. They used the method

for surgery only on animals in the beginning. It was not until 1947 that Ernest A. Spiegel, Henry T. Wycis and Lars Leksell designed the stereotactic apparatus for human brain.

Perhaps the most recognized coordinate space in neurosurgery was developed by Jean Talairach and Gabor Szikla in 1967. It is known as the Talairach coordinate system. The atlas is defined using the line joining the anterior commisure (AC) and the posterior commisure (PC) also known as the AC-PC line. The AC-PC line lies on the mid-sagittal plane. In this coordinate system the AC acts as the origin, the x-axis is defined along the left-right direction, y-axis is defined along the anterior-posterior and the z-axis is along the superior-inferior direction. The coordinate system is used to develop the Talairach brain atlas. The atlas was updated in 1988 and is one of the highly referenced atlas in the literature. As we will see further that this atlas and coordinate system is the basis for developing some of the modern atlases in use today. During the same time (1959) as Jean Talairach developed the Talairach coordinate system, Georg Schaltenbrand and Percival Bailey introduced Schaltenbrand atlas. The atlas was subsequently updated in 1977 and is now one of the most used atlas for brain surgery. There is a subtle difference between the two atlases as in how the AC-PC line is defined.

The atlases discussed so far were based on a single subject. However, with the advent of MRI and a plethora of medical images, it is possible to create population specific atlases. A population specific atlas will better capture the high variability of the human brain across the population under study. The MRI technique was introduced for brain imaging in 1977 by Peter Mansfield and Paul Lauterbur. In 1994, Montreal Neuroimaging Institute (MNI), created the MNI305 atlas from a population of 305 subjects. The AC-PC line were manually delineated in all the subjects and the images were aligned according to the AC-PC line. The aligned images were then averaged to form the initial MNI space. The International Consortium for Brain Mapping (ICBM) was formed in 1993 with a goal to develop probabilistic reference system for human brain. 152 subjects were scanned and linearly registered to the MNI305 atlas. For the first time in 2001, we had brain atlases in three different modalities T1, T2 and proton density weighted images. Thus, the first ICBM152 atlas was created. With respect to the MNI305 atlas, the ICBM152 had improved contrast and resolution, but it lacked spatial details in the cortical regions. Affine registration was used for creating the ICBM152 atlas takes into account the translation, rotation and the scaling. This atlas was known as the linear ICBM average brain atlas. The atlas fails to capture the subtle local changes in the brain. So, the atlas was recreated using nonlinear registration in 2009. This atlas is known as the nonlinear version of the ICBM atlas. It captures the fine cortical detail and subtle changes that were missing in the 2001 version.

So far we have discussed the historical context in the development of brain atlases. The two important atlases for the thesis namely, the Talairach brain and MNI

template will be discussed in the following sections.

5.1.2 The Talairach Brain

The Talairach and Tournoux atlas of 1988 was one of the first brain atlases to be introduced in the community. The Talairach brain was a postmortem specimen from a 60 year old female. A single hemisphere of the brain was sliced sagitally and photographs of the slices were taken and arranged to create drawings of the axial and coronal sections. We have come a long way since the creation of the first brain atlas. However, the Talairach atlas brought us the novelty in the realm of atlas constructions. To summarise, the major contributions of the atlas were [Brett 2001],

- a coordinate system for the brain, commonly referred to as the Talairach coordinate system. According to the system, the anterior commissure (AC) is the origin of the three axes X, Y and Z. The line joining the anterior commissure and the posterior commissure (PC) is horizontal.
- the Talairach transform to match the brains of different shapes and sizes.
- the Talairach brain oriented according to the proposed coordinate system.

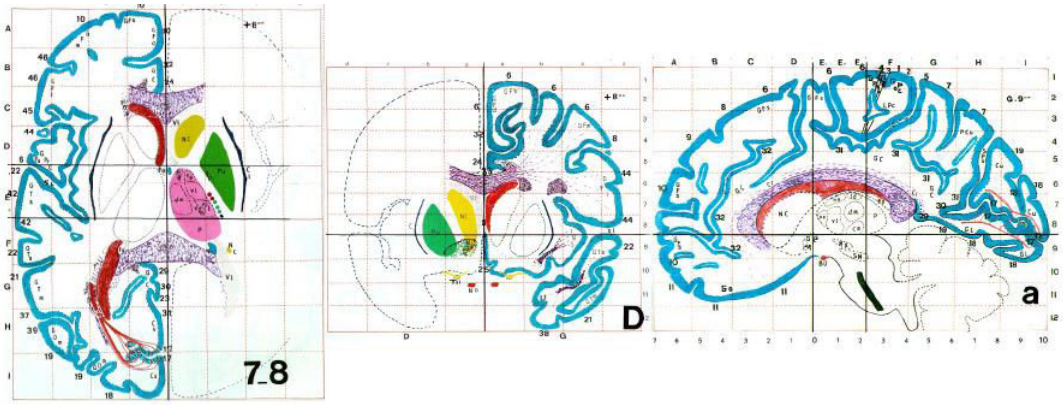

Figure 5.1: The Talairach coordinate system. Source: The AFNI handouts

In the Talairach coordinate system the X-axes is directed from left-to-right, the Y-axes is directed from the posterior-to-anterior and the Z axes is directed along the inferior-to-superior directions.

5.1.3 The ICBM templates

The initiative of the International Consortium of Brain Mapping (ICBM) has provided the community with a number of brain atlases particularly, ICBM 452 T1

atlas, along with number of probabilistic atlases like ICBM tissue atlas, ICBM lobular, sulcal and deep nuclei atlases. The one which is of particular interest in relation to the present work is the ICBM white matter parcellation map (WMPM) [Mori 2008] and the ICBM DTI-81 atlas. The ICBM DTI-81 is a DTI atlas is an atlas of 81 normal subjects acquired under the ICBM initiative. The DTI data was acquired using a Siemens 1.5 T scanner using a single shot, echo-planar imaging sequence with a b-value of 1000 s/mm^2. The images were acquired with 30 gradient encoding directions and had a transverse slice thickness of 2.5 mm.

White matter parcellation map

The white matter parcellation map was provided by Mori et. al. in 2008 [Mori 2008]. The ICBM DTI-81 data is used for the creation of the white matter parcellation map (WMPM). The diffusion weighted images (DWIs) were corrected for head motion and eddy current distortions. All the DWIs were then averaged to a common space and an average DWI (aDWI) was created. The diffusion tensor was then estimated using a linear fit. An affine registration was carried out between the aDWI and the ICBM-152 "linear" template and the transformation matrix was then applied to the calculated diffusion tensor and the FA image was computed.

Figure 5.2 shows the different steps involved in the creation of WMPM. The authors used the automatic image registration (AIR) [Woods 1998] for affine (12 parameter) alignment of the average diffusion images (aDWIs) with that of ICBM T1 template. The diffusion tensors in each voxel is computed using DtiStudio [Jiang 2006]. The DTI thus computed is then resampled in the T1 template space using the transform computed using the AIR. The tensor elements are averaged to create a DTI template and subsequently the average FA is computed. The FA map is color coded according to the common FA color coding standards introduced by Pierpaoli et al. [Pierpaoli 1996].

The white matter tracts were manually segmented on the FA map into fifty anatomic regions. For the manual segmentation, the experts used previously produced histology based atlases. For more details on the segmented regions and the tools used for the WMPM atlas, it is suggested to refer to the original article [Mori 2008].

In the figure 5.3, the white matter regions are overlayed on the average diffusion images. In the figure 5.4, the authors Mori et al. show the segmented regions as parcellated over the FA map.
Though the ICBM-WMPM provides a well defined parcellation map for the white matter, there is still room for an improved DTI atlas. Some of the short comings of the DTI atlas and the WMPM are listed below

1. The DTI-81 data is normalized to ICBM 152 affine atlas (2001 version). The affine T1-atlas is not very detailed as one can see in the figure 5.5.

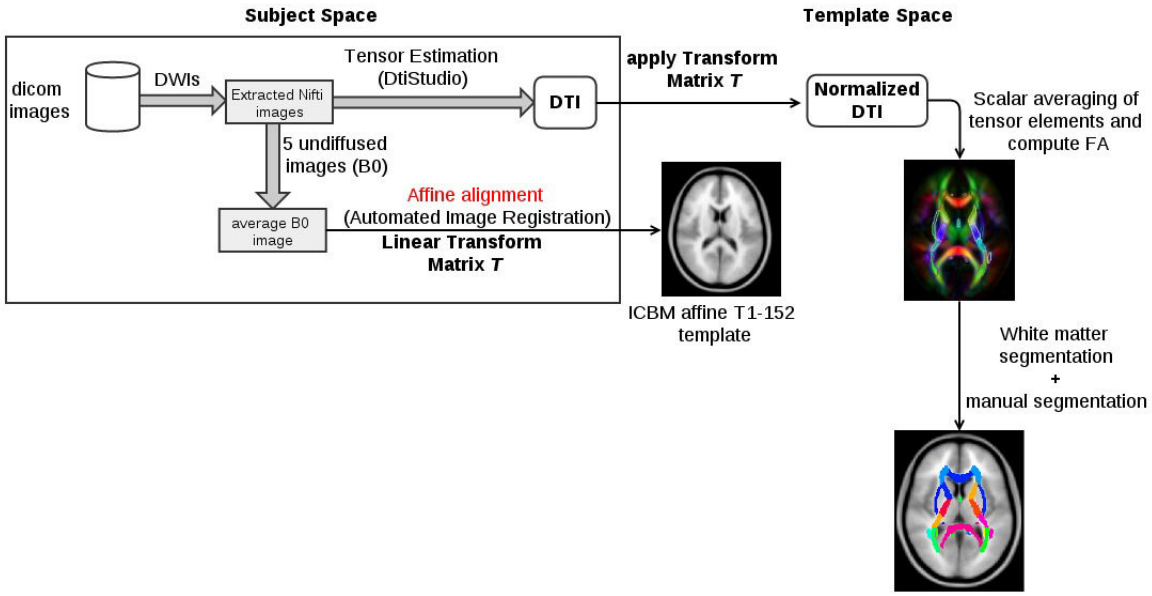

Figure 5.2: Workflow for the creation of white matter parcellation map as described in [Mori 2008]

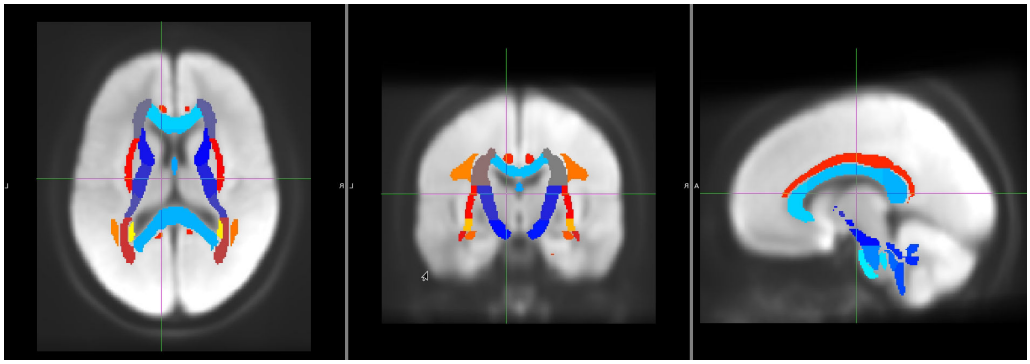

Figure 5.3: An overlay of the white matter parcellation map on the ICBM DWI image. The gray image is the diffusion weighted image and the colored regions shows white matter tracts. The figure shows the axial, coronal and the sagittal slices from left to right.

2. Scalar averaging is performed on the tensor elements. However, it has been argued that a log-Euclidean tensor mean might be more appropriate for averaging tensor fields across subjects [Arsigny 2006b].

3. As the DTI-81 data is normalized using an affine registration, the misalignment chances are higher. Most likely an affine transform of the averaged

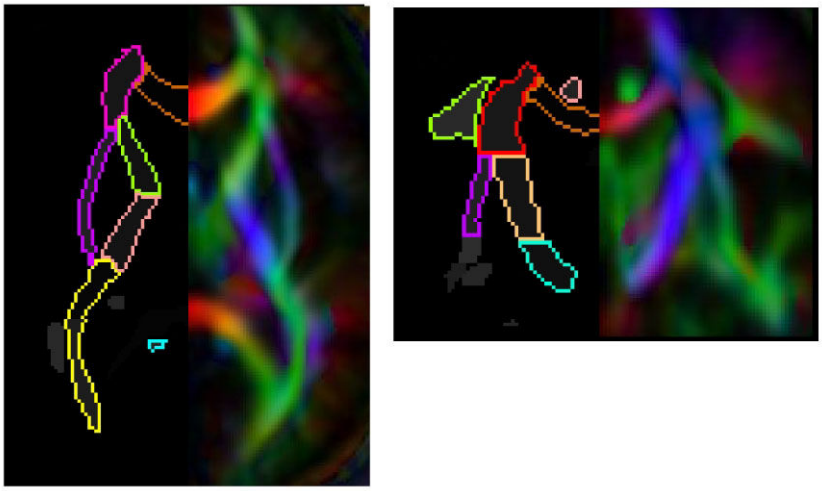

Figure 5.4: White matter parcellation overlay on the color coded FA map. The outline shows the segmented regions. [Mori 2008]

diffusion images to the template T1 image is not a correct approximation for the alignment.

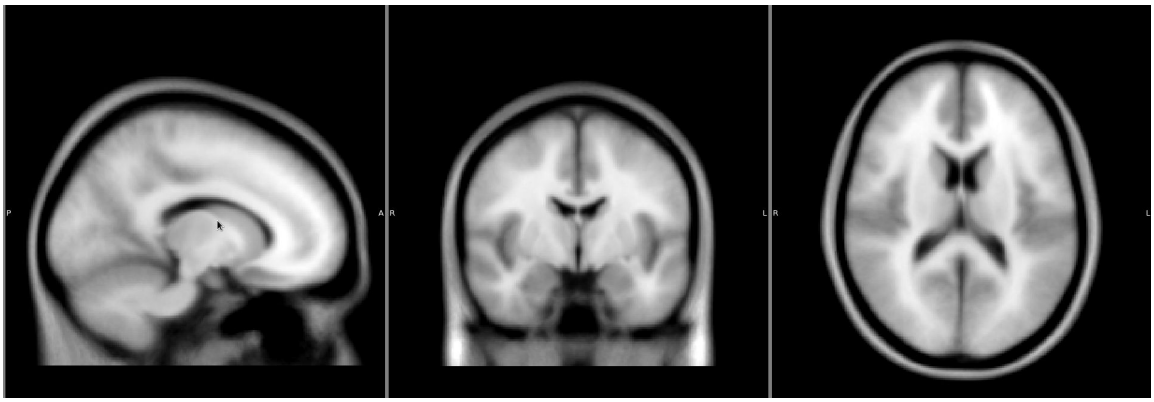

Figure 5.5: ICBM 152 affine template

ICBM-152 T1 template

There are different versions of the ICBM-152 T1 template. One of the earliest versions of this template produced in 2001 was based on linear averaging 5.5. In the subsequent years nonlinear versions of the T1 template were produced (2009 version) [Fonov 2009]. The major difference between the two generations of the template are due to registration.

The ICBM-152 T1 template is a structural template obtained by averaging 152 structural T1 images. The images are nonlinearly registered in the MNI152 coordinate space. Compared to the ICBM T1 affine template this provides a better contrast and is anatomically detailed. This template comes with a brain mask, a T2 template, a tissue mask (white matter, gray matter and cerebro spinal fluid).

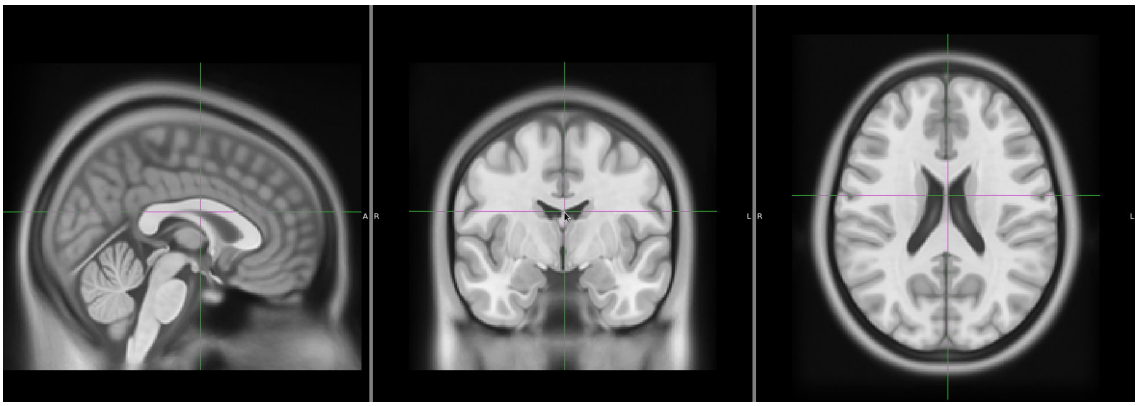

Figure 5.6: The ICBM nonlinear T1 template (2009)

5.2 A need for an unbiased population-specific multimodal atlas

We discussed in the previous sections some of the popular brain atlases and the template spaces in a chronological order. Most of the atlases discussed so far were anatomical atlases with the exception of ICBM-DWI atlas. However, the atlases in different modalities were also in different geometric spaces, hence it was not possible to have a joint statistical analysis of multiple imaging modalities. In this section, we are going to address two issues. The first issue is the motivation to construct a population specific atlas and the second one is the need and relevance of a joint T1 and DTI brain atlas.

Spatial normalization is one of the most important steps in the statistical analysis of a given population. All the subjects can be normalized to a pre-defined template using image registration techniques. The choice of registration algorithm and the target template biases the results in different ways. In statistical studies concerning neuroimaging data, the ICBM-152 T1 template or the MNI template is often used as a target space for spatial normalization of the population. However, the choice is often arbitrary and could lead to erroneous statistical results. For example, in order to study pediatric brain images the use of an atlas constructed from adult brain images (as in the case of ICBM-152) would be inappropriate [Fonov 2009].

The authors argue the need for an age-specific template for statistical studies on pediatric brain images for preventing the introduction of bias due to an arbitrary choice of the template. The argument can also be extended in favor of creating a disease specific atlas. In this chapter, we will focus on creating a joint T1 and DTI template specific to neurocognitive disorders related to HIV/AIDS. The effect of induced bias due to the choice of atlas is discussed in [Thompson 1997]. Such a bias towards the choice of the template can be avoided if a population specific template is created. The population specific alas is also a statistical representative of the given population.

The choice of registration method and the workflow involved in the atlas creation process also effects the statistical results from a population based study. Most of the atlas creation methods follow the workflow suggested by [Guimond 1998, Guimond 2000]. Other methods for unbiased atlas creation using large deformation diffeomorphic setting were reported in [Joshi 2004, Lorenzen 2005]. The latter two methods formulate the mean template creation problem as a Fréchet mean estimation in the space of diffeomorphisms via large deformations metric mapping (LDMM). However, the method presented in [Guimond 2000] is faster and simpler than the ones based on the LDMM approach and also is sufficient for our purposes.

An application of a joint T1 and DTI atlas is presented in [Zhang 2013]. It deals with the consistent prediction of the functional areas in the neocortex via joint modeling of anatomical and connectional profiles . The authors argue that there is a need to have a consistent and meaningful definition of cortical ROIs across different neuroimaging modalities (T1-weighted, DTI and resting state fMRI). So far, the cortical ROIs are either defined on the anatomical T1-weighted images, or on the DTIs or on the resting state fMRI data. These three categories of cortical ROIs are used in their respective areas of application, but their structural correspondences across the different modalities still remains as a question of debate. The cortical ROI definition obtained from task based fMRI data is used as a benchmark approach to identify functionally meaningful cortical ROIs [Haynes 2007, Logothetis 2008, Friston 2009]. However, in a clinical setting it is often time-consuming and cost-prohibitive to acquire a high quality task based fMRI data. It is also unclear if it is possible to infer task based fMRI data from resting state fMRI data. In some cases (for example in ADNI-2), the resting state fMRI and DTI data are not available for the same group of subject. In such clinical contexts, there is a need for predicting funtional cortical ROIs based on structural and DTI data. Such kind of predictive studies make the joint T1 and DTI atlas quite relevant in a clinical context.

Most of the statistical analysis conducted in the past treats the anatomical T1 weighted image and the diffusion tensor images separately. We believe that a joint statistical analysis of the T1 and diffusion tensor images could increase statistical

power and also give a complete picture of the statistical changes across different modalities. In [Lao 2014], the authors have presented a methodology for combining T1 surface based morphometry and a DTI analysis on the surface of the corpus-callosum. It was reported that such a modality fusion leads to increased detection power for detecting differences among pre and post-season contact sports players. Another reason motivating a joint T1 and DTI atlas is that with such an atlas one can draw voxel wise comparison across different modalities and look for correlation between the changes in the white matter regions and the changes observed in structural anatomical images. The DTI atlas can be used for statistical studies on the white matter tracts and will prove complementary to the studies on the T1 weighted images.

5.3 Data

The DTI data used in this chapter was acquired in the NEURADAPT study project conducted at University of Nice hospital using a GE 1.5T scanner with 23 encoding gradient direction and one undiffused B0 image . The diffusion weighted images has 256×256×26 voxels with sizes 0.9375×0.9375×5.5 mm^3. The b-value for the acquisition was 700 s/mm^2. For every subject the T1-weighted anatomical images were also acquired.

An atlas of the acquired T1 images was computed following the methodology outlined in [Commowick 2007]. The first step of the template building process uses the methodology developed by [Guimond 2000]. The method involves an affine registration followed by a nonlinear (elastic) registration between the subject and the chosen template for all the images in a given dataset. The registered images and the nonlinear registrations are then averaged to produce an average intensity image and an average deformation field. The average deformation is then applied to the averaged intensity image to produce the new template image. The process is repeated until desired convergence criteria is met. The workflow is outlined in figure 5.7.

This template creation process is unbiased, so any image from the patient database can be chosen as an initial reference image. However, depending on the orientation of the initial reference image, the final average template might not be symmetric across the mid-sagittal plane. The asymmetry might lead to some biases while performing the patient to template registrations. Thus a symmetrization of the template is necessary. Several algorithms exist for computing the mid-sagittal plane of a brain, for example [Prima 2002] and [Bazin 2007]. We have used the mid-sagittal line alignement tool from the MIPAV library [Bazin 2007] for symmetrizing the template because of the ease of availability and also the results were good enough for our purposes. For symmetrizing, first the minimum resolution of the image is determined and the image is flipped horizontally. The flipped image and the original

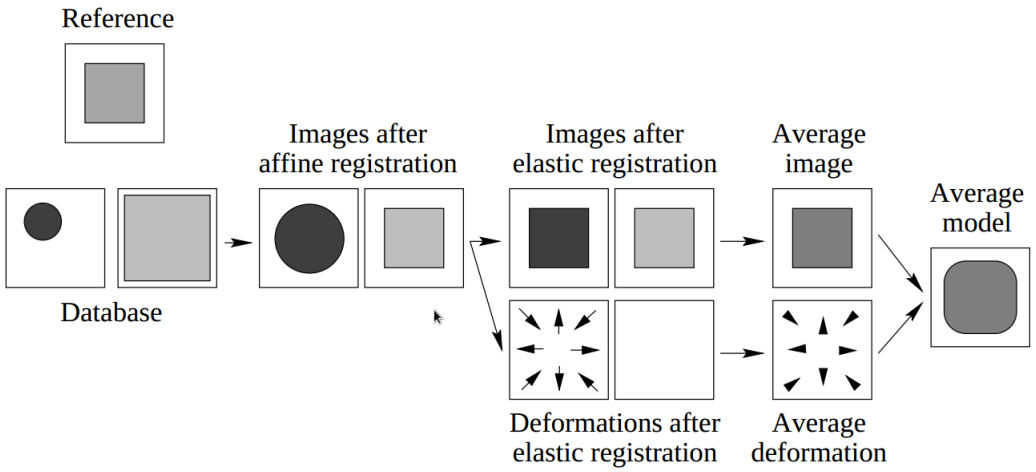

Figure 5.7: Workflow for creating average template. Adapted from [Guimond 2000]

image are resampled using trilinear interpolation to create high reolution isotropic voxels. The center of mass (COM) of both images is computed and the COMs are aligned. The aligned images are then registered using an iterative registration algorithm. In this case, MIPAV uses optimized automatic registration 3D [Bazin 2007]. Few slices from the symmetrized population specific T1 template are produced in figure 5.8.

5.4 Construction of probabilistic multimodal brain template

5.4.1 Joint T1 and DTI template

The dicom images were extracted using the MRIcron software [Rorden 2008] into the nifti image format. The diffusion weighted images were corrected for head motion and eddy current distortion using the FSL tools taking the B0 image as reference. The B0 and the T1 images are first rigidly registered using FSL's *flirt* utility with a 7 degree of freedom (dof) and a mutual information cost function to take into account the multi-modal registration. Seven degrees of freedom for the registration takes into account the rigid motion of the head (rotation and translation) along with the scaling of the voxels that is present due to differences in the field of view of the B0 and the T1 images. The T1 images were corrected for the intensity bias using the N4ITK bias correction tool [Tustison 2010] followed by skull stripping using the ROBEX [Iglesias 2011]. The bias correction and the skull stripping are important for an accurate registration. The subject T1 image is registered to the population specific T1 template shown in figure 5.8. The registration is a two step process, first an affine registration between the subject and the average T1 template followed by a nonlinear registration using

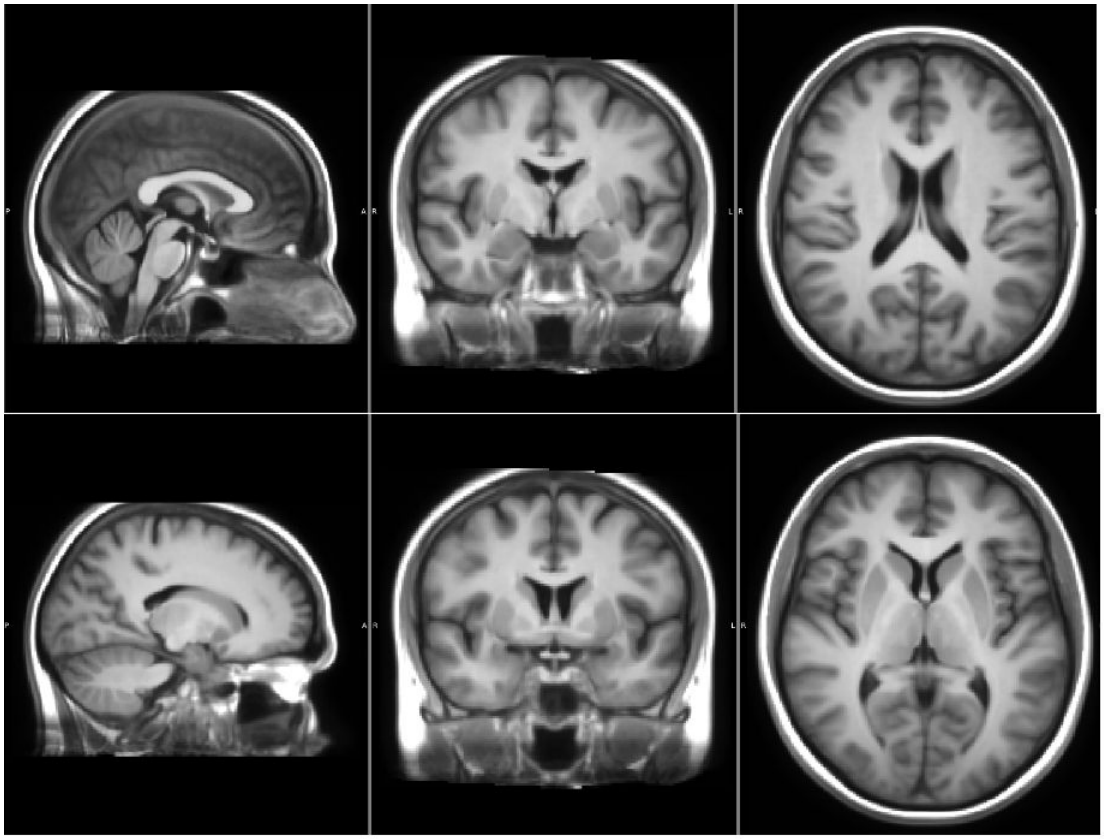

Figure 5.8: The average anatomical template computed using the NEURADAPT study data.

the LCC demons algorithm [Lorenzi 2013]. The combined affine and nonlinear transformations are combined and applied to the 23 diffusion images. The diffusion images are resampled using a b-spline interpolation scheme of order two.

Once the diffusion images are resampled in the average template space, the diffusion tensor is estimated using the variational framework for tensor estimation suggested by [Fillard 2007]. The estimated tensors are resampled using the Log-Euclidean interpolation scheme [Arsigny 2006b]. The FA is computed for the averaged tensor image. A schematic of the whole pipeline is shown in the figure 5.9. The FA image computed using the averaged tensor field is shown in figure 5.11.

The correspondence between the T1 and DTI template is shown in the figure 5.10. The figure shows a close-up of the two images near the ventricles to highlight the accuracy of alignment of features. In figure 5.13, the FA map created is overlayed on top of the T1 template to show correspondences between the white matter regions

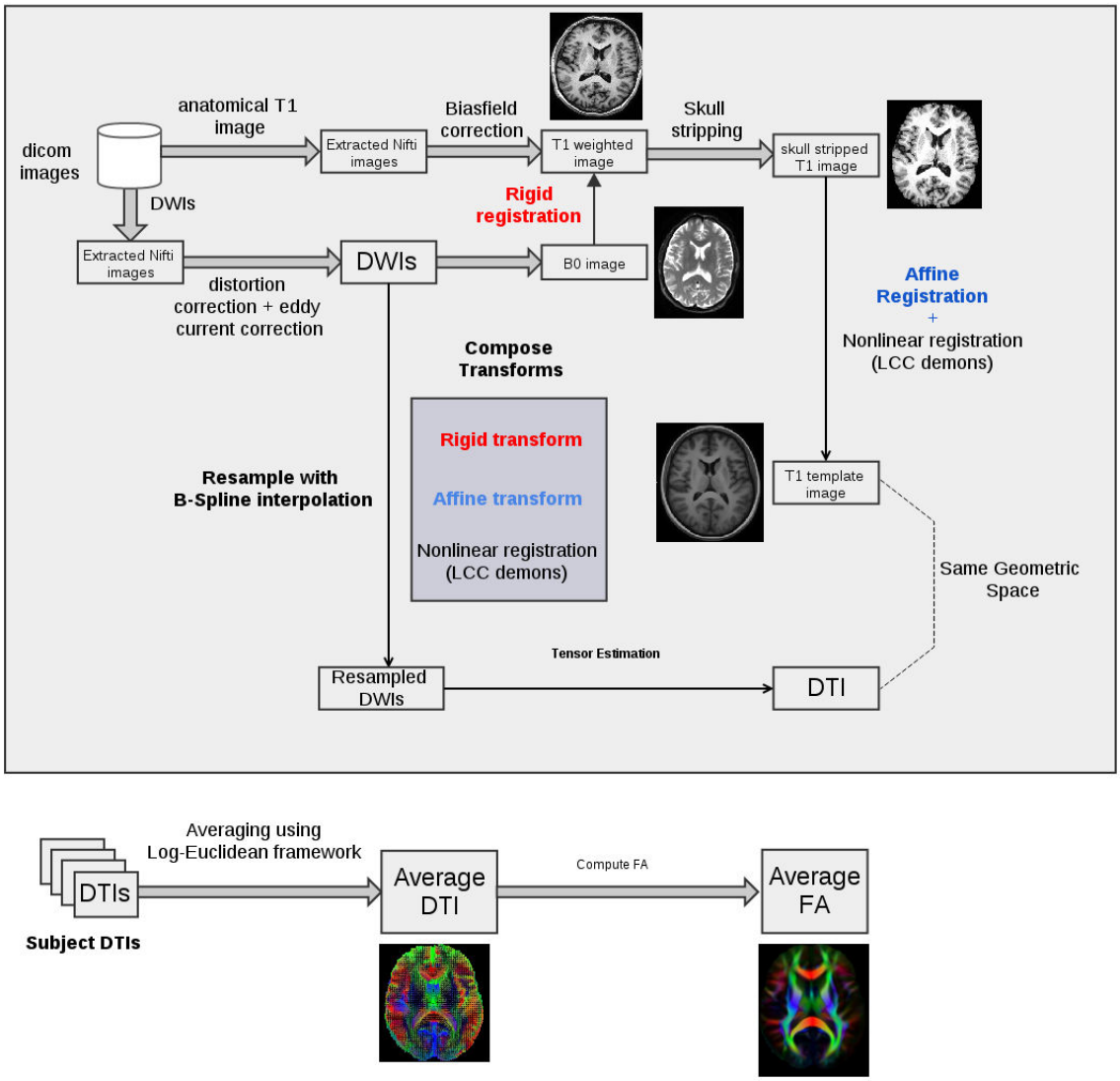

Figure 5.9: Workflow for normalization of diffusion images to the T1 template space. (The registration and the corresponding transforms are denoted with the same color.)

of the brain.

5.4.2 Probabilistic white matter atlas

In the previous section, we discussed the workflow involved in the creation of a joint T1 and DTI template. For doing statistical analysis on specific fiber tracts as well as region of interest (ROI) based statistical analysis of white matter regions [Keihaninejad 2013], it is important to have an accurate segmentation of the major

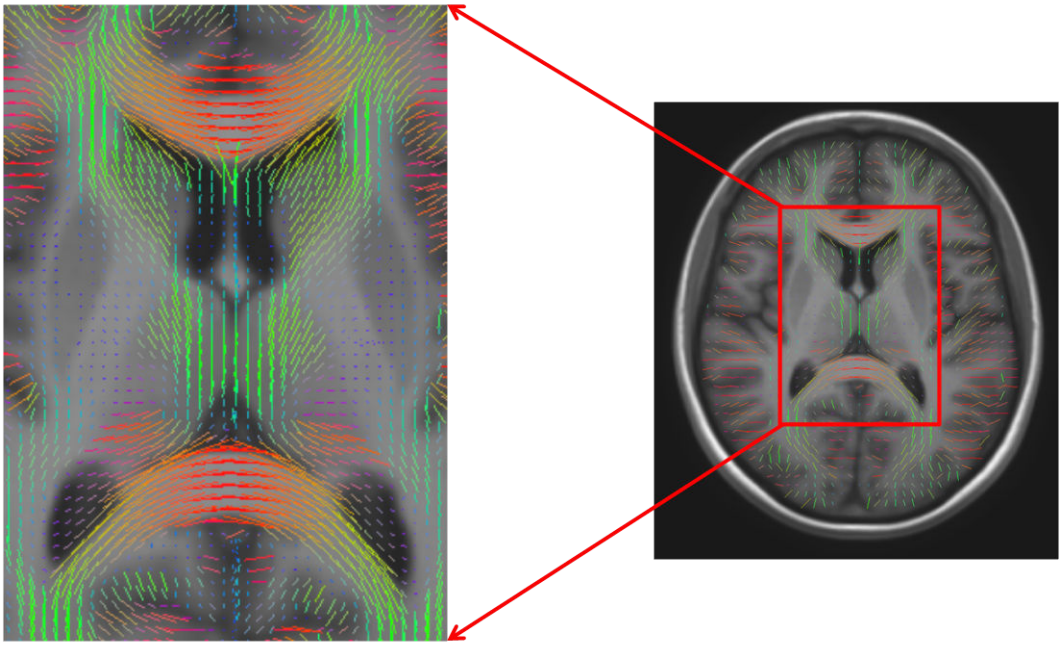

Figure 5.10: A zoomed view of the T1-DTI template to show the accuracy in the alignment of the two modalities.

white matter tracts on the DTI template. However, an accurate segmentation is a difficult problem in itself. Often times, the segmentation performed by an expert is considered as a ground truth for computing ROI based statistics. The manual segmentation results also vary depending on the expertise of the personnel and is certainly not error-free. Moreover, manual segmentation are often expensive and time consuming. In such a scenario, it is desirable to have a probabilistic segmentation of the ROIs. A probabilistic segmentation allows us to attach an additional confidence in the statistical results. One can tune how much conservative one should be in choosing the regions of interest.

Because of the lack of an expert for segmenting the white matter regions, we decided to transfer the ICBM white matter parcellation map (Fig. 5.4) on the template image. In the section, we will discuss a method for generating a probabilistic parcellation map for white matter tracts in the study specific DTI template using the ICBM WMPM as a reference. Of course it is possible to generalize this method to any other studies.

The white matter parcellation map is transferred on the T1 template to generate a probabilistic parcellation map. Originally, the WMPM was generated by experts using the FA maps. However, it is often expensive and not feasible to have a team

of experts for segmenting the intricate regions of the brain. In such scenarios, the probabilistic segmentation maps offer an affordable solution.

As shown in the figure 5.12, the ICBM affine template is registered to the subject space through a series of registrations. First the ICBM-152 affine template is affinely registered to the ICBM-152 nonlinear template. The nonlinear template is then skull stripped and nonlinearly registered to the skull stripped T1 image of the subject. The subject T1 image and the template images are also nonlinearly registered. All the registrations are combined in the righ order and the ICBM-WMPM is resampled using nearest neighbor interpolation with the combined transformations. Similar operations are carried out for every subject. At the end all the WMPM transferred to the template space are normalized with respect to the number of subjects.

5.4.3 Choice of registration tools

An "accurate" registration scheme is the key factor in such spatial normalization processes. In this section, I will discuss the choices that are made during the registration and why the individual choices are important. It is a two step registration process, the first one being the intra-subject registration, in which the B0 image or the undiffused image is aligned with the T1 image of the same subject. In the second step the T1 images of the subject is aligned with the average T1 template. In the second step, first an affine alignment is carried out FSL's flirt followed by the nonlinear registration carried out using the LCC demons algorithm as mentioned above.

FSL's flirt

FSL's flirt (or FMRIB's linear image registration tool) is an automated robust registration tool available for carrying out rigid and affine registrations [Jenkinson 2002]. It supports optimization of different similarity criteria like sum of squared differences, cross-correlation, normalized cross-correlation and mutual information. For the intra-subject rigid registration of the B0 and the T1 images, I used the mutual information as a cost function and seven as the degrees of freedom for the transformation. The mutual information based cost function was chosen to take into account the different modalities of the images under consideration. The images were not skull-stripped in the case of intra-subject registration.

LCC demons

LCC-demons is a fast and robust registration framework based on the log-demons diffeomorphic registration algorithm suggested by [Lorenzi 2013]. The nonlinear transformations is parameterized using stationary velocity fields (SVFs) [Arsigny 2006a] and the similarity metric for the registrations uses a symmetric local correlation coefficient (LCC). The choice of similarity criteria is crucial for

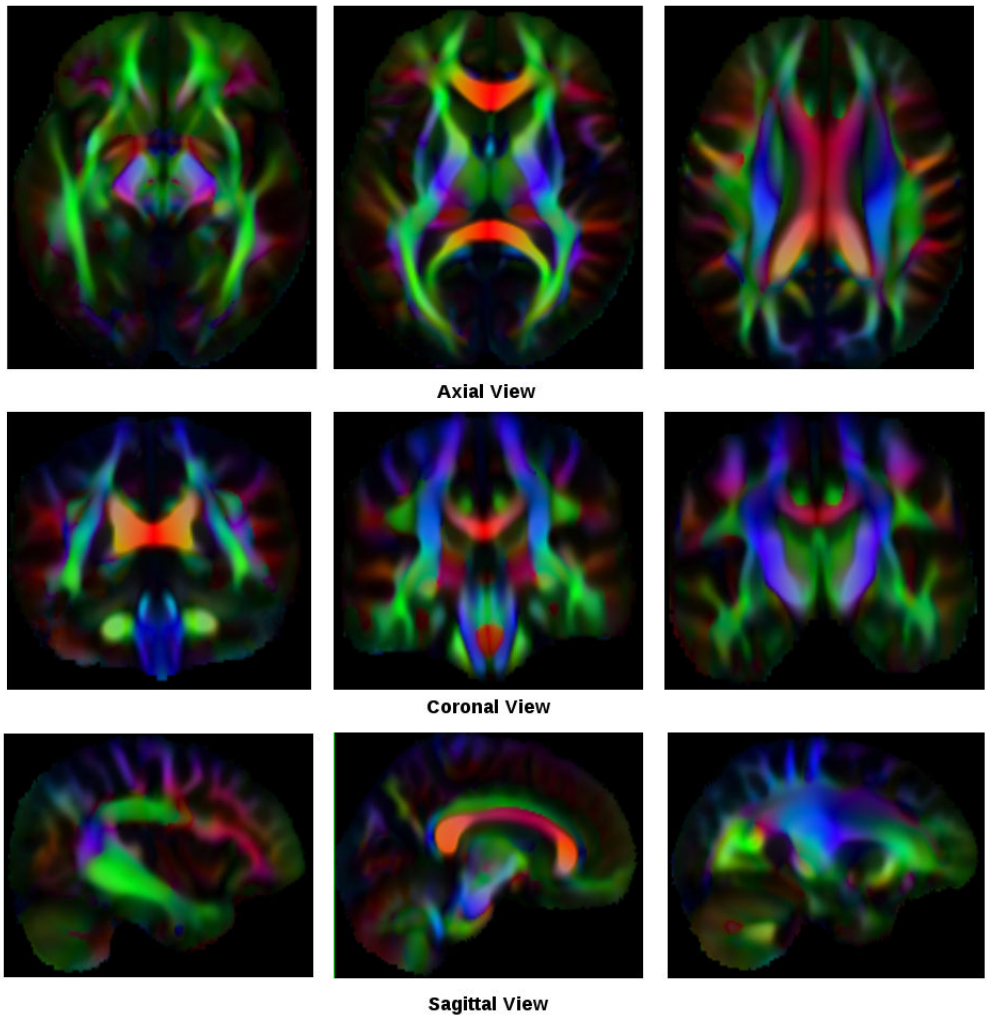

Figure 5.11: The average FA template computed using the NEURADAPT study data.

the image registration quality. Some of the common similarity criteria in common use are the sum of squared differences (SSD), normalized correlation criteria, normalized mutual information. The problem with these criterion is that they are global in nature, that is, they assume a uniform global bias between subject and the target image spaces. Such global biases often overshadow the subtle local changes in the image, which might lead to erroneous estimation of the deformation field. The diffeomorphic nature of the registration algorithm makes it suitable for atlas building applications [Lorenzen 2005]. As mentioned before the diffeomorphic transformations are parameterized using SVFs. The SVF parameterization is a

good compromise between accuracy and computational efficiency. In term of speed it is much faster than the LDMM framework, reducing the computation time for a single registration to a matter of few minutes. The speed of computation makes it suitable candidate for registration on fairly large datasets.

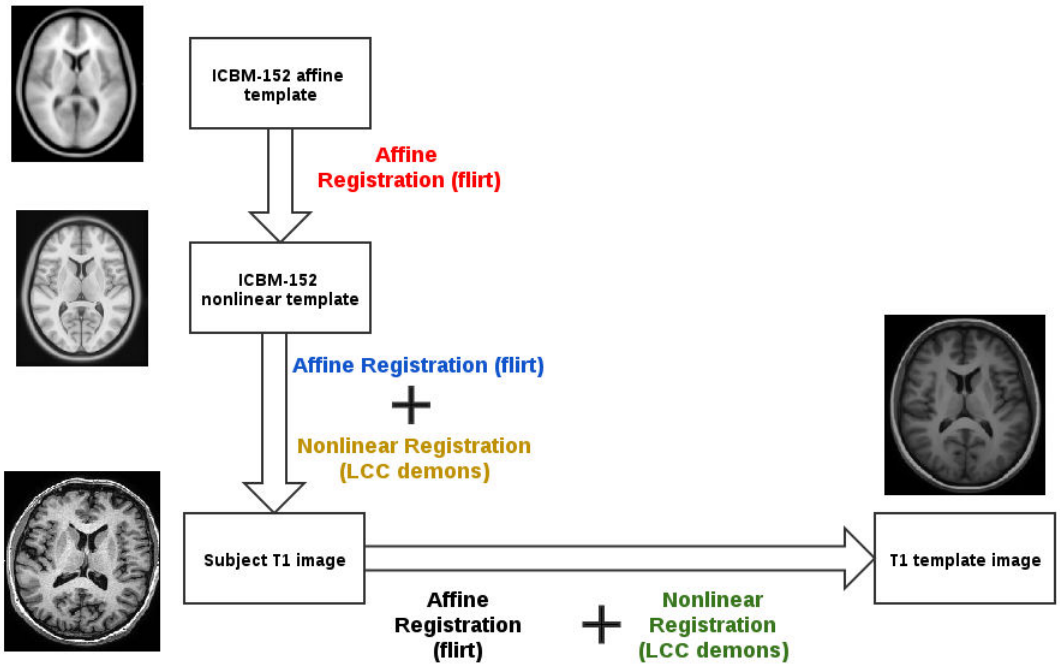

Figure 5.12: Workflow for transferring the white matter parcellation map on to the T1 template.

5.5 Results

The figure 5.13 shows the FA image overlayed on T1 anatomical template. The FA image is shown in red-yellow and the T1 template is in gray scale. In the figure, one can see that the white matter regions in both the T1 template and FA image are aligned very well. This well aligned template allows voxelwise comparison between these two imaging modalities.

The second step of the process was to make a probabilistic white matter parcellation map by transferring the ICBM-WMPM to the joint T1 and DTI template. In the figure 5.14 and 5.15, we have shown corpus callosum (CC), middle cerebellar peduncle (MCP) and internal capsule as probabilistic iso-surfaces. The inner most core of the region is blue with a 100% probability of being classified as the region

under consideration. The outermost shell is in red and is the one with the least probability of classification. All the 52 white matter ROIs in the ICBM-WMPM are transferred to the population specific template discussed in this chapter. The figures 5.16, 5.17, 5.18, 5.19 show the probabilistic parcellations on 2D slices.

The figure 5.20 show the cortical ROIs segmented by an expert and the probabilistic white matter parcellation overlapping on each other. The interesting thing to notice in this figure is the consistent definition of white matter structures and the cortical ROIs on the same template. However, some inaccuracies can be sometimes observed on the boundary of the ROIs. An example is shown in figure 5.21. The right external capsule is sandwiched between the insula and putamen. On a closer look on the three slices presented in the figure, one can see that the boundaries of insula and putamen are such that they overlap with the external capsule. This clearly shows that the cortical ROIs in T1 are not correctly segmented. The inconsistency in cortical ROI segmentation across different modalities was discussed recently in [Zhang 2013]. The regions (putamen and insula) are clearly over-segmented by the expert. The probabilistic mask could also serve as a guiding force for the expert segmentation in the future in order to avoid such errors.

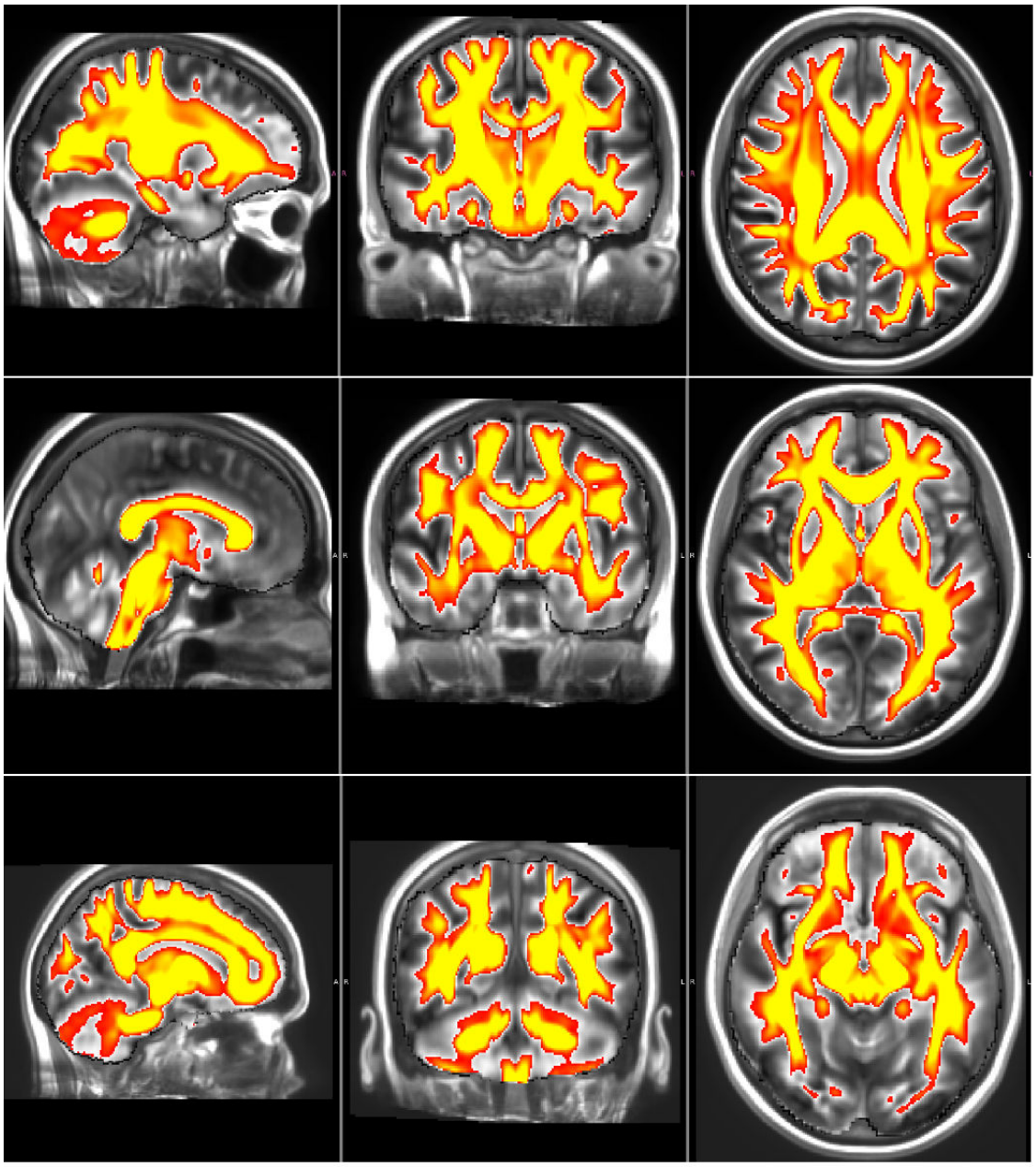

Figure 5.13: The fractional anisotropy image overlayed on top of the anatomical T1 image. The FA image is shown in red-yellow and the T1 template is in gray scale.

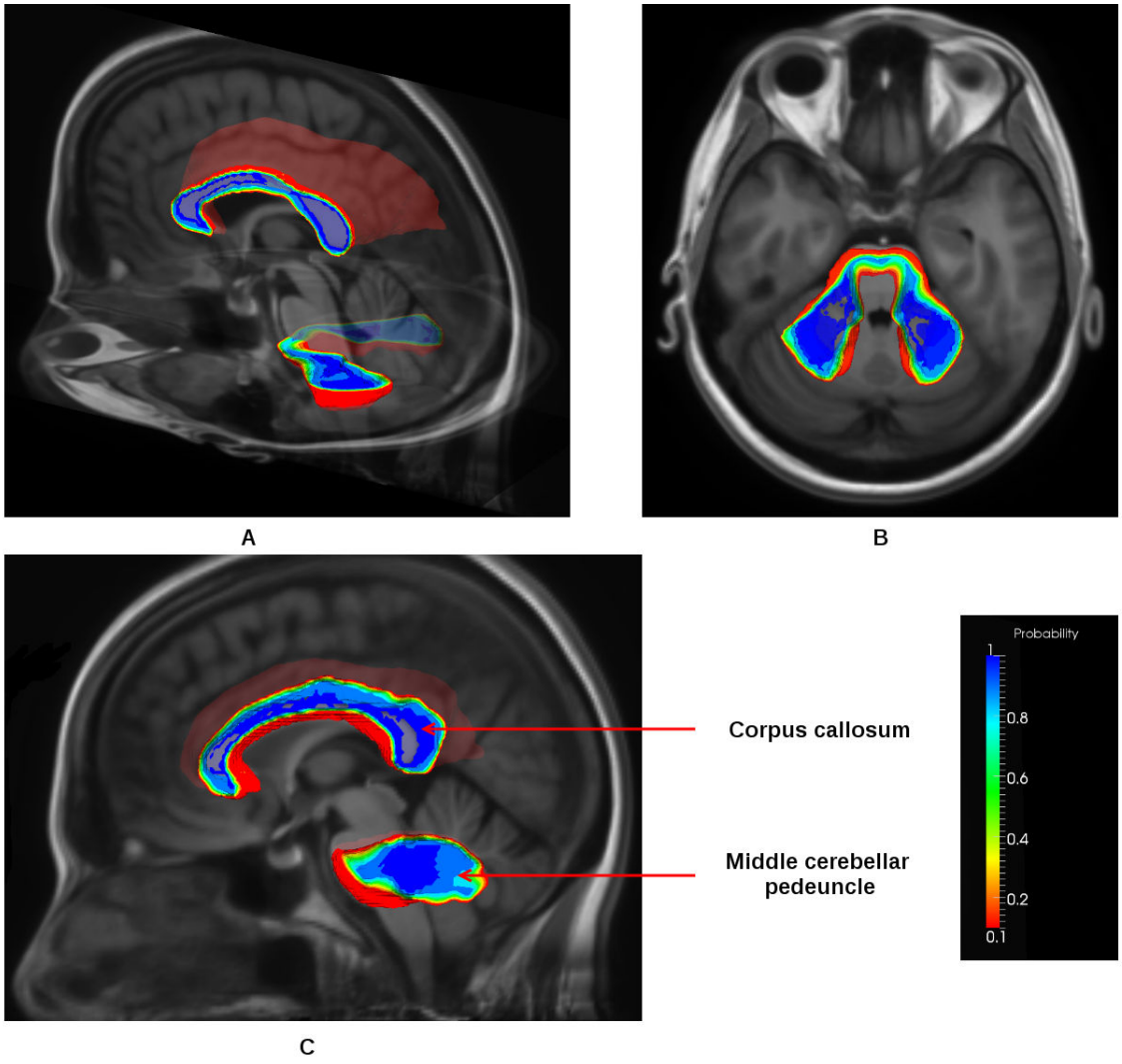

Figure 5.14: 3D rendering of corpus callosum and middle cerebellar pedeuncle in the joint template space. The regions are shown as cut sections of iso-surfaces. The probability of a voxel belonging to the ROI decreases as we move out from the core to the external surfaces. The blue regions have a 100% chance to be in the specific region of interest, while the red regions are least probable to be classified as the ROI. **A:** Isometric view of corpus callosum (CC) and middle cerebellar peduncle (MCP). **B:** Axial view of MCP. **C:** Sagittal view of CC and MCP

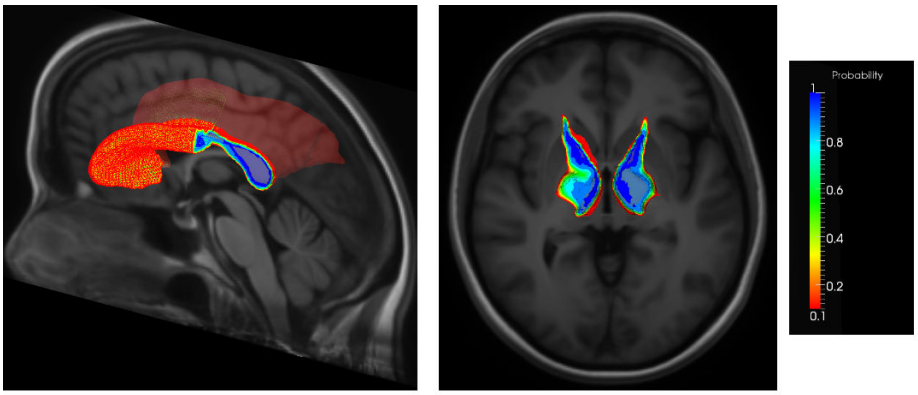

Figure 5.15: Full iso-surface rendering of corpus callosum and axial view of internal capsule.

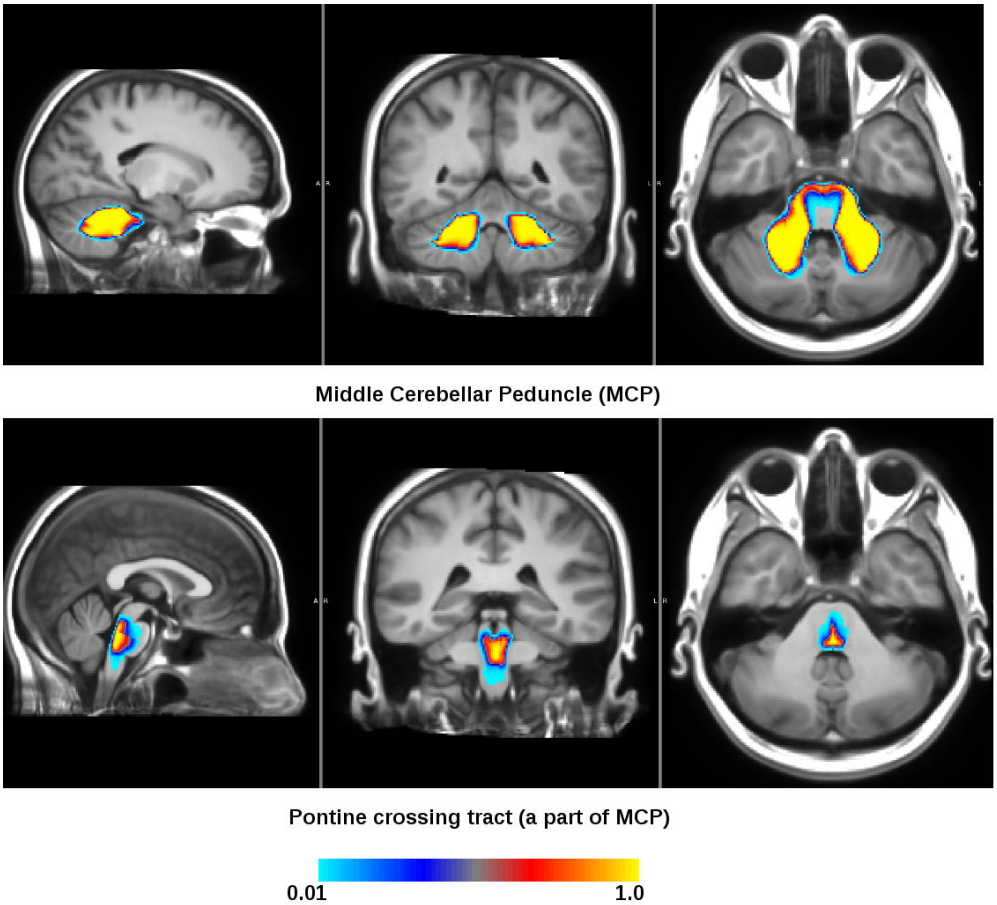

Figure 5.16: Regions of interest overlapped on the anatomical T1-weighted images (part 1)

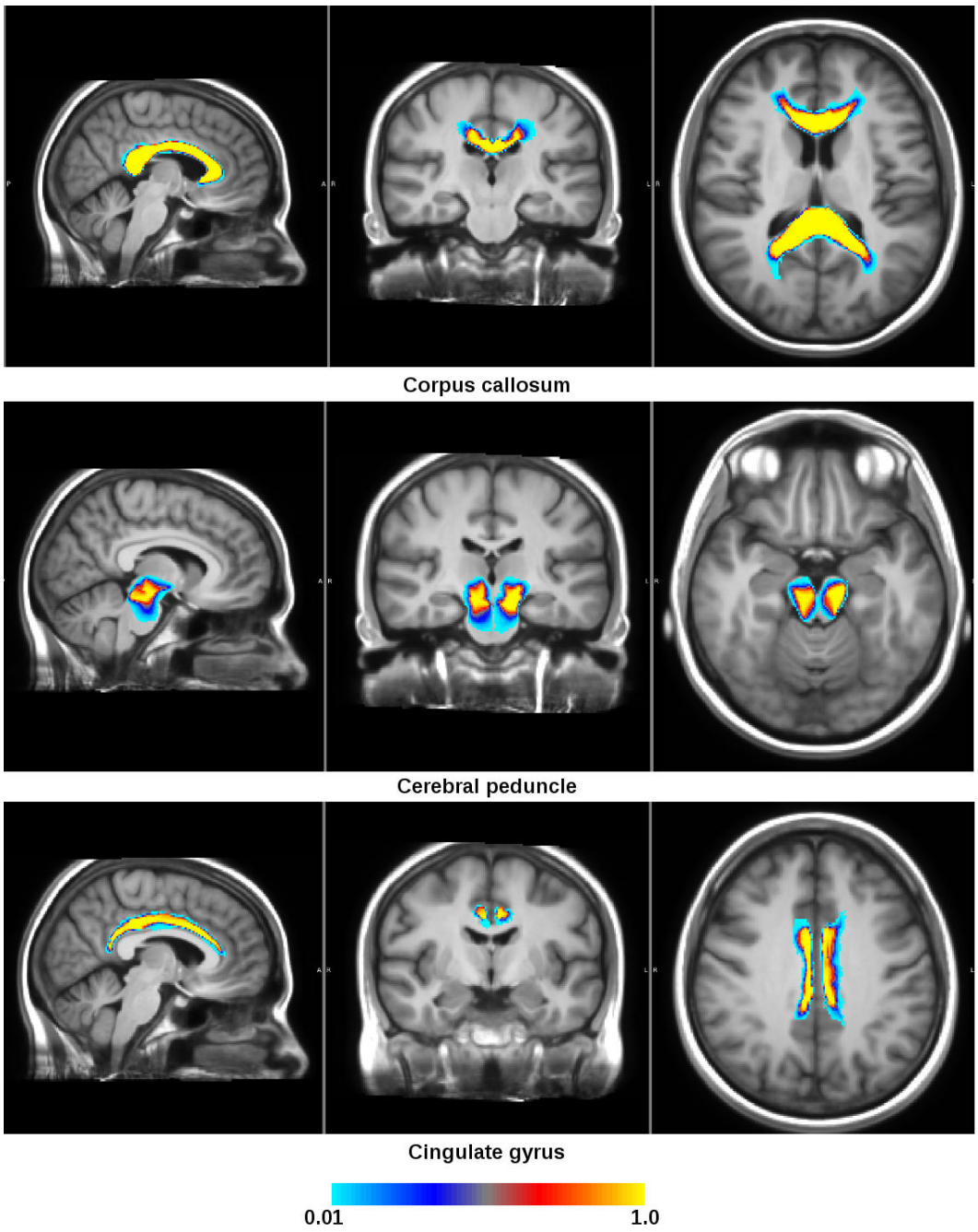

Figure 5.17: Regions of interest overlapped on the anatomical T1-weighted images (part 2)

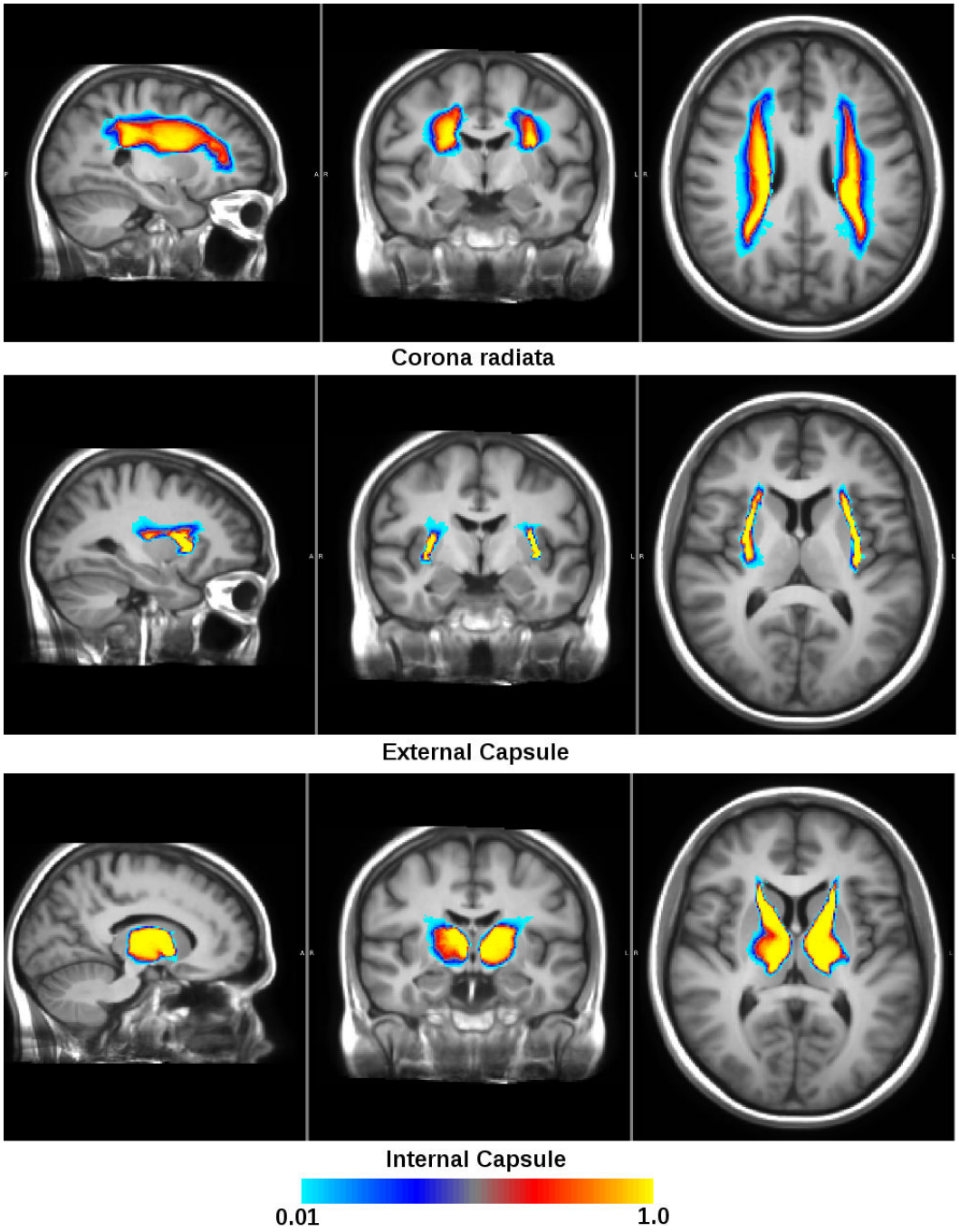

Figure 5.18: Regions of interest overlapped on the anatomical T1-weighted images (part 3)

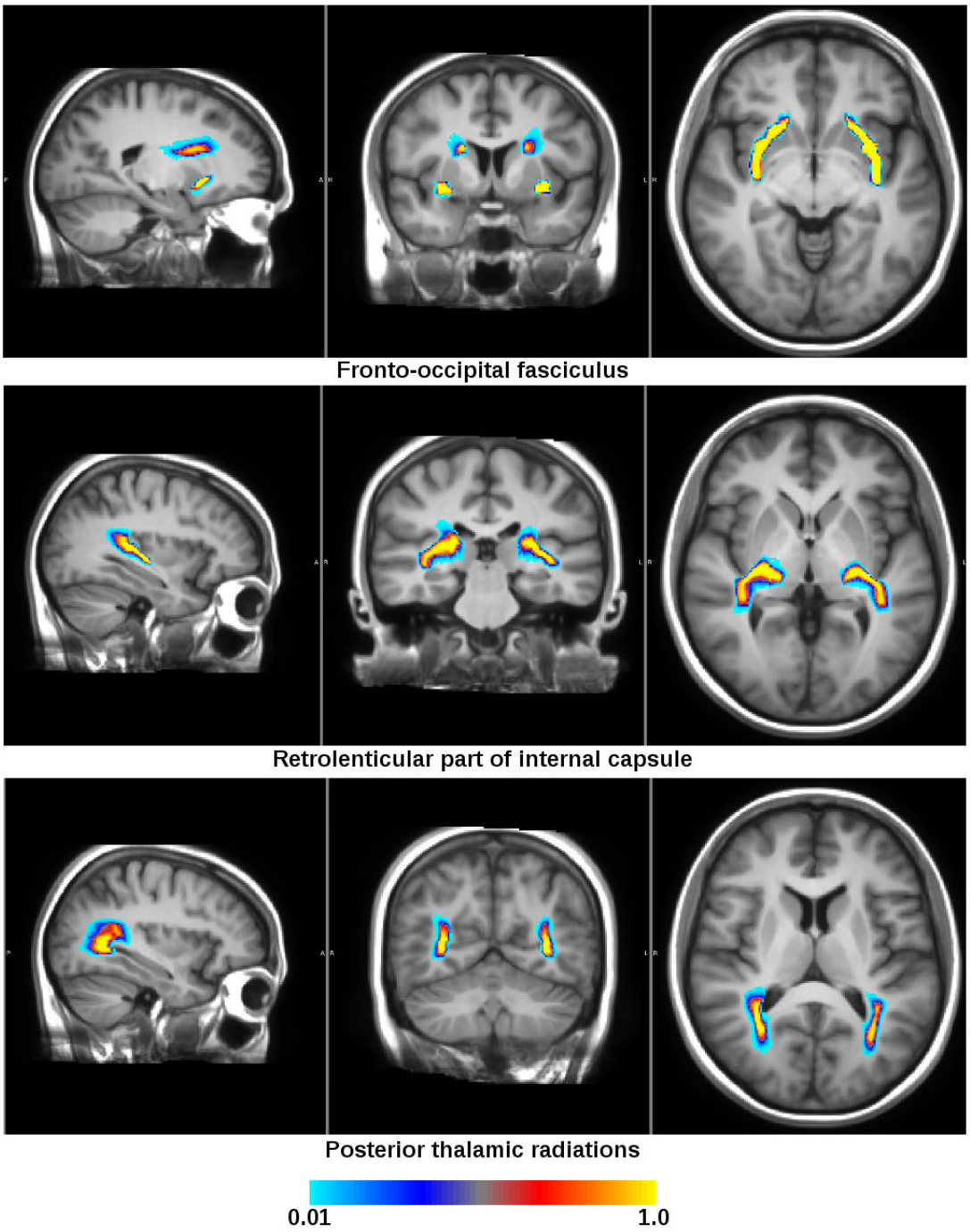

Figure 5.19: Regions of interest overlapped on the anatomical T1-weighted images (part 4)

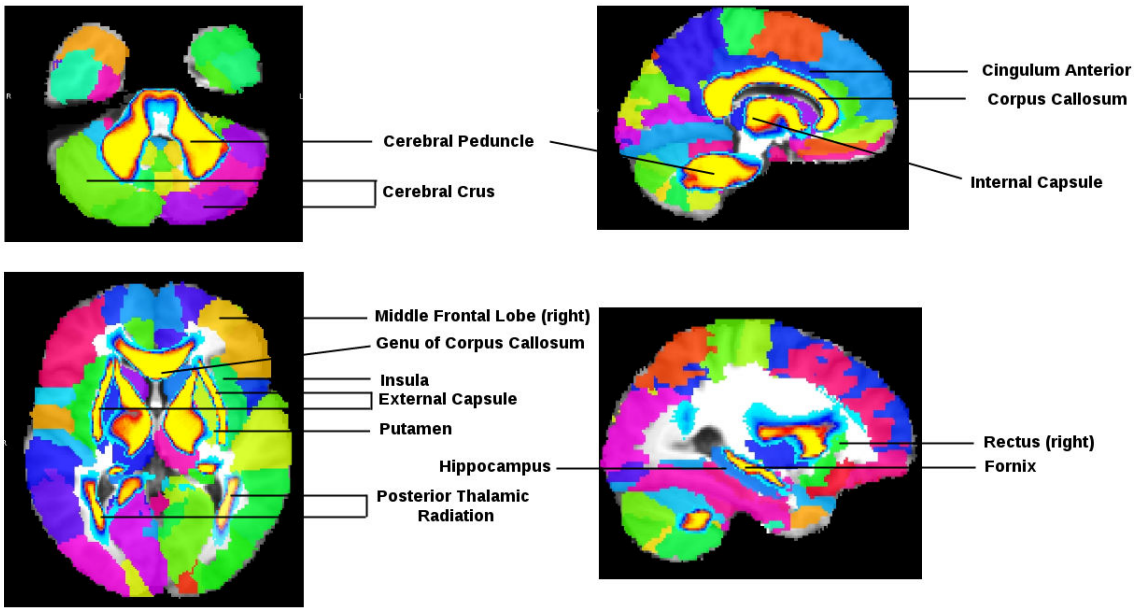

Figure 5.20: The probabilistic white matter parcellation map is overlayed on an atlas showing segmentation of difference regions of the cortex. They are overlayed on each other using FSLVIEW to show the anatomical correspondence between the cortical segmentation and the white matter tracts.

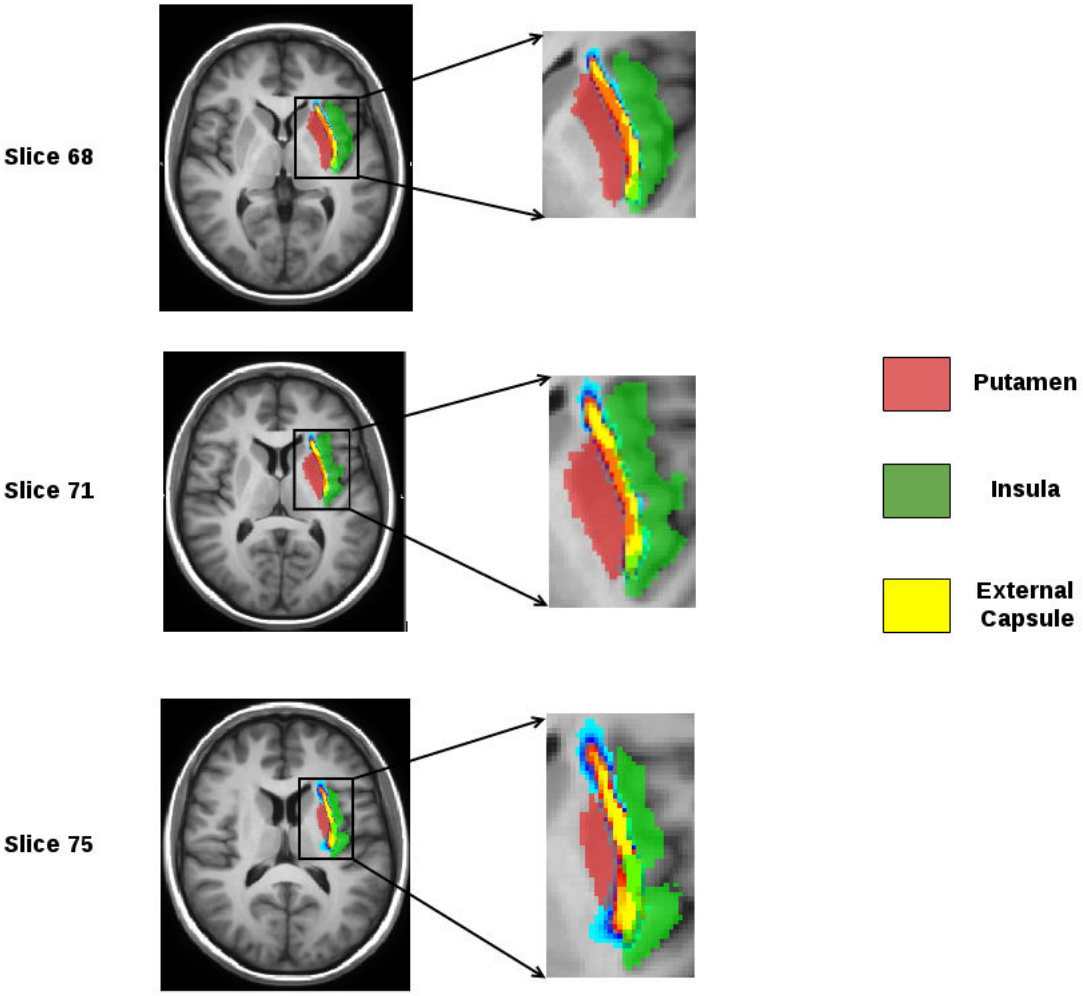

Figure 5.21: Section of the brain showing disagreement in the expert segmentation of the cortical surface. The two regions putamen and insula should be separated by external capsule. The segmented regions overlap the external capsule.

5.6 Conclusions

In this chapter, we have discussed briefly the history of human brain atlases. The earlier brain atlases were made from a single subject. But, a single subject brain atlas does not represent the variability of human brain across population and different age groups. With the increase in digital neuroimaging data, atlases were developed using multiple subjects. These atlases were mostly developed using the anatomical T1 weighted images. Some of the landmark templates were discussed in the chapter. We discussed that a population specific atlas is essential for an unbiased statistical study.

We then proposed a robust framework for developing a joint T1 and DTI template. We showed that the white matter structures in the T1 and DTI templates are well aligned. Such joint template could be useful in carrying out multimodal statistical studies and also study the correlation between longitudinal changes observed across different modalities. For example, in case of neuro-degenerative disease like Alzheimer's disease it will be interesting to see how the changes in one of the structures in the brain affects the changes in the adjoining regions. For example, is there a correlation between the expansion rate of ventricles and the atrophy of corpus callosum in case of Alzheimer's disease.

Along with the template, we also presented a workflow for transferring the ICBM-WMPM labels to the population specific template developed in this chapter. We created an probabilistic atlas of white matter regions using the ROI definitions from the WMPM labels. We believe that such a probabilistic atlas will allow to define levels of confidence more robustly in the ROI definition while computing ROI based statistics. The probabilistic ROI based method presents an alternative to expert segmentation, which is often expensive and also not completely immune to human errors. The probabilistic white matter labels align very well with the cortical ROI definitions. Such cortical segmentation can be obtained using tools like Freesurfer.

We believe that such probabilistic ROI definitions could aid experts in segmenting more accurately and refining their segmentation.

In figure 5.20, we showed the anatomical agreement between the probabilistic white matter parcellation map developed in this chapter and the manually segmented cortical labels. We also showed the error in manual cortical segmentation in figure 5.21. Manual segmentation is expensive and not always a feasible solution. Thus, a completely automatic parcellation algorithm is highly desirable. The probabilisitic white matter atlas can be used as a prior information in automatic cortical parcellation algorithm such as the one presented in [Fischl 2004, Destrieux 2010]. The authors used manually parcellated cortical regions as training dataset to compute automatic parcellation on a new subject. We think the accuracy of the parcellation can be increased if more information on the white matter segmentation. Fusing the cortical and white matter parcellation maps on the same atlas will help as-

sess the connectivity between different cortical regions and refine fiber tractography.

With the multimodal atlas, a combined T1 and DTI statistics needs to be performed in-order to see the correlation between the different modalities and how it enhances the statistical power. It remains to be seen if deformation based morphometry on the T1 images and tract based spatial statistics on the DTI have a strong correlation. With the multimodal atlas, a voxelwise comparison between the results from these two statistical approaches needs to be done. It remains to be seen if the atrophy in white matter regions from ROI based deformation based morphometry and white matter changes observed with TBSS have a strong correlation.

Chapter 6

Tract based spatial statistics using full tensor information on HIV/AIDS patients

Contents

6.1 Clinical studies on HIV/AIDS patients

Clinical and pathological disorders has been observed in the white matter of the central nervous system (CNS) among HIV patients. Significant thinning of the neo-cortex as well as loss of large number of cortical neurons due to HIV infection has been reported [Wiley 1991]. In another study it was found that the the human immunodeficiency virus of type 1 (HIV-1) causes dementia leading to abnormalities in cognition, bad motor performance and behavior, the mechanism of the disease is less understood [Price 1988]. It is believed that the HIV can cross the hematoencephallic barrier [Williams 2002] causing the nervous impairment by

affecting the neuronal connectivity linking the frontal, parietal and sub-cortical regions. HIV commonly invades the brain 15 days after accidental intravenous inoculation. It is also known that the neuron dysfunction or death underlining the clinical symptoms of HIV/CNS disease does not result from direct infection of neurons. Thus, the mechanism of HIV-related brain injury is not well understood so far. The T1 and T2 weighted MR imaging cannot reveal many significant changes in the white matter [Everall 1997], so a systematic study based on DTI parameters is much needed and relevant.

The brain gathers information from the surroundings and normal perception requires integration of these collected information. Studies have confirmed that HIV leads to dysfunctioning cognitive behavior and motor skills due to white matter degeneration. In a study conducted on HIV related disruption of visuospatial and attention process, the DTI metrics revealed poorer fiber integrity of the corpus callosum in the HIV patients compared to the control subjects [Müller-Oehring 2010]. In this study, the participants were supposed to identify large global letters composed of smaller local letters in the presence of distractors at local, global and both levels and their response time was recorded. It was found that the HIV infected patients performed similar to the control group but their response time was different. It was also found that subjects who displayed more global processing advantages and less pronounced local precedence were also suffering from temporal micro-structural compromise of corpus callosum. Also, it can be conclusively demonstrated through the available tests and statistical data [Müller-Oehring 2010] that the laterlized local-global processes require transcallosal integration to enable hierarchal perception via occipito-temporal connectivity and response control via prefrontal connectivity.

Similar study on cognitive performance among HIV patients using quantitative DTI was done in [Tate 2010], which revealed notable correlation between the tractography metrics and the cognitive performance. The tests include motor tapping tests, speed of processing and executive function. These studies corroborates the importance of white matter functions in cognition. Significant differences were measured in global tractography FA among HIV positive and HIV negative patients. It was also reported that among HIV patients there is was a significant reduction in the number of fiber tracts when compared to the control patients. On the contrary another study [Thurnher 2005] suggests that DTI is unable to detect statistically significant differences in FA, when compared to control subjects. Though they corroborate the fact that there was a decrease in FA, in HIV+ patients, when compared to normal control subjects, they deny any statistical differences.

A DTI study on diffusion in corpus callosum of HIV patients reveal reduced FA values in splenium (posterior part of corpus callosum), which relates to dementia

(HIV-D) and reduced motor functions [Wu 2006]. Increase in the values of MD was also found in splenium. The authors suggest that these DTI findings may yield meaningful variation, associated with progression of neurological dysfunction among HIV patients, as symptoms like cognitive decline is only noticeable in advanced stages of the disease.

A multivariate statistical approach on tensor based morphometry to identify group differences between 26 HIV/AIDS patients and 14 matched healthy controls was presented in [Lepore 2008]. Compared to the tensor based morphometry, the method retains the full deformation tensor information and use a manifold version of Hotelling-T^2 test in the Log-Euclidean domain. The authors detected consistent, but more extensive patterns of structural abnormalities using the multivariate approach. The authors found significant atrophy in the genu and splenium of the corpus callosum along with significant reduction in FA. The total surface area of the corpus callosum was also reduced by a significant amount. On a global scale the white matter exhibits whidespread atrophy.

In this chapter, we will discuss the NEURADAPT study designed to study differences in the brain of controls versus patients. The HIV patients were given to neuropschyological tests and were tested on variety of tasks like learning, recalling episodic memories, cognition and motor skills. One of the goals of the study is to correlate the test scores with that of the changes observed in diffusion tensor images. Due to the low resolution and signal-to-noise ratio of the DTI, it is challenging to design a statistical study based on diffusion tensor images. The goal of the chapter is to design a workflow which is best suited for the given population.

In the following sections, I will discuss briefly the different methodological tools used in the analysis of brain images. I will also discuss their shortcomings and the merit of using tract based spatial statistics (TBSS) on DTI. Further in the chapter, we will discuss the results obtained using the classical TBSS workflow. This will be followed by certain improvements made on the TBSS workflow and the results along with the clinical implications of the study.

6.2 Tools used in statistical analysis of brain images

The most commonly employed methods for morphometric studies are deformation based morphometry (DBM) [Ashburner 1998], voxel based morphometry (VBM) [Ashburner 2000] and more recently tract based spatial statistics (TBSS) [Smith 2006]. DBM and VBM are more suited approach for anatomical images, whereas the latter is the one more used in context of diffusion tensor images. For the sake of completeness both deformation and voxel based morphometry are discussed in brief before delving into TBSS.

6.2.1 Deformation based morphometry

In deformation based morphometry (DBM), one analyzes the 3D displacement vector field obtained from a nonlinear registration between a subject and a template brain. The determinant of the Jacobian matrix of deformation field is used to analyze the distortion necessary for matching the subject and the target images. If the value of the determinant is less than unity, it implies local shrinkage, whereas if the value is higher than unity implies a local expansion. In DBM, all the subjects are nonlinearly registered to the template and Jacobian maps can be computed in the template space. Group statistics are computed in order to study local volumetric changes across population with the determinant of the Jacobian maps. The deformation based morphometry has notable advantages over the previously used MRI-based volumetry as it does not require a priori knowledge of the region of interest to perform the morphological analysis and it improves the statistical power of detecting significant change of the volume of the regions of interest within the limits of accuracy of the registration algorithm [Chung 2001]. However, such an analysis does not reveal the direction of volumetric change. DBM is also not well suited for statistical analysis on DTI because spatial normalization involves resampling which leads to erroneous results while characterizing volume changes.

6.2.2 Voxel based morphometry

At the heart of voxel-based morphometry lies the simple idea of voxel-wise comparison across a population of subjects in order to reveal local changes in the grey matter intensities between groups of patients. In VBM, MRI data is spatially normalized to the same template space using nonlinear registration. The quality of the template is also important for VBM: it should be based on a large population and should have a reasonably high resolution (typically anisotropic resolution of 0.5 to 1 mm). It should be noted that the the spatial normalization is not exact and it merely corrects the global brain shape differences only. In contrast to DBM where the group statistics is carried out on the determinant of the Jacobians, in VBM voxel-wise analysis is carried out on the image intensities.

6.2.3 Tract based spatial statistics

Tract based spatial statistics or TBSS is a more recent techniques compared than the above two. TBSS is specifically used in the case of diffusion MRI in contrast to the above two methods. As discussed in section 3.6.1, fractional anisotropy (FA) quantifies the directional strength of white matter tracts. The FA images can be used for voxelwise statistical analysis in order to quantify changes in white matter tract integrity. In TBSS, the diffusion weighted images are first corrected for eddy current distortion and bulk head motion followed by tensor estimation. The FA images are computed from the DTIs. For the spatial normalization, the TBSS suggest either to use a predefined target image (for example, FMRIB158_FA) or use the most central (or most representative)

subject as the target image. For the second method, every image in the dataset is nonlinearly registered with every other image. Thus, if there are n subjects, it will require n^2 registrations. For a large dateset as the one presented in this study with 192 subjects, the second method is computationally challenging. For such scenarios, it is recommended to use the earlier method, that is to normalized all the FA images to a standard template. The mean FA is computed and is *skeletonised* to only contain the most central white matter tracts. Ideally, these skeleton tracts represent the most central tract in a white matter fiber bundle.

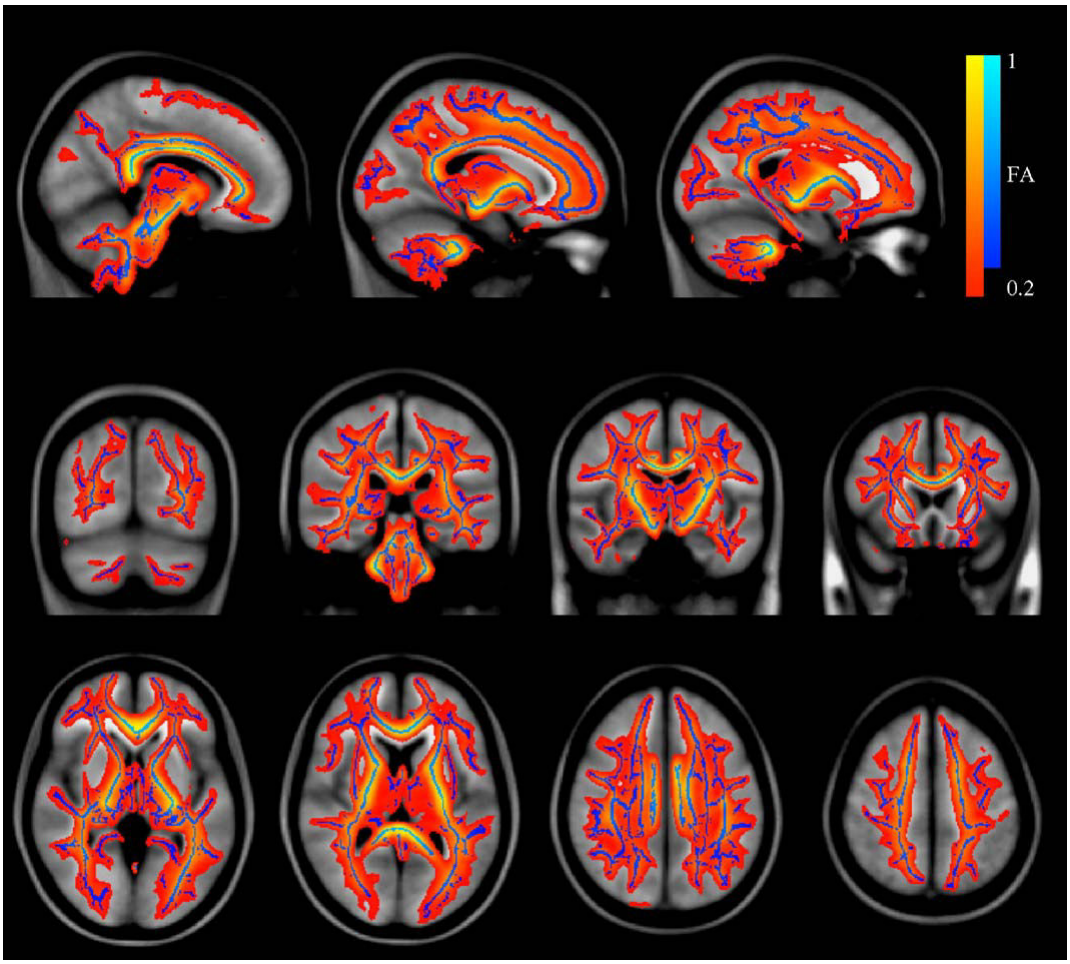

Figure 6.1: An example of mean FA map (red-yellow), overlayed on top of a MNI152 atlas along with the white matter skeleton (blue) [Smith 2006]

The skeleton is projected on all the normalized FA images. The FA skeleton is thresholded at a FA value of 0.2. The authors [Smith 2006] argue that this kind of analysis on the FA skeleton overcomes the misalignment issues that might have happened during the registration. Moreover it considerably reduces the multiple

comparison problem as one focuses only on the voxels belonging to the white matter skeleton and not on all the voxels of the white matter. The skeleton projection step is is followed by a voxel-wise statistics using permutation methods (also known as randomisation methods) on the white matter skeleton. FSL's *randomise* tool is used for the voxel-wise statistics with 5000 random permutations.

This is the most general workflow that is followed for TBSS analysis. Some of the short comings of the method have been a topic of discussion in few recent articles [Groot 2013, Schwarz 2014, Bach 2014].

A recent study compared two ROI based methods for exploratory statistical analysis on white matter tracts of typical specific language impairment in children [Vallée 2014]. The authors created a unbiased population specific DTI template using the method described in [Guimond 2000]. The template is aligned with the Catani's atlas [Catani 2008] for getting the ROI definition. Tractography was performed on each aligned DTI. Two different statistical analysis were carried out on the data. The first one is by comparing the mean FA and ADC values inside the ROIs defined in the Catani's atlas and the second one is by comparing the mean FA and ADC inside the ROIs created by taking the envelope of fiber tracts. We tried an approach similar to the first ROI approach presented by [Vallée 2014]. However, we were not able to detect any statistically significant differences between the controls and the patients. Given that the DTIs have low SNR and spatial resolution, we think that the averaging of FA values over a ROI might lead to loss in statistical power. Thus, the inability to detect any significant difference.

6.2.4 Comparing white matter fiber tracts

The white matter fiber tracts can be compared using the different features such as shape, scale, orientation and position. In [Mani 2010], the authors proposed a Riemannian framework for a joint analysis of these features. For each combination of features, the authors suggest a formula for the geodesics distance between two set of fibers. Though, the method was used for clustering fiber tracts, we think this method can also be used for a statistical comparison of features between two groups of subjects. However, the meaning of such feature differences in the clinical context is less understood and appropriate measure should be taken to correlate the shape features with the DTI metrics used commonly in clinical practice like FA, ADC and MD.

6.3 Data and study design

6.3.1 Background of study design: NEURADAPT

The NEURADAPT study was designed to investigate the prevalance of patients with HIV associated neurocognitive disorders (HAND) among HIV-1 infected

patients, HIV-1 being one of the two sub-types of the HIV disease. The HIV-1 patients were followed in the Nice University Hospital [Vassallo 2013]. The authors studied the effects of microbial translocation lipopolysaccharide (LPS) among HAND patients. The LPS is suspected to trigger monocyte[1] activation and facilitate the penetration of the infected cells into the brain leading to neurocognitive disorders. The goal was to investigate the LPS plasma levels as a possible biomarker for screening patients with mild neurocognitive impairment.

In the study, 322 subjects out of 1,963 were randomly selected and among them 256 patients provided informed consent. Every patient was required to go through a variety of neuropsychological (NP) tests. The subjects were tested on a variety of cognitive domains: learning and recall episodic memories, attention/concentration, working memory, executive functions, language, visual agnosia and motor/psychomotor speed. The NP scores were transformed into Z-scores and were adjusted for age, gender and years of education using standarised norms. Following the NP test results the subjects were divided into two groups, one with HAND and the other without HAND. The study concluded that LPS levels are associated with HAND only among the hepatities C virus (HCV) positive groups.

In a followup study on the same cohort [Vassallo 2014], the authors studied longitudinal changes in the NP test results. The latter study presents the results of similar NP test as carried out in [Vassallo 2013] after two years. Combination antiretroviral therapy (cART) refers to the combination of medications that are used to keep the HIV infections under control. The article investigates if the high central nervous system penetrating antiretroviral therapy prevent the onset of HAND. Out of the 256 patients, 96 agreed for the NP follow-up testing. For this particular study, the cohort was subdivided into five categories: normal controls, neuropsychological deficit (one impaired cognitive domain), asymptomatic neurocognitive disorders or ANI (abnormality in two or more cognitive abilities), mild neurocognitive disorder or MND (cognitive impairment with mild functional impairment) and HIV-associated dementia or HAD (marked cognitive and functional impairment). The article discusses in detail the effect of cART on the neurocognitive impairment among these subgroups. The subgroups are important in order to track the number of patients moving from one to the other in terms of the NP scores. In the study, the CSF drug concentration penetration effectiveness (CPE) scored were recorded along with the demographic and background information. It was concluded that HAND patients with lower CPE scores are at higher risk of increasing cognitive impairment.

[1] a large, circulating white blood cell, formed in bone marrow and in the spleen, that ingests large foreign particles and cell debris.

6.3.2 Rational behind DTI based statistical study

Both the above mentioned studies were based on neuropscychological test scores. The latter tracks the changes in the NP scores over a period of 2 years (from 2009 to 2011). As mentioned in section 6.1, several studies in the past have shown changes in white matter tract integrity and associated the changes with neurocognitive disorders. The motivation behind the statistical DTI study is to design a robust statistical workflow for localizing the changes in the white matter tracts among HAND patients with respect to controls. The localization of changes in the white matter tracts can be correlated with cognitive impairment and loss of motor control observed among the test subjects. It would have been interesting to track these changes and study the deterioration of the WM tract integrity across time. But unfortunately, the DTI data was only available at one time point.

The data are collected under the NEURADAPT initiative at the University of Nice Hospital, France. The diffusion weighted images are acquired with a b-value of 700 s/mm^2, using a GE 1.5 Tesla scanner. One B0 (undiffused image) and diffusion weighted images (DWIs) with 23 gradient directions were acquired. The DWIs has $256 \times 256 \times 28$ voxels of size $0.9375 \times 0.9375 \times 5.5$ mm^3. One anatomical high resolution T1-weighted image is also acquired. The subjects are divided into two groups, controls and HAND patients. There are 18 controls and 174 HAND subjects. The patients are further subdivided into five subgroups based on the level of neuro-cognitive disorder as mentioned earlier.

6.4 Proposed Workflow

The dicom images are extracted using the mricron software [Rorden 2008]. The images are extracted in the Nifti image format. The diffusion images are corrected for head motion for the eddy-current distortion using the FSL's *eddy_correct* tool. The anatomical T1 image is corrected for intensity bias using the tool provided with ANTs [Tustison 2010]. The T1 images are then skull-stripped using ROBEX [Iglesias 2011].

For each subject, the B0 image is rigidly registered with the T1 image after intensity bias correction. The skull stripped T1 images are then affinely registered with that of the template T1 image. The two registrations are then combined and all the diffusion images are resampled with the combined transformation using b-spline interpolation. The diffusion tensor images are estimated using the log-Euclidean tensor estimation algorithm [Fillard 2007]. The DTI for each subject is then registered nonlinearly to the template DTI using the log-domain diffeomorphic diffusion tensor image registration [Sweet 2010].

Once the tensor images are registered nonlinearly to the template space. The mean tensor image is computed using the log-Euclidean framework and subsequently the

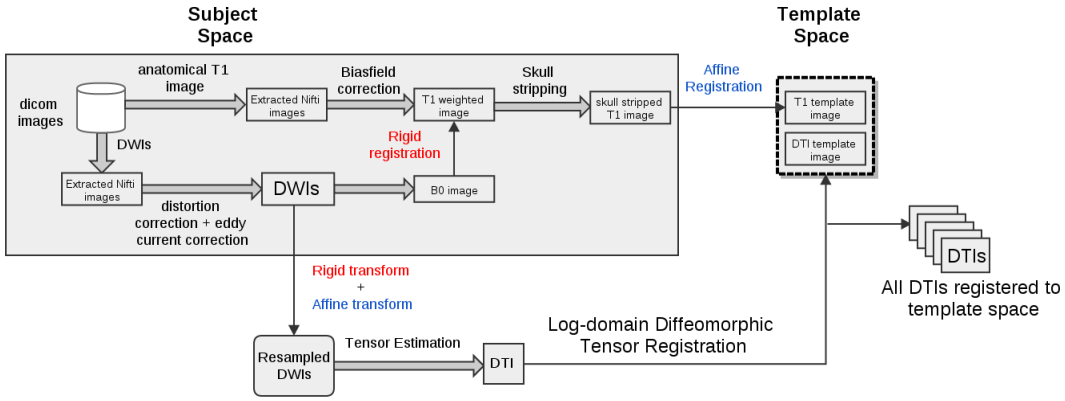

Figure 6.2: Workflow for processing the diffusion images for the TBSS

mean FA image is computed. The white matter skeleton is computed using the FSL's *tbss_skeleton* tool. The skeleton represents the voxels belonging to the central line of the white matter tracts. The figure 6.3 shows the white matter skeleton overlayed on the FA image. A binary skeleton mask is created by thresholding the FA value at 0.2. Voxelwise statistics is carried out on this mask.

6.5 Results

6.5.1 Results on traditional TBSS

In the figure 6.4 the results of a standard TBSS operation described in 6.2.3 is shown. The actual voxel wise results are included in the appendix B. Here and in all the subsequent figures the results are thickened in order to make the visualisation easy. The stat image is thresholded at 0.95 which corresponds to a p-value of 0.05 and thickened using FSL's *tbss_fill* script. For an anatomical reference the white matter skeleton (in green) is overlayed on the mean FA image. The regions in red-yellow show the areas with significant differences (at 5% significance level). It was found that using the standard procedure, there are notable differences in the left and right superior corona-radiata. The corona-radiata is a set of projection fibers[2] and is composed of ascending sensory fibers and descending motor fibers. A small section of corpus callosum also shows significant difference. It is known from earlier studies and in the NEURADAPT study as mentioned in section 6.1 that the HIV patients also show signs of compromised motor skills. However, changes

[2]Projection fibers are the fibers uniting the cortex with the lower parts of the brain and the spinal cord.

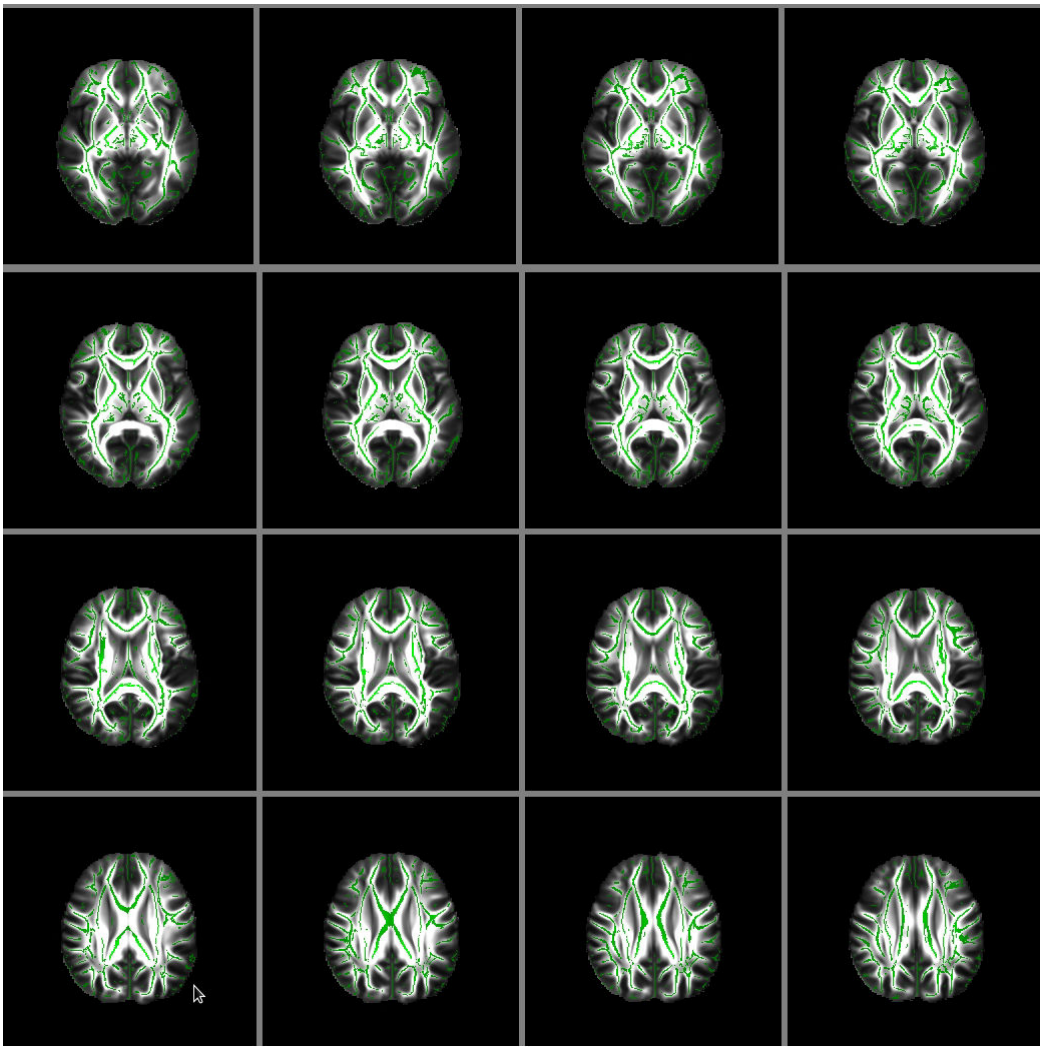

Figure 6.3: White matter skeleton (green) overlayed on the mean fractional anisotropy (FA) image.

in the different regions of brain due to HIV are not only limited to corona radiata as found in other studies discussed in section 6.1.

6.5.2 Results on TBSS using DTI based registration

After the affine alignment of the subject DTI with that of the template, further nonlinear registration can be either computed using the scalar FA images or using a tensor based registration. The usual workflow in the FSL suggests a nonlinear FA based registration using FNIRT. However, in a recent study conducted by [Bach 2014], the authors suggest that a tensor based registration can greatly improve the statistical significance of the results. For the DTI registration,

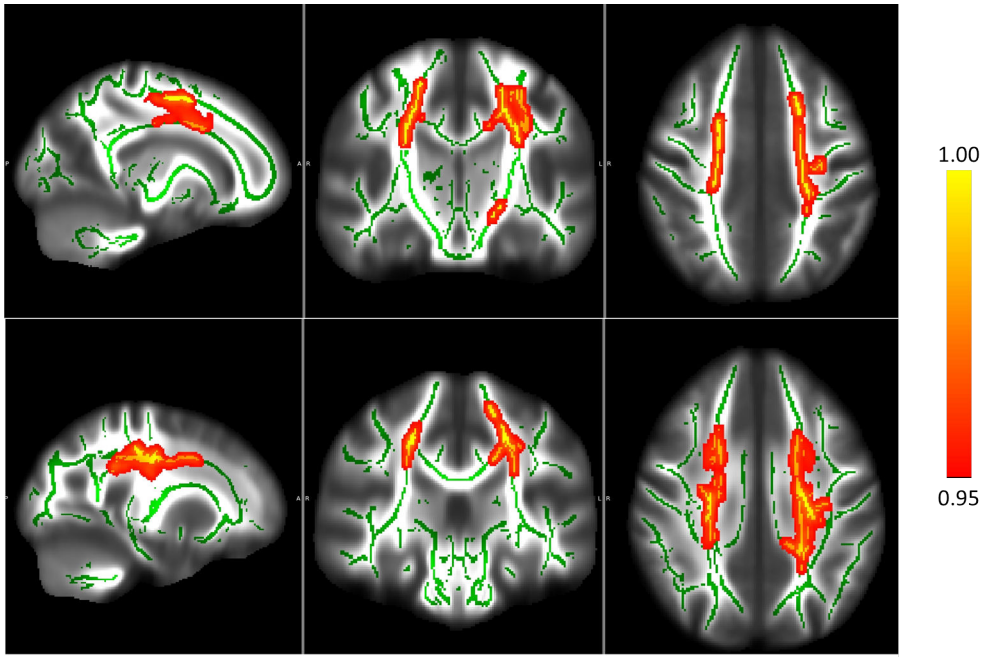

Figure 6.4: The red-yellow sections show the regions with statistically significant difference between the controls and the HAND patients. Green shows the white matter tract skeleton. The test statistic values are thresholded at 0.95 for the ease of display which corresponds to 5% significance test. The significant regions are thickend for better visualization (see appendix B for exact results.)

the in-house developed log-domain diffeomorphic tensor registration algorithm [Sweet 2010] was used. It was found that with the tensor based registration, it was possible to detect more regions of statistically significant difference between the controls and the patients. The tensor registration being used also is a much more appropriate method for nonlinear alignment, as the directionality information is not lost as in the case of scalar FA images. As we will see later in the following chapter that a tensor based nonlinear alignment also leaves the room for a multivariate statistical analysis contrary to the univariate analysis conducted on the FA images in TBSS.

With the FA based registration, a lot of potential information pertaining to the orientation of the tensors contained in the DTI data is lost. Contrarily to the FA registration discussed above, a DTI based nonlinear registration is carried out using the log-demons diffeomorphic tensor registration. The FA values are computed after the DTI normalization and once again the groups are compared using the FSL's *randomise* tool with 5000 random permutations. As expected with this technique, it is possible to detect the differences in many more regions. The regions with statistically significant differences are shown in figure 6.5 in red-yellow.

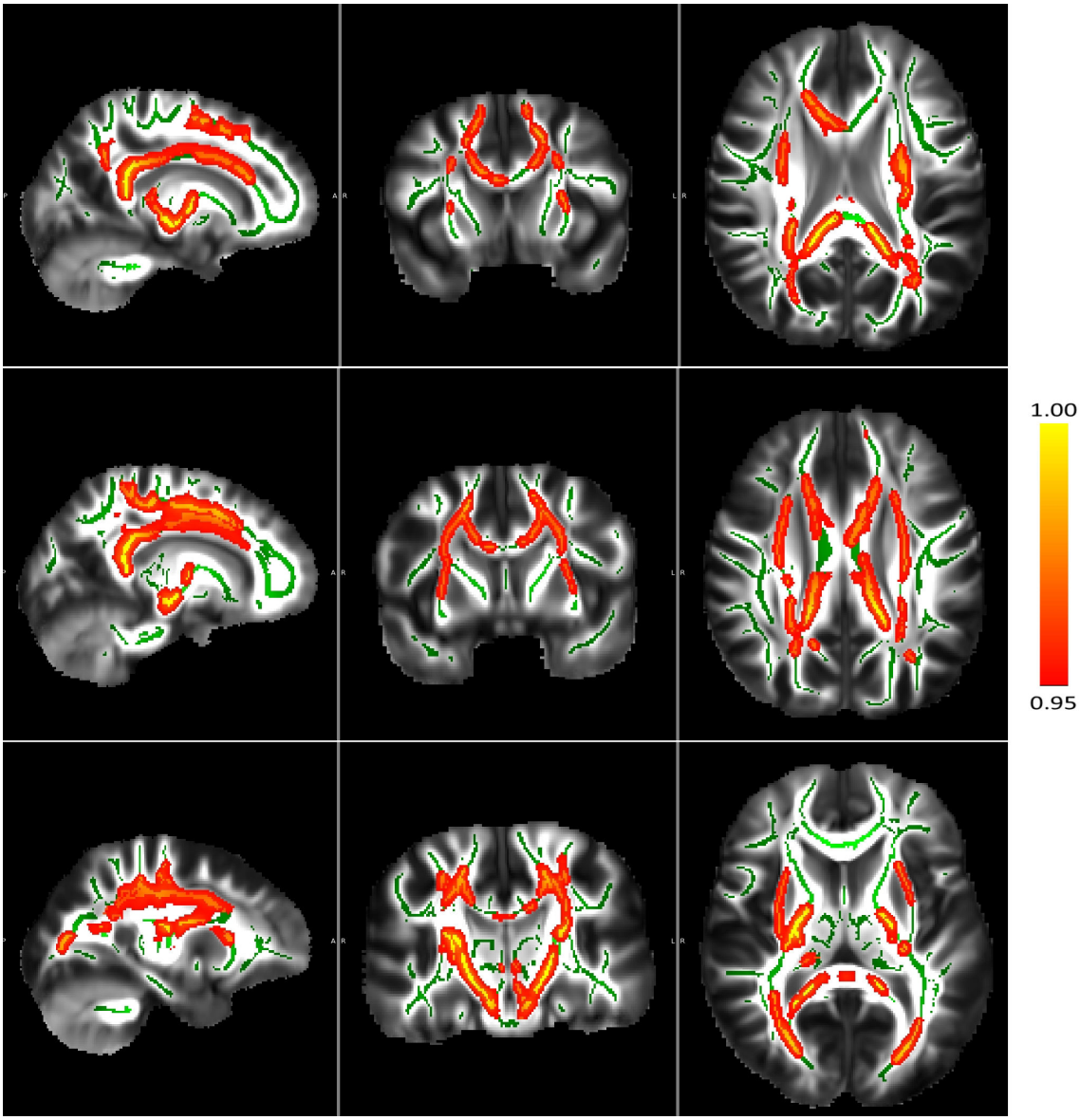

Figure 6.5: TBSS using DTI based registration. White matter tract skeleton is shown in green. The red-yellow sections of the skeleton are the ones with statistically significant differences, i.e., with a p-value < 0.05

In the figure 6.5, notable differences are observed in the splenium and body of corpus callosum, left and right cerebral peduncle and both external capsules along with left and right corona radiata. Thus, a likely conclusion can be drawn that a tensor based registration is more appropriate for TBSS.

6.5.3 Univariate and multivariate hypothesis testing

In the previous sections, it was shown that tensor registration, when used for DTI normalization provides better results. Better in the sense that it is possible to detect differences in many different regions of the brain which were undetectable with the standard TBSS procedures. In the last step of TBSS, the voxelwise statistics is carried out using a non-parametric permutation test. The details of the permutations test are often hidden from the user as it is pretty much an automated process. However, the user has a choice to choose a number of parameters including the number of permutations required to estimate the distribution. A detailed understanding of parameters requires an involved study and users are often advised to go with the recommended setting. The tool is only suited for univariate statistical analysis. But, the idea is to to present a multivariate statistics which uses the whole tensor information. In the following sections a detailed description of the statistical test setup is produced. The tests are first carried out on the FA images and then extended to full tensor.

Univariate hypothesis testing

The $\mathbf{FA_1}$ and $\mathbf{FA_2}$ denote the FA values of the two groups respectively. The FA values are a vector of values on each subject along the white matter skeleton. The groupwise test is carried out on each voxel along the skeleton. The two sample t-test is used to detect the group differences, on the assumption that the FA values in the two groups follow a normal distribution. However, such an assumption on the normal distribution may not be correct because of a variety of reasons. First, the diffusion weighted images have an underlying Rician distribution. Secondly, the FA values, the DWI acquisition and the diffusion tensor has a nonlinear relationship between them. If the Gaussianity assumption does not hold, the results of statistical test (two sample t-test in our case) could be unreliable. Thus, it is wise to choose a non-parametric statistical test, which make no assumption about the probability distribution of the data under consideration. Permutation test is one such non-parametric test and the following tests are done using the same spirit. In the permutation test framework, the null and alternate hypotheses are set up as

$$H_0 = \mathbf{FA_1} \overset{d}{=} \mathbf{FA_2} \; ; H_1 = \mathbf{FA_1} \overset{d}{\neq} \mathbf{FA_2} \tag{6.1}$$

where $\overset{d}{=}$ and $\overset{d}{\neq}$ denotes "equal in distribution" and "not in equal distribution". A multivariate test was introduced in [Baringhaus 2004]. The authors suggest a test statistic based on the sum of all Euclidean interpoint distances between the variables (FA values) from the two different groups and one-half of the two corresponding sums of distances of the variables within the same group. The corresponding proofs

are discussed in the above article. Thus, the test-statistic is as follows,

$$T_{n_1,n_2} = \frac{n_1 n_2}{n_1+n_2}\Bigg[\frac{1}{n_1 n_2}\sum_{i=1}^{n_1}\sum_{j=1}^{n_2}||X_i - Y_j|| - \frac{1}{2n_1^2}\sum_{i=1}^{n_1}\sum_{j=1}^{n_1}||X_i - X_j|| - \frac{1}{2n_2^2}\sum_{i=1}^{n_2}\sum_{j=1}^{n_2}||Y_i - Y_j||\Bigg], \quad (6.2)$$

where $||.||$ is the Euclidean distance. The T_{n_1,n_2} is not distribution free. The authors suggest bootstrapping to obtain the critical values. In the article [Baringhaus 2004], the authors show that the Cramer's test proposed shows power performance comparable to that of Hotelling-T^2 test. An implementation of the Cramer's test is available with the R-package. For the permutation tests, the sample space is the of the order of $(n_1 + n_2)!$. For a large dataset as ours it is not possible to explore the whole permutation space because of computational reasons. For the particular analysis, 5000 random permutations are chosen.

In the figure 6.6 it can be seen that the results of the univariate statistical analysis using the Cramer's test designed in this section is comparable to that of the permutation test offered within the TBSS framework. In the following section the Cramer's test will be used for the multivariate statistical analysis.

Multivariate hypothesis testing

In the previous section, we did a univariate hypothesis testing on the FA values. However, FA being a scalar quantity, we loose the directionality information of the diffusion tensor. In this section we will discuss three different multivariate tests on the NEURADAPT dataset. For the multivariate analysis, I will use the same Cramer's test as described in the previous section. I will show that using the multivariate test, it was possible to detect changes in white matter tracts which were previously undetected using the univariate hypothesis testing using the scalar FA images. For the multivariate hypothesis testing, the tensor is arranged in a vector form as follows

$$\mathbf{D} = [D_{xx} \;\; D_{yy} \;\; D_{zz} \;\; D_{xy} \;\; D_{yz} \;\; D_{zx}] \quad (6.3)$$

where the subscript represent the position of the elements in the diffusion tensor $\mathbf{D}$. One of the easiest way to do a multivariate analysis on the individual elements of the diffusion tensor and then combine the p-values using a combining function. For such an analysis the null and the alternative hypothesis for each univariate analysis of the individual elements is set up as in the previous section and the p-values are computed. Then the p-values are combined using the Fisher-Omnibus combination function [Fisher 1925]. The function is defined as,

$$X_{2k}^2 \sim -2\sum_{i=1}^{k} log(p_i), \quad (6.4)$$

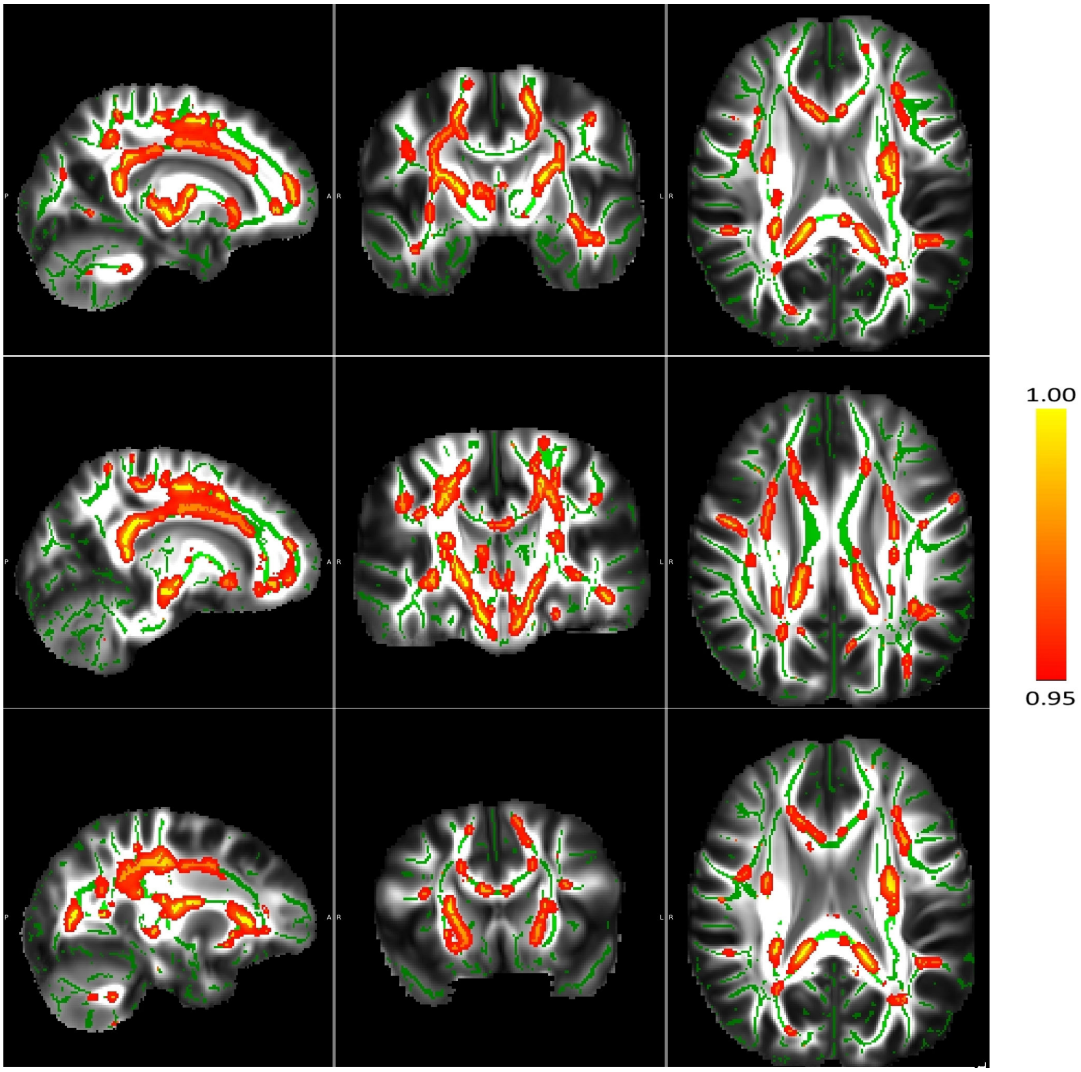

Figure 6.6: Univariate statistical analysis on the FA values after nonlinear tensor based registration.

where X^2 is the test statistic and p_i is the p-value corresponding to the i^{th} univariate test and k is the number of tests being combined (in our case, $k = 6$ corresponding to the number of diffusion elements).

However, for the multivariate test using the full tensor information, the multivariate vector has been constructed from the unique six entries of the diffusion tensor. Two different form of the vector could be used for the multivariate analysis. As suggested in [Arsigny 2006b] a rotationally invariant Euclidean metric vector form of the diffusion tensor could be constructed by applying weights to the off-diagonal

terms as

$$\mathbf{D} = [D_{xx} \;\; D_{yy} \;\; D_{zz} \;\; \sqrt{2}D_{xy} \;\; \sqrt{2}D_{yz} \;\; \sqrt{2}D_{zx}] \tag{6.5}$$

Similarly, a log-Euclidean metric form can also be defined as,

$$\mathbf{L} = [L_{xx} \;\; L_{yy} \;\; L_{zz} \;\; \sqrt{2}L_{xy} \;\; \sqrt{2}L_{yz} \;\; \sqrt{2}L_{zx}] \tag{6.6}$$

where $\mathbf{L} = \mathrm{Log}(\mathbf{D})$, is the matrix logarithm of the diffusion tensor D. Contrary to univariate analysis, a vectorial form of the test-statistic is defined

$$T_{n_1,n_2} = \frac{n_1 n_2}{n_1 + n_2}\left[\frac{1}{n_1 n_2}\sum_{i=1}^{n_1}\sum_{j=1}^{n_2}||\mathbf{V_{1,i}} - \mathbf{V_{2,j}}|| - \frac{1}{2n_1^2}\sum_{i=1}^{n_1}\sum_{j=1}^{n_1}||\mathbf{V_{1,i}} - \mathbf{V_{1,j}}|| - \frac{1}{2n_2^2}\sum_{i=1}^{n_2}\sum_{j=1}^{n_2}||\mathbf{V_{2,i}} - \mathbf{V_{2,j}}||\right] \tag{6.7}$$

where $\mathbf{V}$ is either $\mathbf{D}$ or $\mathbf{L}$ depending on whether Euclidean or log-Euclidean metric is being used as a test-statistic. The subscripts 1 and 2 represent the two groups under consideration.

6.6 Comparison of the univariate and multivariate analysis

The multivariate analysis makes use of the full tensor information for statistical analysis. The multivariate approach is shown to have a higher specificity and sensitivity to the statistical tests [Schwarz 2014]. The statistic images shown in this chapter are thickened around the areas of statistical difference for ease of visualization. In case of multivariate analysis, it is possible to use either the Euclidean or the log-Euclidean metric for the analysis. The figure 6.7 shows the results of the statistics carried out using the log-Euclidean metric.

For the sake of comparison, the univariate results (blue-deepblue) are overlayed on top of the multivariate statistical results (red-yellow). As expected the latter has a higher detection power. The above argument is supported using the p-value image presented in figure 6.9. In this figure, it can be seen that it is possible to detect more differences in the multivariate analysis. The statistical differences in the association fibers were not detectable in the univariate analysis, but are distinctly visible in the latter. A similar image (figure 6.10) also shows an enhanced detection when the log-Euclidean versus Euclidean metric is used. With all these results, it is possible to deduce that the multivariate analysis using the log-Euclidean metric is more suited for the problem at hand.

6.7 Conclusions and clinical perspectives

In this chapter, we have shown that if the diffusion tensor images are normalized using a tensor based registration technique as opposed to the FA based regis-

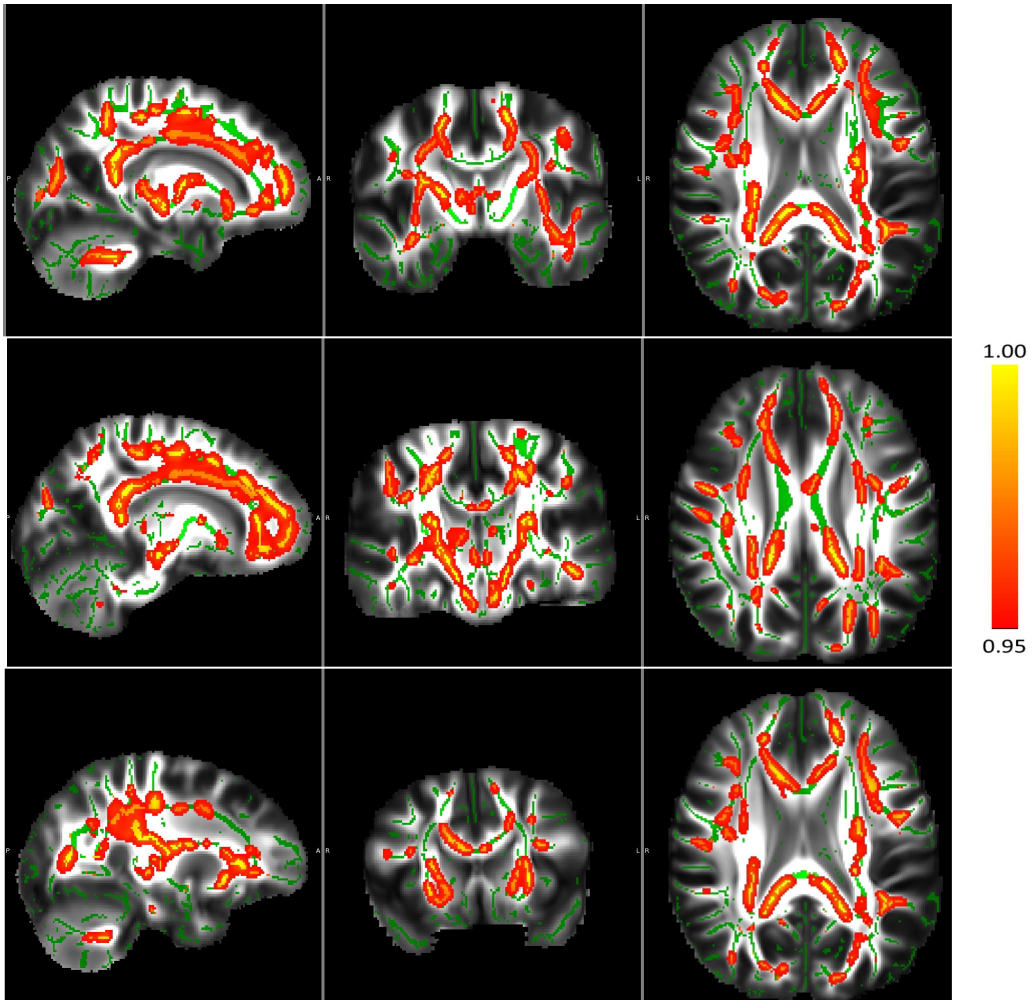

Figure 6.7: Results from multivariate statistical test using the log-Euclidean metric.

tration methods usually followed in the standard tract based spatial statistics. Tensor based normalization also allows for multivariate statistics on full tensor information. We showed that the multivariate statistics shows more regions of statically significant differences compared to the univariate statistics. With the standard TBSS routines, it was only possible to detect significant differences in the left and right superior corona-radiata. However, previous studies have suggested significant differences in the corpus callosum and other white matter regions of the brain. A difference in the corona-radiata regions explains the compromised motor skills of the HIV patients, but the HIV cohort also showed signs of impaired recall and working memory, motor skills, attention/concentration and speed of information processing. All of these impairments cannot be solely related to corona radiata. So, it is possible that a traditional TBSS is not sufficient to detect all the statistical differences in white matter tracts. However, with the suggested DTI normalization and multivariate statistics, it was possible to detect the differences

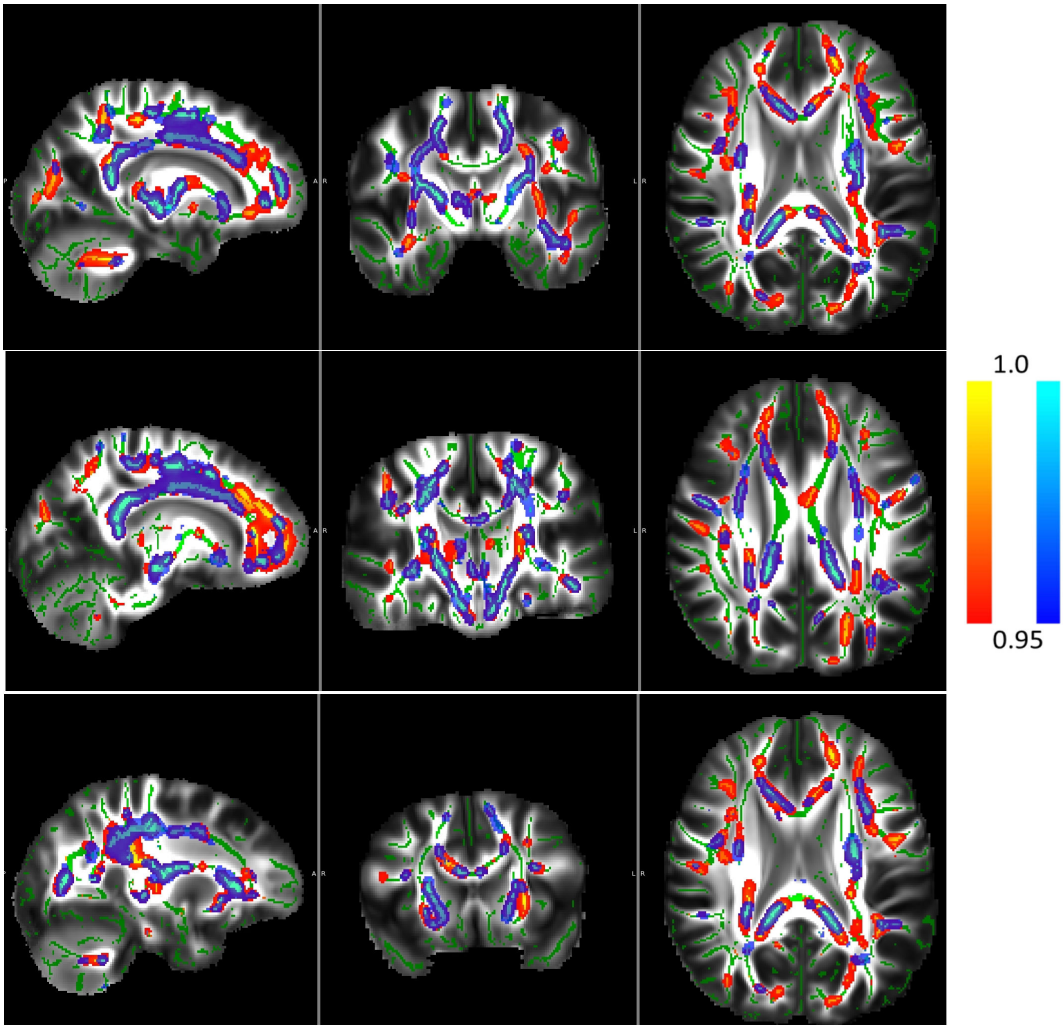

Figure 6.8: Comparison of univariate and multivariate analysis. The univariate statistics is overlayed on top of the statistical results obtained from multivariate statistics. The sections in blue-deepblue show univariate and the sections in red-yellow show the results on the multivariate analysis. It is clear that multivariate analysis can detect more regions of difference between controls and HAND subjects.

in different regions of the brain which account for the brain impairments reported by [Vassallo 2013]. The findings are also in accordance with the state of the art literature.

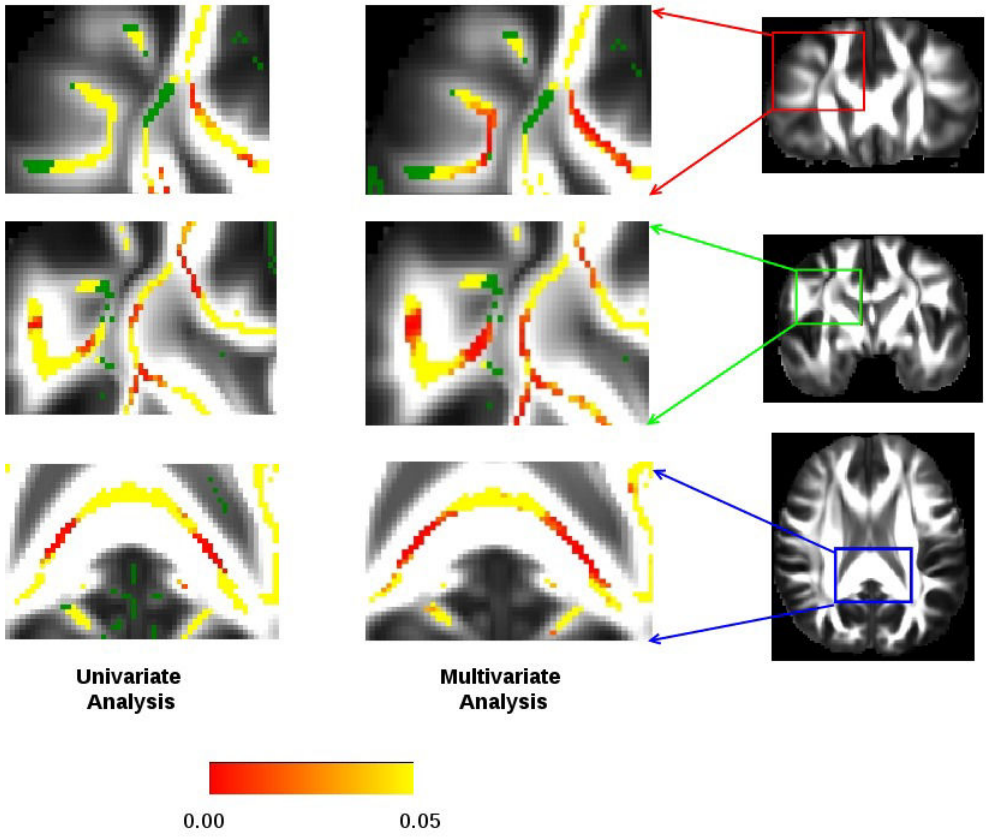

Figure 6.9: A comparison of the univariate FA (left column) and multivariate tensor (right column) statistical analysis. On the right column, one can see that it is possible to detect more regions of significant difference between the contols and the patients at a 5% significance level.

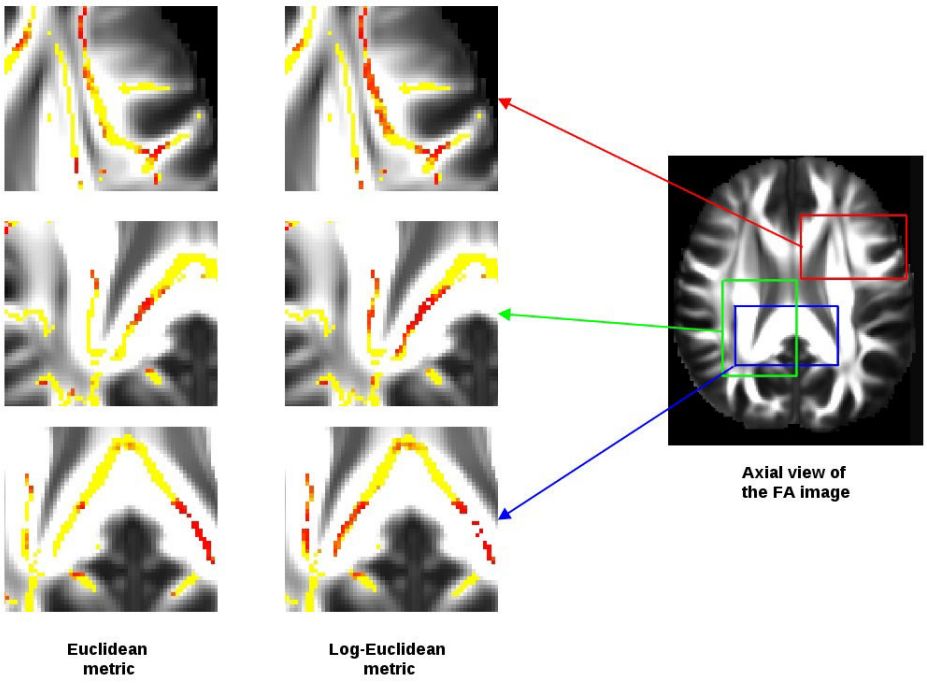

Figure 6.10: Comparison of multivariate statistical analysis using the Euclidean and the log-Euclidean metric. The log-Euclidean metric can detect more regions of statistical significant differences between the controls and the patients.

Chapter 7

Conclusions and Perspectives

Contents

7.1 Conclusions

The thesis presents several workflows created for addressing specific problems pertaining to the clinical DTI study conducted within the NEURADAPT study. Chapter 2 of the thesis give the necessary background information about the anatomy of brain, the structure, organization and function of white matter tracts in the brain. An understanding of the brain anatomy is crucial for correlating the statistical results. This is followed by a chapter discussing the physics behind MR imaging protocols. We discussed in detail the pros and cons of some of the common imaging protocols being used in clinics on a regular basis. We also discussed how the different protocols can be combined based on the specific needs. These two chapters cover most of the background information for the thesis.

In this thesis, we have proposed a new method for improving the resolution of clinical quality brain diffusion tensor images from single diffusion MRI acquisition. The low resolution diffusion images suffer from partial volume effects, which lead to underestimated diffusion tensors. The method build on the variational formulation for joint estimation and denoising of DTIs proposed by [Fillard 2007]. We assumed that the signal observed in a low-resolution diffusion image is a weighted average of the signals that would have been observed for a higher resolution image. With no other information, an infinite number of solutions are possible. Of course not all of them have any physical meaning with regards to diffusion tensor. The tensor estimation being an ill-posed problem, we used an anisotropic regularization prior to better constraint our solution space. We showed that the proposed method produces fractional anisotropy images which are better contrasted than the ones which are obtained using tensor resampling. We proved through tractography results that the super-resolution algorithm produced more consistent fiber tracts compared to the ones produced by tensor resampling. We showed the tractography

improvement in the fornix region of the brain which is known to suffer from partial volume effects because of close proximity to the ventricles.

The human brain's shape and size varies across population and also with time. In order to understand this variability, various atlases were computed. A small history of these atlases was presented in the thesis to give an overview of the developments in the field of brain imaging, in order to understand how we have come far in the field from developing an atlas from a single subject to an atlas comprised of hundreds of subject. There are standard atlases that exists and are *off-the-shelf* tools for doing statistical study on a given population. However, choosing such atlases may often lead to a bias in the statistical results. For example, if the study is being conducted on infant brains, using an ICBM atlas is definitely not a good idea. Doing so, will involve unnecessary stretching of each of the subject brains to match the atlas during subject normalization. These extreme deformations may bias the statistical study. So, there is a need for a population specific atlas. Such an atlas will also be a statistical representative of the population. We used an existing tool to compute the brain template for the NEURADAPT study.

The need for a population specific atlas is well understood and discussed in detail in Chapter 5. However, so far most of the atlases were developed using the anatomical T1-weighted image. The main reason for this is that the T1-weighted images are highly detailed making it easier to register compared to the diffusion tensor images. So, far there were not so many DTI atlases except the ICBM-DWI atlas (which is also a very low resolution). The other problem is that the T1-template and the DTI template occupy different geometric spaces. Because of this mismatch it was not possible to study both the modalities together. It was found that a joint T1 and DTI study may increase the statistical power of the analysis. We presented a workflow for producing a joint T1 and DTI template. The template can be used for voxelwise comparison between the two modalities. Although, the template was generated for the NEURADAPT study, the workflow can be utilised for any given dataset.

For ROI based statistics, it is important to have a segmentation of white matter regions in the brain. These ROI segmentation is performed manually by experts. The process can be expensive, time consuming and often error-prone. Often, experts differ on the accuracy of the segmented regions too. We have developed a workflow for generating a probabilistic white matter atlas with each region of white matter having a probabilistic delineation. Thus a user could choose based on the problem how conservative he or she wants to be in terms of ROI selection for statistical analysis. We also believe that in the future such probabilistic maps can be used to aid manual segmentation.

The DTI template developed in the previous chapter is used for tract based spatial statistics (TBSS) for detecting statistical changes in white matter tracts

between controls and patients. We suggested changes that can be made in the traditional TBSS framework to improve the statistical power of the tests. Using the method suggested in chapter 6 it was possible to detect changes in white matter tracts which were otherwise not detectable using the native TBSS routines. The traditional framework for TBSS uses scalar fractional anisotropy (FA) images for spatial normalization of images. The FA being a scalar metric obtained from the diffusion tensor discards all the directional information. Instead of FA based normalization on a pre-defined template, we used the population specific DTI template as the target space for spatial normalization. Another difference is that the FA based normalization is replaced with the log-domain diffeomorphic tensor registration. This DTI normalization technique allows us to retain the full tensor information in the template space and make voxelwise comparison on the whole tensor using multivariate statistical tests. On the other hand in traditional TBSS such multivariate analysis is not possible because of the FA-based normalization. We compared the results of univariate and multivariate analysis and we can say that the multivariate analysis wins against the univariate analysis in terms of statistical power. The differences were shown in figures 6.8 and 6.9.

The results from TBSS were correlated with the neuropsychological (NP) test scores. It was found that with the traditions TBSS we could detect changes in the corona-radiata, which are related to compromised motor skills. But the HIV/AIDS patient suffer not only from compromised motor skill but dementia, working and episodic memory, attention/concentration, executive functions, language related functions and visual agnosia. Clearly, the cause for compromised behavior in the latter functions and changes in the white matter tract integrity cannot be correlated by using the *off-the-shelf* TBSS routines. However, the modified TBSS coupled with the multivariate analysis could do so.

One might ask the question, why we did not use the super-resolution algorithm developed in chapter 4 during the statistical analysis of the NEURADAPT dataset. As we will see that the proposed algorithm performs well and provides significantly better tensor estimation and tractography results when the data is upsampled by a factor of two. However, the DTI data in the NEURADAPT study has a resolution of $0.9375 \times 0.9375 \times 5.5$ mm^3. The voxels are too big in the z direction and there is just not enough information for the super-resolution algorithm to enhance the quality of the data.

Another reason for not choosing the super-resolution algorithm was the tool used for statistical analysis. We chose to use tract-based spatial statistics (TBSS) methods for comparing the controls and HIV patients. In TBSS, the white matter tracts are skeletonised to a single voxel. The skeleton represents the mid-line of a given tract. A TBSS study conducted on high resolution (smaller voxel size) images looses statistical power as we increase the resolution. An increasingly higher percentage of information is discarded during the skeletonization step. For

example, if there are images with an isotropic voxel size of 2 mm, the volume of a single voxel will be 8 mm^3. Just by increasing the resolution by a factor of 2, the volume of the single voxel will be reduced to 1 mm^3. So, we loose 87.5 % of information per voxel. Thus, it is better to avoid super-resolution algorithms for TBSS type methods.

The NEURADAPT study aims to study the prevalence of patients with HIV associated neurocognitive disorders (HAND) among HIV-1 infected patients. The goal was also to study the effect of microbial translocation of lipopolysaccharide (LPS) among the HAND patients and use the LPS levels as a possible biomarker for screening patients with HAND. It was also found that the combination antiretroviral therapy (cART) can be used to keep the HIV infections under control. So, far in the study the effects of cART were evaluated based on the NP test scores. However, the possibility to see the changes in affected white matter tracts and track the changes over time opens new possibilities for a quantitative measure for evaluating the effects of cART on HAND subjects.

7.2 Failed quests

In this section, I am going to discuss some of the problems we tried to work on but could not get any conclusive result. However, we feel that it is important to point out the reasons for no conclusive results in order to lay a strong foundation for future research in similar directions.

Longitudinal DTI study

Disease progression over time can be evaluated using nonlinear deformation of images. Most of the longitudinal studies involve deformation based morphometry (DBM) on the anatomical T1-weighted images. However, the T1 weighted images do not contain any information about the white matter tracts. In the recent years, a large number of longitudinal DTI data has been collected by the Alzheimer's Disease Neuroimaging Initiative (ADNI). We thought that this longitudinal DTI data can be used for studying temporal deformations in white matter tracts for both subject specific and group wise statistical analysis. Few studies exist which measure the changes in the DTI parameters with respect to disease progression in the case of Alzheimer's disease [Mielke 2009, Keihaninejad 2013]. In [Mielke 2009] the authors employ region-of-interest (ROI) based analysis of target regions of the brain to detect temporal changes in the white matter (WM) regions of brain. However, the ROI based studies are often dependent on accurate delineation of the ROIs. The challenges are even more when it comes to maintaining an inter-subject and within subject consistency, because of the presence of partial volume effects which may lead to inaccurate segmentation of the ROIs. In another study [Keihaninejad 2013], an automated DTI analysis framework for tracking

longitudinal WM changes was presented. In this framework a within-subject template between two time points was generated and then a group wise atlas is created from all the subject templates. The ICBM-DTI-81 is then used to wrap the WM labels on the template image. Longitudinal statistics is then performed on the DTI scalar measures (FA, MD and RA) in selected WM regions. These methods do not use the full tensor information leading to significant loss in statistical power.

On the other end, many longitudinal studies on disease progression on Alzheimer's disease exist based on the T1 images using deformation based morphometry (DBM). The volume changes in the structure can be measured by computing the Jacobian determinant of the deformation field. One of the crucial challenges in such group-wise statistical studies is the choice of an effective registration tool. In [Lorenzi 2013], the authors have presented LCC-Demons, a computationally efficient diffeomorphic registration tool that takes into account the comparison of anatomical regions across the subject through smooth and anatomically pertinent deformations. The local correlation coefficient (LCC) used as a similarity measure in the the log-Demons registration framework [Vercauteren 2008] is robust to intensity biases. The framework also provides a numerical scheme to compute the Jacobian determinant of a deformation parameterized by stationary velocity fields (SVFs). Subject specific brain deformations can be theorized as the variation of an underlying population trend. Thus, it is interesting to study the mean deformation over a population which is essential for understanding disease progression. However, in group-wise longitudinal analysis is that the subject-specific longitudinal trajectories need to be transported to the template space through anatomically meaningful deformations. Lorenzi et. al [Lorenzi 2011] proposed a Schild's Ladder framework for effective tool to transport subject specific longitudinal deformations to a common template space.

Our idea was to merge these two modalities into a single multimodal (T1 and DTI) statistical analysis of the ADNI dataset. We hypothesized that though the T1 image contains detailed anatomical tissue information, it does not contain any information about the white matter micro-structure and its organization. Thus the deformation field in the white matter regions is not regularized and smooth making it difficult to draw any meaningful information from within the white matter ROIs. We also wanted to look at the correlation between the expansion of ventricles and shrinkage of the neighboring white matter tissues for example corpus callosum, internal capsule and fornix. We believe that such kind of multimodal studies are necessary to understand the changes in the brain associated with Alzhiemer's. Another interesting aspect of the study will be to understand the correlation between the non-linear deformation fields generated using the scalar and the DTI registrations. We also wanted to study the principal modes of deformation across the patient groups in case of Alzheimer's disease. There has been cross-sectional group studies to detect differences between controls and the Alzheimer's disease (AD) patients [Jahanshad 2014, Oishi 2011], but not a true longitudinal study

which focuses on tracking the spatio-temporal changes in the DTI data using deformation fields. As mentioned before it will be meaningful to compare the longitudinal deformations seen with the T1-weighted images and diffusion tensor image both at a subject level and group level.

Groupwise longitudinal studies involve two levels of variation within the data, one is the small intra-subject (longitudinal variations) changes and the other is the large deformations (cross-sectional changes) in the involved in the subject to template registrations. These two-levels of deformation must be meaningfully combined to make a spatio-temporal template. For the purpose of this study, we used the log-domain variant of the diffeomorphic tensor based registration [Sweet 2010] for registering the DTI and the LCC-Demons framework to register the T1 weighted images. We use the Schild's ladder framework to effectively transport the anatomical deformations from a subject specific atlas and to a group template image.

Reasons for failure

The reason why the longitudinal DTI study using the ADNI dataset did not quite work as we expected was the intra-subject DTI registration. We actually found that the deformation field obtained from this registration was too noisy to draw any meaningful inference. The ADNI DTI data was accquired using a spin-echo sequence with 3.0 T GE scanner and 41 gradient directions. The voxel-sizes are $1.36 \times 1.36 \times 2.7$ mm^3. The problem was that with the acquired data it was impossible to detect any longitudinal changes in the diffusion tensor images. Probably the artifact generated by the imaging sequence, are larger than the longitudinal signal that we are looking for. In our knowledge, we did not see any longitudinal DTI studies with the ADNI DTI dataset. Efforts should be made to incorporate faster parallel imaging MR sequences like PROPELLER (discussed in chapter 3), which are robust to motion artifacts for acquiring the data, instead of the basic spin-echo sequences. Additional efforts can be made to include motion tracking mechanisms during the MRI scan [Qin 2009]. ADNI should also provide EPI field maps along with the data. These field maps are essential for correcting for distortions due to magnetic field inhomogeneity, geometrical distortions and loss in signal in the inferior frontal and temporal regions. Presently, all the DTI scans in ADNI2 project are acquired using General Electric 3.0 T scanner and they do not have the *Field Mapping Sequence* product. So, they cannot acquire the EPI field maps. But, I think it is crucial that the EPI field maps are acquired inorder to correct the geometric distortions. In lack of the EPI field map, we tried to use the registration based susceptibility correction schemes [Huang 2008]. But, they are only approximations at the best.

7.3 Perspectives

I am going to discuss some of the short-term and long-term perspectives of the thesis in this section. It will also be an opportunity to look back in retrospect and learn from our mistakes in the past and understand what are the steps to be taken in the future for population based studies.

Short-term goals

The super-resolution algorithm presented in chapter 4 can be further modified to incorporate information from other modalities. In the chapter we suggest a method to incorporate the anatomical T1-weighted information in the tensor estimation scheme. It makes sense to exploit the boundary and tissue interface information from the T1 weighted images. Often times these tissue interfaces cannot be delineated in the diffusion images because of the low spatial resolution and partial volume effects.

We would also like to do an error analysis on the proposed tensor computation using multi-resolution acquisition. So far, the validity of the method is proven using indirect means such as tractography and error calculation on simulated low resolution images. However, to make the super-resolution algorithm really useful it should be tested using multi-resolution acquisitions of the same subject.

We discussed the multimodal atlas in 5 and the motivations behind developing such a population specific atlas in 5.2. The multimodal atlas can be used for joint statistical analysis on the T1 and DTI images. Recently, the authors in [Lao 2014] have proposed a method for combining T1 surface based morphometry and DTI based analysis on the surface of corpus callosum for a joint statistical analysis. The authors project the FA values on the surface of the corpus-callosum for a combined study. We believe that such studies can be performed on all major white matter tracts and instead of projecting the scalar FA values the full tensor can be projected for a combined multivariate statistical analysis. How to project the whole tensor on the surface of the white matter regions in a meaningful consistent manner still remains a question to be investigated.

We showed in figure 5.21 that there is a slight disagreement in the delineation of cortical boundaries done by experts. We think that a probabilistic definition will help the experts in manual segmentation. Can the probabilistic ROIs be used as a a-priori information for automatic segmentation algorithms in the future remains to be seen. Another problem that is of interest is consistent ROI segmentation across different modalities. As mentioned in [Zhang 2013], there is a need to have a consistent and meaningful delineation of cortical ROIs across different modalities. Could it be that a joint T1 and DTI atlas be a probable answer to such consistency issues across different modalities? The cortical ROIs are usually

defined on the task based fMRI or the anatomical T1-weighted images and the information regarding the white matter tracts showing connections between the different cortical areas is available with DTI. These two pieces of information need to be fused in a consistent manner for future analysis.

We suggested modifications in the traditional TBSS routines in chapter 6 through which we could detect changes in white matter regions which were not detectable before. These changes are then correlated with the NP test scores of the patients. However, there is more that can be done to improve the statistical analysis. Whether these changes add more value to the results remains to be seen. In TBSS the white matter skeleton is computed from the mean FA image by thinning down the white matter regions to the centers of the tracts. With this method, sometimes there could be discontinuities (or fault lines) in the tracts because of a sudden drop in FA along the tract. The sudden FA drops might happen for a variety of reasons for example partial volume effects, noisy DTI or registration inaccuracies. Another way to find the central tract could be to compute the actual central tract from the tractography data. The mean tract of a fiber bundle can be computed using one of the fiber similarity measures like Hausdroff distance, closest point distance or mean of the closest point distance [O'Donnell 2005, Courouge 2004]. After locating the central tracts voxel wise statistics can be computed on the voxels belonging to the tracts. With this method in place for locating the central tracts, we expect to have a contiguous representation of the tracts which also carry a deeper physical meaning.

In the TBSS analysis, the statistical analysis is done on the voxels comprising the white matter skeletons. The skeletons are computed in the template space and can be projected back on to the subject space. However, if the voxelwise statistical analysis can be performed on the subject space itself, it will be possible to avoid the resampling errors during spatial normalization. The bigger problem that exists in designing such a work flow is to maintain the voxel correspondences between the skeleton in the template space and the subject space. Because of resampling it might so happen that a single voxel in the subject space might correspond to two or three different voxels in the template space. The challenge here is to maintain consistency across the subject space in-order to ensure that anatomically consistent voxels are being compared during the statistical analysis.

Long-term goals

We have come a long way in the field of neuroimaging in the last 50 years and we have a better understanding of the human brain anatomy. There are advanced tools and required computing power for doing image registration, segmentation and statistics. We also realize that in the coming years there will be an exponential increase in digital brain images and we will need more sophisticated tools to understand and capture the variability of human brain.

Many aspects of the work presented in the thesis have the possibilities of further exploration. In particular, longitudinal DTI analysis and multimodal statistical atlases are strong contender for further research. We tried the longitudinal DTI analysis as mentioned earlier and discussed that the noisy levels in the DTI data is too high to detect any subtle spatio-temporal changes. It is important to understand the variability associated with DTI acquisition. The Parkinson's Progression Markers Initiative (PPMI) data contains several back-to-back DTI scans. With such back-to-back scans, it will be possible to evaluate the variability of DTI acquisitions and create a normative atlas from the population. I believe that such atlases are one of the major missing pieces of information required for population based DTI studies. In fact, in any future population based studies few subjects if not all should go through repeated scans, in order to construct a variability atlas specific to the population under consideration. The variability measure can be incorporated in the study for a more robust statistics. With such normative atlas it will be possible to know the normal range of the tensor values and will help the clinicians to detect any abnormal areas in the new patient specific study. It will be necessary to investigate the stability of the atlas with respect to the parameters involved in atlas construction, such as, registration methods used and type of deformations applied. Further the atlas will also help us asses the tractography quality.

With new imaging modalities and increasing number of image data being acquired every day, there is a need to develop sophisticated tools for multimodal statistical analysis. A systematic framework to fuse all these different modalities (like fMRI, MRI, T1, CT and connectivity information) is required and fusing the DTI and T1 images into one could be the first step towards this kind multimodal analysis. The biggest challenge will be to have a consistent definition of ROIs across all the modalities. The information from additional modalities will also help clinicians and neuro-anatomy experts to refine the manual segmentation.

So far we have seen a great deal of enthusiasm for acquiring longitudinal data for diseased or at-risk patients. However, I think it is important to gather more longitudinal and multimodal data on more control groups in order to study normal course of brain development through aging. Generally, in case of progressive neurodegenerative diseases like Alzheimer's, HIV or Huntington's disease to name a few, the deformations observed are a result of combined effects of aging and disease related neurodegeneration. Along with MRI, the longitudinal study should also involve extensive collection of biomaterials (blood, cells, urine etc.), NP test scores and information regarding the daily activities which might effect brain development (alcohol consumption, drug usage, food habits). This kind of data will allow hopefully in future to search for correlation between longitudinal brain degeneration observed through imaging and test samples in-order to search for possible biomarkers for the disease progression.

In the end, I would like to say that with the ever growing computing resources and novel techniques emerging in the field of "Big Data", the future of neuroimaging looks bright and we will be able to unfold more mysteries hidden deep inside the intricate brain structures through robust statistics. Quoting the words of Yutaka Taniyama[1], as he famously said, "It is very difficult to make good mistakes", I hope I made some good mistakes whenever I failed and they will act as landmarks for future research.

[1] A Japanese mathematican famous for his work on Taniyama-Shimura conjecture, which was later used to prove Fermat's Last Theorem by Andrew Wiles.

Appendix A

Gauss-Newton formulation

A.1 Newton's method

For a given function $f(t) : \mathbb{R}^n \rightarrow R$, if t^* be a critical point of the function f, Newton's method provides an iterative scheme for the search of the critical point t^* using second order derivatives. The Taylor expansion for the function f can be written as,

$$f(t + \Delta t) = f(t) + \nabla f(t)^T \Delta t + \frac{1}{2} \Delta t^T \nabla^2 f(t) \Delta t + \text{H.O.T}, \tag{A.1}$$

where H.O.T denotes the higher order terms which are neglected. The $\nabla^2 f$ is also called the Hessian matrix $\mathbf{H}f(t)$. The iterative scheme can be written as

$$t^{n+1} = t^n - [\mathbf{H}f(t^n)]^{-1} \nabla f(t) \tag{A.2}$$

The iteration continues until a desired convergence criteria is met. The following section shows the derivations involved in the computation of an approximate Hessian matrix for the similarity criteria defined in section 4.8.

A.2 Approximating the Hessian of the likelihood criteria

The steepest descent scheme described in chaper 4 suffers from a scaling issue. The derivative of the similarity criteria is highly scaled, making the steepest descent algorithm ineffective. In such scenarios, it is desirable to normalize the derivative under consideration using a pre-conditioner. It goes without saying that the preconditioning term should make a logical sense in the optimization setting. The inverse of the Hessian of the similarity criteria is often considered a suitable candidate in this setting.

For the ease of derivations we denote $f_i(L) = g_i^T \exp(L) g_i$. The Taylor expansion for the term $\exp[-b\, g_i^T \exp(L(y_j)) g_i]$ is:

$$\begin{aligned} \exp[-b\, f_i(L + \delta L)] &= \exp[-b\, f_i(L)] \left(1 - b\, \mathbf{Tr}\left[\frac{\partial (f_i(L))}{\partial L} \cdot \delta L^T\right]\right) \\ &= \exp[-b\, f_i(L)](1 - b\, \mathbf{Tr}\left[\partial_{G_i} \exp(L) \cdot \delta L^T\right]) \end{aligned} \tag{A.3}$$

where **Tr**[.] denotes the trace of a matrix. The Taylor expansion of the term $S_i^{LR}(x_k)(L^{HR}(y_j))$ is,

$$S_i^{LR}(x_k)(L(y_j)+\delta L(y_j)) = \sum_j \alpha_{kj} S_0^{HR}(y_j)\exp[-b\, f_i(L(y_j)+\delta L(y_j))].$$

Using equation A.3,

$$\begin{aligned} S_i^{LR}(x_k)(L(y_j)+\delta L(y_j)) &= \sum_j \alpha_{kj} S_0^{HR}(y_j)\exp[-b\, f_i(L(y_j))]\Big(1 \\ &\quad - b\,\mathbf{Tr}[\partial_{G_i}\exp(L(y_j)\cdot\delta L(y_j)^T]\Big) \\ &= \sum_j \alpha_{kj} S_0^{HR}(y_j)\exp[-b\, f_i(L(y_j))] \\ &\quad - \mathbf{Tr}\left[\sum_j b\,\alpha_{kj} S_0^{HR}(y_j)[\partial_{G_i}\exp(L(y_j)]\cdot\delta L(y_j)^T\right] \\ &= S_i^{LR}(x_k)(L(y_j)) - \mathbf{Tr}\left[\sum_j \underbrace{b\,\alpha_{kj} S_0^{HR}(y_j)[\partial_{G_i}\exp(L(y_j)]}_{-\nabla S_i^j(x_k)}\cdot\delta L(y_j)^T\right] \end{aligned}$$

. (A.4)

To simplify the notation, we define the intermediate variable,

$$\nabla S_i^j(x_k) = -b\,\alpha_{kj} S_0^{HR}(y_j)[\partial_{G_i}\exp(L(y_j)]. \tag{A.5}$$

Finally equation A.4 can be written as

$$S_i^{LR}(x_k)(L(y_j)+\delta L(y_j)) = S_i^{LR}(x_k)(L(y_j)) + \mathbf{Tr}\Big[\sum_j \nabla S_i^j(x_k)\cdot\delta L(y_j)^T\Big]. \tag{A.6}$$

As established before in section 4.14, the similarity criterion in case of a Gaussian noise is the sum of squared difference (SSD) of the observed and the predicted images. The Taylor expansion of the similarity criterion with respect to the logarithm of the diffusion tensor is given by:

$$Sim(L(y_j)+\delta L(y_j)) = \frac{1}{\sigma^2}\sum_i\sum_{x_k}[S_i(x_k)(L(y_j)+\delta L(y_j)) - \tilde{S}_i(x_k)]^2$$

Dropping the standard deviation on the noise (σ^2) term, and using the equation A.6,

$$\begin{aligned} Sim(L(y_j)+\delta L(y_j)) &\approx \sum_i\sum_{x_k}\Big[S_i(x_k)(L(y_j)+\delta L(y_j)) - \tilde{S}_i(x_k)\Big]^2 \\ &\approx \sum_i\sum_{x_k}\Big[S_i^{LR}(x_k)(L(y_j)) + \sum_j \mathbf{Tr}[\nabla S_i^j(x_k)\cdot\delta L(y_j)^T] - \tilde{S}_i(x_k)\Big]^2 \\ &\approx \sum_i\sum_{x_k}\Big[\underbrace{S_i^{LR}(x_k)(L(y_j)) - \tilde{S}_i(x_k)} + \sum_j \mathbf{Tr}[\nabla S_i^j(x_k)\cdot\delta L(y_j)^T]\Big]^2. \end{aligned}$$

Expanding the terms in the above equation using $(a+b)^2 = a^2+b^2+2ab$, by taking the terms under the braces as one single term a and remaining as b:

$$\begin{aligned} Sim(L(y_j)+\delta L(y_j)) \approx & \sum_i \sum_{x_k} \Big[(S_i^{LR}(x_k)(L(y_j)) - \tilde{S}_i(x_k)) \Big]^2 + \sum_i \sum_{x_k} \Big[\sum_j \mathbf{Tr}[\nabla S_i^j(x_k) \cdot \delta L(y_j)^T] \Big]^2 \\ & + 2 \sum_i \sum_{x_k} \Big[\Big(S_i^{LR}(x_k)(L(y_j)) - \tilde{S}_i(x_k) \Big) \sum_j \mathbf{Tr}[\nabla S_i^j(x_k) \cdot \delta L(y_j)^T] \Big] \\ \approx & \; Sim(x_k) + \sum_i \sum_{x_k} \Big[\sum_j \mathbf{Tr}[\nabla S_i^j(x_k) \cdot \delta L(y_j)^T] \Big]^2 \\ & + 2 \sum_i \sum_{x_k} \Big[\Big(S_i^{LR}(x_k)(L(y_j)) - \tilde{S}_i(x_k) \Big) \sum_j \mathbf{Tr}[\nabla S_i^j(x_k) \cdot \delta L(y_j)^T] \Big] \end{aligned}$$

The second order term in the above equation can be further simplified as follows,

$$\begin{aligned} h(\delta L) &= \sum_i \sum_{x_k} \Big[\sum_j \mathbf{Tr}[\nabla S_i^j(x_k) \cdot \delta L(y_j)^T] \Big]^2 \\ &= \sum_i \sum_{x_k} \Big[\sum_j \mathbf{Tr}[\delta L(y_j) \cdot \nabla S_i^j(x_k)^T] \Big] \Big[\sum_m \mathbf{Tr}[\nabla S_i^m(x_k) \cdot \delta L(y_m)^T] \Big] \\ &= \sum_i \sum_{x_k} \sum_m \sum_j \Big[\mathrm{Vect}(\delta L(y_j))^T \mathrm{Vect}(\nabla S_i^j(x_k)) \Big] \Big[\mathrm{Vect}(\nabla S_i^m(x_k))^T \mathrm{Vect}(\delta L(y_j)) \Big] \\ &= \sum_j \sum_m \mathrm{Vect}(\delta L(y_j))^T \underbrace{\Big[\sum_i \sum_{x_k} \mathrm{Vect}(\nabla S_i^j(x_k)) \cdot \mathrm{Vect}(\nabla S_i^m(x_k))^T \Big]}_{H_j} \mathrm{Vect}(\delta L(y_m)) \end{aligned}$$

The H_j is simplified,

$$\begin{aligned} H_j &= \sum_i \sum_{x_k} \mathrm{Vect}(\nabla S_i^j(x_k)) \cdot \mathrm{Vect}(\nabla S_i^m(x_k))^T \\ &= \sum_{x_k} \Big(- b\, \alpha_{kj} S_0(y_j) [\partial_{G_i} \exp(L(y_j))] \Big) \Big(- b\, \alpha_{km} S_0(y_m) [\partial_{G_i} \exp(L(y_m))] \Big) \\ &= \sum_{x_k} \Big(b^2 \alpha_{kj}^2 S_0^2(y_j) \Big) \sum_i [\partial_{G_i} \exp(L(y_j) (\partial_{G_i} \exp(L(y_m))^T] \end{aligned}$$

In practice, the term $\sum_i [\partial_{G_i} \exp(L(y_j))(\partial_{G_i} \exp(L(y_m))^T]$ is close to identity (Id). So, the Hessian can be approximated by:

$$H(y(j)) \approx b^2 S_0(y(j))^2 \sum_{x_k} \alpha_{kj}^2 \tag{A.7}$$

The equation A.7 gives an approximation of the Hessian for the likelihood criteria. This approximated Hessian when used as a preconditioner in the steepest descent scheme will solve the scaling issues discussed in section 4.3.2.

Appendix B

Additional results from TBSS analysis

In chapter 6 results were produced on TBSS. The regions of significant differences were thickened around the skeleton for a better visual interpretation. However, the following figures show the actual raw statistic image obtained from each statistical analysis. In all the figures, the mean FA image is used on the background for anatomical reference. The white matter skeleton is shown in green. The statistic is shown in red-yellow and is thresholded between 0.95 and 1 which corresponds to the $p < 0.05$. The color bar used for quantitative assessment is same as the one used in figure B.1. Since these are statistic images, the higher (yellow regions) the values the better it is in terms of differences.

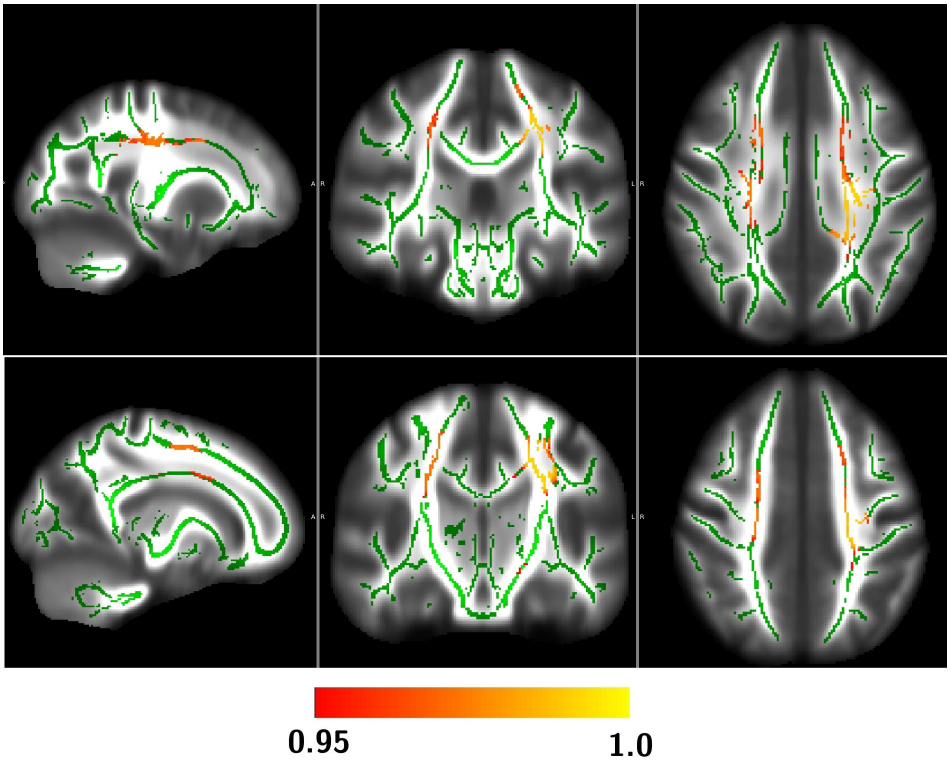

Figure B.1: Standard TBSS workflow

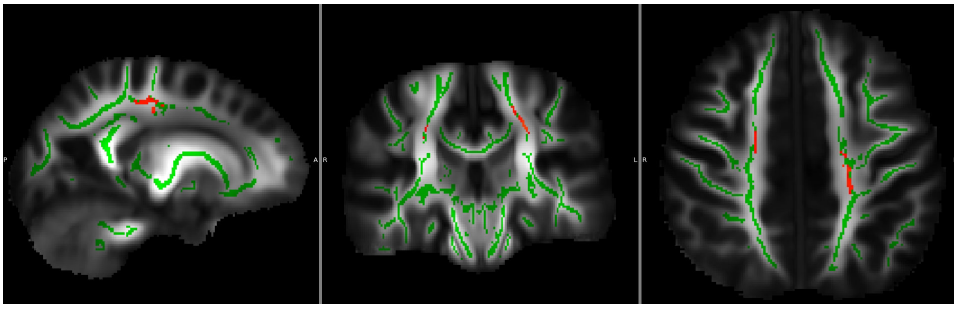

Figure B.2: TBSS using FA based registration

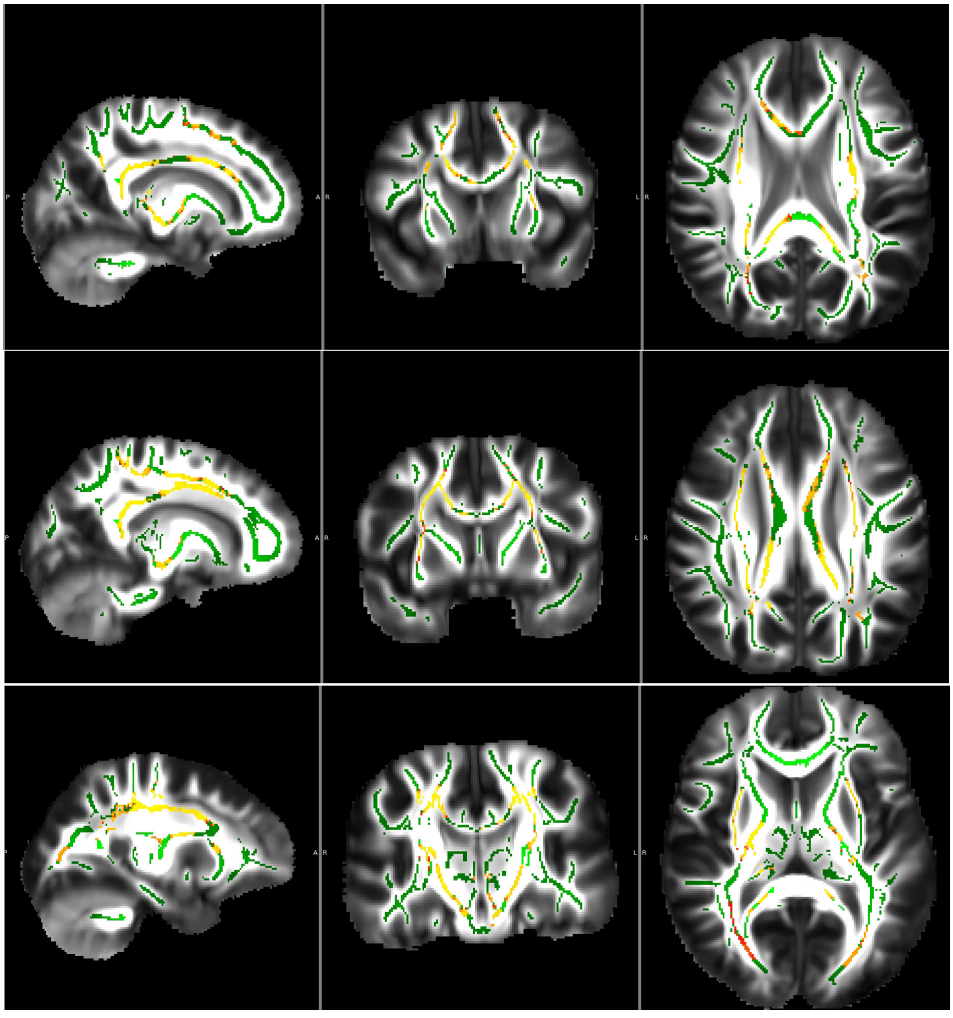

Figure B.3: TBSS DTI based registration

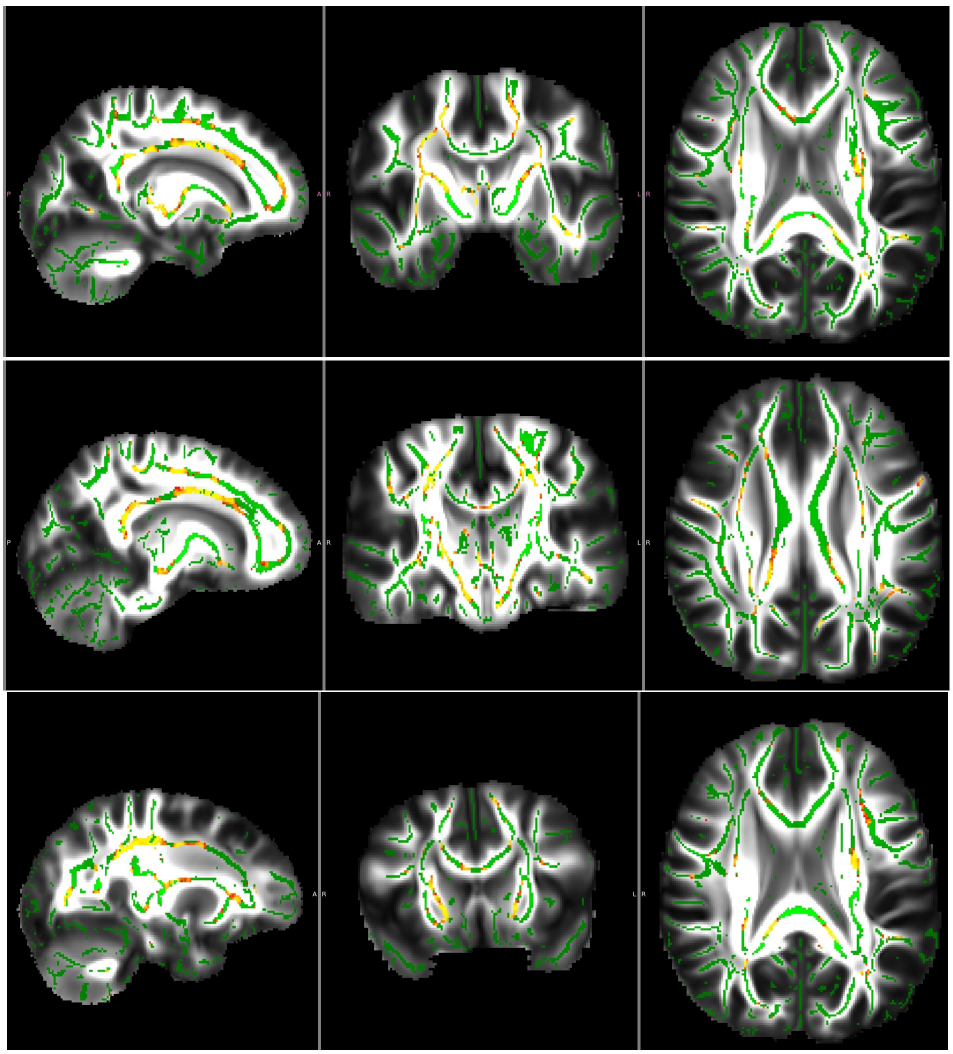

Figure B.4: TBSS univariate analysis

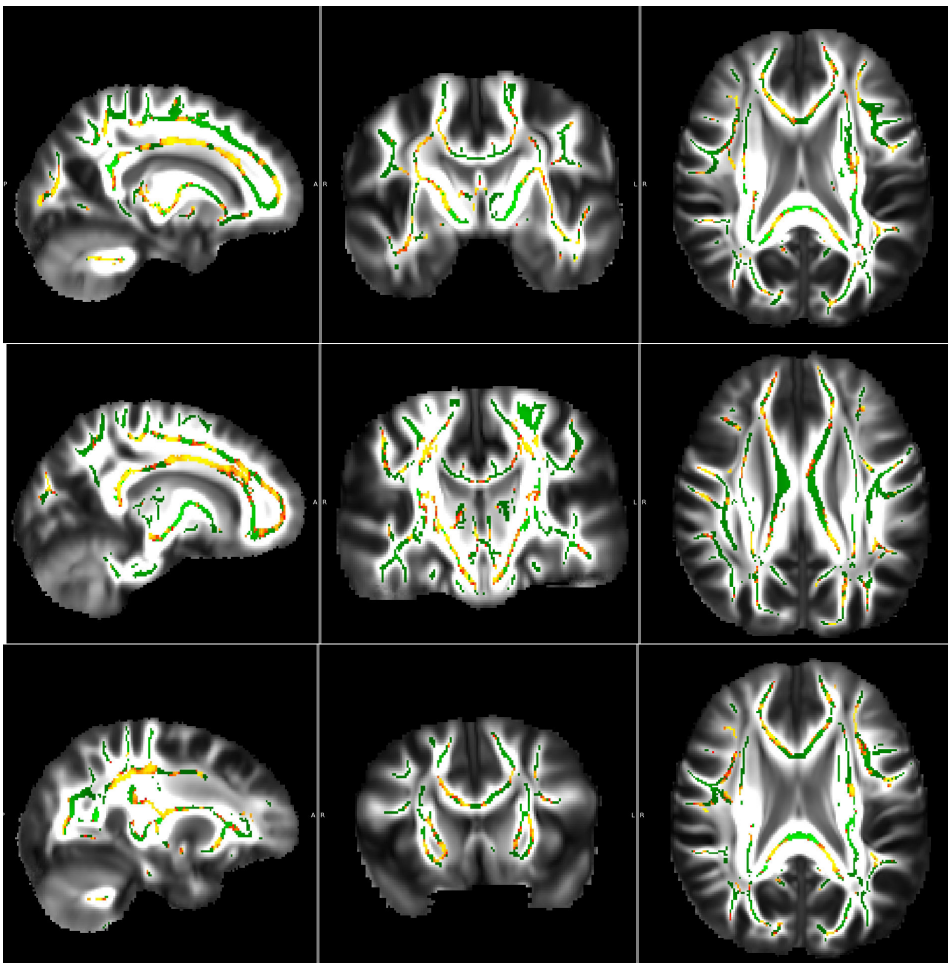

Figure B.5: TBSS multivariate analysis using Euclidean metric

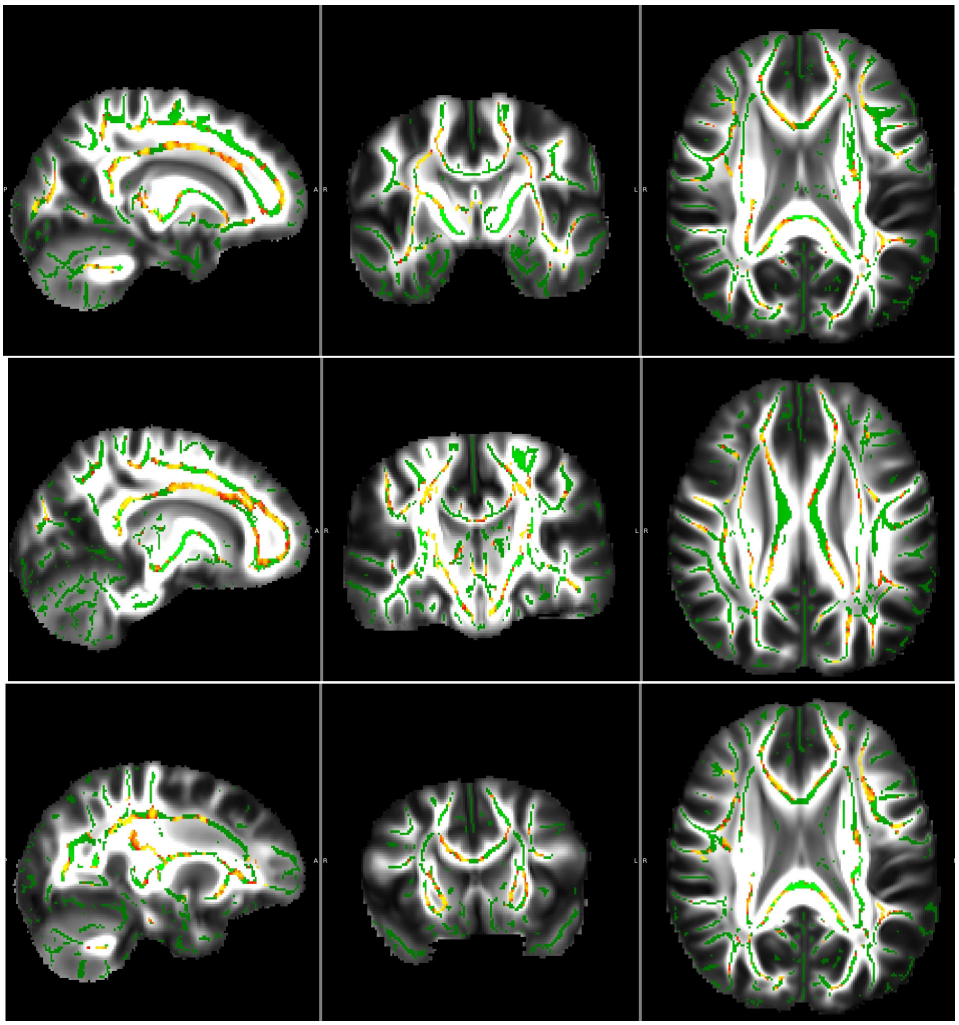

Figure B.6: TBSS multivariate Log-Euclidean metric

Bibliography

[Alexander 2001] Andrew L Alexander, Khader M Hasan, Mariana Lazar, Jay S Tsuruda and Dennis L Parker. *Analysis of partial volume effects in diffusion-tensor MRI.* Magnetic Resonance in Medicine, vol. 45, no. 5, pages 770–780, 2001. (Cited on page 65.)

[Alexander 2008] Daniel C Alexander. *A general framework for experiment design in diffusion MRI and its application in measuring direct tissue-microstructure features.* Magnetic Resonance in Medicine, vol. 60, no. 2, pages 439–448, 2008. (Cited on page 65.)

[Ances 2009] BM Ances, D Sisti, F Vaida, CL Liang, O Leontiev, JE Perthen, RB Buxton, D Benson, DM Smith, SJ Little*et al.* *Resting cerebral blood flow: A potential biomarker of the effects of HIV in the brain.* Neurology, vol. 73, no. 9, pages 702–708, 2009. (Cited on page 7.)

[Arsigny 2006a] Vincent Arsigny, Olivier Commowick, Xavier Pennec and Nicholas Ayache. *A log-euclidean framework for statistics on diffeomorphisms.* In Medical Image Computing and Computer-Assisted Intervention–MICCAI 2006, pages 924–931. Springer, 2006. (Cited on pages 70, 77 and 97.)

[Arsigny 2006b] Vincent Arsigny, Pierre Fillard, Xavier Pennec and Nicholas Ayache. *Log-Euclidean Metrics for Fast and Simple Calculus on Diffusion Tensors.* Magnetic Resonance in Medicine, vol. 56, no. 2, pages 411–421, August 2006. (Cited on pages 88, 94 and 125.)

[Ashburner 1998] John Ashburner, Chloe Hutton, Richard Frackowiak, Ingrid Johnsrude, Cathy Price, Karl Friston*et al.* *Identifying global anatomical differences: deformation-based morphometry.* Human brain mapping, vol. 6, no. 5-6, pages 348–357, 1998. (Cited on page 113.)

[Ashburner 2000] John Ashburner and Karl J Friston. *Voxel-based morphometry-The methods.* Neuroimage, vol. 11, no. 6, pages 805–821, 2000. (Cited on page 113.)

[Ashtari 2012] Manzar Ashtari. *Anatomy and functional role of the inferior longitudinal fasciculus: a search that has just begun.* Developmental Medicine & Child Neurology, vol. 54, no. 1, pages 6–7, 2012. (Cited on page 18.)

[Assaf 2005] Yaniv Assaf and Peter J Basser. *Composite hindered and restricted model of diffusion (CHARMED) MR imaging of the human brain.* Neuroimage, vol. 27, no. 1, pages 48–58, 2005. (Cited on page 66.)

[Bach 2014] Michael Bach, Frederik B Laun, Alexander Leemans, Chantal MW Tax, Geert J Biessels, Bram Stieltjes and Klaus H Maier-Hein. *Methodological considerations on tract-based spatial statistics (TBSS).* NeuroImage, vol. 100, pages 358–369, 2014. (Cited on pages 116 and 120.)

[Bammer 2001] Roland Bammer, Stephen L Keeling, Michael Augustin, Klaas P Pruessmann, Roswitha Wolf, Rudolf Stollberger, Hans-Peter Hartung and Franz Fazekas. *Improved diffusion-weighted single-shot echo-planar imaging (EPI) in stroke using sensitivity encoding (SENSE).* Magnetic resonance in medicine, vol. 46, no. 3, pages 548–554, 2001. (Cited on page 57.)

[Bammer 2003] Roland Bammer. *Basic principles of diffusion-weighted imaging.* European journal of radiology, vol. 45, no. 3, pages 169–184, 2003. (Cited on pages 59 and 62.)

[Barazany 2009] Daniel Barazany, Peter J Basser and Yaniv Assaf. *In vivo measurement of axon diameter distribution in the corpus callosum of rat brain.* Brain, vol. 132, no. 5, pages 1210–1220, 2009. (Cited on page 66.)

[Baringhaus 2004] L Baringhaus and C Franz. *On a new multivariate two-sample test.* Journal of multivariate analysis, vol. 88, no. 1, pages 190–206, 2004. (Cited on pages 123 and 124.)

[Baseer 2009] Peter Baseer and Evren Özarslan. *Introduction to Diffusion MR.* 2009. (Cited on page 52.)

[Basser 1994] Peter J Basser, James Mattiello and Denis LeBihan. *Estimation of the Effective Self-Diffusion Tensor from the NMR Spin Echo.* Journal of Magnetic Resonance, Series B, vol. 103, no. 3, pages 247–254, 1994. (Cited on page 69.)

[Bazin 2007] Pierre-Louis Bazin, Jennifer L Cuzzocreo, Michael A Yassa, William Gandler, Matthew J McAuliffe, Susan S Bassett and Dzung L Pham. *Volumetric neuroimage analysis extensions for the MIPAV software package.* Journal of neuroscience methods, vol. 165, no. 1, pages 111–121, 2007. (Cited on pages 92 and 93.)

[Behrens 2003] TEJ Behrens, MW Woolrich, M Jenkinson, H Johansen-Berg, RG Nunes, S Clare, PM Matthews, JM Brady and SM Smith. *Characterization and propagation of uncertainty in diffusion-weighted MR imaging.* Magnetic resonance in medicine, vol. 50, no. 5, pages 1077–1088, 2003. (Cited on page 65.)

[Bernal 2009] Byron Bernal and Alfredo Ardila. *The role of the arcuate fasciculus in conduction aphasia.* Brain, vol. 132, no. 9, pages 2309–2316, 2009. (Cited on page 18.)

[Breasted 2006] James Henry Breasted. The edwin smith surgical papyrus: Hieroglyphic transliteration, translation and commentary, volume 1. Kessinger Publishing, 2006. (Cited on page 27.)

[Brett 2001] Matthew Brett, Kalina Christoff, Rhodri Cusack and Jack Lancaster. *Using the Talairach atlas with the MNI template*. Neuroimage, vol. 13, no. 6, pages 85–85, 2001. (Cited on page 86.)

[Brodmann 1909] Korbinian Brodmann. Vergleichende lokalisationslehre der grosshirnrinde in ihren prinzipien dargestellt auf grund des zellenbaues. Barth, 1909. (Cited on page 84.)

[Brown 1828] Robert Brown. *XXVII. A brief account of microscopical observations made in the months of June, July and August 1827, on the particles contained in the pollen of plants; and on the general existence of active molecules in organic and inorganic bodies*. The Philosophical Magazine, or Annals of Chemistry, Mathematics, Astronomy, Natural History and General Science, vol. 4, no. 21, pages 161–173, 1828. (Cited on page 51.)

[Catani 2007] Marco Catani, Matthew PG Allin, Masud Husain, Luca Pugliese, Marsel M Mesulam, Robin M Murray and Derek K Jones. *Symmetries in human brain language pathways correlate with verbal recall*. Proceedings of the National Academy of Sciences, vol. 104, no. 43, pages 17163–17168, 2007. (Cited on page 18.)

[Catani 2008] Marco Catani and Michel Thiebaut de Schotten. *A diffusion tensor imaging tractography atlas for virtual in vivo dissections*. Cortex, vol. 44, no. 8, pages 1105–1132, 2008. (Cited on page 116.)

[Chefd'hotel 2002] Christophe Chefd'hotel, David Tschumperlé, Rachid Deriche and Olivier Faugeras. *Constrained flows of matrix-valued functions: Application to diffusion tensor regularization*. In Computer Vision-ECCV 2002, pages 251–265. Springer, 2002. (Cited on page 70.)

[Chenevert 1991] Thomas L Chenevert, James G Pipe, David M Williams and James A Brunberg. *Quantitative measurement of tissue perfusion and diffusion in vivo*. Magnetic resonance in medicine, vol. 17, no. 1, pages 197–212, 1991. (Cited on page 58.)

[Chung 2001] MK Chung, KJ Worsley, T Paus, C Cherif, DL Collins, JN Giedd, JL Rapoport and AC Evans. *A unified statistical approach to deformation-based morphometry*. NeuroImage, vol. 14, no. 3, pages 595–606, 2001. (Cited on page 114.)

[Clifford 2013] David B Clifford and Beau M Ances. *HIV-associated neurocognitive disorder*. The Lancet infectious diseases, vol. 13, no. 11, pages 976–986, 2013. (Cited on page 7.)

[Commowick 2007] Olivier Commowick and Grégoire Malandain. *Efficient Selection of the Most Similar Image in a Database for Critical Structures Segmentation*. In Proceedings of the 10th International Conference on Medical Image Computing and Computer-Assisted Intervention - MICCAI 2007, Part II, volume 4792 of *LNCS*, pages 203–210. Springer Verlag, 2007. (Cited on page 92.)

[Courouge 2004] Isabelle Courouge, Sylvain Gouttard and Guido Gerig. *Towards a shape model of white matter fiber bundles using diffusion tensor MRI*. In Biomedical Imaging: Nano to Macro, 2004. IEEE International Symposium on, pages 344–347. IEEE, 2004. (Cited on page 138.)

[De Witt Hamer 2011] Philip C De Witt Hamer, Sylvie Moritz-Gasser, Peggy Gatignol and Hugues Duffau. *Is the human left middle longitudinal fascicle essential for language? A brain electrostimulation study*. Human brain mapping, vol. 32, no. 6, pages 962–973, 2011. (Cited on page 20.)

[Destrieux 2010] Christophe Destrieux, Bruce Fischl, Anders Dale and Eric Halgren. *Automatic parcellation of human cortical gyri and sulci using standard anatomical nomenclature*. Neuroimage, vol. 53, no. 1, pages 1–15, 2010. (Cited on page 109.)

[Einstein 1905] Albert Einstein. *On the movement of small particles suspended in stationary liquids required by the molecular-kinetic theory of heat*. Annalen der Physik, vol. 17, no. 549-560, page 16, 1905. (Cited on page 52.)

[Everall 1997] IP Everall, WK Chong, ID Wilkinson, MN Paley, RJ Chinn, MA Hall-Craggs, F Scaravilli, PL Lantos, PJ Luthert and MJ Harrison. *Correlation of MRI and neuropathology in AIDS*. Journal of Neurology, Neurosurgery & Psychiatry, vol. 62, no. 1, pages 92–95, 1997. (Cited on page 112.)

[Fick 1855] Adolf Fick. *Ueber diffusion*. Annalen der Physik, vol. 170, no. 1, pages 59–86, 1855. (Cited on page 51.)

[Fillard 2007] P. Fillard, X. Pennec, V. Arsigny and N. Ayache. *Clinical DT-MRI estimation, smoothing, and fiber tracking with Log-Euclidean metrics*. Medical Imaging, IEEE Transactions on, vol. 26, no. 11, pages 1472–1482, 2007. (Cited on pages 65, 67, 70, 71, 72, 73, 94, 118 and 131.)

[Fischl 2004] Bruce Fischl, André van der Kouwe, Christophe Destrieux, Eric Halgren, Florent Ségonne, David H Salat, Evelina Busa, Larry J Seidman, Jill Goldstein, David Kennedy*et al. Automatically parcellating the human cerebral cortex*. Cerebral cortex, vol. 14, no. 1, pages 11–22, 2004. (Cited on page 109.)

[Fisher 1925] Ronald Aylmer Fisher. Statistical methods for research workers. Genesis Publishing Pvt Ltd, 1925. (Cited on page 124.)

[Fonov 2009] VS Fonov, AC Evans, RC McKinstry, CR Almli and DL Collins. *Unbiased nonlinear average age-appropriate brain templates from birth to adulthood*. NeuroImage, vol. 47, page S102, 2009. (Cited on pages 89 and 90.)

[Friston 2009] Karl J Friston. *Modalities, modes, and models in functional neuroimaging*. Science, vol. 326, no. 5951, pages 399–403, 2009. (Cited on page 91.)

[Gaffan 1991] D Gaffan and EA Gaffan. *Amnesia in man following transection of the fornix a review*. Brain, vol. 114, no. 6, pages 2611–2618, 1991. (Cited on page 21.)

[Gluhbegovic 1980] Nedzad Gluhbegovic and Terence H Williams. The human brain: a photographic guide. Harper & Row, 1980. (Cited on page 22.)

[Grabner 2006] Günther Grabner, Andrew L Janke, Marc M Budge, David Smith, Jens Pruessner and D Louis Collins. *Symmetric atlasing and model based segmentation: an application to the hippocampus in older adults*. In Medical Image Computing and Computer-Assisted Intervention–MICCAI 2006, pages 58–66. Springer, 2006. (Cited on page 84.)

[Graessner 2011] Joachim Graessner. *Frequently Asked Questions: Diffusion-Weighted Imaging (DWI)*. MAGNETON Flash, pages 6–9, 2011. (Cited on page 57.)

[Greenspan 2002] Hayit Greenspan, G Oz, N Kiryati and S Peled. *MRI inter-slice reconstruction using super-resolution*. Magnetic Resonance Imaging, vol. 20, no. 5, pages 437–446, 2002. (Cited on page 67.)

[Groot 2013] Marius de Groot, Meike W Vernooij, Stefan Klein, M Arfan Ikram, Frans M Vos, Stephen M Smith, Wiro J Niessen and Jesper LR Andersson. *Improving alignment in Tract-based spatial statistics: Evaluation and optimization of image registration*. NeuroImage, vol. 76, pages 400–411, 2013. (Cited on page 116.)

[Gudbjartsson 1995] Hákon Gudbjartsson and Samuel Patz. *The Rician distribution of noisy MRI data*. Magnetic resonance in medicine, vol. 34, no. 6, pages 910–914, 1995. (Cited on page 70.)

[Gudbjartsson 1996] Hakon Gudbjartsson, Stephan E Maier, Robert V Mulkern, István Á Mórocz, Samuel Patz and Ferenc A Jolesz. *Line scan diffusion imaging*. Magnetic Resonance in Medicine, vol. 36, no. 4, pages 509–519, 1996. (Cited on page 58.)

[Guimond 1998] Alexandre Guimond, Jean Meunier and Jean-Philippe Thirion. *Automatic computation of average brain models*. pages 631–640, 1998. (Cited on page 91.)

[Guimond 2000] Alexandre Guimond, Jean Meunier and Jean-Philippe Thirion. *Average brain models: A convergence study.* Computer vision and image understanding, vol. 77, no. 2, pages 192–210, 2000. (Cited on pages 91, 92, 93 and 116.)

[Hasan 2009] Khader M Hasan, Amal Iftikhar, Arash Kamali, Larry A Kramer, Manzar Ashtari, Paul T Cirino, Andrew C Papanicolaou, Jack M Fletcher and Linda Ewing-Cobbs. *Development and aging of the healthy human brain uncinate fasciculus across the lifespan using diffusion tensor tractography.* Brain research, vol. 1276, pages 67–76, 2009. (Cited on page 17.)

[Hashemi 2012] Ray Hashman Hashemi, William G Bradley and Christopher J Lisanti. Mri: the basics. Lippincott Williams & Wilkins, 2012. (Cited on pages 32, 38, 46, 49 and 50.)

[Haynes 2007] John-Dylan Haynes, Katsuyuki Sakai, Geraint Rees, Sam Gilbert, Chris Frith and Richard E Passingham. *Reading hidden intentions in the human brain.* Current Biology, vol. 17, no. 4, pages 323–328, 2007. (Cited on page 91.)

[Hennig 1986] J Hennig, A Nauerth and H Friedburg. *RARE imaging: a fast imaging method for clinical MR.* Magnetic Resonance in Medicine, vol. 3, no. 6, pages 823–833, 1986. (Cited on page 44.)

[Highley 1999] J Robin Highley, Margaret M Esiri, Brendan McDonald, Mario Cortina-Borja, Brian M Herron and Timothy J Crow. *The size and fibre composition of the corpus callosum with respect to gender and schizophrenia: a post-mortem study.* Brain, vol. 122, no. 1, pages 99–110, 1999. (Cited on page 23.)

[Huang 2008] Hao Huang, Can Ceritoglu, Xin Li, Anqi Qiu, Michael I Miller, Peter van Zijl and Susumu Mori. *Correction of B0 susceptibility induced distortion in diffusion-weighted images using large-deformation diffeomorphic metric mapping.* Magnetic resonance imaging, vol. 26, no. 9, pages 1294–1302, 2008. (Cited on page 136.)

[Hwang 2007] Darryl Hwang, Aarti Shetty, Amrita Rajagopalan and Manbir Singh. *Retrospective processing of DTI tractography to compensate for partial volume effects.* In Society of Photo-Optical Instrumentation Engineers (SPIE) Conference Series, volume 6511, page 70, 2007. (Cited on page 65.)

[Ichikawa 2006] Tomoaki Ichikawa, Sukru Mehmet Erturk, Utarou Motosugi, Hironobu Sou, Hiroshi Iino, Tsutomu Araki and Hideki Fujii. *High-B-value diffusion-weighted MRI in colorectal cancer.* American Journal of Roentgenology, vol. 187, no. 1, pages 181–184, 2006. (Cited on page 56.)

[Iglesias 2011] Juan Eugenio Iglesias, Cheng-Yi Liu, Paul M Thompson and Zhuowen Tu. *Robust brain extraction across datasets and comparison with*

publicly available methods. Medical Imaging, IEEE Transactions on, vol. 30, no. 9, pages 1617–1634, 2011. (Cited on pages 93 and 118.)

[Irani 1993] Michal Irani, Shmuel Peleg*et al. Motion analysis for image enhancement: Resolution, occlusion, and transparency.* Journal of Visual Communication and Image Representation, vol. 4, no. 4, pages 1993–12, 1993. (Cited on page 67.)

[Jahanshad 2014] Neda Jahanshad, Talia M Nir, Arthur W Toga, Clifford R Jack, Matt A Bernstein, Michael W Weiner, Paul M Thompson, Alzheimer's Disease Neuroimaging Initiative*et al. Seemingly Unrelated Regression empowers detection of network failure in dementia.* Neurobiology of aging, 2014. (Cited on page 135.)

[Jang 2013] Sung Ho Jang. *Diffusion tensor imaging studies on arcuate fasciculus in stroke patients: a review.* Frontiers in human neuroscience, vol. 7, 2013. (Cited on page 18.)

[Jellison 2004] Brian J Jellison, Aaron S Field, Joshua Medow, Mariana Lazar, M Shariar Salamat and Andrew L Alexander. *Diffusion tensor imaging of cerebral white matter: a pictorial review of physics, fiber tract anatomy, and tumor imaging patterns.* American Journal of Neuroradiology, vol. 25, no. 3, pages 356–369, 2004. (Cited on page 19.)

[Jenkinson 2002] Mark Jenkinson, Peter Bannister, Michael Brady and Stephen Smith. *Improved optimization for the robust and accurate linear registration and motion correction of brain images.* Neuroimage, vol. 17, no. 2, pages 825–841, 2002. (Cited on page 97.)

[Jiang 2005] Yi Jiang and Edward W Hsu. *Accelerating MR diffusion tensor imaging via filtered reduced-encoding projection-reconstruction.* Magnetic resonance in medicine, vol. 53, no. 1, pages 93–102, 2005. (Cited on page 60.)

[Jiang 2006] Hangyi Jiang, Peter van Zijl, Jinsuh Kim, Godfrey D Pearlson and Susumu Mori. *DtiStudio: resource program for diffusion tensor computation and fiber bundle tracking.* Computer methods and programs in biomedicine, vol. 81, no. 2, pages 106–116, 2006. (Cited on page 87.)

[Johansen-Berg 2009] Heidi Johansen-Berg and Timothy EJ Behrens. Diffusion mri: From quantitative measurement to in-vivo neuroanatomy. Academic Press, 2009. (Cited on page 55.)

[Jones 2010] Derek K Jones. Diffusion mri: Theory, methods, and applications. Oxford University Press, 2010. (Cited on pages 52, 60 and 61.)

[Joshi 2004] Sarang Joshi, Brad Davis, Matthieu Jomier and Guido Gerig. *Unbiased diffeomorphic atlas construction for computational anatomy.* NeuroImage, vol. 23, pages S151–S160, 2004. (Cited on page 91.)

[Keihaninejad 2013] Shiva Keihaninejad, Hui Zhang, Natalie S Ryan, Ian B Malone, Marc Modat, M Jorge Cardoso, David M Cash, Nick C Fox and Sebastien Ourselin. *An unbiased longitudinal analysis framework for tracking white matter changes using diffusion tensor imaging with application to Alzheimer's disease.* NeuroImage, vol. 72, pages 153–163, 2013. (Cited on pages 95 and 134.)

[Kier 2004] E Leon Kier, Lawrence H Staib, Lawrence M Davis and Richard A Bronen. *MR imaging of the temporal stem: anatomic dissection tractography of the uncinate fasciculus, inferior occipitofrontal fasciculus, and Meyer's loop of the optic radiation.* American Journal of Radiology, vol. 25, no. 5, pages 677–691, 2004. (Cited on page 19.)

[Kim 2010] Chan Kyo Kim, Byung Kwan Park and Bohyun Kim. *High-b-value diffusion-weighted imaging at 3 T to detect prostate cancer: comparisons between b values of 1,000 and 2,000 s/mm2.* American Journal of Roentgenology, vol. 194, no. 1, pages W33–W37, 2010. (Cited on page 56.)

[Kubicki 2002] Marek Kubicki, Carl-Fredrik Westin, Stephan E Maier, Melissa Frumin, Paul G Nestor, Dean F Salisbury, Ron Kikinis, Ferenc A Jolesz, Robert W McCarley and Martha E Shenton. *Uncinate fasciculus findings in schizophrenia: a magnetic resonance diffusion tensor imaging study.* American Journal of Psychiatry, vol. 159, no. 5, pages 813–820, 2002. (Cited on page 16.)

[Kubicki 2007] Marek Kubicki, Robert McCarley, Carl-Fredrik Westin, Hae-Jeong Park, Stephan Maier, Ron Kikinis, Ferenc A Jolesz and Martha E Shenton. *A review of diffusion tensor imaging studies in schizophrenia.* Journal of psychiatric research, vol. 41, no. 1, pages 15–30, 2007. (Cited on page 65.)

[Lao 2014] Y1 Lao, Meng Law, Jie Shi, Niharika Gajawelli1, Lauren Haas, Yalin Wang and Natasha Lepore. *A T1 and DTI fused 3D Corpus Callosum analysis in pre- vs. post-season contact sports players.* In 10th International Symposium on Medical Information Processing and Analysis (SIPAIM), 2014. (Cited on pages 92 and 137.)

[Le Bihan 1986] Denis Le Bihan, Eric Breton, Denis Lallemand, Philippe Grenier, Emmanuel Cabanis and Maurice Laval-Jeantet. *MR imaging of ifntravoxel incoherent motions: application to diffusion and perfusion in neurologic disorders.* Radiology, vol. 161, no. 2, pages 401–407, 1986. (Cited on page 56.)

[Lepore 2008] F Lepore, Caroline Brun, Yi-Yu Chou, Ming-Chang Chiang, Rebecca A Dutton, Kiralee M Hayashi, Eileen Luders, Oscar L Lopez, Howard J Aizenstein, Arthur W Toga*et al.* *Generalized tensor-based morphometry of HIV/AIDS using multivariate statistics on deformation tensors.* Medical Imaging, IEEE Transactions on, vol. 27, no. 1, pages 129–141, 2008. (Cited on page 113.)

[Liu 2004] Chunlei Liu, Roland Bammer, Dong-hyun Kim and Michael E Moseley. *Self-navigated interleaved spiral (SNAILS): Application to high-resolution diffusion tensor imaging.* Magnetic resonance in medicine, vol. 52, no. 6, pages 1388–1396, 2004. (Cited on page 61.)

[Logothetis 2008] Nikos K Logothetis. *What we can do and what we cannot do with fMRI.* Nature, vol. 453, no. 7197, pages 869–878, 2008. (Cited on page 91.)

[Lorenzen 2005] Peter Lorenzen, Brad C Davis and Sarang Joshi. *Unbiased atlas formation via large deformations metric mapping.* In Medical Image Computing and Computer-Assisted Intervention–MICCAI 2005, pages 411–418. Springer, 2005. (Cited on pages 91 and 98.)

[Lorenzi 2011] Marco Lorenzi, Nicholas Ayache and Xavier Pennec. *Schild's ladder for the parallel transport of deformations in time series of images.* In Information Processing in Medical Imaging, pages 463–474. Springer, 2011. (Cited on page 135.)

[Lorenzi 2013] Marco Lorenzi, Nicholas Ayache, Giovanni B Frisoni and Xavier Pennec. *LCC-Demons: a robust and accurate symmetric diffeomorphic registration algorithm.* NeuroImage, vol. 81, pages 470–483, 2013. (Cited on pages 94, 97 and 135.)

[Makris 2009] Nikos Makris, George M Papadimitriou, Jonathan R Kaiser, Scott Sorg, David N Kennedy and Deepak N Pandya. *Delineation of the middle longitudinal fascicle in humans: a quantitative, in vivo, DT-MRI study.* Cerebral Cortex, vol. 19, no. 4, pages 777–785, 2009. (Cited on page 19.)

[Maldonado 2013] Igor Lima Maldonado, Nicolas Menjot Champfleur, Stéphane Velut, Christophe Destrieux, Ilyess Zemmoura and Hugues Duffau. *Evidence of a middle longitudinal fasciculus in the human brain from fiber dissection.* Journal of anatomy, vol. 223, no. 1, pages 38–45, 2013. (Cited on pages 19 and 20.)

[Mani 2010] Meena Mani, Sebastian Kurtek, Christian Barillot and Anuj Srivastava. *A comprehensive Riemannian framework for the analysis of white matter fiber tracts.* In Biomedical Imaging: From Nano to Macro, 2010 IEEE International Symposium on, pages 1101–1104. IEEE, 2010. (Cited on page 116.)

[Mazziotta 2001] John Mazziotta, Arthur Toga, Alan Evans, Peter Fox, Jack Lancaster, Karl Zilles, Roger Woods, Tomas Paus, Gregory Simpson, Bruce Pike*et al. A probabilistic atlas and reference system for the human brain: International Consortium for Brain Mapping (ICBM).* Philosophical Transactions of the Royal Society of London. Series B: Biological Sciences, vol. 356, no. 1412, pages 1293–1322, 2001. (Cited on page 84.)

[Metzler-Baddeley 2012] Claudia Metzler-Baddeley, Derek K Jones, Jessica Steventon, Laura Westacott, John P Aggleton and Michael J O'Sullivan. *Cingulum microstructure predicts cognitive control in older age and mild cognitive impairment.* The Journal of Neuroscience, vol. 32, no. 49, pages 17612–17619, 2012. (Cited on page 17.)

[Meyer 2000] Joel R Meyer, Arturo Gutierrez, Bryan Mock, Delon Hebron, Jordan M Prager, Michael T Gorey and Daniel Homer. *High-b-value diffusion-weighted MR imaging of suspected brain infarction.* American journal of neuroradiology, vol. 21, no. 10, pages 1821–1829, 2000. (Cited on page 56.)

[Mielke 2009] MM Mielke, NA Kozauer, KCG Chan, M George, J Toroney, M Zerrate, K Bandeen-Roche, M-C Wang, P Vanzijl, JJ Pekar*et al.* *Regionally-specific diffusion tensor imaging in mild cognitive impairment and Alzheimer's disease.* Neuroimage, vol. 46, no. 1, pages 47–55, 2009. (Cited on page 134.)

[Mori 2008] Susumu Mori, Kenichi Oishi, Hangyi Jiang, Li Jiang, Xin Li, Kazi Akhter, Kegang Hua, Andreia V Faria, Asif Mahmood, Roger Woods, Arthur W. Toga, G. Bruce Pike, Pedro Rosa Neto, Alan Evans, Jiangyang Zhang, Hao Huang, Michael I. Miller, Peter van Zijl and John Mazziota. *Stereotaxic white matter atlas based on diffusion tensor imaging in an ICBM template.* Neuroimage, vol. 40, no. 2, pages 570–582, 2008. (Cited on pages 87, 88 and 89.)

[Müller-Oehring 2010] Eva M Müller-Oehring, Tilman Schulte, Margaret J Rosenbloom, Adolf Pfefferbaum and Edith V Sullivan. *Callosal degradation in HIV-1 infection predicts hierarchical perception: a DTI study.* Neuropsychologia, vol. 48, no. 4, pages 1133–1143, 2010. (Cited on page 112.)

[Myung 2003] In Jae Myung. *Tutorial on maximum likelihood estimation.* Journal of mathematical Psychology, vol. 47, no. 1, pages 90–100, 2003. (Cited on page 71.)

[O'Donnell 2005] Lauren O'Donnell and Carl-Fredrik Westin. *White matter tract clustering and correspondence in populations.* In Medical Image Computing and Computer-Assited Intervention–MICCAI 2005, pages 140–147. 2005. (Cited on page 138.)

[Oishi 2011] Kenichi Oishi, Michelle M Mielke, Marilyn Albert, Constantine G Lyketsos and Susumu Mori. *DTI analyses and clinical applications in Alzheimer's disease.* Journal of Alzheimer's Disease, vol. 26, pages 287–296, 2011. (Cited on page 135.)

[Peled 2001] S. Peled and Y. Yeshurun. *Superresolution in MRI: Application to human white matter fiber tract visualization by diffusion tensor imaging.*

Magnetic resonance in medicine, vol. 45, no. 1, pages 29–35, 2001. (Cited on page 66.)

[Peltier 2006] Johann Peltier, Nadine Travers, Christophe Destrieux and Stéphane Velut. *Optic radiations: a microsurgical anatomical study.* Journal of neurosurgery, vol. 105, no. 2, pages 294–300, 2006. (Cited on page 21.)

[Pfefferbaum 2003] Adolf Pfefferbaum and Edith V Sullivan. *Increased brain white matter diffusivity in normal adult aging: relationship to anisotropy and partial voluming.* Magnetic Resonance in Medicine, vol. 49, no. 5, pages 953–961, 2003. (Cited on page 65.)

[Pierpaoli 1996] Carlo Pierpaoli and Peter J Basser. *Toward a quantitative assessment of diffusion anisotropy.* Magnetic resonance in medicine, vol. 36, no. 6, pages 893–906, 1996. (Cited on page 87.)

[Pipe 2002] James G Pipe, Victoria G Farthing and Kirsten P Forbes. *Multishot diffusion-weighted FSE using PROPELLER MRI.* Magnetic resonance in medicine, vol. 47, no. 1, pages 42–52, 2002. (Cited on page 60.)

[Pipe 2006] James G Pipe and Nicholas Zwart. *Turboprop: improved PROPELLER imaging.* Magnetic resonance in medicine, vol. 55, no. 2, pages 380–385, 2006. (Cited on page 61.)

[Poupon 1999] Cyril Poupon. *Détection des faisceaux de fibres de la substance blanche pour l'étude de la connectivité anatomique cérébrale.* PhD thesis, 1999. (Cited on page 69.)

[Price 1988] Richard W Price, Bruce Brew, John Sidtis, Marc Rosenblum, Adrienne C Scheck and Paul Cleary. *The brain in AIDS: central nervous system HIV-1 infection and AIDS dementia complex.* Science, vol. 239, no. 4840, pages 586–592, 1988. (Cited on page 111.)

[Prima 2002] Sylvain Prima, Sébastien Ourselin and Nicholas Ayache. *Computation of the mid-sagittal plane in 3-D brain images.* Medical Imaging, IEEE Transactions on, vol. 21, no. 2, pages 122–138, 2002. (Cited on page 92.)

[Qin 2009] Lei Qin, Peter van Gelderen, John Andrew Derbyshire, Fenghua Jin, Jongho Lee, Jacco A de Zwart, Yang Tao and Jeff H Duyn. *Prospective head-movement correction for high-resolution MRI using an in-bore optical tracking system.* Magnetic Resonance in Medicine, vol. 62, no. 4, pages 924–934, 2009. (Cited on page 136.)

[Rorden 2008] C Rorden. *MRIcron.* version beta, vol. 12, 2008. (Cited on pages 93 and 118.)

[Sandrone 2014] Stefano Sandrone, Marco Bacigaluppoi, Marco R Galloni, Stefano F Cappa, Andrea Moro, Marco Catani, Massimo Filippi, Martin M

Monti, Daniela Perani and Gianvito Martino. *Weighing brain activity with the balance: Angelo Mosso's original manuscripts come to light.* Brain, vol. 137, no. 2, pages 621–633, 2014. (Cited on page 27.)

[Sarlls 2005] Joelle E Sarlls, Rexford D Newbould, Maria I Altbach, Arthur F Gmitro, Joachim Seeger and Theodore P Trouard. *Isotropic diffusion weighting in radial fast spin-echo magnetic resonance imaging.* Magnetic resonance in medicine, vol. 53, no. 6, pages 1347–1354, 2005. (Cited on page 60.)

[Scherrer 2012] Benoit Scherrer, Ali Gholipour and Simon K. Warfield. *Super-resolution reconstruction to increase the spatial resolution of diffusion weighted images from orthogonal anisotropic acquisitions.* Medical Image Analysis, vol. 16, no. 7, pages 1465–1476, 2012. (Cited on pages 65 and 67.)

[Schouten 2011] Judith Schouten, Paola Cinque, Magnus Gisslen, Peter Reiss and Peter Portegies. *HIV-1 infection and cognitive impairment in the cART era: a review.* Aids, vol. 25, no. 5, pages 561–575, 2011. (Cited on page 7.)

[Schwarz 2014] Christopher G Schwarz, Robert I Reid, Jeffrey L Gunter, Matthew L Senjem, Scott A Przybelski, Samantha M Zuk, Jennifer L Whitwell, Prashanthi Vemuri, Keith A Josephs, Kejal Kantarci*et al. Improved DTI registration allows voxel-based analysis that outperforms Tract-Based Spatial Statistics.* NeuroImage, vol. 94, pages 65–78, 2014. (Cited on pages 116 and 126.)

[Shinoura 2007] Nobusada Shinoura, Yuichi Suzuki, Masanobu Tsukada, Shizuka Katsuki, Ryozi Yamada, Yusuke Tabei, Kuniaki Saito and Kazuo Yagi. *Impairment of inferior longitudinal fasciculus plays a role in visual memory disturbance.* Neurocase, vol. 13, no. 2, pages 127–130, 2007. (Cited on page 18.)

[Sijbers 1998] Jan Sijbers, Arnold J Den Dekker, Paul Scheunders and Dirk Van Dyck. *Maximum-likelihood estimation of Rician distribution parameters.* Medical Imaging, IEEE Transactions on, vol. 17, no. 3, pages 357–361, 1998. (Cited on page 73.)

[Smith 2006] Stephen M Smith, Mark Jenkinson, Heidi Johansen-Berg, Daniel Rueckert, Thomas E Nichols, Clare E Mackay, Kate E Watkins, Olga Ciccarelli, M Zaheer Cader, Paul M Matthews*et al. Tract-based spatial statistics: voxelwise analysis of multi-subject diffusion data.* Neuroimage, vol. 31, no. 4, pages 1487–1505, 2006. (Cited on pages 113 and 115.)

[Stamm 2011] Aymeric Stamm, Patrick Perez and Christian Barillot. *Diffusion directions imaging (DDI).* 2011. (Cited on page 66.)

[Stamm 2012a] Aymeric Stamm, Patrick Pérez and Christian Barillot. *A new multi-directional fiber model for low angular resolution diffusion imaging.* In In-

ternational Society for Magnetic Resonance in Medicine, 2012. (Cited on page 66.)

[Stamm 2012b] Aymeric Stamm, Patrick Pérez and Christian Barillot. *A new multi-fiber model for low angular resolution diffusion MRI.* In Biomedical Imaging (ISBI), 2012 9th IEEE International Symposium on, pages 936–939. IEEE, 2012. (Cited on page 66.)

[Stamm 2014a] Aymeric Stamm, Olivier Commowick, Patrick Pérez, Christian Barillot*et al. Fast identification of optimal fascicle configurations from standard clinical diffusion MRI using Akaike information criterion.* In IEEE International Symposium on Biomedical Imaging, pages 238–241, 2014. (Cited on page 66.)

[Stamm 2014b] Aymeric Stamm, Benoit Scherrer, Olivier Commowick, Christian Barillot, Simon K Warfield*et al. Fast and robust detection of the optimal number of fascicles in diffusion images using model averaging theory.* In ISMRM Proceedings, 2014. (Cited on page 66.)

[Stejskal 1965] EO Stejskal and JE Tanner. *Spin diffusion measurements: spin echoes in the presence of a time-dependent field gradient.* The journal of chemical physics, vol. 42, no. 1, pages 288–292, 1965. (Cited on pages 55, 56 and 67.)

[Sweet 2010] Andrew Sweet and Xavier Pennec. *Log-domain diffeomorphic registration of diffusion tensor images.* In Biomedical Image Registration, pages 198–209. Springer, 2010. (Cited on pages 118, 121 and 136.)

[Talairach 1988] Jean Talairach and Pierre Tournoux. *Co-planar stereotaxic atlas of the human brain. 3-Dimensional proportional system: an approach to cerebral imaging.* 1988. (Cited on page 84.)

[Tanner 2010] Jared Tanner. *An Overview of and Introduction to the Cingulum*, 2010. (Cited on page 17.)

[Tate 2010] David F Tate, Jared Conley, Robert H Paul, Kathryn Coop, Song Zhang, Wenjin Zhou, David H Laidlaw, Lynn E Taylor, Timothy Flanigan, Bradford Naviaet al. *Quantitative diffusion tensor imaging tractography metrics are associated with cognitive performance among HIV-infected patients.* Brain imaging and behavior, vol. 4, no. 1, pages 68–79, 2010. (Cited on page 112.)

[Thomas 2011] Adam G Thomas, Panos Koumellis and Robert A Dineen. *The fornix in health and disease: an imaging review.* Radiographics, vol. 31, no. 4, pages 1107–1121, 2011. (Cited on page 21.)

[Thompson 1997] Paul M Thompson and Arthur W Toga. *Detection, visualization and animation of abnormal anatomic structure with a deformable probabilistic brain atlas based on random vector field transformations.* Medical image analysis, vol. 1, no. 4, pages 271–294, 1997. (Cited on page 91.)

[Thompson 2005] Paul M Thompson, Rebecca A Dutton, Kiralee M Hayashi, Arthur W Toga, Oscar L Lopez, Howard J Aizenstein and James T Becker. *Thinning of the cerebral cortex visualized in HIV/AIDS reflects CD4+ T lymphocyte decline.* Proceedings of the National Academy of Sciences of the United States of America, vol. 102, no. 43, pages 15647–15652, 2005. (Cited on page 7.)

[Thurnher 2005] Majda M Thurnher, Mauricio Castillo, Alfred Stadler, Armin Rieger, Brigitte Schmid and Pia C Sundgren. *Diffusion-tensor MR imaging of the brain in human immunodeficiency virus–positive patients.* American journal of neuroradiology, vol. 26, no. 9, pages 2275–2281, 2005. (Cited on page 112.)

[Torrey 1956] Henry C Torrey. *Bloch equations with diffusion terms.* Physical Review, vol. 104, no. 3, page 563, 1956. (Cited on page 55.)

[Tschumperlé 2003] David Tschumperlé and Rachid Deriche. *DT-MRI images: estimation, regularization, and application.* In Computer Aided Systems Theory-EUROCAST 2003, pages 530–541. Springer, 2003. (Cited on page 70.)

[Tucker 2004] Karen A Tucker, Kevin R Robertson, Weili Lin, J Keith Smith, Hongyu An, Yasheng Chen, Stephen R Aylward and Colin D Hall. *Neuroimaging in human immunodeficiency virus infection.* Journal of neuroimmunology, vol. 157, no. 1, pages 153–162, 2004. (Cited on page 7.)

[Türe 1997] Ugur Türe, M Gazi Yasargil and T Glenn Pait. *Is there a superior occipitofrontal fasciculus? A microsurgical anatomic study.* Neurosurgery, vol. 40, no. 6, pages 1226–1232, 1997. (Cited on page 19.)

[Tustison 2010] Nicholas J Tustison, Brian B Avants, Philip A Cook, Yuanjie Zheng, Alexander Egan, Paul A Yushkevich and James C Gee. *N4ITK: improved N3 bias correction.* Medical Imaging, IEEE Transactions on, vol. 29, no. 6, pages 1310–1320, 2010. (Cited on pages 93 and 118.)

[Vallée 2014] Emmanuel Vallée, Olivier Commowick, Camille Maumet, Aymeric Stamm, Elisabeth Le Rumeur, Catherine Allaire, Jean-Christophe Ferré, Clément De Guibert and Christian Barillot. *Statistical Analysis of White Matter Integrity for the Clinical Study of Typical Specific Language Impairment in Children.* In Computational Diffusion MRI and Brain Connectivity, pages 187–195. Springer, 2014. (Cited on page 116.)

[Vassallo 2013] Matteo Vassallo, Brigitte Dunais, Jacques Durant, Helene Carsenti-Dellamonica, Alexandra Harvey-Langton, Jacqueline Cottalorda, Michel Ticchioni, Muriel Laffon, Christine Lebrun-Frenay, Pierre Dellamonica and Christian Pradier. *Relevance of lipopolysaccharide levels in HIV-associated neurocognitive impairment: the Neuradapt study.* Journal of neurovirology, vol. 19, no. 4, pages 376–382, 2013. (Cited on pages 117 and 128.)

[Vassallo 2014] Matteo Vassallo, Jacques Durant, Virginie Biscay, Christine Lebrun-Frenay, Brigitte Dunais, Muriel Laffon, Alexandra Harvey-Langton, Jacqueline Cottalorda, Michel Ticchioni, Helene Carsenti*et al. Can high central nervous system penetrating antiretroviral regimens protect against the onset of HIV-associated neurocognitive disorders?* Aids, vol. 28, no. 4, pages 493–501, 2014. (Cited on page 117.)

[Vercauteren 2008] Tom Vercauteren, Xavier Pennec, Aymeric Perchant and Nicholas Ayache. *Symmetric log-domain diffeomorphic registration: A demons-based approach.* In MICCAI 2008, pages 754–761. Springer, 2008. (Cited on page 135.)

[Vos 2011] Sjoerd B Vos, Derek K Jones, Max A Viergever and Alexander Leemans. *Partial volume effect as a hidden covariate in DTI analyses.* Neuroimage, vol. 55, no. 4, pages 1566–1576, 2011. (Cited on page 65.)

[Wang 2004] Zhizhou Wang, Baba C Vemuri, Yunmei Chen and Thomas H Mareci. *A constrained variational principle for direct estimation and smoothing of the diffusion tensor field from complex DWI.* Medical Imaging, IEEE Transactions on, vol. 23, no. 8, pages 930–939, 2004. (Cited on pages 70 and 73.)

[Westin 2002] C-F Westin, Stephan E Maier, Hatsuho Mamata, Arya Nabavi, Ferenc A Jolesz and Ron Kikinis. *Processing and visualization for diffusion tensor MRI.* Medical image analysis, vol. 6, no. 2, pages 93–108, 2002. (Cited on pages 56 and 69.)

[Wiest-Daesslé 2007] Nicolas Wiest-Daesslé, Sylvain Prima, Pierrick Coupé, Sean Patrick Morrissey and Christian Barillot. *Non-local means variants for denoising of diffusion-weighted and diffusion tensor MRI.* In Medical Image Computing and Computer-Assisted Intervention–MICCAI 2007, pages 344–351. Springer, 2007. (Cited on page 70.)

[Wiest-Daesslé 2008] Nicolas Wiest-Daesslé, Sylvain Prima, Pierrick Coupé, Sean Patrick Morrissey and Christian Barillot. *Rician noise removal by non-local means filtering for low signal-to-noise ratio MRI: applications to DT-MRI.* In Medical Image Computing and Computer-Assisted Intervention–MICCAI 2008, pages 171–179. Springer, 2008. (Cited on page 70.)

[Wiley 1991] Clayton A Wiley, Eliezer Masliah, Mitchel Morey, Cindy Lemere, Richard DeTeresa, Marjorie Grafe, Lawrence Hansen and Robert Terry. *Neo-*

cortical damage during HIV infection. Annals of neurology, vol. 29, no. 6, pages 651–657, 1991. (Cited on page 111.)

[Williams 2002] Kenneth C Williams and William F Hickey. *Central nervous system damage, monocytes and macrophages, and neurological disorders in AIDS*. Annual review of neuroscience, vol. 25, no. 1, pages 537–562, 2002. (Cited on page 111.)

[Woods 1998] Roger P Woods, Scott T Grafton, John DG Watson, Nancy L Sicotte and John C Mazziotta. *Automated image registration: II. Intersubject validation of linear and nonlinear models*. Journal of computer assisted tomography, vol. 22, no. 1, pages 153–165, 1998. (Cited on page 87.)

[Wu 2006] Y Wu, P Storey, BA Cohen, LG Epstein, RR Edelman and AB Ragin. *Diffusion alterations in corpus callosum of patients with HIV*. American Journal of Neuroradiology, vol. 27, no. 3, pages 656–660, 2006. (Cited on page 113.)

[Zhang 2013] Tuo Zhang, Dajiang Zhu, Xi Jiang, Lei Guo and Tianming Liu. *Predicting functional cortical ROIs via joint modeling of anatomical and connectional profiles*. In Biomedical Imaging (ISBI), 2013 IEEE 10th International Symposium on, pages 516–519. IEEE, 2013. (Cited on pages 91, 100 and 137.)

[Zimmer 2010] Carl Zimmer. *100 trillion connections*. Scientific American, vol. 304, no. 1, pages 58–63, 2010. (Cited on page 1.)